Turbulent Entrainment Fluxes within the Eastern Pacific Warm Pool

John B. Mickett

A dissertation submitted in partial fulfillment
of the requirements for the degree of

Doctor of Philosophy

University of Washington

2007

Program Authorized to Offer Degree: Oceanography

ProQuest Information and Learning Company
300 North Zeeb Road
P.O. Box 1346
Ann Arbor, MI 48106-1346

University of Washington
Graduate School

This is to certify that I have examined this copy of a doctoral dissertation by

John B. Mickett

and have found that it is complete and satisfactory in all respects,
and that any and all revisions required by the final
examining committee have been made.

Chair of the Supervisory Committee:

Michael C. Gregg
Michael C. Gregg

Reading Committee:

Michael C. Gregg
Michael C. Gregg

Meghan F. Cronin

Eric A. D'Asaro

Date: 10/17/07

Signature John B

Date 10/11/07

University of Washington

Abstract

Turbulent Entrainment Fluxes within the Eastern Pacific Warm Pool

John B. Mickett

Chair of the Supervisory Committee:
Professor Michael C. Gregg
Oceanography

Mechanisms controlling turbulent entrainment fluxes, or vertical turbulent fluxes at the mixed layer base ($z = -h$), and the specific influence of heat entrainment on SST within the eastern Pacific warm pool (EPWP) are investigated using a 19-day timeseries of upper-ocean and atmospheric measurements collected in September 2001 at 10 ° N, 95° W, co-located buoy measurements, and a semi-empirical entrainment model. Buoyancy entrainment scaled with the cube of the friction velocity, u_*, and the inverse finescale (8-m) gradient Richardson number at $z = -h$, $Ri^{-1}(-h)$, with the variance of the latter largely due to both near-inertial and sub-inertial shear. These two parameters explained more than half of buoyancy entrainment variance over the 19-day timeseries. Surface buoyancy flux also modulated entrainment with heavy rainfall and intense solar radiation suppressing and buoyant convection generating entrainment. Variability of vertical gradients of temperature and salinity at $z = -h$ due to coincident large surface heat and freshwater (rainfall) fluxes and the comparable roles of temperature and salinity in determining the stratification at h were also found to modulate entrainment heat and salt fluxes produced by elevated turbulence at h.

The 19-days of entrainment observations allowed the evaluation and modification of the Niiler and Kraus (1977) (N-K) entrainment parameterization, which was used with mooring buoy measurements to obtain entrainment estimates over 2001. The three empirically-motivated modifications reduced the base N-K model root-mean-square error by 35% and mean bias from +40% to less than +2%. Mixed layer temperature budget inferences and entrainment model results indicate

that changes in h associated with Ekman pumping and Rossby waves strongly controls entrainment and, thus, SST. Large entrainment heat fluxes and large resultant drops in SST occur when Ekman pumping decreases h, exposing the concentrated temperature gradients at $z = -h$ to stronger, surface-forced turbulence. With changes in depth-averaged mixed layer temperature due to entrainment inversely proportional to h, shoaling h also amplifies the effect of these fluxes on SST changes. Entrainment may account for most of the cooling needed to offset the net annual $\sim$ 23°C of warming that would result from the divergence of the surface and penetrative heat fluxes acting alone, and, thus, strongly controls the region's SST.

TABLE OF CONTENTS

LIST OF FIGURES

LIST OF TABLES

ACKNOWLEDGMENTS

I would like to express sincere gratitude to the many people who helped me along the way on this long, difficult, but fruitful journey. To my advisor, Michael Gregg, your patience, scientific guidance and encouragement are greatly appreciated. Thank you for permitting unfettered intellectual freedom as I conducted my research while still providing insightful and needed critique that allowed me to more clearly develop and present my ideas. To both my Master's and Doctoral committees, which included my advisor, Mike Gregg, along with Matthew Alford, Tom Sanford, Meghan Cronin, Eric D'Asaro, Jeff Parsons, Andrea Ogsten, and Eric Kunze, thank you for providing invaluable guidance and demonstrating exceptional patience. It is difficult to list all of the fellow students, postdocs, researchers, and friends who provided scientific guidance, moral support and sometimes a needed distraction along the way. Certainly among them are Glenn Carter, Dave Winkel, Sam Brody, Phil Hosegood, Andrew Cookson, Steve Bayer, Laura DeSteur, Hjalmar Hatun, Jordan Dawe, Amanda Babson, Susanne Menden-Deuer, Tatiana Rynearson, Tim Crone, Neil Banas, John Crockett, J.P. Walsh, Kim Martini, and Jen MacKinnon. I also would like to thank those who helped collect the data that made this research possible, including Mike Gregg, Chris Fairall, Frank Bradley, Dave Winkel, Jack Miller, Earl Krause, Art Bartlett, Paul Aguilar, and Glenn Carter as well as the National Science Foundation for funding this research. Finally, I could not have completed this thesis without the unwavering support of my close friends and family, and in particular my wife, Amity, who deserves as much credit for its completion as I do.

Chapter 1

INTRODUCTION

Over the past several decades it has become clear that in order to predict El Niño–Southern Oscillation (ENSO) events with qualitative accuracy, we must more closely understand the role of the eastern tropical Pacific in modulating these events. As with other low-latitude ocean regions, here SST and SST gradients strongly couple the atmosphere and ocean (Lindzen and Nigam, 1987; Wallace et al., 1998; Chelton et al., 2001; Wijesekera et al., 2005). These coupled dynamics are critical to the annual evolution of SST and the associated atmospheric patterns of heating and cloudiness. It is thought that this annual evolution of the ocean and atmosphere interacts with the seasonal-to-interannual climate anomalies to influence ENSO (Zebiak and Cane, 1987; Schopf and Suarez, 1988; Battisti and Hirst, 1989; Latif et al., 1994). To date, coupled global climate models (CGCMs) have been unable to successfully reproduce key features of the eastern tropical Pacific including the annual evolution of the pattern of cool sea-surface temperature (SST) associated with equatorial upwelling and the position and intensity of the Intertropical Convergence Zone (ITCZ), suggesting that we do not yet have a basic understanding of the region's dynamics (Mechoso et al., 1995; Davey et al., 2004; Large and Danabasoglu, 2006).

One apparent problem with the various CGCMs is the sensitivity of their respective ocean general circulation models (OGCMs) to the parameterization of the vertical turbulent fluxes of heat, buoyancy and momentum within the surface boundary layer (SBL) (Ma et al., 1994). Although significant advances have been made in parameterizing these fluxes [e.g. Pollard et al. (1973); Niiler and Kraus (1977); Mellor and Yamada (1982); Price et al. (1986); Kantha and Clayson (1994); Large et al. (1994)], considerable progress needs to be made if we expect to accurately predict climate. Here we attempt to improve upon this situation by investigating processes governing the generation and modulation of vertical turbulent fluxes at the mixed layer base, or entrainment fluxes, within the eastern Pacific warm pool (EPWP) as well as the influence of these fluxes on SST on timescales of several days to a year.

The processes driving and modulating entrainment are first investigated in Chapter 2 primarily using a 19-day timeseries of atmospheric and upper-ocean observations that were collected in September 2001 within the EPWP. These findings are then used as the basis for a simple semi-empirical entrainment model that is presented and discussed in Chapter 3. Measurements from the 19-day, September 2001 timeseries are then used along with the semi-empirical entrainment model, TAO (Tropical Ocean-Atmosphere) buoy data and satellite wind data to investigate the role of entrainment heat fluxes in changing SST over both the 19-day timeseries and over 2001. With SST closely following the depth-averaged mixed layer temperature on timescales of typically several days and longer, this goal is accomplished through an investigation of the mixed layer temperature budget.

Chapter 2

THE GENERATION AND MODULATION OF TURBULENT ENTRAINMENT FLUXES WITHIN THE EASTERN PACIFIC WARM POOL

2.1 Introduction and Background

Large et al. (1994) notes that one of the major obstacles to improving surface boundary layer (SBL) turbulent flux parameterizations used in ocean general circulation models is the lack of direct observations—which are essential for testing parameterizations and identifying physics absent from the models. Although concerted observational research efforts over the past several decades have significantly advanced our understanding of turbulence in the SBL, [e.g. Oakey and Elliott (1982); Shay and Gregg (1986); Peters et al. (1988); Brainerd and Gregg (1993a); D'Asaro (2004)], we still have an incomplete understanding of SBL turbulent fluxes. This situation exists largely because of the difficulty of measuring turbulent fluxes directly (Moum, 1990; D'Asaro, 2004) and the lack of a straightforward way to estimate vertical turbulent fluxes within unstratified regions such as within active buoyant convection.

The vertical turbulent fluxes at the mixed layer base, or entrainment fluxes, are of particular importance. Here the turbulence works against typically-large vertical gradients (density, heat, momentum, etc.) to generate large vertical turbulent fluxes. Despite this importance there have been surprisingly few direct measurements of entrainment fluxes [e.g. Wijesekera and Gregg (1996); D'Asaro (2003)], and we continue to have an incomplete understanding of the various processes that control these fluxes and the relative importance of these processes. With this understanding gap in mind, this chapter uses a 19-day timeseries of extensive upper-ocean and meteorological observations collected in the eastern Pacific warm pool to investigate processes both driving and modulating entrainment fluxes. These observations were collected during the Eastern Pacific Investigation of Climate (EPIC) survey cruise in September of 2001 (Fig. 2.1). The observations indicate that entrainment fluxes were predominantly generated when turbulence produced by direct wind stress and

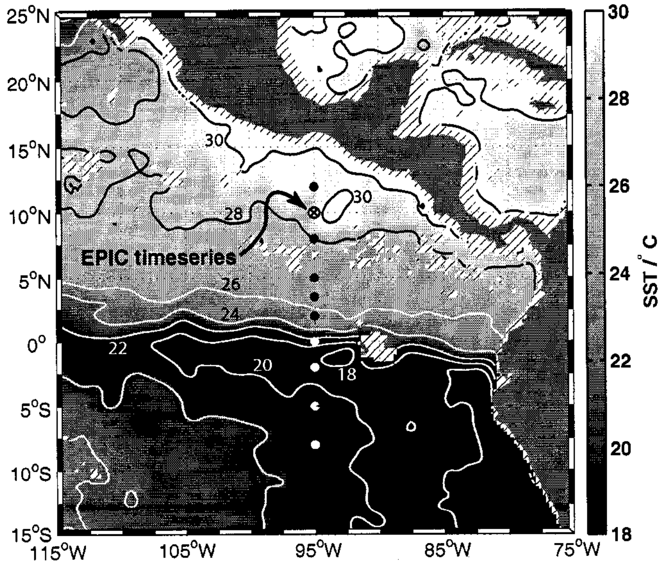

Figure 2.1: SST for the EPIC study region as measured by the TRMM (Tropical Rainfall Measuring Mission) satellite. The location of the 10° N, 95° W EPIC timeseries and TAO (Tropical Ocean-Atmosphere) buoy is indicated with other 95° W TAO buoys. SST at 0.25° resolution is smoothed over 2° and averaged over 4 days (9/11/01–9/14/01). Hatching indicates data gaps.

destabilizing surface buoyancy fluxes reached the top of the seasonal thermocline—or the mixed layer base as defined here—where it encountered typically-large vertical scalar gradients (e.g. $\frac{\partial \rho}{\partial z}$, $\frac{\partial T}{\partial z}$, $\frac{\partial S}{\partial z}$). This occurred about 1/3 of the total time and mostly in the second half of the timeseries when wind stress was large and heavy cloud cover interrupted daytime restratification due to solar heating. Despite the relatively shallow depth of the well-defined mixed layer ($\sim 25 \pm 5$ m), at other times stratification within the mixed layer—principally a consequence of the region's heavy rainfall and intense solar insolation—prevented the turbulent boundary layer from reaching the mixed layer base, consequently interrupting direct, surface-driven entrainment fluxes. During these times entrainment fluxes were very weak. Entrainment was extremely episodic, with over 70% of the total buoyancy entrainment occurring within about 16% of the 19-day timeseries and $> 50\%$ of the total heat entrainment occurring within just the last two days, or 10% of the timeseries.

Here we conduct a statistical investigation of several factors influencing entrainment using primarily linear regression analysis. Results indicate that when the turbulent boundary layer reaches the mixed layer base entrainment scales with the cube of the friction velocity, u_*^3, where $u_* = \left(\frac{|\tau|}{\rho}\right)^{1/2}$ and represents the turbulent velocity scale within the boundary layer. This result is consistent with fundamental turbulence theory (Taylor, 1935), the u_*^3 power-law in the Monin-Obukhov similarity scaling for dynamically (wind)-generated turbulent dissipation within the central boundary layer $[\varepsilon_w \propto u_*^3/(\kappa z)]$, as well as the wind stress mixing term in the entrainment parameterization of Niiler and Kraus (1977). Here κ is the empirically-derived Von Karman's constant and is equal to 0.4. Because of the relative constancy of the mixed layer depth, h, a depth-dependence of the entrainment fluxes was not observed. Although work by Oakey and Elliott (1982) and Lombardo and Gregg (1989) found a strong correlation between u_*^3 and ε within the central boundary layer, these are the first results specifically showing that this scaling describes much of the variability of turbulent entrainment fluxes at the stratified mixed layer base. Observations indicated that entrainment was also significantly correlated with wind stress when weak stratification separated the mixed layer base from the turbulent SBL. However, during these times the linear regression results show a weaker dependence with entrainment proportional to roughly $u_*^{3/2}$.

At all times the entrainment fluxes scaled with the finescale (8-m) gradient Richardson number at the mixed layer base, $Ri(-h) \equiv N(-h)^2/Sh(-h)^2$, with entrainment approximately proportional to $Ri^{-1}(-h)$. As with direct wind stress, observations suggest that the functional relationship between entrainment and $Ri^{-1}(-h)$ is stronger when the mixed layer base is exposed to the turbulent boundary layer (power of $Ri \sim -0.9$) than when the depth of the SBL was less than the mixed layer depth (power of $Ri \sim -0.5$). Although the dependence of entrainment fluxes on some form of local shear instability has long been suggested by theory [e.g. Pollard et al. (1973)], laboratory experiments [e.g. Ellison and Turner (1959); Lofquist (1960); Thorpe (1971)] and the relative success of a host of SBL vertical mixing parameterizations that are based on some form of a Richardson number [e.g. Price et al. (1986); Large et al. (1994)], there have been surprisingly few direct SBL observations showing this connection [e.g. Price (1979)]. Although instability on the scales of Ri (8-m) was likely not responsible for entrainment since measured (resolved) values of Ri were never supercritical ($< 1/4$), the strong correlation of Ri with entrainment indicates that the former was connected to—possibly facilitating—unresolved (high frequency and/or small scale) shear-instability. Furthermore, $Ri^{-1}(-h)$ was largely *uncorrelated* with the scaling for SBL turbulence expected from direct wind stress [$u_*^3/(\kappa h)$], and predominantly a function wind stress that occurred roughly 3 or more hours in the past. Thus, both the relatively slowly evolving finescale stability conditions and the (unresolved) rapidly evolving shear/turbulence due to direct wind stress are important to the generation of entrainment fluxes. Multiple regression results support this conclusion by showing that together $Ri^{-1}(-h)$ and $u_*^3/(\kappa h)$ can describe more than 65% of the log-space variance of the entrainment buoyancy flux, whereas individually they can only account for 38% and 41% percent respectively.

Entrainment buoyancy fluxes also showed a correlation with surface buoyancy flux, $J_b(0)$, although weaker than that with direct wind stress and $Ri^{-1}(-h)$. Stabilizing or negative surface buoyancy fluxes were found to suppress entrainment fluxes by shoaling the depth of the SBL and removing the SBL turbulence from direct contact with the large vertical gradients at the mixed layer base. Paralleling the findings of Wijesekera and Gregg (1996) and Anderson et al. (1996) within the western Pacific warm pool, heavy rainfall (> 0.4 m over 19 days) and associated negative surface buoyancy flux was found to be particularly effective at suppressing the penetration of SBL turbulence and thus entrainment fluxes. Positive or destabilizing surface buoyancy fluxes elevated entrainment by driving buoyant convection that deepened the turbulent SBL to the base of the mixed layer. Consequently, a diel pattern of surface buoyancy fluxes over much of the first half of the timeseries resulted in a diurnal modulation of buoyancy entrainment. Relatively weak entrainment fluxes over the first half of the timeseries when winds were weak but nighttime convection robust indicates that destabilizing surface buoyancy fluxes are not as effective as direct wind stress at generating entrainment. Thus, the primary role of $J_b(0)$ within the EPWP may not be the direct generation of entrainment fluxes through mechanical mixing (Imberger and Ivey, 1991), but instead the creation/destruction of mixed layer stratification which influences the ability of wind-driven SBL turbulence and shear (momentum) to penetrate to the mixed layer base.

These observations also show that near-inertial motions generated by local wind stress dominated the measured shear variance in the entrainment zone and, thus, were an important mechanism for generating entrainment fluxes. Wind-driven near-inertial (frequency close to the Coriolis frequency, f) internal motions have long been known to contribute significantly to the shear at the mixed layer base, and upper-ocean mixing models have shown that increases in near-inertial shear are linked to mixed layer entrainment events (Pollard et al., 1973; Large and Crawford, 1995). However, these observations show that relatively steady sub-inertial shear—although relatively weak—was also important. Over the first half (9 days) of the timeseries—a period of light winds following local generation of strong mixed layer near-inertial motions—the linear addition of the near-inertial and sub-inertial shear resulted in a modulation of $Sh^2(-h)$, $Ri^{-1}(-h)$, and thus entrainment at a near-inertial period. Three entrainment events which were influenced by this near-inertial variability of Ri^{-1} contributed to about 20% of the timeseries-total entrainment heat flux.

Finally, results also show that the variability of $\frac{\partial T}{\partial z}$ and $\frac{\partial S}{\partial z}$ at the mixed layer base occurring on timescales of hours to several days at times modulated the entrainment heat and salt fluxes produced by elevated turbulence. Changes in the vertical gradients of T and S primarily resulted from the combined cooling and freshening the mixed layer in response to large positive surface heat fluxes and intense rainfall. The significant reduction of $\frac{\partial T}{\partial z}$ during one two-day storm had the effect of reducing the timeseries-averaged entrainment heat flux by roughly 30%.

This chapter begins by defining the methodology (Section 2.2), including nomenclature, sampling and the approach for estimating the vertical turbulent fluxes. Section 2.3 presents the general upper-ocean observations, the atmospheric forcing and the subsequent SBL response to this forcing to provide a context Section 2.4, which describes the turbulent entrainment flux observations and investigates several mechanisms controlling these fluxes. Section 2.5 reviews the findings, discusses the larger implications, and suggests future research direction.

2.2 Methodology

2.2.1 Boundary Layer Nomenclature and Definitions

Prior to discussing the observations it is necessary to clarify the terminology used in this and subsequent chapters. As noted by Brainerd and Gregg (1995) the definition of the mixed layer may vary considerably depending on the objective of the analysis, or specifically the timescale of interest. In all definitions it refers to the unstratified or weakly-stratified upper layer of the ocean that is directly influenced by the atmosphere.

Here the mixed layer refers to the fraction of the upper-ocean above the seasonal pycnocline, describing a layer that is unstratified or weakly stratified has been well-mixed by direct surface forcing within the recent past (several days to a week) (Figure 2.2). This definition was chosen because of both limitations in the turbulence measurements (only depths $\gtrsim$ 8 m) and the primary goal of calculating the mixed layer temperature budget (Chapter 4), which is greatly simplified by defining h as above.

Using profiles of density with 1-m vertical resolution and sampled at $\sim$20-minute intervals, a vertical density gradient threshold is used to identify the above-defined mixed layer depth, with h equal to the maximum depth at which $\Delta\sigma_\theta/\Delta z > -0.07$ kg m^{-4}, or equivalently the 1-m buoyancy frequency squared $N^2 < 6.7 \times 10^{-4}$ s^{-2} ($\sim$15 cph) when decreasing in depth from the seasonal thermocline.

This approach has the advantage of excluding short-lived instances when the transient pycnocline (see Fig. 2.2) is strongly stratified. This definition captures the depth of the sharp, persistent density interface between the seasonal pycnocline and the weakly stratified/unstratified water above to result in a relatively steady value of h ($\sim$ 25 $\pm$ 5 m). It is also rather robust for the conditions encountered in that subsequent increases in the minimum stratification result in only small increases in h. With the maximum depth of the SBL (h_b) reaching h at least every several days over the EPIC timeseries this specific definition of h appears to be appropriate given the research objectives. However, it is important to note that the influence of SBL turbulent fluxes on SST and potential air-sea coupling may be unresolved on timescales of less than this period. The depth of the *instantaneous* mixed layer, h_i, or the layer that is always well-mixed and extends from the surface to the top of the transient pycnocline, is estimated using the canonical mixed layer definition of the shallowest depth where $[\sigma_\theta(z) - \sigma_\theta(2m)] \geq 0.01$ kg m^{-3}. A close agreement between the depth of the *instantaneous* mixed layer and the maximum penetration depth of the largest density overturns within the SBL suggests that this is an appropriate definition.

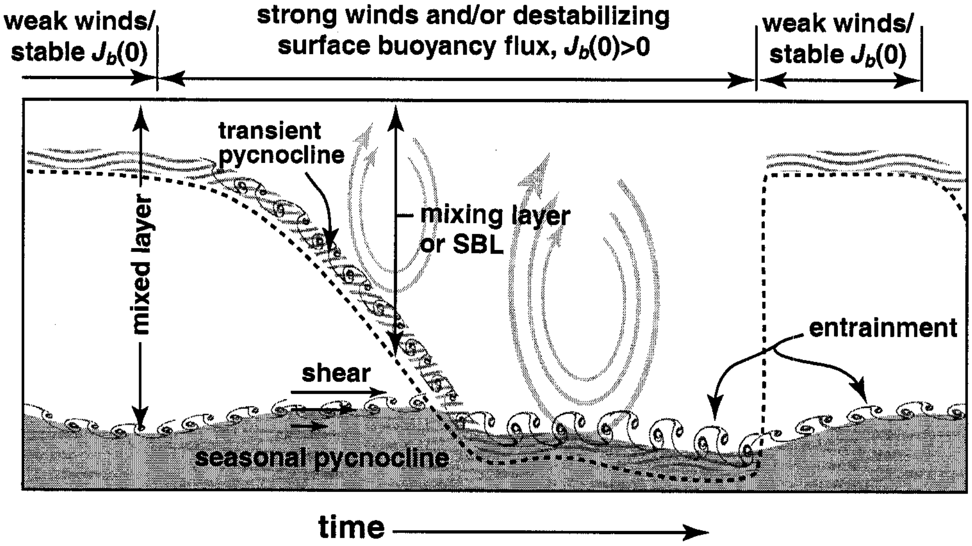

Figure 2.2: Schematic showing surface boundary layer (SBL) time-evolution and terminology, with the maximum depth of the SBL or mixing layer indicated by the dashed line. Rapid shoaling of the SBL depth occurs when the restratifying influence of stabilizing surface buoyancy fluxes overcome the turbulence production of direct wind stress.

The *mixing* layer as defined by Brainerd and Gregg (1995) is the depth range over which surface fluxes are actively being mixed by direct, surface-forced turbulence. Since this definition is

Table 2.1: SBL definitions

Variable	Symbol	Approximation/Definition
mixed layer depth	h	greatest depth above seasonal thermocline where $N^2 < 6.7 \times 10^{-4}\ \mathrm{s}^{-2}$
instantaneous mixed layer depth	h_i	shallowest depth where $[\sigma_\theta(z) - \sigma_\theta(2\ \mathrm{m})] \geq 0.01\ \mathrm{kg\ m}^{-3}$
SBL (mixing layer) depth	h_b	shallowest depth where $\varepsilon(z) \leq 1 \times 10^{-8}\ \mathrm{W\ kg}^{-1}$
entrainment depth	h_e	$h_e = h$

equivalent to the canonical definition of the surface boundary layer (SBL), here the mixing layer is simply referred to as the SBL to avoid confusion between *mixed* and *mixing* (Fig. 2.2). The SBL extends from the surface to the maximum penetration depth of the directly surface-forced turbulence, h_b. As has been shown in a number of previous observations and large eddy simulation (LES) results, the SBL is capable of penetrating up to 10's of meters into the seasonal pycnocline (Large et al., 1986; Brainerd and Gregg, 1993a; Large and Crawford, 1995; Wang et al., 1998). Here direct turbulence measurements allow physically-based estimates of the extent of the SBL, with the SBL depth, h_b, quantified as the shallowest depth at which the dissipation rate of turbulent kinetic energy, ε, falls below a threshold value. This value (1×10^{-8} W kg^{-1}) is set as a typical background/pycnocline dissipation level with the intention of separating directly surface-forced turbulence from background/pycnocline turbulence due to dynamics other than direct surface forcing, and is consistent with the definition used by Lombardo and Gregg (1989); Brainerd and Gregg (1993a) and Brainerd and Gregg (1995). As will be shown, this choice typically captures the strong transition between turbulent and quiescent regions of the upper-ocean. It is important to note here that since ε measurements were restricted to depths > 8 m and are somewhat suspect $\lesssim 12$ m due to the ship's propellor wash, estimates of the penetration depth of the SBL (h_b) are restricted to depths greater than 8 m. Thus, values of h_b are potentially over-estimated when the transient pycnocline (see 2.2) is strong and shallow ($\lesssim$ 12 m). However, a comparison to the penetration depth of potential and active density overturns within the upper $\sim$30 m suggests that this is a good estimate for

h_b. Here entrainment fluxes are simply defined as the vertical turbulent fluxes at the mixed layer base, and, thus, the entrainment depth, h_e, is equivalent to the mixed layer depth. This definition is used for a number of reasons including limitations of the turbulence measurements and of the assumptions used to estimate J_b as well as a desire to estimate turbulent fluxes along a relatively constant interface for mixed layer budget calculations.

Although this definition departs somewhat from the strict definition of the "instantaneous" entrainment depth which refers to the depth at which the vertical turbulent buoyancy flux, $J_b \equiv -\frac{g}{\rho}\overline{\rho' w'}$ (where the overbar denotes some amount of time-space averaging), is the most negative *within* the SBL (Large et al., 1994) (equivalently the depth of the greatest upward flux of density), observations indicate that the definition used here is consistent with the instantaneous definition in a time-averaged sense. Specifically, as will be shown, a timeseries-averaged turbulent buoyancy flux profile shows a local maximum of negative J_b at h—as well as local maxima in negative (downward) heat (J_q) and positive (upward) salt (J_s) fluxes. One implication of this choice for the entrainment depth is that the entrainment fluxes are not *directly* influenced by SBL turbulence when $h_b < h$. For this reason, when investigating potential dynamical dependencies between entrainment and other variables we separate observations into times when $h_b \geq h$ (when h can be considered in a instantaneous sense) and times when $h_b < h$.

2.2.2 *Sampling*

The observations presented in this chapter are from a timeseries of upper-ocean microstructure and velocity profiles complimented by extensive atmospheric measurements collected within the EPWP from September 12 to October 1, 2001 aboard the R/V *R. H. Brown* while the ship maintained position within 5 nm (9.25 km) radius of 9° 56′ N, 95° W (hereafter referred to as the EPIC timeseries) (Fig. 2.1). The primary oceanographic instruments were the free-falling, loosely-tethered Modular Microstructure Profiler (MMPs 1-3) and a hull-mounted, 150 khz, narrowband RD Instruments ADCP. The MMPs recorded profiles of microscale pressure, conductivity, temperature, and velocity shear to nominally 300 m about every 20 minutes, and the ADCP recorded profiles of upper-ocean finescale velocity to about 250 m every minute. The MMP microscale velocity shear and pressure measurements allowed the calculation of the dissipation rate of turbulent kinetic energy, ε, which, as will be discussed, was used along with the other MMP measurements to estimate turbulent entrainment fluxes. In addition to providing estimates of absolute upper-ocean velocity when used along with shipboard GPS, ADCP data were also used to estimate finescale vertical shear, Sh, which along with MMP density data allowed estimates of the finescale gradient Richardson number, Ri. Appendix A provides more details of MMP and ADCP sampling methods. Surface heat and buoyancy fluxes were calculated using the COARE 2.6 algorithm (Fairall et al., 1996). The vector surface wind stress used to force the Pollard and Millard (1970) slab model was computed with the Large and Pond (1981) bulk algorithm. All dates and times referenced are based upon UTC and, when indicated, yearday values are days elapsed in 2001 starting with yearday zero at midnight on December 31, 2000.

2.2.3 *Estimating vertical turbulent fluxes*

Because of large time-variability in turbulence levels as well as the presence of positive turbulent buoyancy fluxes associated with buoyancy-driven (free) convection, estimating turbulent fluxes within the SBL requires exceptional care. Vertical fluxes are estimated using the dissipation method presented by Osborn (1980) and reviewed by Gregg (1987) and (Moum, 1990) (Appendix B addresses the assumptions of this approach and includes details of flux estimates), which assumes that the turbulent kinetic energy (TKE) equation reduces to a balance between shear production (l.h.s. of Eqn. 2.1), dissipation (ε) and buoyant suppression (or the vertical turbulent buoyancy flux, J_b) for a one-dimensional, stratified shear flow. Using tensor notation this is formally

$$\overline{u_i'u_j'}\frac{\partial U_i}{\partial x_j} = J_b - \varepsilon \quad [\mathrm{W\ kg^{-1}}]\,. \tag{2.1}$$

The validity of this balance, which is supported by scaling arguments (Monin and Yaglom, 1975) as well as LES results, is discussed in Appendix B. In short, observations indicate that although instantaneous values for ε, J_b and shear production may not uphold the assumed balance, some amount of time-averaging will improve the applicability of the assumptions. An averaging window of 4 hours is taken to be sufficient for the EPIC timeseries data. Although the turbulent fluxes were not measured directly (i.e. the correlations of the turbulent velocities with fluctuating scalars or other velocities), if we assume that the fluxes behave similarly to molecular diffusion, they can be represented by a turbulent diffusivity multiplied by a background gradient—an assumption referred to as the eddy coefficient and mixing length hypothesis. Specifically this gives:

$$J_b \equiv -\frac{g}{\rho}\overline{\rho' w'} = -\frac{g}{\rho} K_\rho \frac{\partial \rho}{\partial z} \quad = \quad -K_\rho N^2 \,, \tag{2.2}$$

where K_ρ is the vertical turbulent diffusivity of density. Combining the above relation and the balanced TKE equation (Eqn. 2.1) yields:

$$K_\rho \; = \; \frac{R_f}{(1 - R_f)} \frac{\varepsilon}{N^2} = \gamma \frac{\varepsilon}{N^2} \,. \tag{2.3}$$

where R_f is the flux Richardson number and equivalent to the ratio of buoyant suppression to shear production $\left(R_f \equiv J_b / \overline{u_i' u_j'} \frac{\partial U_i}{\partial x_j}\right)$ and γ is the mixing efficiency. Osborn (1980) has shown that $R_f \leq 0.15$ giving the familiar relationship for the vertical eddy diffusivity for density:

$$K_\rho < 0.2 \frac{\varepsilon}{N^2} \,. \tag{2.4}$$

As discussed in Appendix B, the validity of using the canonical flux Richardson number ($R_f = 0.15$) was tested using a functional form for a general flux Richardson number presented in Ivey and Imberger (1991). Results show that within stratified regions of the mixed layer and upper thermocline, R_f was surprisingly close to the canonical value. Additionally, including all the mechanical energy terms in the generalized form of R_f suggests that the requirement of a balance between production, dissipation and buoyant suppression may not be entirely necessary to obtain reasonable estimates of turbulent buoyancy flux (Ivey and Imberger, 1991).

Assuming that the mixing of scalars can be estimated with a single eddy diffusivity, the turbulent diffusivity for heat K_T and salt K_S are set to be equal to K_ρ ($K_\rho = K_T = K_S$). The vertical turbulent flux equations are then:

$$\text{heat}: \quad J_q \cong -\rho c_p K_T \frac{\partial T}{\partial z} \tag{2.5}$$

$$\text{salt}: \quad J_s \cong -K_S \frac{\partial S}{\partial z} \tag{2.6}$$

$$\text{buoyancy}: \quad J_b \cong -K_\rho N^2 < |-0.2\varepsilon| \,, \tag{2.7}$$

with c_p the specific heat of water ($\approx 4000\ \mathrm{J\ kg^{-1}\ K^{-1}}$) and $N^2 = -g/\rho_0\,(\partial\sigma_\theta/\partial z)$ is the buoyancy-frequency squared. Here the convention is that positive turbulent fluxes indicate an upward flux of the scalar quantity.

The diapycnal diffusivity of density is estimated using an upper bound for the mixing efficiency ($\gamma = 0.2$), or $K_\rho = 0.2\varepsilon/N^2$. This does not, however, represent an upper bound of the flux estimates since there is roughly a factor of two uncertainty in ε measurements (Peters et al., 1988; Moum et al., 1995). For simplicity the turbulent buoyancy flux, J_b, is estimated directly from time-averaged values of ε (Eqn. 2.7). Because of inadequate vertical resolution of the shear flow ($\frac{\partial U_i}{\partial z}$), estimates of the vertical eddy viscosity, K_m, (which can also be estimated from Equation 2.1) are unrealistic and are not presented. Also, since the assumption of a stratified shear flow is not met in regions undergoing buoyant convection (buoyant production and transport terms of the TKE equation are large), these regions preclude the estimation of turbulent fluxes by this method. Finally, as the ship's propellor wash may significantly contribute to ε near the surface, dissipation data < 12 m are not used in turbulent flux estimates. Thus, there are large time and space gaps in the turbulent flux estimates above the mixed layer depth.

Turbulent buoyancy fluxes (J_b) were computed using 1-m ε data that were averaged over 4 hours. Entrainment buoyancy fluxes [$J_b^e \equiv J_b(-h)$] were specifically computed by averaging ε over a 4-m depth range centered on the mixed layer depth and then in time (4 hrs). Profiles of ε indicate that 4-m window for depth-averaging largely spans a local maximum of ε (or maximum of -J_b). Diapycnal diffusivity, K_ρ, was computed using 1-m, 4-hr averaged ε as above and 4-hr averaged N^2 that was computed by first-differencing 1-m σ_θ data over 2 m. Turbulent fluxes of heat (J_q) and salt (J_s) were computed using 4-hour averaged $\frac{\partial\theta}{\partial z}$ and $\frac{\partial S}{\partial z}$ respectively. As with J_b^e, the entrainment fluxes of heat (J_q^e) and salt (J_s^e) were computed by averaging J_q and J_s over a 4-m depth range about h.

2.3 Average Mixed Layer Properties and Time-Evolution

2.3.1 Timeseries-average profiles

The EPIC timeseries upper-ocean observations within the EPWP show a relatively shallow mixed layer ($\sim$25 m) that was exceptionally warm with SST always warmer than 28°C and at times exceeding 30°C (Fig. 2.3a). The shallow mixed layer depth/thermocline within the EPWP contrasts with observations showing a relatively deep thermocline ($>$ 60 m) within the western Pacific warm pool (WPWP) (Wijesekera and Gregg, 1996). At all times SST was greater than the air temperature at the ocean surface, indicating an unstable atmospheric boundary layer (Pyatt et al., 2003) and consistently positive (upward) sensible heat fluxes at the air-sea interface (Fig. 2.5c). Due to the net freshwater input from the region's heavy rainfall (Fig. 2.5b), the mixed layer was significantly fresher than the pycnocline. On average, vertical salinity gradients were found to contribute to most of the density stratification within the mixed layer and roughly half of the stratification at the mixed layer base. As noted by Wijesekera et al. (2005), the slight difference in the depth of the top of the halocline and thermocline, with the former several meters shallower than the latter, may be a consequence of solar penetrative radiation. A timeseries-averaged profile of 4-m N^2 (Fig. 2.3) shows the rapid increase in stratification at the mixed layer base, with $\overline{N_4^2}$ (where the over-bar denotes the time-average) remaining relatively constant for the next $\sim$10–20 m. Below about 40–50 m, N_4^2 then decays steadily with depth to near canonical open-ocean thermocline stratification values ($N_0^2 = 2.7 \times 10^{-5} s^{-2}$) at about 200 m. To avoid ambiguities with the treatment of unstratified regions of the mixed layer in the time-mean profile of N_4^2, the time-average profile of N_4^2 was computed from the time-averaged profiles of potential density. Profiles of 4-m shear-squared (Sh_4^2) [1] (where $Sh^2 = Sh_x^2 + Sh_y^2$) showed values greater than N_4^2 within the mixed layer and values less than N_4^2 below the mixed layer, with a local peak in Sh_4^2 at h.

Both average profiles of diapycnal diffusivity of density (K_ρ) and TKE dissipation rate (ε) (Fig. 2.3b, c) show a rapid, roughly exponential decay with depth within the mixed layer and upper

---

[1] For timeseries-averaged profiles, noisier 4-m shear could be used instead of 8-m shear because the large averaging period sufficiently reduced the high noise levels.

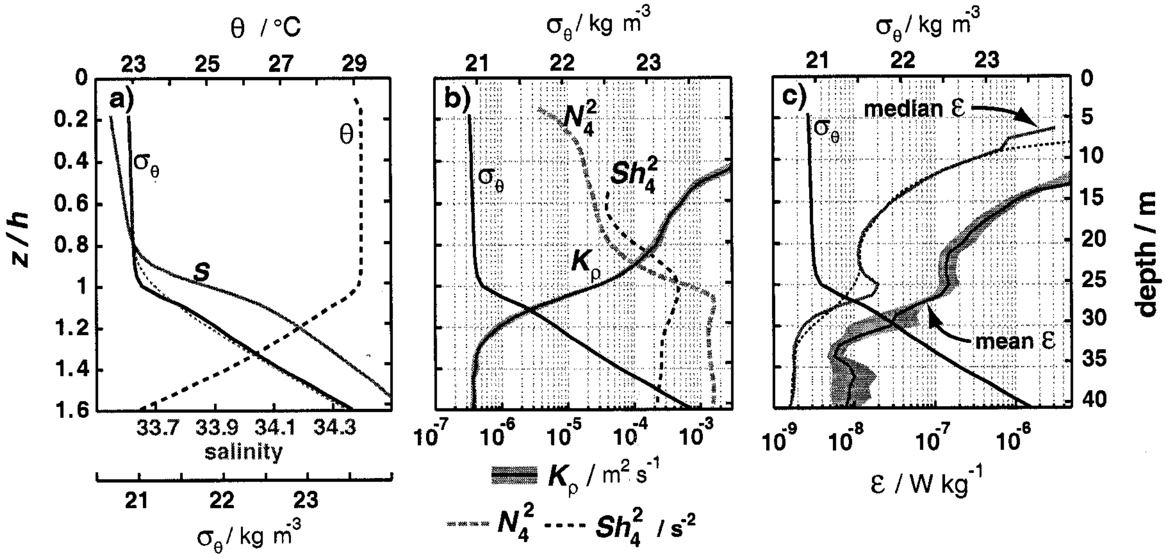

Figure 2.3: a) Timeseries-mean profiles of potential temperature (θ), salinity (S) and potential density (σ_θ) with the depth normalized by the mixed layer depth, h, to reduce blurring of vertical structure that would result from time-averaging variations in h. The profile of σ_θ without this normalization is shown with the thin, gray dashed line. The timeseries-mean depths corresponding to the normalized depth values are shown on the right axis with labeling given in plot (c). b) as in (a) but timeseries-mean profiles of 4-m buoyancy frequency-squared (N_4^2), 4-m shear-squared (Sh_4^2), diapycnal diffusivity (K_ρ) and σ_θ for reference. Here the mean N_4^2 profile was computed from the mean profile of σ_θ and the mean K_ρ profile excludes unstratified regions of the mixed layer from the time-average. c) as in (a) but timeseries-median (solid gray) and mean (thin black) TKE dissipation rate (ε). The timeseries-median profile of ε without h-normalization (dashed black) and σ_θ (heavy black) are also shown. Bootstrap 95% confidence intervals of the sampled mean are indicated with gray shading about the time-mean K_ρ and ε profiles.

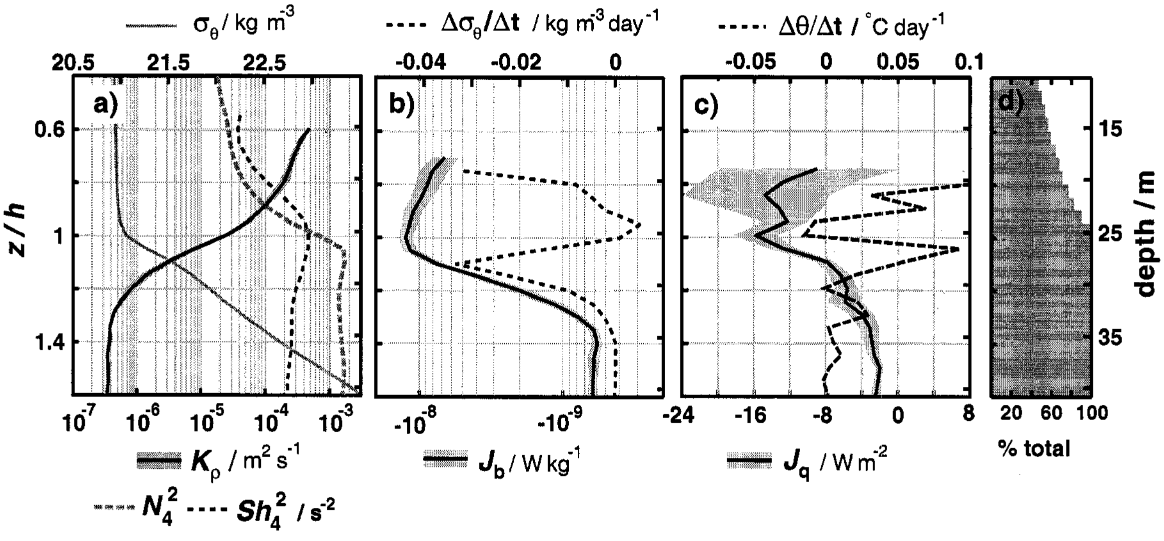

Figure 2.4: Timeseries-averaged profiles along depths normalized by h: a) $\overline{\sigma_\theta}$ (gray solid), $\overline{N_4^2}$ (gray dashed), $\overline{Sh_4^2}$ (black dashed) and $\overline{K_\rho}$ (black solid). b) J_b (solid line) and time-changes in σ_θ due to $\frac{\partial J_b}{\partial z}$ (dashed). c) J_q (solid line) and time-changes of θ due to $\frac{\partial J_q}{\partial z}$ (dashed). d) % of total profiles used in turbulent flux and diffusivity averages (convecting and unstratified regions are necessarily excluded). The average depth corresponding to the normalized depths is given on the right axes. Gray shading about $\overline{K_\rho}$ and flux profiles indicates the 95% bootstrap confidence intervals.

thermocline. As previously discussed, here K_ρ is only calculated in stratified regions where N^2 is well-defined and, thus, the timeseries-average excludes much of the depth-time coverage within the mixed layer. It is worth noting that at about 1.4 h or roughly 35 m, $\overline{K_\rho}$ has dropped to near molecular levels at $\sim 4 \times 10^{-7}$ m^2 s^{-2}. The TKE dissipation rate also shows very low values at this depth with $\overline{\varepsilon} \approx 2 \times 10^{-9}$ W kg^{-1}. For ε, the timeseries-median value is shown in addition to the timeseries-mean to emphasize the persistent vertical structure and to de-emphasize isolated mixing events. A local peak in ε at h is present in both profiles but is more apparent in the timeseries-median profile. It is absent from the timeseries-median profile that is not normalized by h (Fig. 2.3c, dashed line), showing how these features can be washed out by averaging along a constant depth. This local peak in $\overline{\varepsilon}$ is a feature that is often observed in large eddy simulations (LES), and in particular was observed in a LES study modeling a westerly wind burst in the WPWP (Skyllingstad et al., 1999). This LES study found that the local maximum in $\overline{\varepsilon}$ at the mixed layer base was due to local shear production, suggesting that this may also be the case for these observations.

The observation of a local peak in ε at $z = -h$ also supports the choice for the entrainment depth ($h_e = h$) since there is a resultant local minimum in the vertical turbulent buoyancy flux at this depth (Fig. 2.4). Again, here $\overline{J_b}$ is computed after excluding regions of the mixed layer that are buoyantly convecting or unstratified since these areas do not meet the requirements of the dissipation method for determining J_b. The percent of the profiles used at a particular normalized depth in the time-average of J_b is shown in Figure 2.4d, with almost 100% of the profiles used at $z = -h$ but less than 50% at normalized depths shallower than 0.6 h. It is important to clarify, then, that above the mixed layer base $\overline{J_b}$ represents the timeseries average profile of *negative* turbulent buoyancy flux. If we were also able to estimate the positive values of J_b within convecting regions, $\overline{J_b}$ would likely show an even more pronounced peak at $z = -h$ with values becoming more positive with distance above the mixed layer base (Large et al., 1994). Although there is large uncertainty in estimates of K_ρ (and K_T) above the mixed layer base because of weak stratification, a profile of $\overline{J_q}$ also shows a local minimum or a peak in upwards turbulent flux of cold water at $z = -h$, further supporting the choice for the entrainment depth. As with $\overline{\varepsilon}$, both profiles of $\overline{J_b}$ and $\overline{J_q}$ rapidly decay below the base of the mixed layer reaching background levels by about 1.4h or roughly 10 m below the mixed layer base.

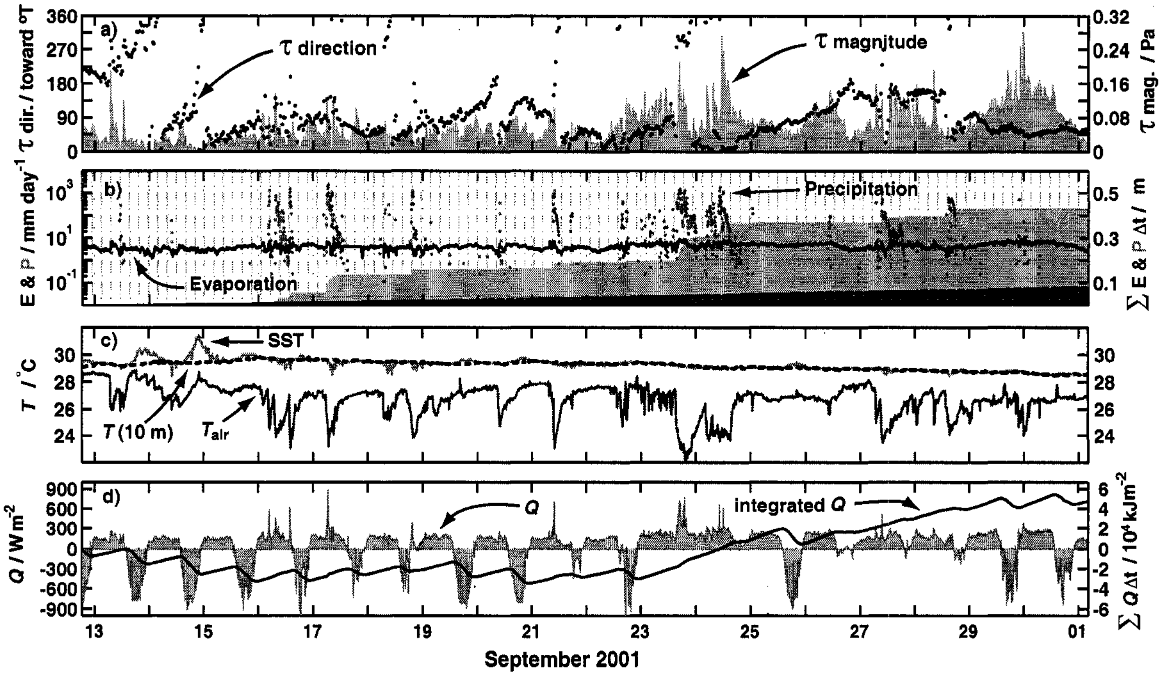

Figure 2.5: a) Wind stress magnitude (shaded) and direction (points). b) Evaporation, E, (black) and precipitation, P, (gray points) rates with cumulative values over the timeseries. Note that E and P rates are plotted on a $\log_{10}$ scale due to their large differences. c) Sea-surface temperature (gray), mixed layer temperature at 10 m depth (dashed black) and air temperature at 15.5 m (black). d) Net surface heat flux, Q, (shaded) and the time-integrated surface heat flux, $\sum Q\Delta t$, (black line).

2.3.2 *Atmospheric forcing and mixed layer evolution*

The surface buoyancy fluxes, $J_b(0)$, and surface wind stress, τ, at the EPIC timeseries location—the primary means by which the atmosphere forces the SBL—were shaped by the presence of the ITCZ with intense clear-sky daytime solar radiation (at times > 1000 W m^{-2}), rapidly passing squalls and thunderstorms with moderate winds and heavy rainfall (up to 90 mm hr^{-1}), and larger-scale tropical depressions and storms that brought moderate to strong winds and heavy rainfall. Petersen et al. (2003) linked the larger scale patterns of atmospheric forcing at the EPIC timeseries location with the passage of three easterly waves with periods of 3–5 days. These waves were found to significantly modulate winds and the patterns of atmospheric convection on these timescales, and thus the surface fluxes of heat, freshwater and momentum. With cumulative precipitation over the timeseries > 0.4 m, (5.46 times the cumulative evaporation) (Fig. 2.5b), rainfall significantly influenced surface buoyancy fluxes and, thus, SBL turbulence and entrainment. Although surface buoyancy fluxes were largely modulated by solar radiation and out-going latent, sensible and IR heat fluxes, at times $J_b(0)$ associated with rainfall was up to 10 times that from solar radiation. The 19-day timeseries spanned roughly two forcing regimes. Over much of the first half of the timeseries weak winds and a robust diurnal cycle of surface heat and buoyancy fluxes (Figure 2.5 a,d) resulted in a diurnal cycle of nighttime convection and daytime restratification within the SBL. On about September 22 this cycle was interrupted by a deep convective system bringing heavy cloud-cover, heavy rainfall and strong winds. After the passage of this system, wind stress remained elevated and/or cloud-cover heavy until the end of the timeseries, preventing the re-establishment of a diurnal cycle.

Mixed layer velocity was dominated by near-inertial (frequencies close to the local inertial frequency, f) and sub-inertial flow (Fig. 2.6) with a smaller but significant contribution from the tides, which were largely M_2 (43%), N_2 (16%) and S_2 (10%) as indicated by the TPXO model (Egbert et al., 1994). The sub-inertial flow was strongly influenced by the presence of an anticyclonic mesoscale eddy, with the EPIC timeseries situated within the southern half of the eddy as the eddy propagated westward at roughly 0.05 m s^{-1} (Shay et al., 2003; Wijesekera et al., 2005). The sub-inertial flow, which had a continuous westerly component, rotated counterclockwise and decayed as the eddy passed, with flow initially to the W-NW at $\sim$0.3 m s^{-1} changing to SW flow at $\sim$0.2 m s^{-1} in the second half of the timeseries. As will be discussed in Chapter 4, this eddy likely resulted in an anomalously deep mixed layer (+10 meters) and, consequently, reduced entrainment fluxes.

Due to strong density gradients at the mixed layer base, mixed layer velocities were slab-like with relatively uniform velocities from the shallowest ADCP measurement at 13 m to the mixed layer base and then a rapid decay and change in direction of the velocity vector below the mixed layer base. This change in both the magnitude and direction of the velocity vector contributed to the

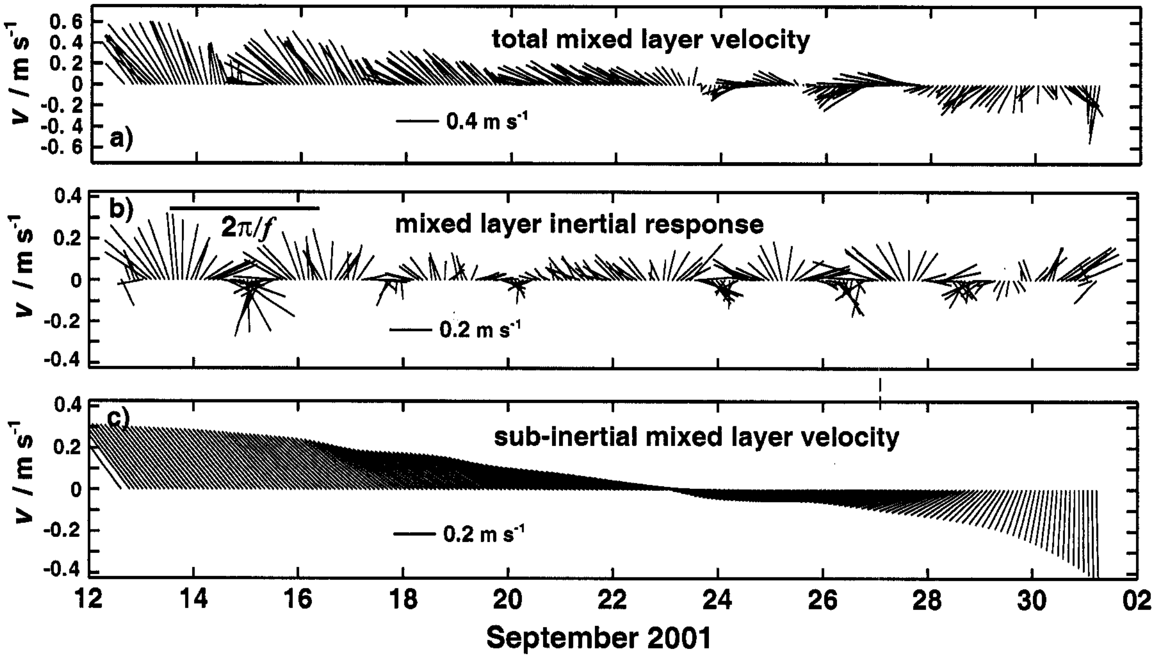

Figure 2.6: Quiverplots of total (a), inertial-response (b), and sub-inertial (c) mixed layer velocity as determined from 4-meter ADCP bins from 13–25 m.

local maximum in finescale shear near $z = -h$.

Wind stress occurring just prior to the timeseries (Sept. 9–13) generated the strong mixed layer near inertial currents observed at the beginning of the timeseries (Fig. 2.6). While winds were not particularly strong over the several days just prior to the timeseries (wind speed < 10 m s^{-1}), they rotated anticyclonically through 360 ° over a period of ~3.5 days, cumulatively adding kinetic energy at close to the local inertial period of 69.7 hours or 2.9 days. Results from the Pollard and Millard (1970) slab-model, with the model describing about 70% of the measured mixed layer current variance, indicates that the near-inertial motions were likely generated locally (Fig. 2.7). The near-inertial motions significantly increased finescale (8-m) shear-squared and decreased the finescale (8-m) gradient Richardson number at the mixed layer base and within the upper pycnocline. It is also noteworthy that both near-inertial and tidal velocities appeared to be important to altering the mixed layer depth, with the largest variability of the latter over the 19-days at these frequencies (Fig. 2.8e).

The diurnal cycle that dominated the first half of the timeseries is evident in the time-depth maps of the dissipation rate of TKE (ε) overturn scales (L_T), and 2-m buoyancy frequency squared (N_2^2) (Fig. 2.8 c–e). The Monin-Obukhov length, $-L \equiv u_*^3/\kappa J_b(0)$—a measure of the relative importance of wind to buoyancy forcing in the active SBL—had negative values that were typically less negative than $-h$, suggesting that most of the nighttime turbulence in the central SBL was due to convection. As previously observed by Brainerd and Gregg (1993a), the penetration depth of the convection is dictated by pre-existing SBL stratification (and thus prior surface buoyancy fluxes) as well as by the magnitude of the destabilizing surface buoyancy fluxes. This is apparent over the first several days of the timeseries when a strong, shallow transient pycnocline (and thermocline) suppressed the penetration depth of nighttime convection (shown by h_b and overturning scales) despite consistent, large destabilizing nighttime buoyancy fluxes. For much of the first half of the timeseries, in fact, negative (stabilizing) surface buoyancy fluxes and resultant weak mixed layer stratification prevented the SBL from penetrating to the mixed layer base, with $h_b \geq h$ only for short periods of time that were typically coincident with night-time buoyant convection (Fig. 2.8 c–e).

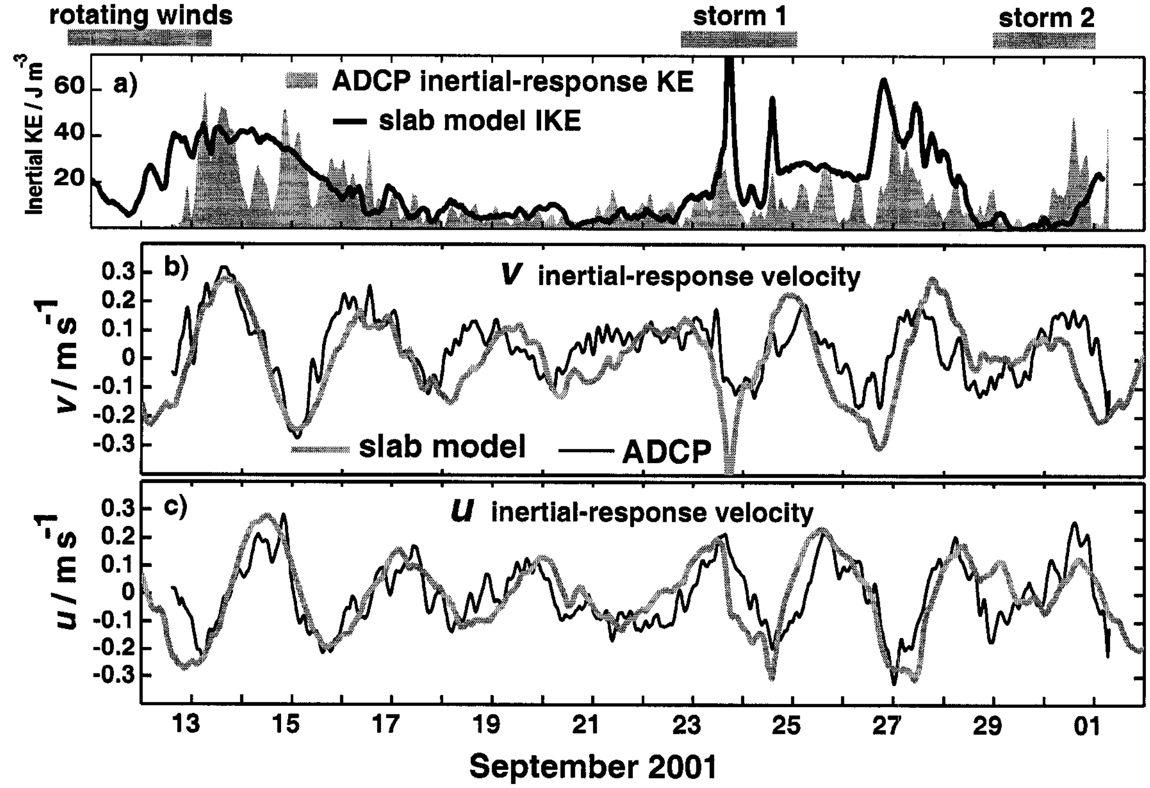

Figure 2.7: a) Measured (ADCP) vs. Pollard and Millard (1970) slab model mixed layer inertial-response kinetic energy (IKE). b) as in a) but mixed layer zonal (v) inertial-response velocity. c) as in b) but mixed layer meridional (u) inertial-response velocity. Model settings are: h=25 m, Lat=10° N, and a Rayleigh damping of 1/5 days $^{-1}$. The average r^2 (squared correlation) of the model and observed velocities is 0.67.

The diurnal cycle of surface buoyancy fluxes and convection was regularly interrupted and/or weakened by cloud-cover and rainfall associated with squall/thunderstorm activity. Modulated by convection over Central America, the squalls and cloud cover also followed a diurnal cycle with most rain falling between local midnight and noon (0600 and 1800 UTC) (Boccippio et al., 2002). By forming a strong, shallow transient (temporary) halocline within the mixed layer, the heavy rainfall associated with these squalls would often rapidly shut down nighttime convection. Like the diurnal cycle of convection/restratification in the SBL, the diurnal squall pattern was strongest over the first half of the timeseries. Section 2.4 will show that although the diurnal cycle of mixed layer convection/restratification clearly modulated the turbulent entrainment fluxes, it was not a dominant mechanism for generating entrainment.

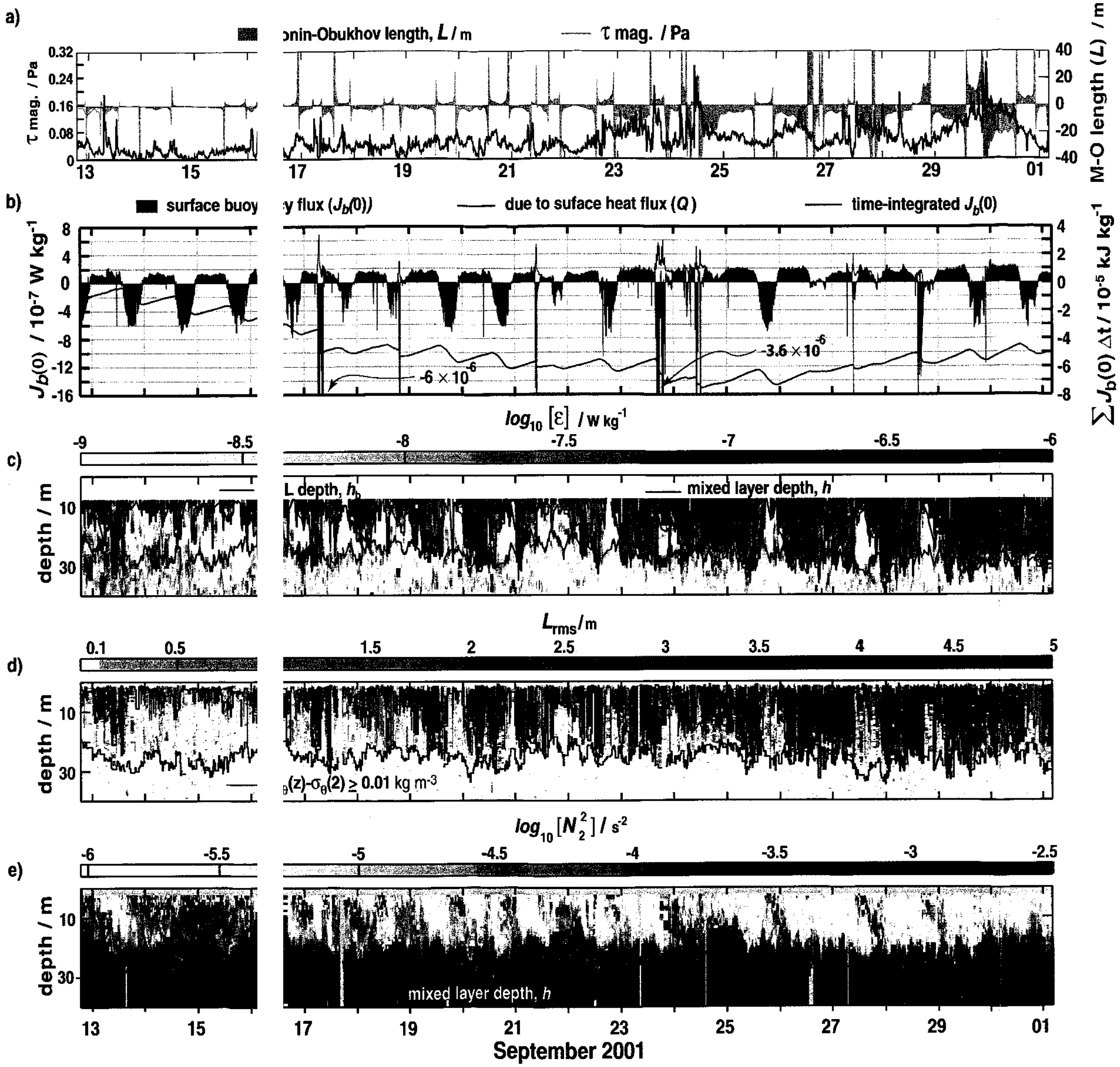

Figure 2.8: a) Monin-Obukhov (M-O) length, L, (gray shaded) and wind stress magnitude, $|\tau|$ (black). b) Surface buoyancy flux, $J_b(0)$, (gray shaded) with that due to surface heat flux, $J_b(0)(Q)$ (blue line). The time-summed $J_b(0)$ is show in red. c) Depth-time map of $log_{10}[\varepsilon]$, showing the mixing layer or SBL depth, h_b (red) and the mixed layer depth, h (blue). d) Depth-time map of overturning scales with the vertical extent of the shaded bars indicating the overturn size (L_t) and shading indicating the rms value of displacements within the overturn (L_{rms}). A canonical definition of the instantaneous mixed layer depth, h_i (red), and the time-averaged definition chosen here (blue) are over-plotted. e) Depth-time map of log_{10} of the 2-m buoyancy frequency, N_2^2, with unstratified regions shown in white and data gaps in light gray. The mixed layer depth is indicated in red.

As suggested by Figure 3 of Wijesekera et al. (2005), the two-day storm that commenced on Sept. 22 may have been linked to developing Tropical Storm Juliette, which eventually became category 5 hurricane Juliette as it tracked to the northwest of the EPWP. Mainly through associated latent heat loss and interrupted shortwave (on Sept. 23 the maximum shortwave flux was only about 3% of the clear-day maximum), this storm event significantly decreased the mixed layer heat content ($\Delta\theta \approx -0.3°\mathrm{C}$). Storm rainfall (over 1/3 of the timeseries total) also cooled the mixed layer and reduced mixed layer salinity by 0.3. With the SBL depth reaching the mixed layer depth for much of the storm duration (Fig. 2.8c), among the largest entrainment buoyancy and salt fluxes occurred during the storm's passage from Sept. 24 and 25 with $J_b^e < -4 \times 10^{-8}$ W kg^{-1} and $J_s^e > 1 \times 10^{-5}$ m s^{-1} psu. As will be discussed in Section 2.4, during this storm the entrainment *heat* fluxes remained weak despite the strong turbulence at h because of a weakening of $\frac{\partial\theta}{\partial z}$ at the mixed layer base. This storm also contributed significantly to SBL momentum and kinetic energy—again largely in the form of near-inertial oscillations (Fig. 2.7). However, unlike the first half of the timeseries, substantial wind forcing following the storm continued to modify the phase and amplitude of mixed layer near-inertial motions.

With the passage of the this two-day storm, winds remained relatively strong (typically with $|\tau| > 0.08$ Pa, wind speed $\sim$ 8 m s^{-1}) with minor wind events on Sept. 26 and 27. It was also much cloudier than prior to the storm, resulting in much-reduced solar heating and somewhat-reduced outgoing IR. The increased latent heat loss (from stronger winds) and reduced incoming solar shortwave resulted in a mixed layer (and SST) cooling trend that continued through the end of the timeseries (Fig. 2.5c and 2.5d). The Monin-Obukhov length, L, was mostly negative and of a larger magnitude than during the first half of the timeseries (Fig. 2.8a), reflecting predominantly positive (destabilizing) surface buoyancy fluxes and stronger wind stresses. On about Sept. 24, a trend of a net surface input of buoyancy since the beginning of the timeseries switched to a net surface loss that persisted until the end of the timeseries (Fig. 2.8b). As with the SBL cooling trend, this switch was predominantly caused by reduced solar radiation from heavy cloud cover. Because of the surface cooling and increased wind stress, over much of this period $h_b \geq h$, which as will be shown was associated with elevated entrainment fluxes.

Just prior to the end of the timeseries on September 29 and 30, winds slowly ramped up to a maximum stress of > 0.25 Pa ($\sim$12 m s^{-1}) on the 30th and then decayed over the next day to < 0.05 Pa. During this wind event the SBL depth was almost continuously greater than h (Fig. 2.8c), and consequently the entrainment fluxes—including entrainment heat fluxes ($J_q^e < -200$ W m^{-2})—were the largest observed over the 19-days. The atmospheric forcing associated with this wind event was significantly different than during the previous storm on Sept. 23–25, with much less rainfall and cloud-cover as well as steadier wind direction that was predominantly from the SW. The drop in mixed layer temperature over this period (28.8 ° C to 28.45° C from yearday Sept. 29–Oct. 1) was largely due to advective fluxes and entrainment (see Chapter 4), with the surface heat fluxes playing a smaller role than in the previous storm. Again, there was a net transfer of kinetic energy and momentum from the wind to the ocean during this event, although it appeared to interrupt the phase of the inertial motions generated by the storm 6 days earlier (Fig. 2.7).

2.4 Processes Controlling the Entrainment Fluxes

In this section we investigate processes generating and modifying entrainment fluxes, which is approached primarily through a linear regression analysis of turbulent buoyancy entrainment and other measured parameters—specifically $u_*^3/(\kappa h)$, the finescale (8-m) inverse gradient Richardson number at the mixed layer base, $Ri^{-1}(-h)$, and surface buoyancy flux, $J_b(0)$. The specific forms for the influence of surface wind stress $[u_*^3/(\kappa h)]$ and surface buoyancy flux on entrainment were chosen because of their theoretical justification in mixed layer entrainment models (Niiler and Kraus, 1977) and as scalings for turbulent dissipation within the SBL [e.g. Lombardo and Gregg (1989)]. Here Von Karman's constant ($\kappa = 0.4$) in the wind stress term is simply included by convention and has no bearing on the results of this analysis. The investigation of the relationship of $Ri^{-1}(-h)$ to entrainment is motivated by theory [e.g. Pollard et al. (1973)], laboratory experiments [e.g. Ellison and Turner (1959); Lofquist (1960); Thorpe (1971)], and by the relative success of upper-ocean models that use a mixing scheme based on some form of Richardson number [e.g. Price et al. (1986); Large et al. (1994)]. With J_b^e, Ri^{-1} and $u_*^3/(\kappa h)$ all lognormally distributed, the regression analysis between these variables is performed after taking the $\log_{10}$ of each variable (or in log-space)—which meets the assumption of linear regression analysis that the samples are taken from normal distributions (Snedecor and Cochran, 1967). Thus, slopes (m) of the regressions correspond to powers [e.g. $(Ri^{-1})^m$] and the intercepts (b) translate to coefficients (10^b).

Because of likely differences in dynamics between times when the turbulent boundary layer penetrates to the entrainment depth ($h_b \geq h$) and times when it was shallower than the entrainment depth ($h_b < h$), the analysis includes results for both cases as well as for all data. Also, the analysis focuses on the entrainment buoyancy flux (J_b^e) with results assumed to hold for the salt and heat entrainment fluxes—which is an extension of the assumption that the scalar diffusivities are equal or at least closely correlated. Since the estimates of the entrainment buoyancy flux are determined directly from the turbulent dissipation rate, or $J_b^e = -0.2\varepsilon(-h)$ (where ε has been time-averaged over 4 hours), the results also directly apply to ε.

2.4.1 *A qualitative comparison of the time-variability of J_b^e to $u_*^3/(\kappa h)$, $Ri^{-1}(-h)$ and $J_b(0)$*

The largest entrainment fluxes and about 85% of the timeseries total J_b^e occurred when $h_b \geq h$, or when the turbulent SBL was directly acting on the typically-large scalar gradients at the mixed layer base. These times, which are indicated with black shading above Figure 2.9c, occurred primarily during the second half of the timeseries when wind stress was large and there were prolonged periods of destabilizing (positive) surface buoyancy fluxes. Buoyancy entrainment was also extremely episodic with $> 1/3$ of the timeseries total occurring within only about 6% of the timeseries.

A qualitative comparison of the three above parameters to the entrainment buoyancy flux over the EPIC timeseries shows a number of general features. Buoyancy entrainment is typically largest (most negative) when both $Ri^{-1}(-h)$ and $u_*^3/(\kappa h)$ are large—as is the case over the last several days of the timeseries (Fig. 2.9b, c). It appears that if one of the two latter variables is relatively small but the other is large, entrainment buoyancy fluxes will still be relatively weak. This is the case over the first several days of the timeseries when $Ri^{-1}(-h)$ is relatively large and $u_*^3/(\kappa h)$ is small and also for short periods of time on September 22 and 24 when the opposite situation exists [$u_*^3/(\kappa h)$ is larger than average and $Ri^{-1}(-h)$ is relatively small]. Over the first 9 days of the timeseries there were three moderate entrainment events that were spaced at about the local inertial period (69 hrs/2.9 days) that were coincident with three peaks in $Ri^{-1}(-h)$. Also readily apparent from a comparison of the surface buoyancy flux to J_b^e is that large stabilizing buoyancy fluxes [$J_b(0) \lll 0$] which were usually a consequence of heavy rainfall, are associated with rapid drops in $-J_b^e$. Conversely, there is also a general correlation between positive (destabilizing) surface buoyancy fluxes and increases in $-J_b^e$ (Fig. 2.9a, c).

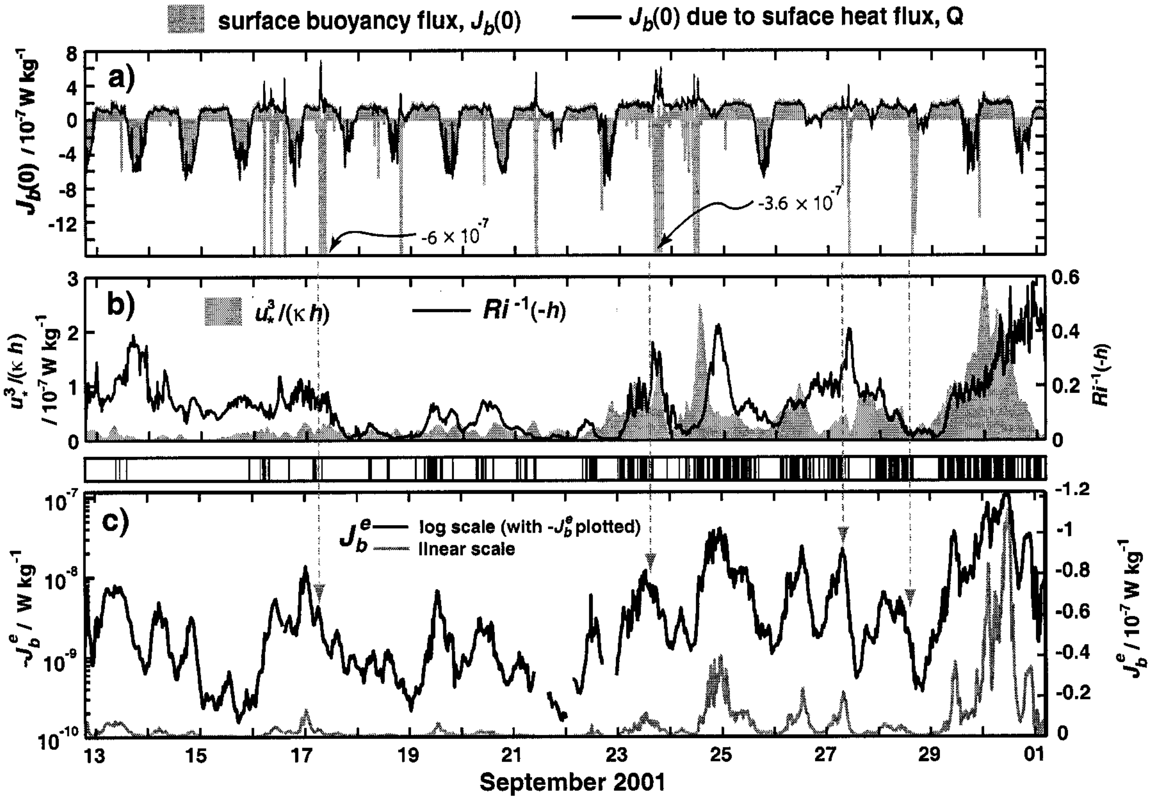

Figure 2.9: a) $J_b(0)$ (gray shaded) with that due to surface heat flux, Q (black line). b) Scaled wind stress $[u_*^3/(\kappa h)]$ and $Ri^{-1}(-h)$. c) J_b^e plotted on linear (gray) and $\log_{10}$ scales (black). Black shading above the top axis of plot (c) indicates times when $h_b \geq h$. Vertical dashed arrows show several instances of rapid drops in $-J_b^e$ coincident with the start of heavy rainfall.

2.4.2 *Direct Wind Stress*

Results from the linear regression analysis of J_b^e and $u_*^3/(\kappa h)$ provide support for the theoretical dependence of J_b^e on the cube of the friction velocity, with a strong correlation between the two variables and a regression slope of nearly one (0.99) when using all data and 0.87 using only J_b^e values when $h_b \geq h$ (Fig. 2.10a, b, Tab. 2.2). As shown in Tab. 2.2, the maximum log-space correlations (r_{no}) of 0.70 and 0.61 respectively are significant at >95% level, and as expected occur when the observed J_b^e slightly lags the wind stress (by 3 and 2.3 hrs respectively) (Fig. 2.10a–d, Tab. 2.2). The robustness of this finding is further indicated by the fact that the regression slope remains above 0.9 for all lags less than 10 hours for the case when using all data.

This result adds to the findings of Oakey and Elliott (1982) showing that ε integrated over a shallow, wind-driven mixed layer is related to U_{10}^3 (where U_{10} is the wind speed at 10 m), and Lombardo and Gregg (1989) who found that wind-driven ε in the central part of the active SBL follows the M-O scaling. Because the variability of h was relatively weak compared to that of u_*^3, observations did not allow an evaluation of the specific h^{-1} dependence. However, including the form with the h^{-1} dependence for the case of using all data increased the log-space correlation (r_{no}) by 0.01 and the linear-space correlation (r) by 0.03.

Although computing the $\log_{10}$-space correlation (r_{no}) is statisitically consistent—or it meets the linear regression requirement that the samples are from normally-distributed populations—it is not particularly meaningful in terms of variance described. Thus, the linear-space correlation is also computed to evaluate the relative importance of direct wind stress to entrainment observations over the 19 days. Results suggest that variability in direct wind stress forcing can account for more than 65% of the observed variance of J_b^e over the EPIC timeseries, or $r^2 = 0.65$ (Fig. 2.10a). If we compute the linear-space regression considering that $-J_b^e$ is positive-definite, and, thus, requiring the fit to also be positive-definite, the variance explained drops to roughly 50% with a slope of ~ 0.3. With entrainment strongly dependent upon the cube of the friction velocity and thus the wind speed, a disproportionately large fraction of the entrainment is produced during the timeseries' two short-lived storms. Specifically, more than 43% of the total entrainment of buoyancy occurred when wind speeds were in excess of 8 m s^{-1}, which accounted for less than 8% of the timeseries.

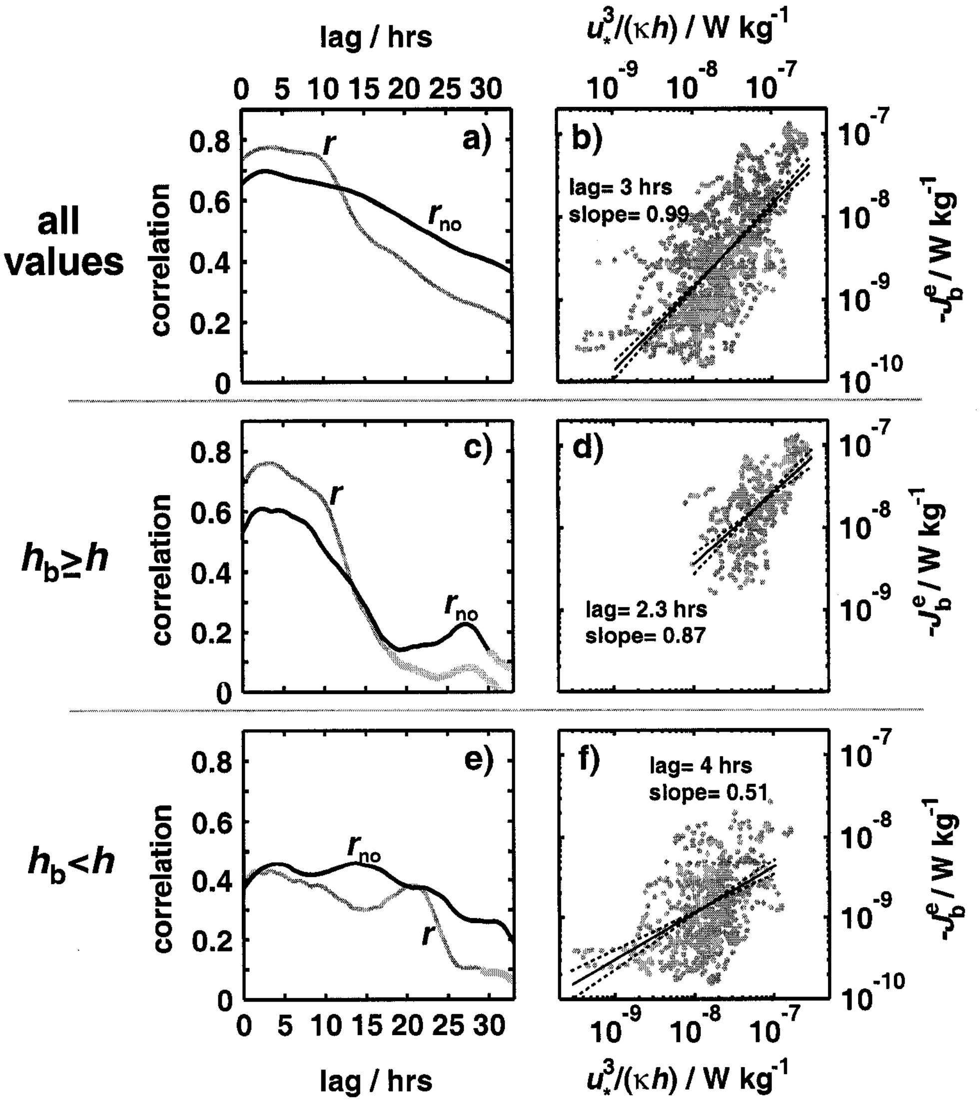

Figure 2.10: a) Correlation of $u_*^3/(\kappa h)$ with $-J_b^e$ vs. lag time [with $-J_b^e$ lagging $u_*^3/(\kappa h)$] in both linear space (r, gray) and after taking the $\log_{10}$ of both variables (r_{no}, black). b) Log-log scatterplot of $u_*^3/(\kappa h)$ vs. $-J_b^e$ at the lag showing the maximum r_{no} (3 hrs). The linear regression is shown with 99% confidence intervals. c) as in (a) but only using values of J_b^e during times when the SBL depth is equal to or greater than the mixed layer depth, $h_b \geq h$. d) as in (b) but only using values of J_b^e when $h_b \geq h$. e) as in (a) but only using values of J_b^e when $h_b < h$. f) as in (b) but only using values of J_b^e when $h_b < h$. In the lagged correlation plots (a, c, e) values not significant at the 95% level are shown in light gray.

Entrainment modulation by $u_*^3/(\kappa h)$ *when* $h_b < h$

There was also a significant positive correlation between $-J_b^e$ and $u_*^3/(\kappa h)$ when the boundary layer depth was less than the mixed layer depth ($h_b < h$) (Fig. 2.10c). Although there is more scatter in the data than the previous cases with the maximum $r_{no} = 0.46$ at a lag of 4 hrs, the linear regression shows a weaker functional dependence with a slope of 0.51—or about half of that for the case using all data. Since more than 1/3 of the values of J_b^e are above the cut-off level used to define h_b ($\varepsilon = 1 \times 10^{-8}$ W kg^{-1} or $J_b^e = 2 \times 10^{-9}$ W kg^{-1}), this positive correlation is likely not due to the h_b estimates under-representing the actual times when the SBL depth reaches $z = -h$. This is consistent with observations showing a persistent local minimum of ε within the mixed layer that drops well below the h_b cut-off level and then a local maximum at the mixed layer base that is about twice the minimum (Fig. 2.11). Because most of the values for this case are from the first half of the timeseries when h_b infrequently reached h, it is also unlikely that the significant correlation is due to decaying turbulence at h that was generated when $h_b \geq h$. Although the measurements do not permit a rigorous investigation of the mechanism by which wind stress appears to be modulating entrainment when $h_b < h$, one possibility could be a process similar to that suggested by Gregg et al. (1985) and Peters et al. (1988) and modeled by (Wang et al., 1998) whereby the intermediary of high-frequency internal waves can transfer energy from the turbulent SBL to the upper pycnocline, causing local shear-instability. Regardless of the mechanism, these results show a significant, short-lag correlation between direct wind stress forcing and entrainment levels that does not appear to be a consequence of elevated SBL turbulence penetrating to h.

2.4.3 $Ri^{-1}(-h)$

The regression analysis indicates that $-J_b^e$ was also strongly positively correlated with the finescale (8-m) gradient Richardson number at the mixed layer base $Ri^{-1}(-h)$, with a regression slope not significantly different from one for the case of using all data (0.96) and when $h_b \geq h$ (0.89) (Fig. 2.12a–d and Table 2.2). With variability of $Ri^{-1}(-h)$ largely due to changes in Sh^2 since N^2 was nearly constant at $z = -h$ (by definition of h), there was a similar relationship between entrainment buoyancy flux and $Sh^2(-h)$. The maximum correlation (r_{no}) was significant at >95%

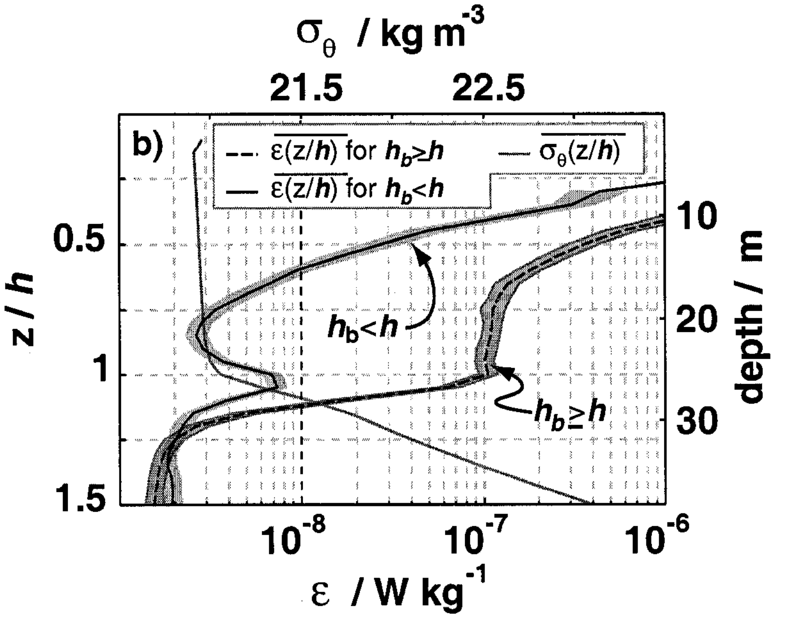

Figure 2.11: Timeseries-average profiles of ε for the cases when $h_b < h$ and $h_b \geq h$, with averages computed in $\log_{10}$-space (or $10^{\overline{\log_{10}[\varepsilon]}}$) to show the dominant vertical structure. There is a persistent local minimum within the mixed layer when $h_b < h$ that is not present when $h_b \geq h$. The cut-off value used to estimate the penetration depth of SBL turbulence (1×10^{-8} W kg^{-1}) is shown as a black, dashed line.

Table 2.2: Linear regression statistics for J_b^e, $Ri^{-1}(-h)$ and $u_*^3/(\kappa h)$.

using all values

Var 1	Var 2	r_{no}	lag (hrs)	slope (m)	y-int (b)
J_b^e	$u_*^3/(\kappa h)$	0.70	3	0.91, **0.99**, 1.06	-1.54, **-0.97**, -0.39
J_b^e	$Ri^{-1}(-h)$	0.62	0	0.89, **0.96**, 1.02	-7.55, **-7.48**, -7.39
$Ri^{-1}(-h)$	$u_*^3/(\kappa h)$	0.34	8.3	0.26, **0.31**, 0.35	0.88, **1.25**, 1.62

for case: $h_b \geq h$

Var 1	Var 2	r_{no}	lag (hrs)	slope (m)	y-int (b)
J_b^e	$u_*^3/(\kappa h)$	0.61	2.3	0.71, **0.87**, 1.02	-2.61, **-1.53**, -0.45
J_b^e	$Ri^{-1}(-h)$	0.64	0	0.78, **0.89**, 1.00	-7.14, **-7.04**, -6.95
$Ri^{-1}(-h)$	$u_*^3/(\kappa h)$	0.55	8.3	0.46, **0.54**, 0.62	2.51, **3.11**, 3.71

for case: $h_b < h$

Var 1	Var 2	r_{no}	lag (hrs)	slope (m)	y-int (b)
J_b^e	$u_*^3/(\kappa h)$	0.46	4	0.42, **0.51**, 0.61	-5.63, **-4.88**, -4.13
J_b^e	$Ri^{-1}(-h)$	0.47	0	0.41, **0.48**, 0.55	-8.40, **-8.31**, -8.22
$Ri^{-1}(-h)$	$u_*^3/(\kappa h)$	$0.02^{\dagger}$	0	no significant correlation	

Because all quantities are lognormally distributed, regressions are calculated and results given in $\log_{10}$-space (with absolute value of J_b^e used). In linear space y-intercepts translate to constant coefficients (i.e. 10^b) and slopes correspond to powers (e.g. $[Ri(-h)^{-1}]^m$). Lags refer to the time Var 1 follows Var 2 at the peak correlation (r_{no}) value. Regression slopes and intercepts are shown in bold with 99% conf. intervals in regular weight. All correlations are significant at the 95% conf. level except for those indicated with a $\dagger$.

level (0.62, 0.64 and 0.47 for all data, $h_b \geq h$, and $h < h_b$ respectively) and occurred at a lag of zero for all three cases. This finding is consistent with the expectation that Ri is related to the potential for local shear-instability and resultant entrainment generation. However, it is important to point out that measured 8-m $Ri(-h)$ at the mixed layer base was subcritical at all times ($> 1/4$), indicating that there were no resolved shear-instabilities at this scale. However, the strong correlation of $Ri^{-1}(-h)$ with $-J_b^e$ indicates Ri^{-1} was connected to—possibly facilitating—unresolved (higher frequency and/or smaller scale) shear-instability. The correlation in linear-space using all data shows that $Ri^{-1}(-h)$ can describe as much as 30% of the variance of J_b^e over the EPIC time-series (Fig. 2.12a). As with $u_*^3/(\kappa h)$, if we restrict the fit to only positive definite values (since $-J_b^e$ is positive-definite as determined here), then $Ri^{-1}(-h)$ describes roughly 22% of the variance of J_b^e over the 19 days.

As with the regression analysis results of J_b^e and $u_*^3/(\kappa h)$, there were marked differences in the regression results between times when the turbulent boundary layer was in contact with the mixed layer base ($h_b \geq h$) and times when the SBL penetration depth was less than h. In the former case there was a stronger relationship with $r_{no} = 0.66$ and a slope of 0.89 than when $h_b < h$ with $r_{no} = 0.47$ and a slope of 0.48 (Fig. 2.12c–f and Table 2.2). Although the 99% confidence intervals in the slopes suggest this difference is significant, there is considerable scatter in the data for both cases. The reason for this difference remains unclear, but it may be related to differences in the dominant mechanisms producing the turbulence as suggested by D'Asaro and Lien (2000b).

The correlation of $Ri^{-1}(-h)$ *and* $u_*^3/(\kappa h)$

With buoyancy entrainment strongly correlated with both $Ri^{-1}(-h)$ and $u_*^3/(\kappa h)$, it is desirable to investigate the correlation of these latter two variables to gain some insight into the physical mechanisms driving entrainment. Results are consistent with the expectation that $Ri^{-1}(-h)$ is strongly influenced by relatively recent ($\lesssim$1 day) wind stress forcing. For the range of lags investigated (0–33 hrs), the largest positive correlation between the two variables ($r_{no} = 0.55$) occurs when $Ri^{-1}(-h)$ lags $u_*^3/(\kappa h)$ by roughly 8 hours and specifically when $h_b \geq h$ (Fig. 2.13, Tab. 2.2). This statistical lag time is physically interpreted as the mean response time for momentum input into the mixed

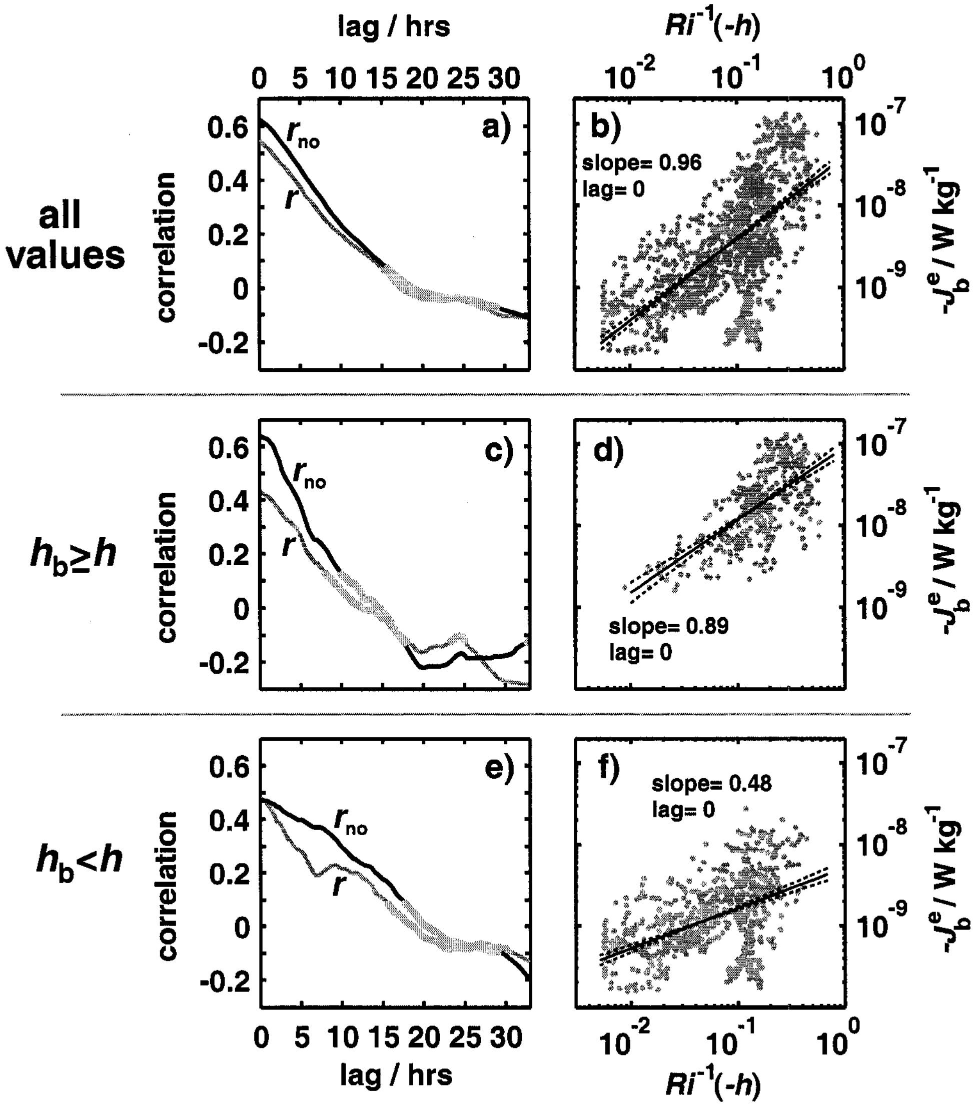

Figure 2.12: a) Correlation of $Ri^{-1}(-h)$ with J_b^e vs. lag time [with J_b^e lagging $Ri^{-1}(-h)$] in both linear space (r, gray) and after taking the $\log_{10}$ of both variables (r_{no}, black). b) Log-log scatterplot of $Ri^{-1}(-h)$ vs. $-J_b^e$ at the lag showing the maximum r_{no} (0 hrs). The least-squares linear fit is shown with 99% confidence intervals. c) as in (a) but only using values of J_b^e during times when the SBL depth is equal to or greater than the mixed layer depth, $h_b \geq h$. d) as in (b) but again only showing values of J_b^e when $h_b \geq h$. e) as in (a) but only using values of J_b^e when $h_b < h$. f) as in (b) but only using values of J_b^e when $h_b < h$. In the lagged correlation plots (a, c, e) values not significant at the 95% level are shown in light gray.

layer by wind stress to modify the local finescale shear at $z = -h$ and, thus, $Ri^{-1}(-h)$. The finding that the largest correlation occurs when the SBL penetrates to the mixed layer base is consistent with the fact that the mixed layer is largely unstratified (and slab-like) during these times. In contrast, for the case when $h_b < h$ the two variables are not significantly correlated at lags less than 17 hours within the 95% confidence limits—indicating that the typically weak wind stress during these times has little influence on $Ri^{-1}(-h)$.

One of the more important findings of this particular analysis is that $Ri^{-1}(-h)$ is only weakly correlated with $u_*^3/(\kappa h)$ at lags when J_b^e is most strongly correlated with $u_*^3/(\kappa h)$ (~3 hrs) (Fig. 2.13). This observation suggests that $Ri^{-1}(-h)$ and direct $u_*^3/(\kappa h)$ influence J_b^e somewhat independently of one another. A physical interpretation of this finding is that both the relatively slowly evolving finescale stability conditions and the rapidly-evolving (and unresolved by measured finescale Ri) shear and turbulence at $z = -h$ due to direct wind stress are important to the generation of entrainment fluxes. This conclusion is supported by a log-space multiple linear regression that describes $\log_{10}[-J_b^e]$ with the weighted addition of $\log_{10}[u_*^3/(\kappa h)]$ and $\log_{10}[Ri^{-1}(-h)]$ (Fig. 2.14, Tab. 2.3). Here performing a log-space multiple regression meets the requirement that the regression variables are normally-distributed, and, thus, when added will give a (log-space) normally-distributed result. The other option, or adding the weighted lognormal quantities in linear space [e.g. $aRi^{-1} + bu_*^3/(\kappa h)$] does not meet the requirements of linear regression analysis and does not necessarily give a lognormally-distributed result, which is inconsistent with the expectation that J_b^e is lognormally distributed (Gregg et al., 1993).

The multiple linear regression fit describes more than 65% of the log-space variance of the entrainment (using all data values), whereas alone $Ri^{-1}(-h)$ and $u_*^3/(\kappa h)$ described 38% and 41% of the log-space variance respectively (Tables 2.2 and 2.3). The significant increase in r_{no} in the multiple linear regression implies that much of the scatter apparent in the log-log scatterplots of J_b^e vs. $u_*^3/(\kappa h)$ and $Ri^{-1}(-h)$ (Figs. 2.10, 2.12), then, is due to variability in J_b^e caused by either or $Ri^{-1}(-h)$ or $u_*^3/(\kappa h)$ respectively. A simple transform of the log-space regression equation to linear space implies that J_b^e is a function of the *product* of $u_*^3/(\kappa h)$ and $Ri^{-1}(-h)$. Consistent with qualitative observations discussed earlier, this suggests that the largest entrainment fluxes are generated when both quantities are large. Although this result is empirical, it is constrained by the expectation that J_b^e is lognormally distributed (Gregg et al., 1993). A more complete discussion of the implications of this result will be given in Chapter 3.

Table 2.3: Details of the multiple linear regression to J_b^e.

coefficient of $Ri^{-1}(-h)$	coefficient of $u_*^3/(\kappa h)$	constant	r_{no}	lag (hrs)
0.62, **0.69**, 0.76	0.74, **0.80**, 0.86	-2.08, **-1.62**, -1.15	0.82	2.3

Because all quantities are lognormally distributed, the regression is calculated and results given in $\log_{10}$-space (with absolute value of J_b^e used). Lags refer to the time J_b^e and $Ri^{-1}(-h)$ follow $u_*^3/(\kappa h)$ at the peak correlation value. Regression values are given in bold with 99% conf. intervals in regular weight. The correlation is significant at the 99% conf. level.

2.4.4 Surface Buoyancy Forcing

For a number of reasons, it is somewhat difficult to extract the dependence of J_b^e on $J_b(0)$ from observations. Among these reasons are the dependence of $J_b(0)$ on u_* through latent and sensible heat fluxes and the SBL's dynamically-different responses to stable and unstable $J_b(0)$. Because $J_b(0)$ can be both positive and negative (with negative values undefined in log-space) and is not lognormally distributed, here the functional relationship between $J_b(0)$ and J_b^e is investigated in linear space. The linear regression shows that $J_b(0)$ is only weakly correlated with $-J_b^e$ with the largest values of r (~0.2) at zero lag for the cases of using all data and when $h_b \geq h$ (Fig. 2.15a–d). For these two cases, the correlation results are strongly influenced by the dependence of $J_b(0)$ on wind speed, which is apparent from the steep slope in the scatterplot points near the right vertical axis. For the case of $h_b < h$—when winds were typically light—the lagged correlation plot shows a diurnal variability that is due to the diurnal cycle of convection/restratification within the mixed layer (Fig. 2.15e, f). The largest correlation value lagged the positive surface buoyancy fluxes by about 4 hours, with another significant peak in r about 24 hours later. Although not significant at the 95% level, there were also peaks in negative r that occurred at roughly 24-hr intervals.

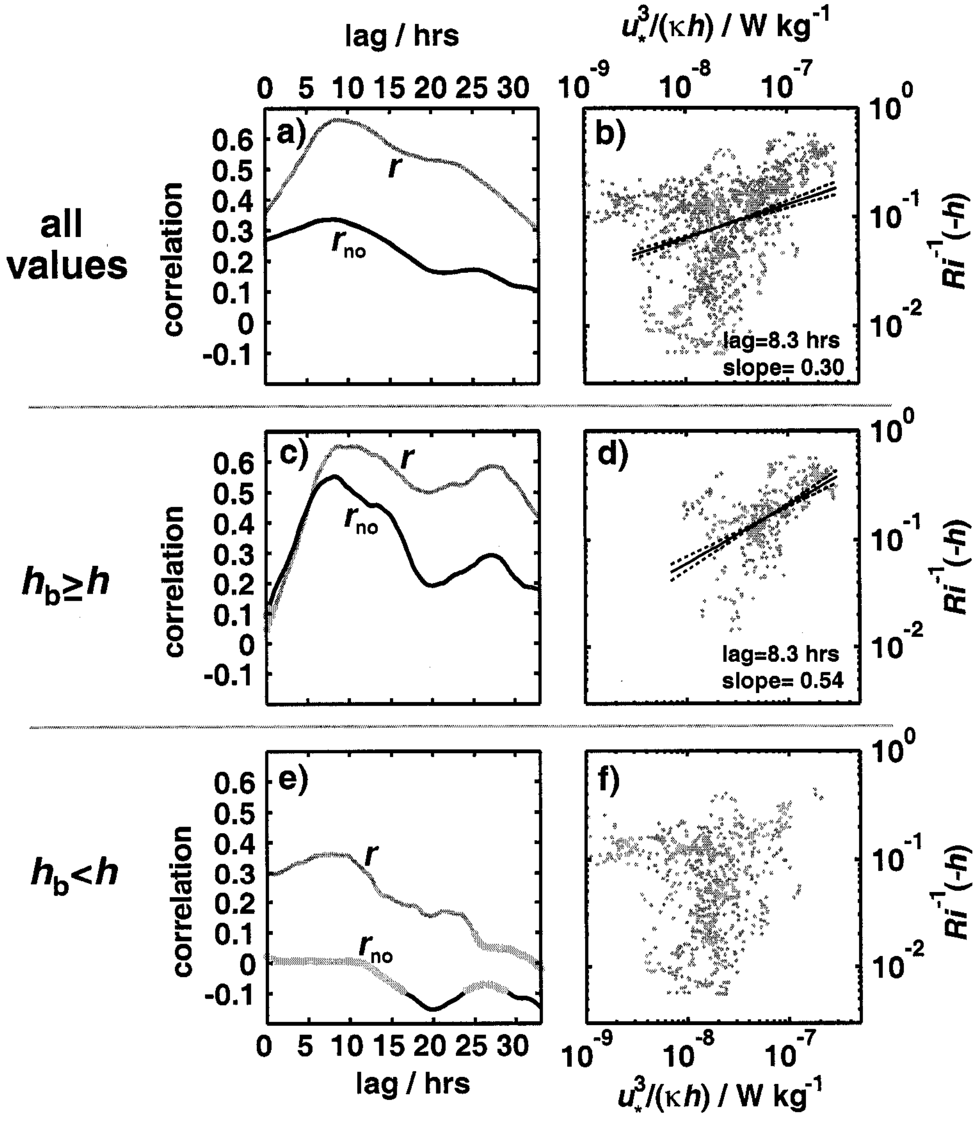

Figure 2.13: a) Correlation of $Ri^{-1}(-h)$ with $u_*^3/(\kappa h)$ vs. lag time [with $Ri^{-1}(-h)$ lagging $u_*^3/(\kappa h)$] in both linear space (r, gray) and after taking the $\log_{10}$ of both variables (r_{no}, black). b) Log-log scatterplot of $Ri^{-1}(-h)$ vs. $u_*^3/(\kappa h)$ at the lag giving the maximum r_{no} (8.3 hrs). The linear regression is shown with 99% confidence intervals. c) as in (a) but only using values of $Ri^{-1}(-h)$ during times when the SBL depth is equal to or greater than the mixed layer depth, $h_b \geq h$. d) as in (b) but again only showing values of $Ri^{-1}(-h)$ when $h_b \geq h$. e) as in (a) but only using values of $Ri^{-1}(-h)$ when $h_b < h$. f) as in (b) but only using values of $Ri^{-1}(-h)$ when $h_b < h$ with a linear fit absent since the variables are largely uncorrelated. In the lagged correlation plots (a, c, e) values not significant at the 95% level are shown in light gray.

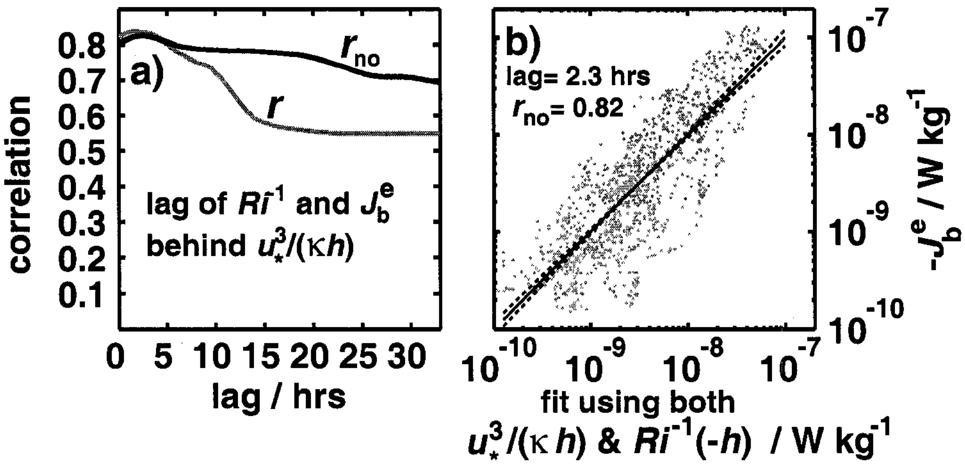

Figure 2.14: a) Correlation of measured J_b^e with a multiple regression fit to J_b^e using both $Ri^{-1}(-h)$ and $u_*^3/(\kappa h)$. The lag time represents the time that both $Ri^{-1}(-h)$ and J_b^e follow the wind stress forcing $[u_*^3/(\kappa h)]$. The fits and correlations are computed in both linear space (r, gray) and after taking the $\log_{10}$ of all variables (r_{no}, black) with all values plotted significant at the 95% level. b) Log-log scatterplot of the multiple regression fit (in $\log_{10}$-space) vs. $-J_b^e$ at the lag giving the maximum r_{no} (2.3 hrs). The least-squares linear regression of the fit to the observations (which always has a slope of one and intercept of zero) is shown with 99% confidence intervals.

Removing much of the influence of direct wind forcing and local shear instability on J_b^e more clearly shows the dependence of J_b^e on $J_b(0)$ (Fig 2.16). This is accomplished by subtracting the log-space multivariate linear regression fit (J_b^e with $Ri^{-1}(-h)$ and $u_*^3/(\kappa h)$, Table 2.3) from $\log_{10}[J_b^e]$ to yield a "residual", $J_{b,r}^e$. The residual simply indicates the departure of J_b^e in *decades* from the log-space multiple linear regression fit. Because it consists of both positive and negative values in log-space, it can not be transformed to linear space [2].

In Figure 2.16 $J_{b,r}^e$ typically declines with the onset of stabilizing, negative $J_b(0)$ and increases with positive $J_b(0)$. Although the influence of rainfall on J_b^e is complicated by solar heating as well as both the spatial patchiness of rainfall events and the spatial variability introduced by the measurement methods, Figure 2.17 shows that there was a significant, rapid drop in $J_{b,r}^e$ following a number of the events. A plot of h_b/h shows that this drop is due to the rapid shoaling of h_b. For these events $J_{b,r}^e$ declined by 0.5–1 decades over a period of several hours—although 4-hr averaging of ε used in the calculation of J_b^e likely under-represents rapidity of the actual SBL response. The largest values of $J_{b,r}^e$ occur near the end of periods of positive $J_b(0)$ (Sept. 19–23 and 26–30 in Fig. 2.16) and typically correspond to $h_b \geq h$ (top axis, Fig. 2.16). This is consistent with h_b continuing to deepen throughout the period of unstable buoyant convection. Figure 2.18 shows the connection of the diurnal cycle of entrainment buoyancy flux, $J_{b,r}^e$, (black line) to the diurnal cycle of surface buoyancy fluxes, $J_b(0)$ (gray shading), with data from the 9-day period indicated between vertical arrows in Figure 2.16. Again, it is clearly apparent that the largest values of $J_{b,r}^e$ on average occur at the end of the period of nighttime convection. Excluding the influence of the frequent rain squalls (evident as negative values of the time-averaged $J_b(0)$ during the night) this is coincident with a maximum in the diurnally-integrated $J_b(0)$.

2.4.5 *Near-inertial modulation of* J_b^e

During the first half of the timeseries the linear addition of strong near-inertial shear and weaker sub-inertial shear resulted in the modulation of $Sh^2(-h)$ (8-m shear-squared), $Ri^{-1}(-h)$ and con-

---

[2] Because J_b^e is lognormally-distributed, computing the residual in linear space, i.e. transforming the multiple linear regression to linear space and then subtracting from J_b^e, does not clearly show the role of $J_b(0)$ in modifying J_b^e.

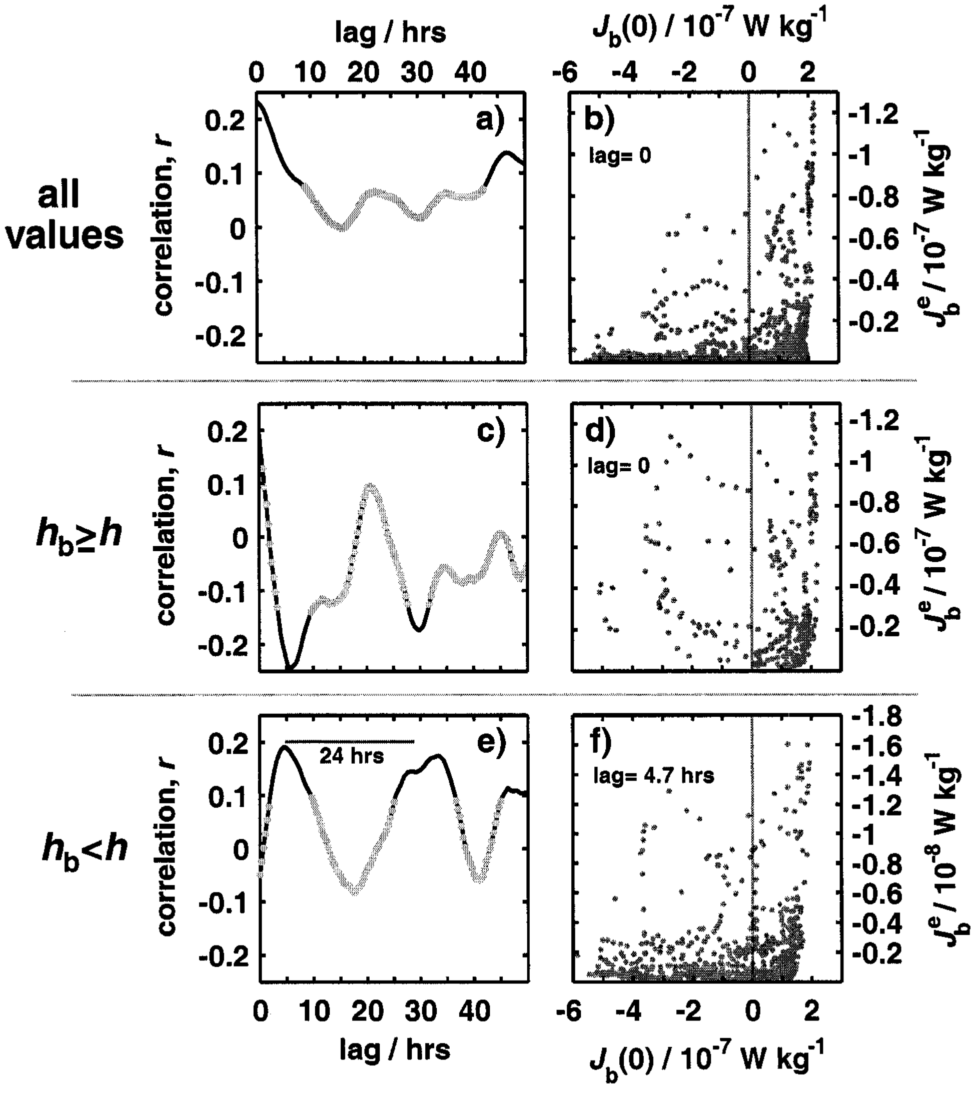

Figure 2.15: a) Correlation of $J_b(0)$ with $-J_b^e$ vs. lag time [with $-J_b^e$ lagging $J_b(0)$]. b) Scatterplot of $J_b(0)$ vs. J_b^e at the lag showing the maximum r (0 hrs) with a line showing $J_b(0) = 0$. c) as in (a) but only using values of J_b^e during times when the SBL depth is equal to or greater than the mixed layer depth, $h_b \geq h$. d) as in (b) but only for values of J_b^e when $h_b \geq h$. e) as in (a) but only using values of J_b^e when $h_b < h$. f) as in (b) but only using values of J_b^e when $h_b < h$. In the lagged correlation plots (a, c, e) values not significant at the 95% level are shown in light gray. Note that the positive slope of points near the right y-axis of the scatterplots is largely a consequence of the dependence of both $J_b(0)$ and J_b^e on wind speed.

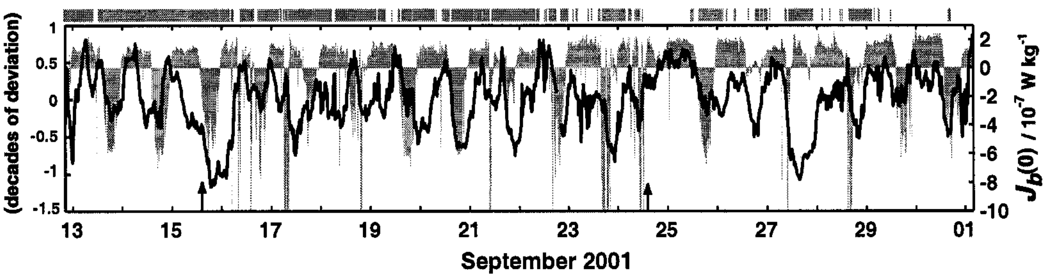

Figure 2.16: Timeseries of $J_b(0)$ (gray shaded) and residual buoyancy flux, $-J^e_{b,r}$ (black). The log-space multiple linear regression fit to $-J^e_b$ using wind stress and $Ri^{-1}(-h)$ (Table 2.3) were subtracted from $\log_{10}[J^e_b]$ to yield $J^e_{b,r}$. Gray shading above the top axis indicates times when $h_b < h$.

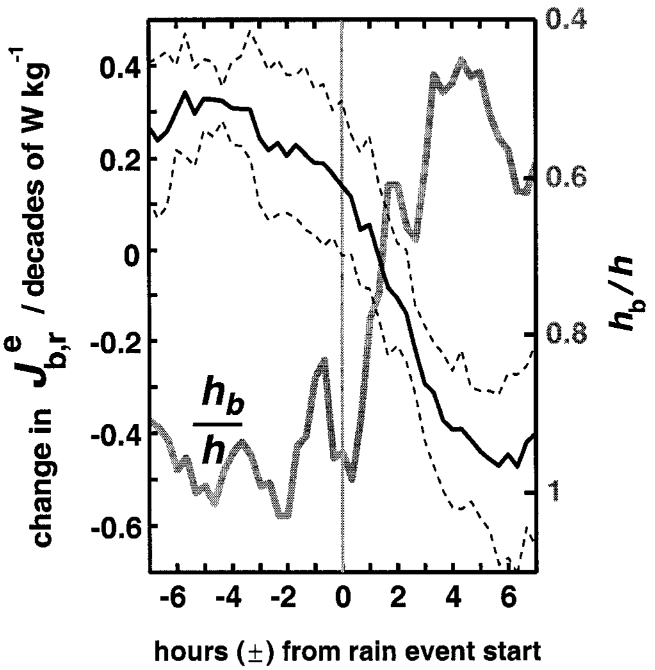

Figure 2.17: The residual buoyancy entrainment $-J^e_{b,r}$ averaged over ±7 hours from the start of 7 major rain events (black line) with a plot of h_b/h (gray line), showing that heavy rainfall reduces buoyancy entrainment by shoaling the SBL. The mean of the $-J^e_{b,r}$ for each event was removed prior to averaging. 95% bootstrap conf. intervals are indicated as dashed lines.

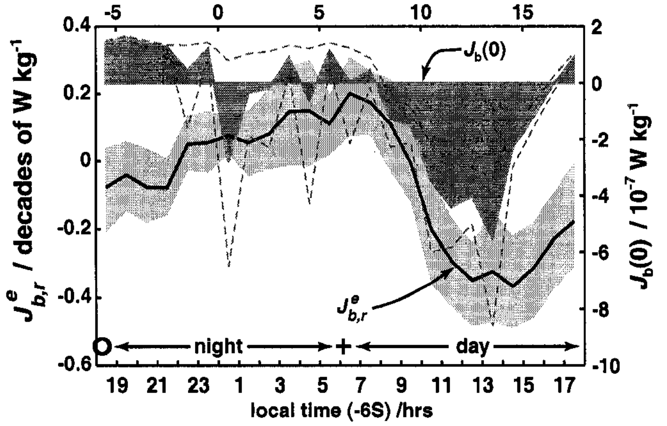

Figure 2.18: A diurnal cycle in residual entrainment buoyancy flux, $J^e_{b,r}$, (black line) linked to the diurnal cycle of surface buoyancy fluxes, $J_b(0)$ (dark gray shading). Bootstrap 95% confidence limits are shown by light gray shading and dashed gray lines respectively. Data are from the 9-day period indicated between vertical arrows in Figure 2.16.

sequently J^e_b at a near-inertial frequency. The near-inertial shear was due to the mixed layer near-inertial motions that, as discussed in Section 2.3, were likely generated by local wind stress prior to the start of the timeseries (Fig. 2.7). With only weak wind forcing until the storm beginning on September 23, these motions were observed to decay without significant wind-modification over the subsequent 9 days. As indicated in Figure 2.6, the near-inertial motions were superimposed upon a strong > 0.4 m s^{-1} relatively steady sub-inertial flow that decayed rapidly with depth below the mixed layer and, thus, had associated sub-inertial shear.[3] Together the sub-inertial and near-inertial shear were responsible for over 60% of the measured variance of 8-m shear at h over the full timeseries (Fig. 2.19). Thus, variations in the magnitude of the combined sub-inertial and near-inertial shear significantly modulated the total shear magnitude—and, thus, $Sh^2(-h)$ and $Ri^{-1}(-h)$. Although the near-inertial motions within and just below the mixed layer were super-inertial ($1.15f$ within and $1.05f$ just below), associated shear was significantly sub-inertial at $0.75f$. This differ-

---

[3] Sub-inertial flow was removed from 150-min averaged, mixed-layer ADCP velocities using a quadratic fit, with the residual boxcar-averaged over 12 hours to yield an estimate of the inertial motions. Near and sub-inertial shear was similarly separated.

ence can partly be attributed to time-changes in the relative magnitudes of the velocity vectors used to calculate shear at h, with decay of the near-inertial velocity amplitude within the mixed layer and a rough increase with time below the mixed layer. Consistent with near-inertial wave energy propagating downward (or phase upward) the velocity vector just below the mixed layer was nearly always rotated clockwise (looking down) with respect to the vector within the mixed layer. This change in relative magnitude with time resulted in a counter-clockwise rotation of the shear vector that was superimposed upon the super-inertial frequency of the velocity vectors to result in a sub-inertial frequency of finescale shear. The near-inertial frequencies of both velocity and shear were determined with a linear fit to phase (direction) from 1200 on 9/13 to 9/21. The fits had remarkable skill with $r^2 > 0.99$ for both shear and velocity and 95% confidence intervals spanning less than $\pm 0.01f$.

The sub-inertial shear frequency (ω_{si}) was the opposite sign of and significantly smaller than the near-inertial shear frequency ($\omega_{si} \approx -0.1f$, $\omega_{ni} = 0.75f$), with sub-inertial shear rotating counter-clockwise over $\pi/2$ radians over the first half of the timeseries (Fig. 2.21). A linear addition of the near-inertial and sub-inertial shear, however, resulted in a frequency modulation that was nearly the same as that for near-inertial shear, or $0.75f$. This is a consequence of the importance of both amplitude and frequency when adding vector quantities. The most significant influence of the sub-inertial shear was that it resulted in a modulation of shear magnitude at a near-inertial period that was amplified in $Sh^2(-h)$ (Fig. 2.20 a–c). This modulation of $Sh^2(-h)$ and $Ri^{-1}(-h)$ was likely the cause of the modulation of entrainment at a near-inertial period over the first half of the timeseries with three entrainment events coincident with three near-inertially-spaced peaks in $Sh^2(-h)$ (Fig. 2.20d). Additionally, the decrease of total $Sh^2(-h)$ resulting from the destructive addition of the near and sub-inertial shear appeared to reduce entrainment levels. The near-inertial modulation of entrainment by $Ri^{-1}(-h)$ is also evident in the log-space lagged correlation plot of these two variables over the first half of the timeseries (Fig. 2.22). As expected, $\log_{10}[-J_b^e]$ is modulated at a frequency near $0.75f$, with the best estimate at $0.85f$ (or a period of $(2\pi/f) + 12$ hrs). The $0.1f$ difference in the modulation frequency may be attributable to other mechanisms influencing the variability of $\log_{10}[-J_b^e]$ or simply error in the correlation estimates. Although these entrainment events were relatively weak compared to entrainment occurring during the two storms later in the timeseries, they accounted for about 20% of the timeseries-total entrainment heat flux and a somewhat smaller but still significant percent of the buoyancy and salt entrainment fluxes. Thus, although the mechanism leading to shear instability and entrainment is purely a consequence of kinematics, it has dynamical importance.

Manifested as a diurnal modulation of J_b^e that is superimposed upon the near-inertial modulation (Fig. 2.20d), the influence of the surface buoyancy fluxes on entrainment also appears to be modulated by $Sh^2(-h)$. The diurnal variability is strongest over the peaks in $Sh^2(-h)$ and $Ri^{-1}(-h)$, suggesting that these variables may enhance the penetration of turbulence associated with buoyant convection. This is consistent with large eddy simulations showing that the background dynamic stability conditions can enhance the penetration depth of convection Wang et al. (1998). Also supporting this conclusion, over the first half of the timeseries values of $h_b > 15$ m were significantly correlated (99% level) with detrended $Ri^{-1}(-h)$ ($r = 0.37$)—or h_b was greater when $Ri^{-1}(-h)$ was greater. With winds light over the first half of the timeseries, this correlation was likely not influenced by the correlation of wind stress and $Ri^{-1}(-h)$.

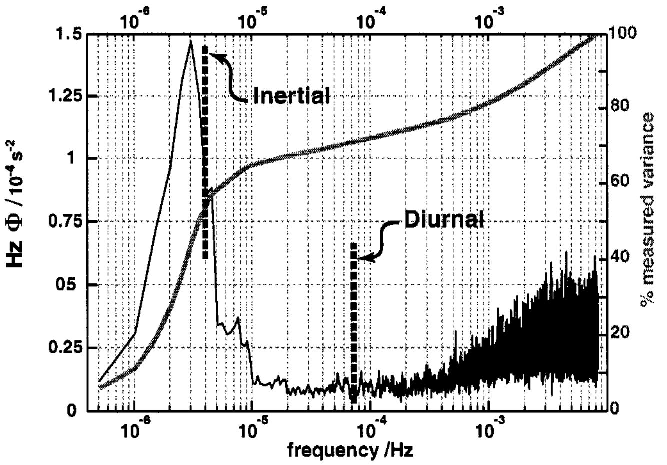

Figure 2.19: Variance-preserving spectral estimate of shear at the mixed layer base (black) and cumulative measured variance plot (gray).

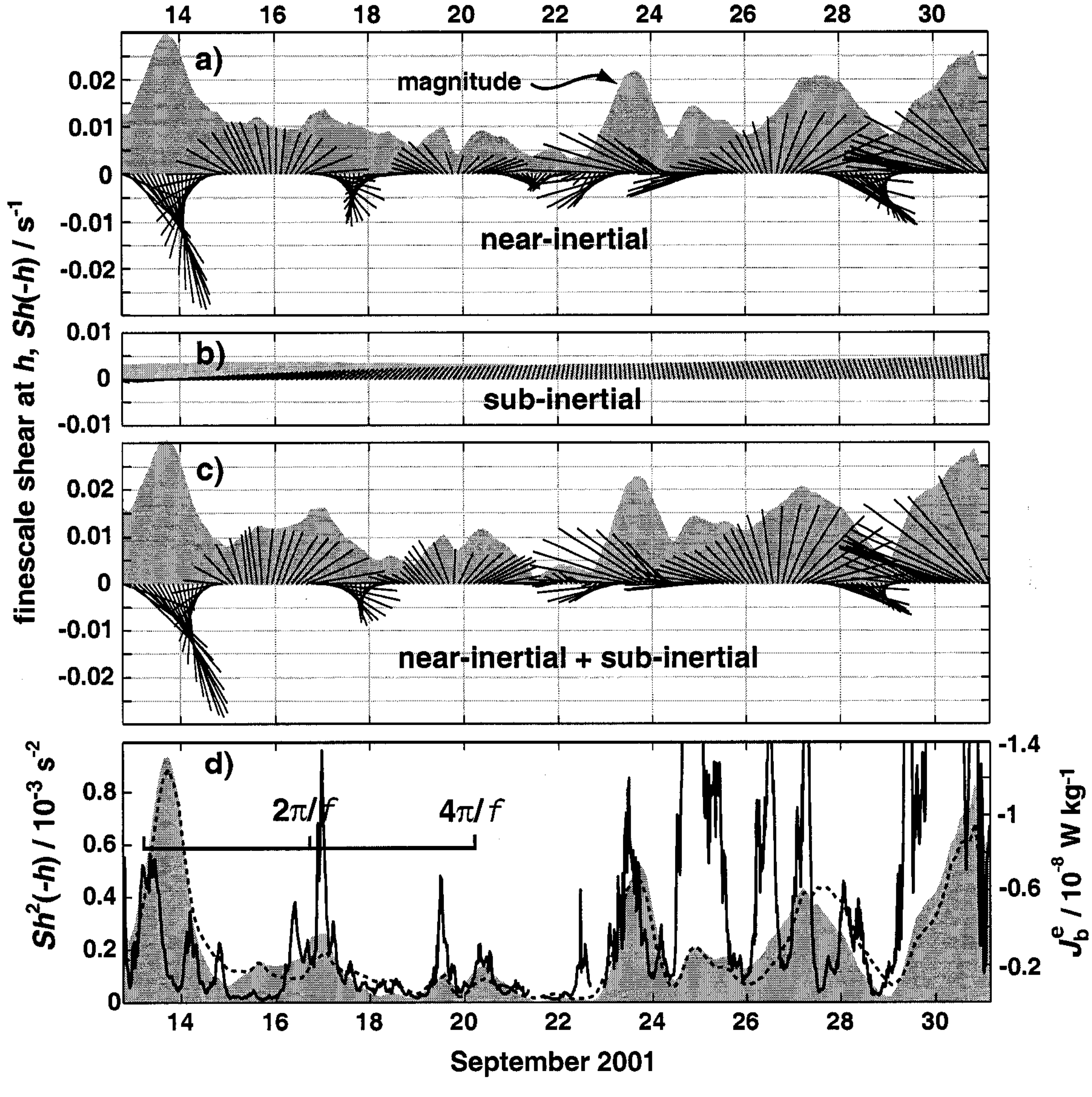

Figure 2.20: a) Quiverplot of 8-m meridional, $Shy(-h)$, and zonal, $Shx(-h)$, near-inertial shear with near-inertial shear magnitude (shaded gray). b) Sub-inertial shear quiverplot and magnitude. c) Near-inertial + sub-inertial shear. d) Total $Sh^2(-h)$ boxcar-smoothed over 15 hrs (shaded), near-inertial $Sh^2(-h)$ (dashed line) and J_b^e (black line).

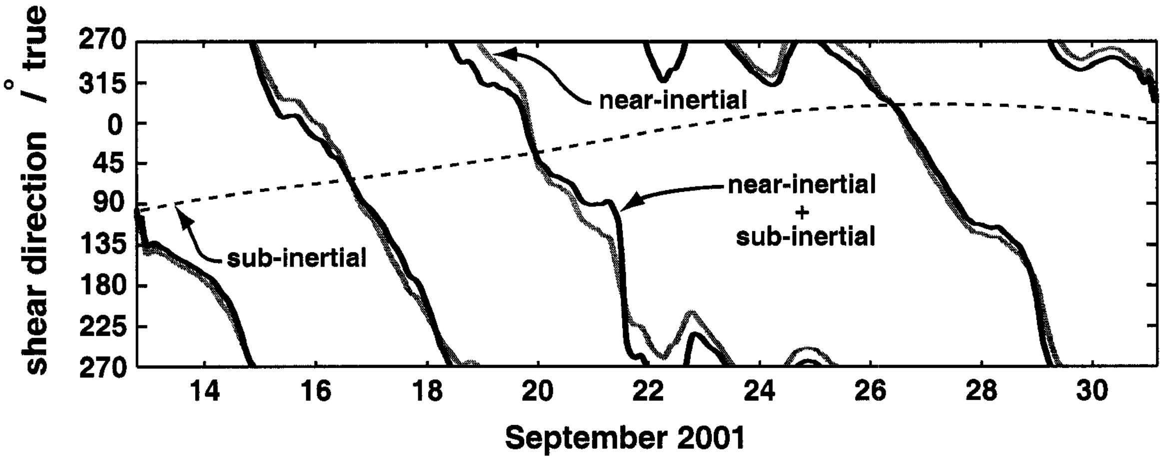

Figure 2.21: Direction of the finescale shear vector at $z = -h$ for sub-inertial (dashed), near-inertial (gray) and sub-inertial + near-inertial (black) shear.

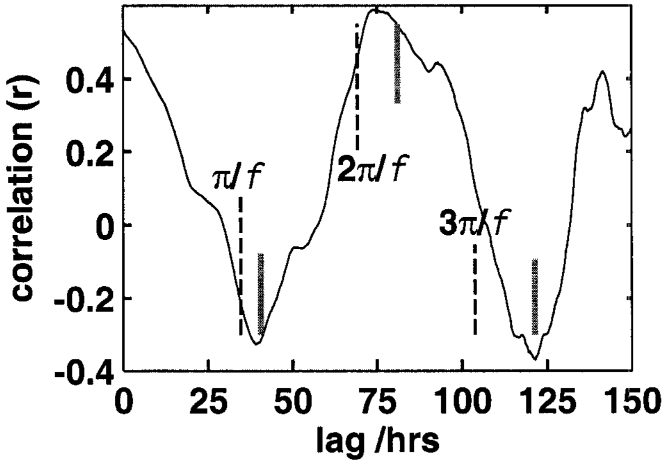

Figure 2.22: Lagged correlation of $log_{10}[-J_b^e]$ and $log_{10}[Ri^{-1}(-h)]$ (where J_b^e follows $Ri^{-1}(-h)$). The inertial period ($2\pi/f$) and fractions thereof are indicated with vertical dashed lines, and $2\pi/f$ + 12 hrs ($0.85f$) and fractions thereof are shown as gray lines. All values of $|r|$ above 0.15 are significant at the 99% confidence level.

2.4.6 Time-variability of vertical scalar gradients

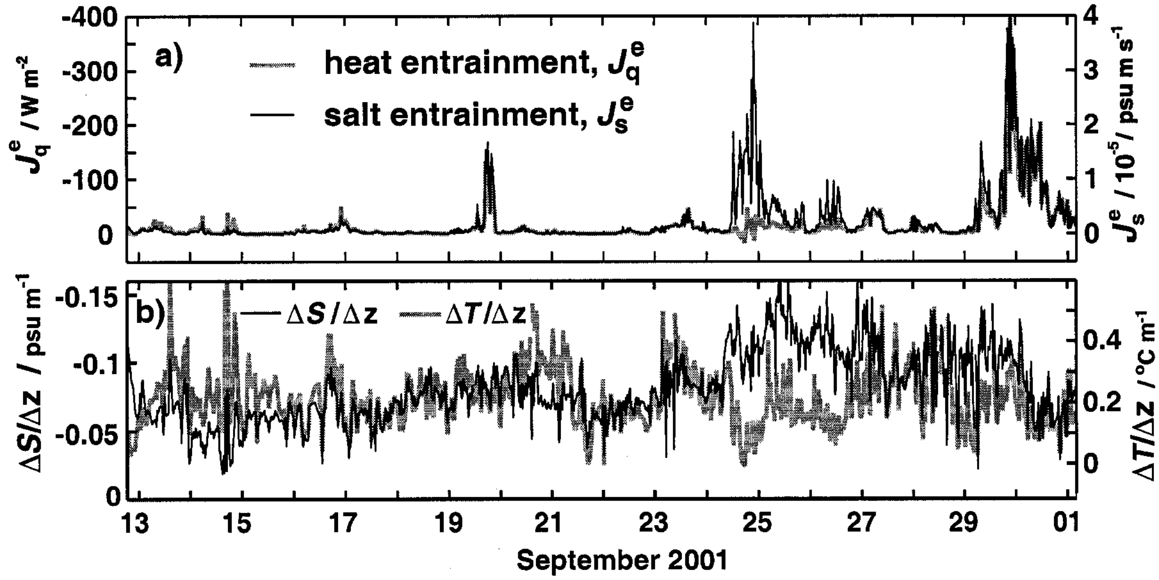

Figure 2.23: a) Heat entrainment flux, J_b^q (gray), and salt entrainment flux, J_s^e (black). b) 1-m $\Delta T/\Delta z$ (gray) and $\Delta S/\Delta z$ (black) at h.

Assuming that the vertical eddy diffusivity for heat and salt are equal to that for buoyancy (or density), time-variability of $\frac{\partial T}{\partial z}$ and $\frac{\partial S}{\partial z}$ at h was found to significantly modulate the fluxes produced by the turbulence at h (Fig. 2.23). Large variability of $\frac{\partial T}{\partial z}$ and $\frac{\partial S}{\partial z}$ at h on timescales of hours to days was a direct consequence of the region's heavy rainfall and the comparable roles of salinity and temperature in determining the mean stratification at h (the time-mean density ratio $R_\rho(-h) \approx -1$). Although surface cooling at times significantly reduced mixed layer temperature, the coincident addition of freshwater offset the tendency of this cooling to increase mixed layer density. Thus, the mixed layer depth—as defined by vertical density gradients—often remained relatively constant while $\partial T/\partial z$ at h was reduced and $-\partial S/\partial z$ increased.

The above set of conditions developed during the storm on September 24–25 when strong surface cooling was coupled with heavy rainfall. Although turbulent diffusivity was greatly elevated above background conditions during this storm, small and at times negative $\partial T/\partial z$ at h resulted in small (and even positive) entrainment heat fluxes (Fig. 2.23). The storm's intense rainfall caused an increase in $-\partial S/\partial z$ at h elevating entrainment salt fluxes over levels anticipated considering only increased diffusivity (K_S). The rainfall also decreased mixed layer density despite the rapid surface cooling (Fig 4.6), consequently preventing h (and h_b) from deepening—which would have worked to maintain a large, positive temperature gradient. In contrast, during the storm from September 29 to October 1, which had strong winds but much less precipitation, large vertical gradients of T, S and σ_θ persisted at h, and as a result J_q^e varied similarly to J_s^e and J_b^e (Fig. 2.23). The significant reduction of $\frac{\partial T}{\partial z}$ during the first storm had the effect of reducing the timeseries-averaged entrainment heat flux by roughly 30%.

2.5 Discussion

As discussed in Section 2.2, one significant limitation of the approach for estimating the vertical turbulent fluxes used here [the dissipation method of Osborn (1980)] is the inability to estimate fluxes within buoyant convection and/or unstratified regions. This constraint precludes the estimation of vertical turbulent fluxes over much of the boundary layer, and, thus, complicates direct comparisons to turbulent flux estimates from upper-ocean models or large-eddy simulations. Since, as suggested by Large et al. (1994), the advancement of entrainment parameterizations is severely limited by a lack of oceanic observations, improving our ability to observe (measure) turbulent fluxes within the SBL is paramount to improving entrainment models and also our general understanding of the dynamics controlling SBL vertical turbulent fluxes. For these reasons, continuing to develop techniques for directly measuring vertical turbulent fluxes (or the correlation of the perturbations) by building upon the pioneering work of Moum (1990) and D'Asaro (2004) will likely be fruitful.

Despite this observational limitation, the results presented here have a number of important implications to modeling entrainment fluxes—both in general and specifically within the EPWP. The finding that relatively slowly-evolving finescale shear at the mixed layer base strongly influences entrainment fluxes indicates that accurately modeling its evolution is essential to correctly determining the entrainment fluxes. Research indicates that the decay of mixed layer inertial motions, which dominated measured finescale shear variance at h in these observations, is strongly influenced by the radiation of near-inertial internal waves (Gill, 1982; D'Asaro, 1995). Thus, it is likely that successful efforts to model $Ri(-h)$ will include internal wave dynamics or at least effective parameterizations of these dyanmics. Although an investigation of the mixed layer energy budget is beyond the scope of this chapter, EPIC timeseries observations are qualitatively consistent with previous findings. A depth-time map of total kinetic energy computed from ADCP velocities shows an increase in energy within the upper pycnocline that is coincident with the rapid loss of inertial-response kinetic energy from the mixed layer (an average rate of 1.3×10^{-7} W kg^{-1}) (Fig. 2.24a,b). Both the downward propagation of energy with time within the pycnocline and the clear presence of a robust, downward-propagating (upward phase) near-inertial internal wave in depth-time maps of finescale shear direction (Fig. 2.24c) suggest that much of the energy loss from the mixed layer is due to the radiation of near-inertial internal waves. Since our understanding of the decay of mixed layer energy and shear at the mixed layer base due to the radiation of internal waves remains incomplete (Levine and Zervakis, 1995; D'Asaro et al., 1995; D'Asaro, 1995), a clear direction for future research is to use these and other data to investigate the role of near-inertial wave radiation in the decay/modulation of $Sh^2(-h)$, $Ri^{-1}(-h)$ and entrainment.

A cubic dependence on the friction velocity indicates that accurately modeling the largest surface stresses, thus the fastest wind speeds, is also vitally important to obtaining proper estimates of entrainment. Recent work indicating that surface wave effects strongly influence air-sea momentum transfer (Moon et al., 2004) suggests that improvements to bulk wind stress parameterizations may require sub-models of surface wave characteristics. An equally-difficult challenge is to properly model the highly spatially-variable (Wijesekera et al., 2005) but often intense rainfall within the EPWP, which was not only found to suppress entrainment by shoaling the SBL but also contributed to the modulation of the vertical gradients of temperature and salinty at the mixed layer base—which in turn modulated the entrainment fluxes. In short, the sensitivity of entrainment to surface forcing indicates that even if the entrainment parameterizations are dynamically-accurate, the modeled fluxes will only be as accurate as the model input parameters.

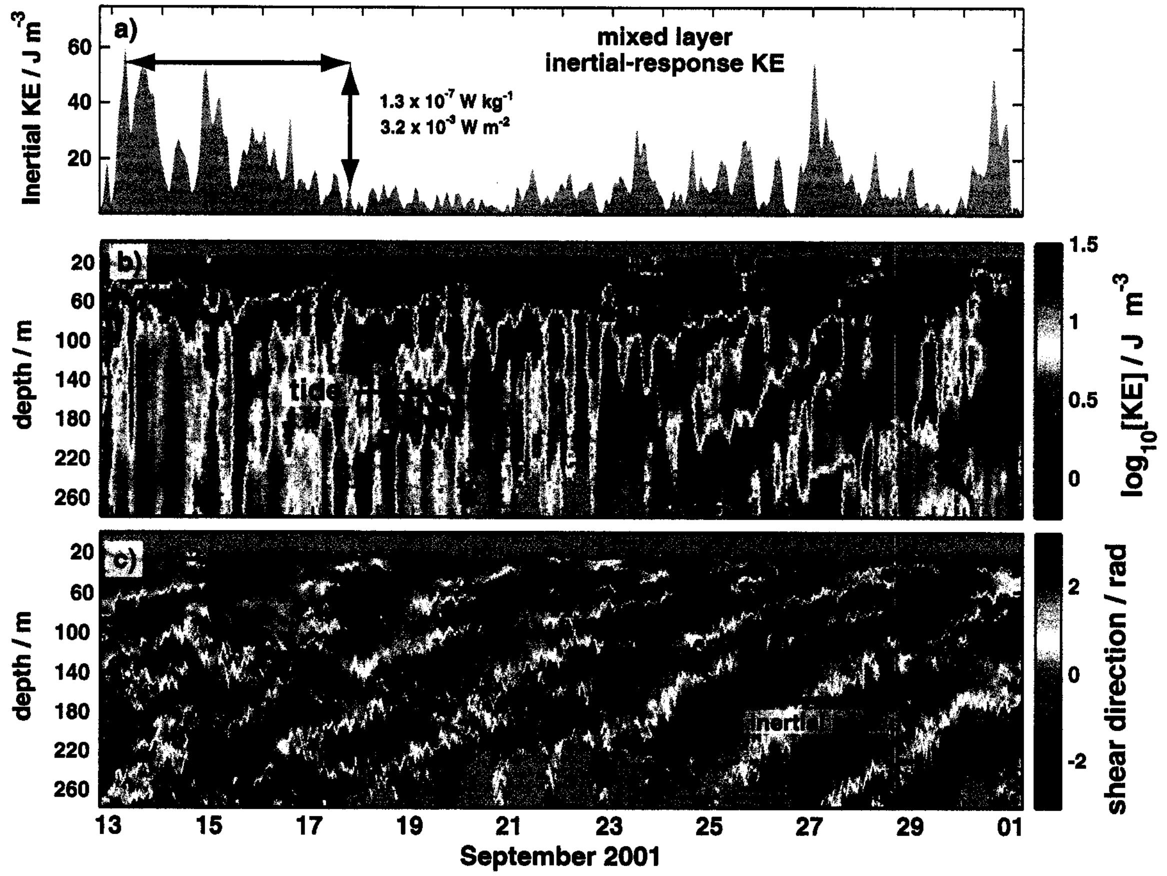

Figure 2.24: a) Mixed layer kinetic energy associated with the inertial response, showing a rapid decay over the first 5 days of the timeseries. b) Depth-time map of total kinetic energy computed from ADCP velocity showing a downward propagation of energy out of the mixed layer. c) Direction of the finescale (8-m) shear vector indicating the presence of a robust, downward-propagating near-inertial internal wave. The mixed layer depth is shown in black in panels (b) and (c).

2.5.1 Resonant mixed layer forcing by atmospheric easterly waves

As previously indicated, the strong mixed layer inertial currents at the start of the EPIC timeseries were not generated by strong, impulse-like winds but by the steady clockwise rotation of moderate winds by 360 degrees over a time-span roughly equal to the local inertial period ($\sim$3 days). Because the wind stress vector was nearly always pointing in the direction of the mixed layer inertial currents that it generated ($\vec{\mathbf{U}}_i$), the rate of energy input from the wind to the mixed layer inertial motions (approx. $\vec{\tau} \cdot \vec{\mathbf{U}}_i$) is nearly always positive. A number of recent studies [e.g. Petersen et al. (2003); Serra and Houze (2002)] have shown that much of the high-frequency variability of the climatological mean pattern of convection and wind of the eastern tropical Pacific ITCZ is dominated by the passage of atmospheric easterly waves with periods of about 3–5 days. With this period close to the local inertial period over much of the meridional range of the ITCZ, or about 5 ° N–10° N, there is the possibility that these waves may resonantly force mixed layer inertial motions.

Previous model-based investigations of resonant forcing of mixed layer inertial motions at mid-latitudes by storms occurring on short timescales (1–2 days) (Crawford and Large, 1996) found that resonant wind-forcing maximizes not only the mixed layer kinetic and potential energy, but also SST changes as a direct consequence of elevated entrainment. As with all resonant forcing, however, results showed that the phase or timing of the storms with respect to pre-existing mixed layer currents was critical to whether energy was added or removed from the mixed layer motions. Here a simplistic investigation of resonant forcing by easterly waves within the EPWP using observed TAO buoy winds over 2001 and results from the 1-D Pollard and Millard (1970) slab model indicates that easterly waves resonantly force inertial motions within the EPWP, and, thus, may significantly influence SST through entrainment heat fluxes.

The influence of wind rotation on the flux of kinetic energy from the wind into mixed layer motions is demonstrated by running the Pollard and Millard (1970) model using both the observed wind stress and winds altered so that the direction of rotation is always opposite to that in the observations. This is achieved by simply changing the sign of either the meridional or zonal wind stress, with the wind stress magnitude preserved. Here TAO buoy thermistor data are used to estimate a time-variable mixed layer depth and the model decay coefficient ($r = 1/5$ days^{-1}) is based upon a fit of model to observed mixed layer inertial velocities over the EPIC timeseries (see Fig. 2.7). Integrating the model KE flux from the wind stress to mixed layer motions (both Ekman and inertial) over 2001 for the two cases shows that the rotation direction of the observed winds is important to the KE flux from the wind to mixed layer inertial motions. Results show that from July to December 2001 the observed winds add about five times more net KE to the mixed layer than winds with reversed rotation but equal magnitude (Fig. 2.25a). Although research by Plueddemann and Farrar (2006) conducted at the western edge of the EPWP suggests that the Pollard and Millard (1970) model can significantly over-estimate the cumulative kinetic energy flux from the wind to the mixed layer there, for determining resonant forcing we are more interested in the difference in the two cases (real vs. reversed wind rotation) than in absolute KE fluxes.

Rotary spectra (Gonella, 1972; Leaman and Sanford, 1976) of wind stress over the period from July–December 2001 indicate that there was about 2–3 times more variance at inertial and easterly wave periods in the clockwise component of the observed winds than in the counter-clockwise component (Fig. 2.25b). Thus, it appears that the much greater addition of KE to mixed layer motions from the observed winds than the "reversed-rotation" winds is due to the fact that observed winds at near-inertial frequencies over the period from July–December are dominated by clockwise rotation—and, thus, resonantly force mixed layer motions. The connection of this clockwise-rotation of wind stress to easterly waves is supported by both the frequency range dominated by the clockwise response as well as by the fact that the largest differences between clockwise and counter-clockwise spectra occur when the ITCZ spans 10° N, or about July through October. With the typical period of easterly waves slightly longer than the inertial period at 10 ° N, there is the expectation that this resonance may be stronger around 6 °–7°N where the two periods overlap more closely.

Although these results show that resonant forcing is likely, a much more comprehensive analysis of the influence of easterly waves on mixed layer dynamics is needed. Future studies should include specific case studies of the passage of several wave periods to test the suggestion that the enhanced clockwise rotation of the wind stress vector from July–December is, in fact, due to the passage of easterly waves. Although Petersen et al. (2003) showed that meridional and zonal winds were positively correlated in the troughs of the three waves spanning the EPIC timeseries, they did not observe a consistent clockwise rotation with time with the passage of the waves. Additionally, a detailed investigation of the influence of these waves on entrainment fluxes and SST would be an invaluable contribution to our understanding of air-sea interaction and the processes controlling SST within the ITCZ.

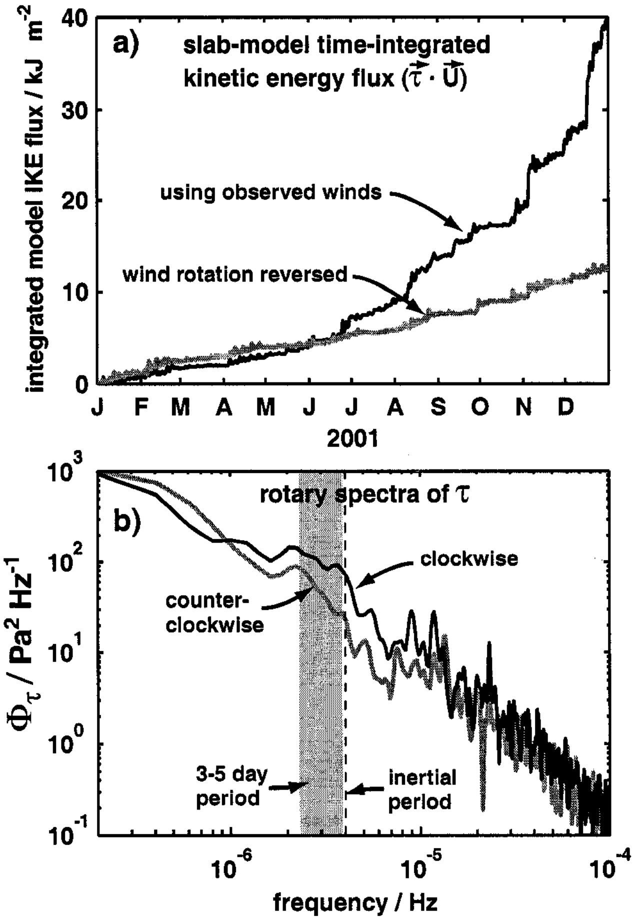

Figure 2.25: Evidence of resonant forcing of inertial motions by easterly waves. a) Time-integrated kinetic energy flux from the wind to the mixed layer as estimated from the Pollard and Millard (1970) 1-D slab model. Model results using observed winds are shown in black, and results using altered winds with the direction of rotation reversed (changing sign of either meridional or zonal stress) is shown in gray. b) Rotary spectra [clockwise (black), counter-clockwise (gray)] for wind stress from July–December 2001. The approx. 3–5 day period of easterly waves is shown with gray shading and the local inertial period at 10 ° N is indicated with a dashed line.

Chapter 3

AN OBSERVATIONALLY-BASED EVALUATION AND MODIFICATION OF THE NIILER-KRAUS (1977) ENTRAINMENT PARAMETERIZATION

3.1 Background

With an end goal of obtaining reliable estimates of entrainment fluxes at 10° N, 95° W on seasonal to annual timescales, here we investigate the skill of the 1-D Niiler and Kraus (1977) (N-K) mixed layer model at estimating entrainment by comparison of model values with the EPIC timeseries observations. As in Chapter 2, entrainment fluxes are defined as vertical turbulent fluxes at the mixed layer base. EPIC observations are used to justify several empirically-based modifications to the N-K model which significantly improve model skill. The choice to specifically investigate the N-K model is motivated by several factors. First, the functional form of the N-K model entrainment parameterization closely parallels a form suggested by the results of the multiple linear regression of $\log_{10}[J_b^e]$ with both $\log_{10}\,[u_*^3/(\kappa h)]$ and $\log_{10}[Ri^{-1})]$ shown in Chapter 2 (i.e. $J_b^e \propto [u_*^3/(\kappa h)]Ri^{\varphi}$), except that the N-K form also includes the influence of both destabilizing and stabilizing surface buoyancy fluxes. Thus, there is an expectation that the N-K model will improve on the already respectable skill of the above linear regression that describes about 70% of the variance of J_b^e over the 19-day EPIC timeseries. It is important to note, however, that the form for buoyancy entrainment given by the N-K model is not empirically-based but was arrived at through a rigorous derivation centered on the integration of the steady-state turbulent kinetic energy (TKE) equation over the mixed layer.

A second reason for choosing the N-K model is the ease at which it can be evaluated in diagnostic (vs. prognostic) mode to obtain estimates of entrainment flux from time-dependent observations of mixed layer properties and surface fluxes. This is primarily because unlike most other 1-D mixed layer models [e.g. Price-Weller-Pinkel (PWP) (Price et al., 1986) and KPP (Large et al., 1994)] the N-K model includes an explicit equation for turbulent buoyancy entrainment. Since in diagnostic mode all variables except for entrainment are model inputs, the model's skill at estimating entrainment is not dependent upon the accurate prediction of quantities that influence entrainment [e.g. $Ri(-h)$, h]. With entrainment fluxes strongly dependent upon h, the explicit determination of this quantity from measurements is particularly important for modeling entrainment fluxes within the EPWP since it has been shown that the dominant seasonal to annual variability of h in this region (with h roughly equivalent with the top of the seasonal thermocline as per the definition in Chapter 2, Section 2.2.1) is due to Ekman and Rossby wave dynamics—processes that can not be simulated by a 1-D model. Thus, even though time-changes in h are partly due to entrainment, because of the strong influence of vertical and horizontal advection on $\partial h/\partial t$ within the EPWP, in diagnostic mode the model does not mathematically equate $\partial h/\partial t$ with entrainment. In fact, using the measured value of h has the advantage of implicitly accounting for the influences of advection and restratification on $\partial h/\partial t$ and, thus, on entrainment. Another way of looking at this is that entrainment is a better indicator of model skill than mixed layer depth. Although it is possible to run other 1-D mixed layer models such as Price-Weller-Pinkel (PWP) (Price et al., 1986), KPP (Large et al., 1994), Mellor-Yamada (Mellor and Yamada, 1982) in diagnostic mode, doing so is significantly more cumbersome than with the N-K model.

Interest in the N-K model also stems from its potential to provide entrainment estimates from a relatively basic set of observations including τ, $J_b(0)$, $Ri(-h)$, and h, that are provided by most TAO buoys. With a TAO buoy adjacent to the EPIC timeseries location, this would permit entrainment flux estimates at the 10°N, 95° W EPIC timeseries location at times other than during the EPIC timeseries (Chapter 4). In their investigation of the mixed layer temperature budget within the western equatorial Pacific warm pool, Cronin and McPhaden (1997) took this approach—using TAO buoy observations to evaluate the N-K entrainment parameterization—but lacked direct entrainment observations to allow evaluation and tuning of the model.

One of the largest limitations of the N-K entrainment parameterization is that the three primary constants used to tune the model have been shown with laboratory experiments to be a function of both external forcing (u_*) as well as the stratification, and, thus, one would expect these constants to change in time and space. However, since in this study entrainment measurements are available to tune the N-K model to local conditions and entrainment is only to be modeled at one location

(10°N, 95° W), this shortcoming is of less of a concern. It is important to note that if this approach applied to other locations it is likely that direct observations would be needed to tune the model to local conditions.

Three observationally-based modifications are made to the N-K model in an attempt to improve model skill and address physical inconsistencies within the model that are a consequence of the chosen definition of the mixed layer depth. One modification relaxes the assumption that temperature, salinity and velocity are at all times quasi-uniform within the mixed layer by allowing the accumulation of implied stratification within the mixed layer when destabilizing forcing is weaker than stabilizing forcing. Another modification allows weak surface-forced entrainment during these latter conditions, where the basic N-K model sets entrainment to zero at these times. A third modification changes the specific dynamic stability formulation used in the N-K entrainment parameterization to a simple gradient Richardson number dependence.

A comparison of EPIC timeseries observations of entrainment to those estimated by the modified N-K model indicate that the model has exceptional skill ($r > 0.90$ for 4-hr smoothed data over 19-days), and improves significantly on the multiple linear regression fit presented in Chapter 2 ($r = 0.83$) which simply used 8-m $Ri(-h)$ and $u_*^3/(\kappa h)$ to describe J_b^e. This large correlation is despite the ten-fold variability in J_b^e and large variability of model inputs (except h). When compared to the un-modified N-K model run over the EPIC timeseries, the modified model reduced root-mean-square error (RMSE) over the 19-day EPIC timeseries by 35% and a mean bias of +40% to less than +2%. It is important to note, however, that despite this significant model skill, an estimated factor-of-two uncertainty in the EPIC timeseries buoyancy entrainment measurements (Peters et al., 1988) sets uncertainty of model entrainment estimates to this uncertainty or greater.

3.2 The N-K Model Entrainment Parameterization

In addition to its one-dimensionality, which assumes that horizontal gradients of momentum and scalars are negligible, the primary assumptions of the N-K model are that, 1) the mean temperature, salinity and horizontal velocity are quasi-uniform over the mixed layer, 2) at the depth and time scales of the model there is a quasi-discontinuous distribution of the above properties at the sea surface and at the mixed layer base, and 3) time-changes of turbulent kinetic energy are significantly smaller than turbulence generation and dissipation terms. The first of these assumptions allows the vertical integration of the conservation equations for mixed layer momentum, temperature, salinity, and buoyancy (or density). This integration yields expressions for the time evolution of the bulk (depth-averaged over the mixed layer) quantities themselves as a function of the external inputs—or exchanges with the air above and the interior ocean below the mixed layer. The EPIC timeseries observations indicate that the first and second assumptions are reasonable, with a well-defined mixed layer and rapid changes in momentum and scalars at the surface and mixed layer base.

The third assumption allows the integration of the steady-state turbulent kinetic energy (TKE) equation over the mixed layer to give an explicit equation for buoyancy entrainment. All terms of the depth-integrated TKE equation are parameterized or represented in terms of external forcing variables (see Niiler and Kraus (1977) for details). Specifically, buoyancy entrainment is parameterized as the product of a term accounting for the bulk mixed layer stability conditions and the sum of several surface forcing terms including a wind-work term, surface buoyancy flux terms and a term accounting for the influence of penetrative solar radiation on mixed layer TKE. Arranging terms of N-K Equation 10.30 to give buoyancy entrainment, this is formally:

$$\tilde{J}_b^e = \left[\overbrace{2m\frac{u_*^3}{h}}^{1} + \overbrace{nJ_b(0)^+}^{2} + \overbrace{J_b(0)^-}^{3} + \overbrace{\left[(1-\frac{2}{h\lambda}) + (1+\frac{2}{h\lambda})e^{-\lambda h}\right] J_b^{sw}(0)}^{4} \right] \overbrace{\frac{1}{(sRi_b^{-1}-1)}}^{5}, \quad (3.1)$$

where $\tilde{J}_b^e$ is the modeled entrainment buoyancy flux, m, n and s are proportionality constants, $J_b(0)^+$ and $J_b(0)^-$ are the positive and negative surface buoyancy fluxes minus the contribution from the buoyancy equivalent of the penetrative heat flux at the surface, $J_b^{sw}(0)$, and λ^{-1} is the extinction length scale of solar penetrative radiation. To evaluate term 4 we use the decay scale ($\lambda = 0.076$) and $J_b^{sw}(0)$ from the penetrative radiation model of Ohlmann (2003) that is largely based on EPIC timeseries data. The specific form for the surface buoyancy flux, or separating the positive and negative fluxes into two terms, was chosen to make the equations less cumbersome and to show the individual and dynamically-different contributions to entrainment from stabilizing and destabilizing fluxes. Here it is important to clarify that when the positive surface buoyancy flux $[J_b(0)^+]$ is nonzero, the value of the negative surface buoyancy flux $[J_b(0)^-]$ will necessarily be zero and vice-versa, or mathematically:

$$\begin{aligned}
&\text{when } [J_b(0) - J_b^{sw}(0)] > 0 \\
&\qquad J_b(0)^+ = J_b(0) - J_b^{sw}(0) \\
&\qquad J_b(0)^- = 0 \\
&\text{when } [J_b(0) - J_b^{sw}(0)] < 0 \\
&\qquad J_b(0)^- = J_b(0) - J_b^{sw}(0) \\
&\qquad J_b(0)^+ = 0
\end{aligned}$$

Term 1 in Equation 3.1 is the mixed layer averaged net rate of wind working, or TKE production and fluxes minus dissipation, with the relative importance of these terms accounted for by the coefficient m. Terms 2 and 3 represent sources and sinks of TKE respectively, with positive surface buoyancy fluxes generating mixed layer TKE and negative surface buoyancy fluxes suppressing TKE. The coefficient of term 2 (n) accounts for the fraction of buoyancy-driven TKE production that is not dissipated within the mixed layer. Term 4 accounts for the stabilizing influence of solar penetrative radiation, which acts to suppress TKE. As in Cronin and McPhaden (1997), here we assume a single-exponential decay in term 4 that accounts for mixed layer depths that are less than or similar to λ^{-1}. Term 5 represents the influence of the mixed layer bulk Richardson number, $Ri_b \equiv \Delta b h / \vec{v}^2$, where Δb is the (step-like) change in buoyancy at the mixed layer base and $\vec{v}$ the mixed layer velocity. This term arises from considering both the energy required to lift and mix dense entrained water as well as the reduction of mixed layer kinetic energy by momentum mixing at the mixed layer base, and is required to be negative-definite (or $sRi_b^{-1} < 1$) to prevent model instability. The coefficient s accounts for the efficiency of shear-driven mixing at the mixed layer base. As $sRi_b^{-1} \rightarrow 1$ term 5 becomes large and increases the efficiency of wind stress and destabilizing surface buoyancy fluxes at generating entrainment. Physically, N-K related this multiplicative-dependence on the bulk mixed layer dynamic stability conditions to the availability of energy from the non-turbulent mixed layer flow which can assist direct surface forcing in entraining and mixing dense thermocline water. It can be shown that the form of term 5 is similar to a bulk reduced shear-squared $(Sh^2 - 4N^2)$ dependence, where like Ri reduced shear-squared gives an indication of the potential for shear-instability, with $Sh^2 - 4N^2 > 0$ equivalent to $Ri < 1/4$.

To simplify notation throughout this Chapter, here we define a quantity J_b^* that is simply the sum of terms 1 through 4 of Equation 3.1, so that:

$$\tilde{J}_b^e = J_b^* \frac{1}{(sRi_b^{-1} - 1)} . \tag{3.2}$$

Within the N-K formulation, when the r.h.s. of the above equation is positive, or when stabilizing surface and penetrative buoyancy fluxes overcome the turbulent energy supplied by the wind (or wind mixing), entrainment is set to zero and the observed mixed layer depth is expected to decrease or remain at a constant depth in the absence of advective effects. The model assumes that when entrainment is zero, the mixed layer is decoupled from the interior ocean. As specifically stated in Niiler and Kraus (1977), "In the absence of entrainment, all the turbulent fluxes become zero at $z = -h$. In physical terms, this means that there is just not enough turbulence energy available in this case to overcome the stable stratification at the base of the layer and to produce any mixing with the lower water. The mixed layer becomes then effectively decoupled from the ocean interior. In the model presented here, this decoupling is assumed to be absolute."

3.3 Empirically-based Modifications to the N-K Entrainment Parameterization

3.3.1 A gradient $Ri(-h)$ dependence

The simplest of three N-K modifications employed here is to use a finescale gradient Richardson number and not the bulk N-K formulation (term 5 of Eqn. 3.1). This modification is included largely because of the strong empirical support for a $Ri(-h)$-dependence presented in Chapter 2 and because of the significantly greater model skill that results from using $Ri(-h)$. Additionally, using $Ri(-h)$ instead of the N-K bulk instability parameter avoids inconsistencies that could potentially occur when the latter quantity is greater than or equal to zero. Specifically, this modification replaces term 5 of Equation 3.1 with $sRi(-h)^{\varphi}$, where the constant coefficient s is negative and chosen to maximize r or minimize model error (RMSE). Although the exponent ($\varphi = -0.87$) was also selected to maximize the correlation between modeled and observed J_b^e, it is worth noting that its value is consistent with the slope of the regression of $\log_{10}[Ri]$ and $\log_{10}[J_b^e]$ presented in Chapter 2 (Tab. 2.2).

It is important to clarify that the *measured* finescale $Ri(-h)$ over the EPIC timeseries [1] is never supercritical ($< 1/4$), indicating that shear-instability is unlikely at this scale and, thus, it is unlikely that finescale shear instability is the sole cause of entrainment generation. As discussed in Chapter 2, however, the significant correlation between $Ri(-h)$ and J_b^e indicates that finescale $Ri(-h)$ is either facilitating or statistically-related to unresolved shear-instabilities. This is consistent with the N-K formulation, which requires $sRi_b > 1$ for model stability with s found to be < 1, or $Ri_b \gtrsim 1$. Thus, it is expected that using the above model form with a scale of $Ri(-h)$ that *does* resolve instability scales may be inappropriate and may result in large model errors. Unfortunately, the shallow mixed layer depth and relatively coarse vertical resolution of the ADCP used over the EPIC timeseries preclude an investigation of the sensitivity of the model to variations in the scale of $Ri(-h)$.

3.3.2 Accounting for weak mixed layer stratification and indirect entrainment

The remaining two modifications suggested here are relevant because of the specific definition of the mixed layer depth used here, where the mixed layer is viewed in a time-averaged sense (over at least several days) and its base is co-located with the top of the seasonal pycnocline (see Chapter 2 for the quantitative definition). This particular definition was chosen for a number of practical reasons, among which observational limitations are the most significant. It is consistent with mixed layer definitions used in a number of other applications of the N-K model [e.g. Cronin and McPhaden (1997); Wang et al. (1995)]. Defined as such the mixed layer depth does not capture diurnal and shorter cycling of the mixed layer depth, and, thus, on these short timescales does not shoal as a consequence of stabilizing surface forcing overcoming destabilizing (turbulent) forcing at $z = -h$.

Within the N-K model framework, this means that when entrainment equals zero (or more correctly the quantity on the l.h.s. of Eqn. 3.1 is > 0) the observed mixed layer depth does not decrease

---

[1] Finescale (8-m) Ri is computed with 8-m Sh^2 derived from 1-minute, 4-m binned ADCP velocities averaged over 150 minutes and roughly 30-minute, 8-m N^2 computed from MMP profiles (see Appendix A)

as a consequence but remains relatively constant. This creates a physical inconsistency within the N-K model when the instantaneous destabilizing forcing once again overcomes the instantaneous stabilizing forcing (the quantity on the l.h.s. of 3.1 is < 0). At this time the model expects entrainment to resume, under the incorrect assumption that turbulent energy has overcome the stabilizing forces within the mixed layer. For a mixed layer depth defined in a instantaneous sense, which would decrease when the l.h.s. of Eqn. 3.1 is > 0, this would be an appropriate assumption. However, because stratification within the mixed layer as defined here increases during the time that stabilizing forcing dominates, before entrainment can once again resume the destabilizing forcing has to overcome this accumulated stratification in addition to the instantaneous stabilizing forcing. In observations this influence of mixed layer stratification is often exhibited as a lag between the times of the onset of strong destabilizing forcing and elevated entrainment fluxes. Specifically, EPIC timeseries observations show that short-lived but intense rainfall would often suppress entrainment for more than several hours after the rain ceased despite strong destabilizing surface forcing. This persisting stabilizing influence of heavy rainfall was also observed within the western Pacific warm pool (Wijesekera and Gregg, 1996; Anderson et al., 1996). Surface-driven TKE working against this accumulated mixed layer stratification can also be thought of in terms of deepening an instantaneously-defined mixed layer to its "pre-shoaling" depth—or its depth before stabilizing surface and/or penetrative heat fluxes caused the instantaneous mixed layer to shoal.

The amount of work required to overcome this accumulated stratification can be thought of in terms of a deficit of depth-integrated mixed layer potential energy (E_p), with surface-forced turbulence having to increase E_p by some amount ΔE_p by erasing mixed layer stratification before entrainment can resume. Following Winters et al. (1995) the mixed layer-integrated potential energy is:

$$E_p = \frac{g}{\rho_0}\int_{-h}^{0} \rho z dz \quad [\mathrm{J\,m\,kg^{-1}}]\,. \tag{3.3}$$

As indicated by Niiler and Kraus (1977), if terms 1–4 in Equation 3.1 are multiplied by h (to give depth-integrated values vs. depth-averaged) they can be thought of in terms of rates of change of E_p. This relationship can be illustrated by considering the equation describing buoyancy time-changes resulting from only turbulent buoyancy fluxes:

$$\frac{\partial b}{\partial t} = -\frac{\partial}{\partial z}\overline{w'b'} \,. \tag{3.4}$$

Assuming that density is constant with depth within the mixed layer, integrating the above relation from 0 to $-h$ two times gives rates of change of E_p in terms of the fluxes at the boundaries ($z = 0, -h$):

$$\begin{aligned}
\frac{\partial}{\partial t}\left[-\frac{g}{\rho_0}\int_{-h}^{0}\int_{-h}^{0}\rho dz' dz\right] &= -\int_{-h}^{0}\left(\overline{w'b'}|_{-h}^{0}\right) dz \,, && (3.5)\\
\frac{\partial}{\partial t}\left[\frac{g}{\rho_0}\int_{-h}^{0}\rho h dz\right] &= \int_{-h}^{0}\left[J_b(0)^+ + J_b(0)^- - J_b^e\right] dz \,, && (3.6)\\
\frac{\partial}{\partial t}\left[\frac{g}{\rho_0}\rho h^2\right] &= \left[J_b(0)^+ + J_b(0)^- - J_b^e\right] z|_{-h}^{0} \,, && (3.7)\\
\frac{\partial}{\partial t}[E_p] &= \frac{h}{2}\left[J_b(0)^+ + J_b(0)^- - J_b^e\right] \,, && (3.8)
\end{aligned}$$

where positive surface buoyancy fluxes and entrainment fluxes increase E_p and negative (stabilizing) surface buoyancy fluxes reduce E_p. It is important to recognize that the above relation implies that buoyancy changes from these fluxes are mixed throughout the mixed layer. Additionally, although the influence of penetrative solar radiation on E_p was excluded in the above derivation for the sake of simplicity, it can be included without much difficulty (see N-K Equations 10.4, 10.23 and 10.24).

Within the N-K model framework, the amount of work required to erase mixed layer stratification (ΔE_p) is approximated by maintaining a running time-summation of negative E_p rates of change, which occur when the sum of the first four terms of Equation 3.1 is negative—or when the magnitude of the sum of the (negative) stabilizing terms (terms 3+4) is larger than the sum of the destabilizing (terms 1+2). Thus, wind stress $[u_*^3/h]$ and destabilizing surface buoyancy flux, $J_b(0)^+$, increase E_p by both mechanically mixing dense water upwards and, specifically for $J_b(0)^+$, by "filling" the mixed layer with more dense water during convection. Stabilizing surface buoyancy fluxes, $J_b(0)^-$, and the buoyancy flux equivalent of the penetrative heat flux, J_b^{sw}, work to stratify the mixed layer or to create an E_p deficit. In order to account for the influence of variations in h on E_p changes, terms 1 through 4 are multiplied by h prior to their time-summation, which also converts from mixed layer-averaged to mixed layer-integrated rates of change of E_p. The specific summation is then:

for $t = t_0, t_1, t_2 ... t_n$,

$$\Delta E_p(t) \equiv \Delta E_p(t - \delta t) + J_b^* h(t) \delta t \; , \tag{3.9}$$

where δt is the interval between observations. The first term in the above summation carries forward negative ΔE_p from the previous time-step. While $\Delta E_p < 0$, the mixed layer is assumed to be stratified. Work done by wind stress and destabilizing surface buoyancy fluxes (if any) is acting primarily to erase this stratification (and reduce the E_p deficit) as well as against any instantaneous stabilizing force from negative surface buoyancy fluxes or penetrative solar radiation. When mixing increases ΔE_p to zero, the mixed layer is assumed to be well mixed, with subsequent destabilizing forcing acting against the instantaneous stabilizing forcing as well as stratification at the mixed layer base, driving entrainment buoyancy fluxes.

Since the mixing (positive) terms within J_b^* (terms 1 and 2 of Equation 3.1) no longer work against residual mixed layer stratification once $\Sigma[\Delta E_p](t)$ increases to ≥ 0, term 1 above, $[\Sigma[\Delta E_p](t - \delta t)]$, is set to zero. This is equivalent to permitting only the stabilizing terms in J_b^* (i.e. not the destabilizing terms) to have a cumulative influence on stratification over time. Once the mixed layer is well-mixed, further mixing works only against the instantaneous stratifying tendency of negative surface buoyancy fluxes and penetrative heat fluxes (terms 3 and 4 of Eqn. 3.1) and to mix the dense entrained water throughout the mixed layer. When $\Delta E_p \geq 0$, the basic N-K formulation (Eqn. 3.1 with the term 5 modification) is used to estimate the entrainment buoyancy flux. Thus, maintaining this sum is simply a means of estimating times when turbulence from direct surface forcing re-gains the mixed layer base and once again directly generates entrainment fluxes. As expected and as will subsequently be discussed, including this modification significantly improves the skill of the basic N-K model at estimating the times of entrainment events.

One of the largest assumptions implicit in Equation 3.9 is that the efficiency of mixing from wind-stress and buoyancy-driven convection remains constant when the mixed layer changes from a stratified to a well-mixed state (or that the constants m and n of terms 1 and 2 of Eqn. 3.1 are indeed constant). In fact, with the instantaneous mixed layer depth, h_i, shallower than h as defined here when the mixed layer is stratified, we would expect the coefficient of the wind-mixing term to increase by h/h_i during these times. However, adjusting the coefficients to account for a potential change in efficiency does not significantly improve model skill and, thus, they are held constant.

Indirectly-forced entrainment

As shown in Chapter 2, when the SBL depth, h_b, is less than the mixed layer depth, there is a weak correlation at a short lag ($<$ 5 hours) of buoyancy entrainment (J_b^e) with both wind stress $[u_*^3/(\kappa h)]$ and destabilizing surface buoyancy flux (Fig. 3.1, Tab. 2.2). This suggests that despite the presence of weak stratification within the mixed layer, surface forcing is still able to influence entrainment generation—possibly through the intermediary of internal waves as suggested by observations within the Pacific equatorial undercurrent (Gregg et al., 1985; Moum and Caldwell, 1985; Peters et al., 1994; Lien et al., 1996).

Regardless of the exact mechanism, below we describe a formulation for including relatively weak indirect entrainment within the N-K model that physically represents entrainment that is correlated with destabilizing surface forcing despite the SBL being shallower than the mixed layer depth (or $\Delta E_p \leq 0$). This modification to the N-K model, then, removes the absolute decoupling between the mixed layer and interior ocean when directly surface-forced entrainment is zero (l.h.s. of Eqn. 3.1 is $>$ 0). The term "indirect" simply refers to the fact that SBL turbulence does not appear to be directly working against density gradients at $z = -h$, but instead may be driving or modulating entrainment fluxes through intermediary dynamics. As will be shown, this term has the form of the destabilizing surface forcing terms (terms 1 and 2 of Eqn. 3.1) but with smaller coefficients—equating to reduced efficiency of wind stress and destabilizing buoyancy flux at generating entrainment during these times. Algorithmically, this modification to the N-K model is:

$$\text{when } \Delta E_p(t) \leq 0 \ : \ \tilde{J}_b^e(t) = -\left[m_i \frac{u_*^3}{h}(t) + n_i J_b(0)^+(t)\right] sRi(-h)^{\varphi} \quad [\mathrm{W\,kg^{-1}}]\,, \tag{3.10}$$

where, as with other coefficients, the constants m_i and n_i are selected to maximize the correlation

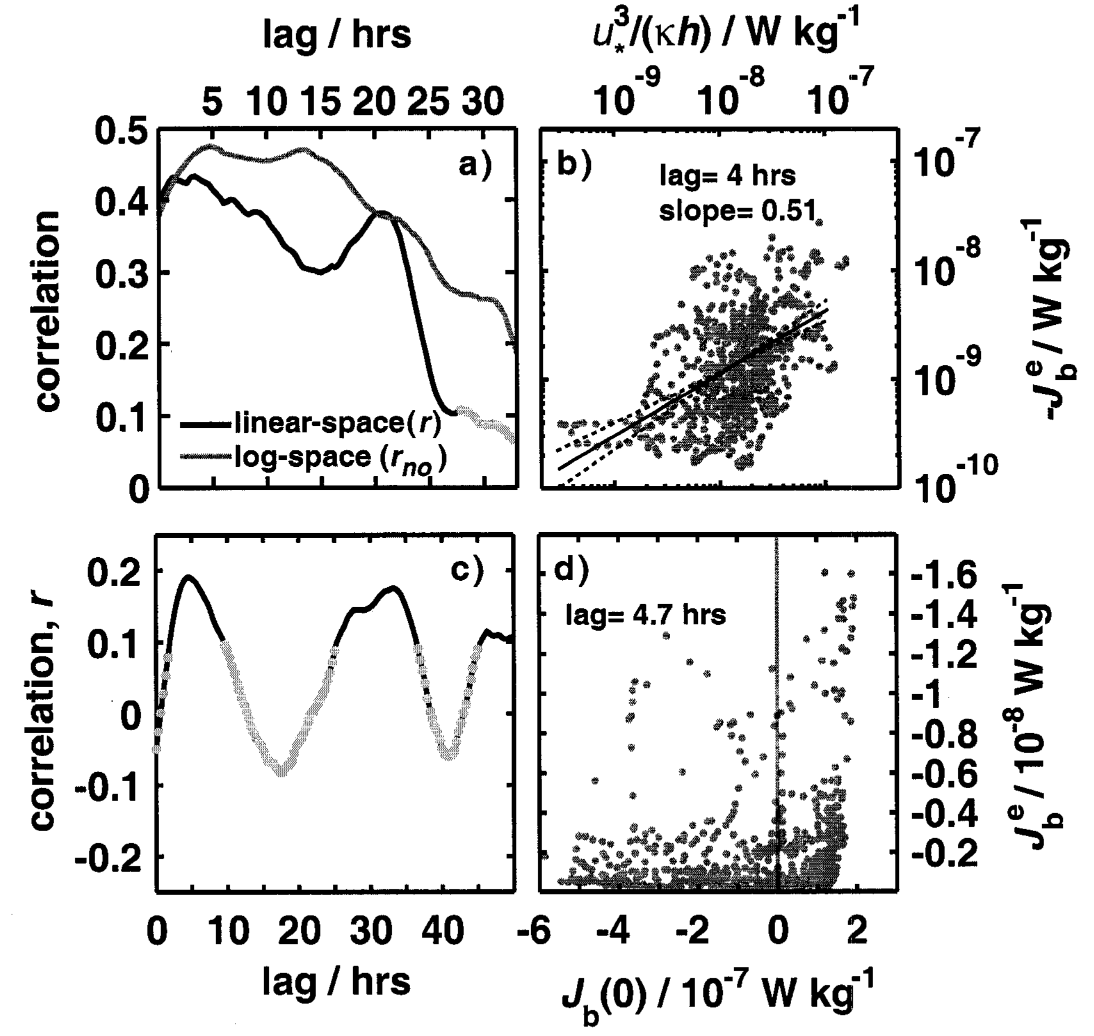

Figure 3.1: Plots showing the correlation of $-J_b^e$ with $u_*^3/(\kappa h)$ and $J_b(0)$ for times when the SBL depth is less than the mixed layer depth, or $h_b < h$. a) Lagged correlation of $-J_b^e$ with $u_*^3/(\kappa h)$ (with wind stress leading entrainment) showing both the correlation coefficient calculated in linear-space, r, (black) and after taking the $\log_{10}$ of each variable, r_{no} (gray). b) Log-log scatterplot of $u_*^3/\kappa h$ vs. $-J_b^e$ for a lag of 4 hours. c) as for (a) but J_b^e with $J_b(0)$ and only for the linear-space correlation since $\log_{10}[J_b(0)]$ is undefined when $J_b(0) \leq 0$. d) as in (b) but a linear-space scatterplot of $J_b(0)$ vs. J_b^e for a lag of 4.7 hours with a line showing $J_b(0) = 0$. Note that the positive slope of points near the right y-axis of plot (d) is largely a consequence of the dependence of both $J_b(0)$ and J_b^e on wind speed. In plots (a) and (c) values not significant at the 95% level are shown in light gray. Also note that the x-axis in plot (c) covers longer lag times than (a) in order to show the diurnal cycle.

of model and observations. Consistent with the expectation that the efficiency of the destabilizing terms at generating entrainment would be reduced when the mixed layer is stratified, the coefficients are roughly half of m and n (Tab. 3.2). Although the skill of the model as measured by r and RMSE is rather insensitive to the exact values of m_i and n_i, including a scheme for background entrainment significantly improves model skill (a 13% reduction in RMSE)—with agreement particularly improved at weaker levels of J_b^e. Although admittedly somewhat ad-hoc, the form for the indirect surface forcing term is motivated by the form of the surface forcing terms in the N-K model, dimensional consistency, and by the empirical findings.

Also, instead of unrealistically assuming that turbulence levels at the mixed layer base respond instantaneously to surface forcing, the model applies a lag that results in $\tilde{J}_b^e$ variability following changes in surface forcing by about an hour on average. Not knowing the details of the exact mechanism by which energy from the SBL is transferred to the mixed layer base (e.g. turbulent or wave processes), for lack of a better approach this lag (dT) is simply based on h and SBL friction and convective velocity scales u_* and w_* (where $w_* \equiv [J_b(0)h]^{1/3}$ when $J_b(0) > 0$) or specifically, $dT = h/(u_* + w_*)$. Since the background entrainment values are weak, the application of this lag only makes slight improvements in model skill as indicated by r (+0.02).

3.3.3 The model sequence

The sequence of the N-K model with the three modifications applied is conceptually depicted in Figure 3.2, which tracks the evolution of a mixed-layer density profile from an initially-stratified state to a final well-mixed state with surface forcing driving entrainment. Here the stratification within the mixed layer has been exaggerated for clarity. Panel (a) shows the initial state of a stratified mixed layer with only stabilizing surface forcing ($\tau = 0$, $J_b(0) < 0$) and some (stable) finescale dynamic stability conditions at h. In panel (b) destabilizing surface forcing (in this case only τ) begins to mix the upper mixed layer and increases E_p. During destabilizing surface forcing but while $h_b < h$ the model engages the weak background entrainment term that is dependent upon this surface forcing and $Ri(-h)$. Wind-mixing continues in panel (c) until mixing has erased mixed layer stratification (panel d). At this point $h_b \geq h$ and the surface-driven turbulence begins to erode the stratification at h, or turbulently entrain thermocline water. The schematic attempts to capture the theoretical connection between the effectiveness of the surface-driven turbulence at generating entrainment and the dynamic stability conditions at $Ri(-h)$. As represented by this schematic, a direct consequence of the modified N-K model's mixing scheme is that it inherently includes a physically-based means of accounting for varying lag times between the time of destabilizing surface forcing and resultant entrainment. Unlike the purely empirical approach used in the multiple linear regression of Chapter 2 whereby the lag between u_*^3/h and J_b^e is set to a constant selected to maximize the correlation coefficient of the fit and observations, the lag-time in this modification of the N-K model is a function of u_*^3/h, $J_b(0)^+$, the prior and present stratifying influence of $J_b(0)^-$ and J_b^{sw}, and h.

3.4 *Model Skill, Error and Limitations*

3.4.1 Model skill

Despite obvious model limitations such as its one-dimensionality, the neglect of processes that influence mixed layer turbulence such as surface wave-breaking and Langmuir cells, and a bulk instead of a depth-dependent approach to the competing effects of stratification and turbulent mixing, the modified N-K model does remarkably well at capturing the decade-plus variability of J_b^e over the 19-day EPIC timeseries with $r = 0.905$ (Fig. 3.3 3.4, Tab. 3.1). Here all the model constants (φ, s, m, n, m_i and n_i), with values given in Table 3.2, are chosen to maximize r or minimize the RMSE between modeled and observed entrainment. Values of m and n, or the two constants from the base N-K model, are somewhat consistent with previous observationally-determined values (Turner, 1969; Ball, 1960)—although some difference is expected because of the use of a modified dynamic stability term. Model skill at low-level values of J_b^e ($\lesssim -1 \times 10^{-9}$ W kg^{-1}) is improved somewhat by explicitly setting a y-intercept—interpreted as a constant model "noise level"—at 10^{-10} W kg^{-1}, or a value similar to measurement noise levels. However, since the levels of $\tilde{J}_b^e$ influenced by this term are very small, it has an insignificant impact on r or RMSE, and since it is intended to mimic measurement noise, it has no physical basis.

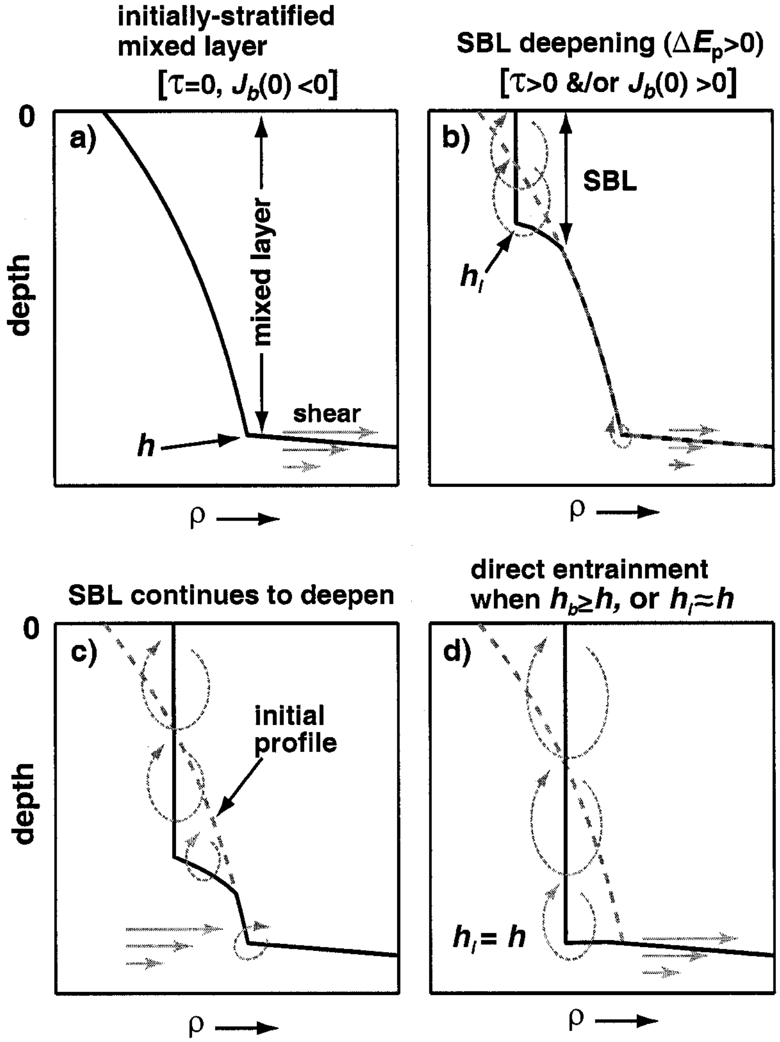

Figure 3.2: Schematic of the entrainment model showing a time-progression of mixed layer density profiles (a–d), where density stratification within the mixed layer has been exaggerated for clarity. a) An initially-stratified mixed layer with only stabilizing surface forcing ($\tau = 0$, $J_b(0) < 0$) and some (stable) finescale dynamic stability conditions at h. b) Destabilizing surface forcing (in this case only τ) begins to mix the upper mixed layer, increasing E_p. During destabilizing surface forcing but while $h_b < h$ the model also includes weak background entrainment that is dependent upon this surface forcing and $Ri(-h)$. c) mixing continues to increase E_p. d) Mixing has erased mixed layer stratification. At this point $h_b \geq h$ ($h_i \approx h$) and the surface-driven turbulence begins to erode the stratification at h. The effectiveness of the surface-driven turbulence at generating entrainment is dependent upon $Ri(-h)$.

The interpretation of the strong correlation in terms of model skill requires some discussion because J_b^e is distributed lognormally (Fig. 3.5), which is expected for a quantity that is directly proportional to ε (Gregg et al., 1993). The lognormality of J_b^e (and $\tilde{J}_b^e$) is also indicated by a chi-square goodness of fit test showing that the null hypothesis (i.e. the distribution is lognormal) is not rejected at the ~ 0.40 significance level with 25 d.o.f., or that there is about a 40% chance of obtaining a sample distribution from a lognormally-distributed quantity that has greater deviations from the theoretical distribution. Strictly speaking, the Pearson correlation is a statistical measure between two quantities that are from normally-distributed populations. Thus, using this measure to evaluate the similarity of two lognormally-distributed quantities violates its basic assumptions.

Table 3.1: Model skill statistics

parameter	**value**
total r	0.905 [0.90, 0.92]
total r_{no}	0.81 [0.78, 0.83]
total $r_{\log}$	0.74 [0.71, 0.77]
RMSE (19 days)	5.79×10^{-9} $[5.81 \times 10^{-9}]$ W kg^{-1}
$\overline{\tilde{J}_b^e/J_b^e}$	1.015 [0.775, 1.349]

99% conf. intervals are shown within brackets.

However, if we ignore the fact that they are lognormally-distributed and use the definition of variance for a normal distribution $[\sigma^2 = (J_b^e - \mu)^2]$, the Pearson correlation coefficient gives $r = 0.905$, indicating that the model describes 82% of the variance of J_b^e. Because J_b^e and $\tilde{J}_b^e$ are lognormally-distributed, however, it is more statistically-correct to calculate the Pearson correlation coefficient between the normal quantities $\log_{10}[J_b^e]$ and $\log_{10}[\tilde{J}_b^e]$, giving $r_{\text{no}} = 0.81$ (Tab. 3.1). However, the variance of $\log_{10}[J_b^e]$ has little physical meaning. Finally, we can also look at the correlation between J_b^e and $\tilde{J}_b^e$ as defined for lognormally-distributed quantities (Hutchinson and Lai, 1991). This, correlation ($r_{\log} = 0.74$), however, holds even less meaning than r_{no} since it is dependent upon

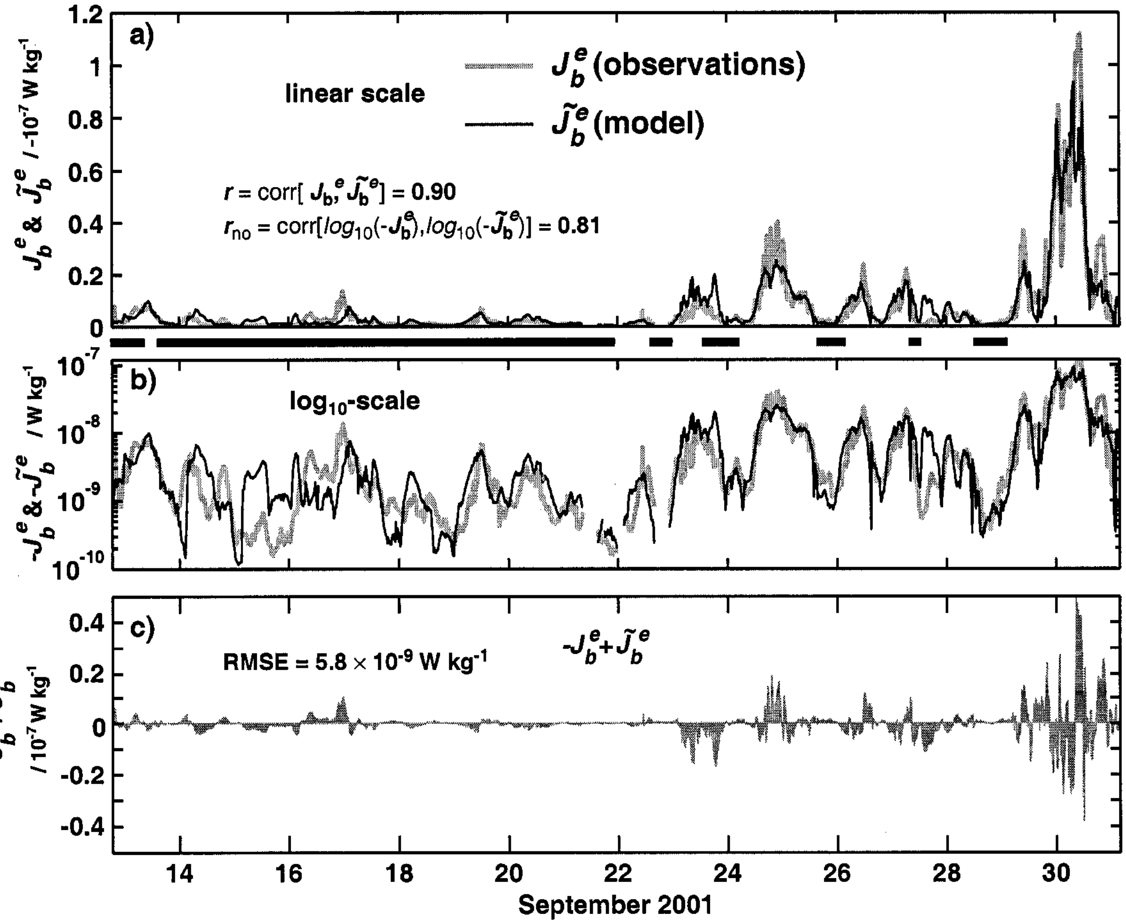

Figure 3.3: Comparison of observed (J_b^e) and modeled ($\tilde{J}_b^e$) entrainment buoyancy flux over the EPIC timeseries. a) J_b^e (gray) and $\tilde{J}_b^e$ (black). b) same as (a) but with a $\log_{10}$-scale y-axis. c) $J_b^e - \tilde{J}_b^e$. Black-filled regions between panels (a) and (b) indicate times when $\tilde{J}_b^e$ is determined by the indirect entrainment scheme.

Table 3.2: Constants for the modified N-K model.

constant	value	description
primary constants		
φ	-0.87	power of $Ri(-h)$
s	-0.31	coefficient of $Ri^(- h)\varphi$
m	5.59	coefficient of u_*^3/h
n	1.14	coefficient of $J_b(0)^+$
indirect entrainment term constants		
m_i	3.82	coefficient of u_*^3/h
n_i	0.59	coefficient of $J_b(0)^+$

σ of the two distributions, and as shown by Hutchinson and Lai (1991), very small values of $r_{\log}$ (e.g. < 0.1) can represent perfectly-correlated variables, or $r = 1$—but that are *non-linearly* correlated. Thus, although the distributions are lognormal, calculating the Pearson correlation coefficient in linear-space (r) appears to be the most physically-meaningful indicator of how well the model does at replicating observed J_b^e and suggests that the model has significant skill at replicating observations over the EPIC timeseries.

An investigation of other statistical properties indicates that the arithmetic mean of $\tilde{J}_b^e$ over the EPIC timeseries (6.72×10^{-9} W kg^{-1}) is only 1.5% greater than the arithmetic-mean of J_b^e (6.62×10^{-9} W kg^{-1}), suggesting the model gives an unbiased estimate of time-averaged entrainment levels (Tab. 3.1). This result holds particular significance when time-integrating $\tilde{J}_b^e$ for mixed layer budget calculations. Other statistical parameters, such as the mean and median as defined for logarithmic distributions, indicate that the model gives a relatively unbiased and statistically-consistent estimate of J_b^e (Tab. 3.1).

Also, despite the number of assumptions and the simplifications, the entrainment model is rel-

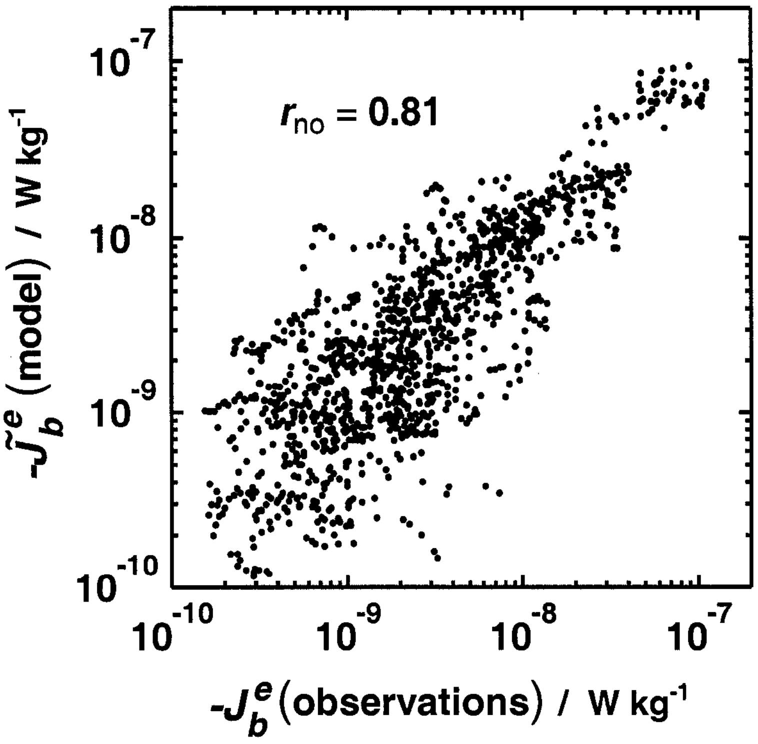

Figure 3.4: Log-log scatterplot of observed (J_b^e) vs. modeled $(\tilde{J}_b^e)$ entrainment buoyancy flux over the EPIC timeseries. The correlation of $\log_{10}[J_b^e]$ and $\log_{10}[\tilde{J}_b^e]$, r_{no}, is 0.81 $(n = 1276)$.

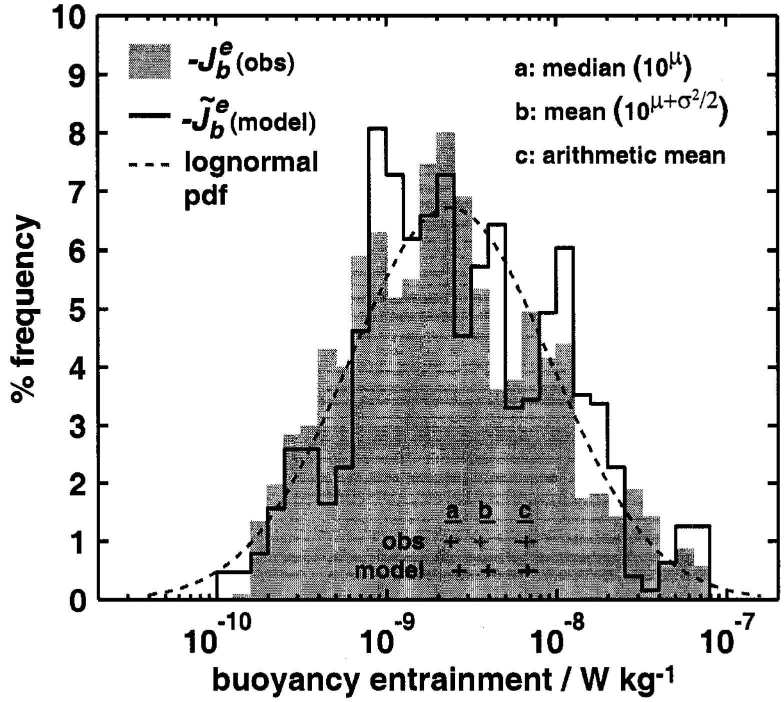

Figure 3.5: Histograms of J_b^e (gray fill) and $\tilde{J}_b^e$ (black) over the EPIC timeseries with a comparison to the theoretical lognormal PDF for the mean (μ) and standard deviation (σ) of $\log_{10}(J_b^e)$. A comparison of the median, mean and arithmetic mean for J_b^e and $\tilde{J}_b^e$ is shown just above the bottom y-axis, with the width of the horizontal lines showing bootstrap 99% conf. intervals.

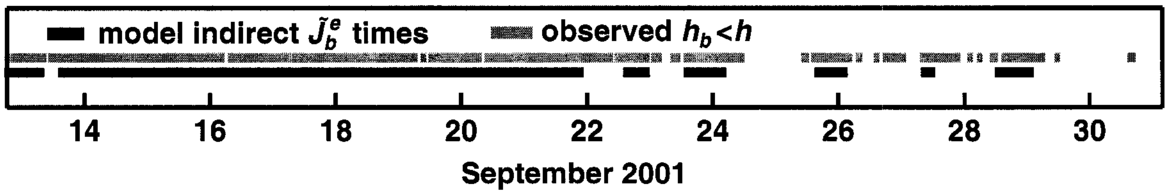

Figure 3.6: Comparison of observed times when $h_b < h$ (gray) to the model-predicted times of indirectly-driven entrainment.

atively effective at estimating the times when direct surface-forced turbulence reaches the mixed layer base $(h_b \geq h)$, or equivalently the times when $h_b < h$ (Fig. 3.6). The robustness this scheme is likely attributable to the fact that the times when the SBL penetrated to h were often a result of a rapid increase in destabilizing surface forcing (u_*^3 and/or $J_b(0)^+$) and not a consequence of a slow increase in destabilizing surface forcing that eventually overcomes mixed layer stratification. When there is a rapid increase in the magnitude of the surface mixing terms there is a significantly smaller potential for error in determining times when $h_b \geq h$. Although in a general sense the model was fairly successful at estimating when $h_b < h$, the model often overestimated when $h_b \geq h$ and was not particularly effective at capturing short-duration periods of either a stratified or a well-mixed condition. Differences between the model and observations could stem from any of the assumptions of the E_p budget or the root N-K parameterization, but it is expected that horizontal advection of the ubiquitous, small-scale freshwater pools in the EPWP may cause much of the error. It is important to note, however, that the observations are not necessarily an infallible indicator of when SBL turbulence reaches h since the determination of h_b is based on a somewhat arbitrary threshold value for ε (see Chapter 2).

3.4.2 Error and Limitations

It is important to recognize that even if the model perfectly predicted the observations, the model output carries the uncertainty of the observations used to tune the model as well as uncertainty in the input variables. Although it is difficult to determine the actual uncertainty in ε (or J_b^e) measurements, estimates are on the order of a factor of two for time-averaged ε (Peters et al., 1988; Moum et al., 1995). Thus, at best the model gives an estimate of the entrainment buoyancy flux with the same uncertainty. The largest differences between the model and observations occurred during times when observed entrainment fluxes were largest (Fig. 3.3c) with the model regularly underestimating the peaks in J_b^e. The $\log_{10}$-scale comparison of the observations and the model (Fig. 3.3b) indicates differences of over a factor of ten between the two around September 15 with the model typically giving the larger values. A strong diurnal pattern of squalls during this period and relatively weak winds suggests that this large difference may be due to lateral advection (or unresolved changes in mixed layer stratification). However, since entrainment was near background levels during these times this error is actually quite small (Fig. 3.3c) when compared to that when entrainment is large, and, therefore is not of a concern.

Because the model does not use the instantaneous mixed layer depth, h_i, but instead a definition of h that roughly follows the top of the seasonal thermocline, it is unable to accurately resolve SST changes on timescales shorter than a period spanning two well-mixed states, or when h_i is continuously less than h. For the first half of the EPIC timeseries this can be several days or longer because of the weak winds and frequent, heavy rainfall. Thus, this model is unable to capture a diurnal cycle of SST that would result from the formation of a shallow diurnal thermocline when winds are weak and solar heating strong. Altering the definition of h to follow the instantaneous mixed layer depth, h_i, would significantly improve the model time-resolution, but would complicate or even preclude the measurement of input variables such as Ri because of the rapid vertical fluctuations of h_i and the fact that it is often shallower than the depth range of measurements. Since the main purpose of the model is to investigate the variability of entrainment and SST-changes on week+ timescales over 2001, this limitation is acceptable.

Another constraint of this model that is common to all 1-D upper-ocean models is the inability to capture changes in stratification from lateral advective effects, which observations indicate can be important (Brainerd and Gregg, 1993a; Hosegood et al., 2007). If the influence of lateral processes on mixed layer stratification were steady in time, the empirical fit of the model to the observations would potentially account for these dynamics by adjusting the coefficients for the surface forcing terms. However, lateral processes, which are likely influenced by a number of factors including the spatial scales of surface forcing and mixed layer density, undoubtedly vary with time. It is expected that unaccounted-for variablity in lateral restratification could lead to significant errors in $\tilde{J}_b^e$.

The influence of surface wave-breaking

The underestimate of entrainment levels when wind stress was largest (and entrainment largest) suggests that processes not captured by the model may be contributing to entrainment during these times. One of these is mixing from breaking surface waves. Observations (Anis and Moum, 1995;

Terray et al., 1996; Drennan et al., 1996) show that near-surface turbulent dissipation (ε) is significantly greater than expected from classic wall layer behavior or the Monin-Obukhov scaling for wind stress-driven turbulence, with decay rates in the region of wave influence on the order of z^{-2} to z^{-4}. Thus, neglecting the contribution of wave-breaking to turbulence levels at h could result in a significant underestimate of the entrainment fluxes.

A scaling based on significant wave height (H_s) introduced by Terray et al. (1999) indicates that wave-breaking influences ε above depths of roughly $10H_s$. Around this depth, the z^{-2} to z^{-4} decay rate tends asymptotically to the classic z^{-1} dependence in the SBL. The significant wave height, H_s, and thus the maximum depth of surface-wave turbulence, are estimated here using the results of Donelan et al. (1992) who found an empirical relationship between H_s and the 10-m wind speed, U_{10}. Assuming a fully developed sea state for the wind conditions,

$$H_s = 4[\varsigma \mathrm{U}_{10}^4/g^2]^{1/2}\,, \tag{3.11}$$

where ς is a non-dimensional constant (5×10^{-3}). Wind speeds from the R/V *R. H. Brown* are averaged over 4 hours to better meet the assumption of a fully-developed sea-state and adjusted to a 10-m height using a log-profile based on EPIC timeseries LIDAR vertical wind profiles. Although including the influence of surface wave-breaking in the N-K model is beyond the scope of this work, applying the above empirical formula to the EPIC dataset suggests there were several short-lived periods over the EPIC timeseries when entrainment may have been directly and significantly enhanced by breaking surface waves. The potential influence of breaking surface waves on J_b^e is specifically indicated by a timeseries of $10H_s/h$. Values greater than one suggest entrainment (or specifically turbulence at $z = -h$) may be directly influenced by turbulence from surface wave-breaking (Fig. 3.7). The two short periods when $10H_s/h > 1$ match or slightly lead times when the model underestimated peaks in J_b^e—suggesting that the absence of these dynamics (or a parameterization of them) in the model may be at least partially responsible for these underestimates. As will be discussed in Chapter 4, breaking surface waves may become particularly important to entrainment during periods of 2001 when h decreases to exceptionally shallow depths of less than 15 m.

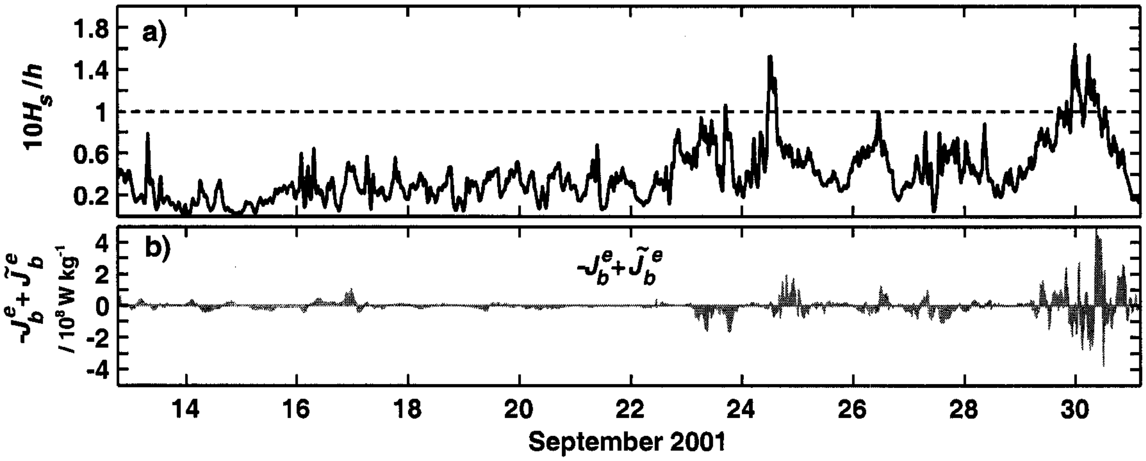

Figure 3.7: a) Plot of $10H_s/h$ where H_s is the significant wave height of surface waves and $10H_s$ indicates the maximum penetration depth of turbulence from breaking surface waves. Thus, $10H_s/h > 1$ indicates periods when turbulence from breaking surface waves may penetrate to h and drive entrainment. Agreement between times when $10H_s/h > 1$ and model underestimates of J_b^e (b) suggests that the absence of surface wave-breaking in the model may be at least partially responsible for these underestimates.

3.4.3 A comparison to the base N-K entrainment parameterization

A comparison of the modified N-K entrainment parameterization to the root or un-modified N-K parameterization shows that including the three modifications reduces the 19-day RMSE by about 35% and reduces the average bias of the N-K estimate from a 40% over-estimate to less than a 2% over-estimate. A 19-day value of $r = 0.81$ suggests that the modified N-K accounts for about 15% more of the variance of the observations than the base N-K model. Because the N-K model assumes entrainment responds instantaneously to surface forcing, the largest advantage of the modified N-K model is its built-in lag, with the N-K model frequently predicting increases in entrainment that are several hours to a 1/2-day too early (Fig. 3.8a). The root N-K model error over the 19 days was almost always greater than that of the modified model (Fig. 3.8b), with the largest errors also occurring when the entrainment fluxes were largest. As expected, the root N-K model also significantly over-estimates entrainment fluxes when the mixed layer was weakly stratified—as was the case for much of the first half of the timeseries. Including a formulation for indirect entrainment significantly reduced model error during these times.

3.5 Further Justification for the Model Form

Strong observational support for the form of both the modified and base N-K models is provided by close agreement of modified N-K model contours in $Ri(-h)$-J_b^*-space with observations (Fig. 3.9). The close similarity of the model functional dependence ($\tilde{J}_b^e$ contours) and the variation of observed J_b^e suggests that the model form may be capturing a true dynamical dependence. A broader sampling of the functional space (i.e. low Ri^{φ} and high J_b^* or vice-versa) would help to verify this conclusion, but unfortunately may be limited by the dynamical dependence of $Ri(-h)$ on wind stress and possibly $J_b(0)$.

The statistical consistency of the model form arises from the multiplicative property of lognormal distributions with the *product* of two or more lognormally-distributed variables resulting in a lognormally-distributed quantity (Limpert et al., 2001). The *addition* of lognormally-distributed variables, on the other hand, does not necessarily result in a lognormally-distributed quantity. Thus, with both $Ri(-h)$ and u_*^3/h having distributions that are close to lognormal and the anticipation

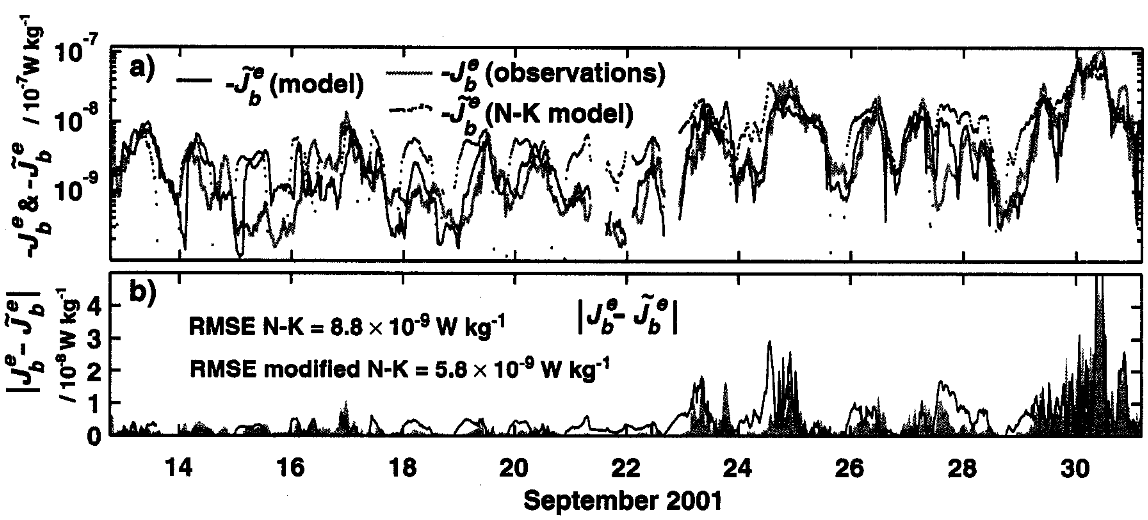

Figure 3.8: a) Comparison of observed (J_b^e) with modeled entrainment $(\tilde{J}_b^e)$ for the modified N-K model presented here (blue) and the original N-K model form (red). Note the $\log_{10}$-scale y-axis. b) The absolute value of $J_b^e - \tilde{J}_b^e$ for both the modified (gray fill) and the root N-K model (black line).

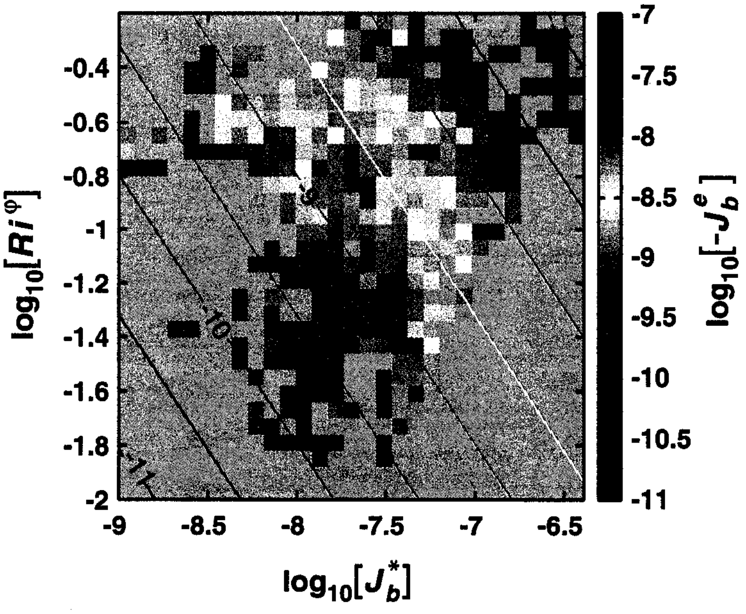

Figure 3.9: Map of $\log_{10}[J_b^e]$ (color) averaged into bins of $\log_{10}[J_b^*]$ and $\log_{10}[Ri^{\varphi}]$. Model contours of $\log_{10}[\tilde{J}_b^e]$ are over-plotted with the contour lines colored according to their value. There is good agreement between the observations and the model, suggesting that the model form may be capturing a true non-linear dynamical relationship between J_b^e, J_b^* and $Ri(-h)$. A simple example of this non-linearity is that if Ri^{φ} and J_b^* each increase (decrease) by a decade, J_b^e increases (decreases) by 100-fold.

that $\tilde{J}_b^e$ is lognormally-distributed (Gregg et al., 1993), we expect that a parameterization that is a function of these two quantities would have a product functional form.

As well as being constrained by statistical consistency, the functional form of the entrainment model must also be dimensionally consistent, resulting in units of W kg $^{-1}$ (equivalently m^2 s^{-3}). This is true of the product functional form of model, but would not be true for a linear form unless the coefficient scaling the dimensionless $Ri(-h)$ is assumed to have units of W kg^{-1}. Although dimensional consistency has required a number of other mixing parameterizations to adopt dimensional coefficients [e.g. Peters et al. (1988); MacKinnon and Gregg (2003b)], the often-limited justification for doing so suggests that important parameters may be missing from these models. Peters et al. (1988) acknowledged this shortcoming in their parameterization and suggested that in addition to a Richardson number dependence, mixing (specifically eddy diffusivity) in the upper-ocean "may also depend on the external forcing of the turbulence by wind stress and surface buoyancy flux."

3.6 Discussion

3.6.1 Dynamical implications

Because the model has a product functional form, the sensitivity of entrainment to variations of an individual model term (Ri^{φ} or J_b^*) is dependent upon the variability of the other term. This consequence of the model form is apparent from contours of $\tilde{J}_b^e$ in Figure 3.9, where a decade increase (decrease) in both terms results in a 100-fold increase (decrease) of $\tilde{J}_b^e$. If the model functional form is capturing a true dynamical dependence, it implies that the correlation of Ri^{φ} and J_b^* is very important to entrainment generation. Supporting this conclusion, the largest observed levels of entrainment occur when both Ri^{φ} and J_b^* are large and the smallest values of J_b^e when both are small (Fig. 3.10, 3.9). Although this could also be a consequence of a linear combination of terms, the close agreement between the distribution of J_b^e and model contours in Figure 3.9 suggests otherwise.

The possibility of this functional relationship has important implications to modeling entrainment in that it requires a correct determination of the variability of $Ri(-h)$ and J_b^* with respect to one another. Since near-inertial internal wave dynamics are important to the evolution of shear at

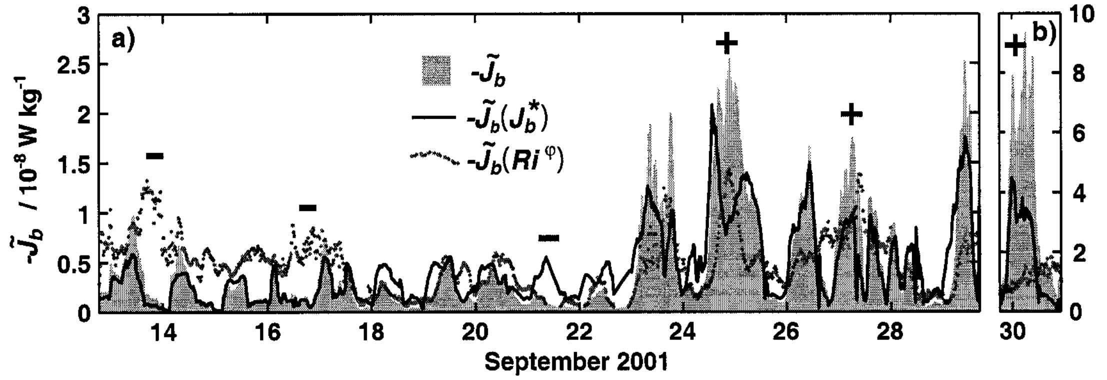

Figure 3.10: Comparison of the relative roles of Ri^{φ} and J_b^* in the model, showing that each term modulates the effectiveness of the other term at producing $\tilde{J}_b^e$. Shown are: modeled entrainment as a function of J_b^* only (black line), $\tilde{J}_b^e$ as a function of Ri^{φ} only (dotted line), and total $\tilde{J}_b^e$ (gray fill). Positive signs (+) indicate several instances when J_b^* and Ri^{φ} are positively correlated resulting in enhanced entrainment and negative signs ($-$) indicate instances when they are negatively correlated, with the smaller term often offsetting the influence of the larger to result in weak entrainment. In order to more clearly show differences between the terms the EPIC timeseries is divided into two panels (a & b) with different y-axis scales.

the mixed layer base as shown in Chapter 2 and in a number of other studies (Gill, 1984; D'Asaro et al., 1995; Levine and Zervakis, 1995), there is strong motivation to include these dynamics or effective parameterizations of them in upper-ocean models.

The weak entrainment fluxes over the first half of the EPIC timeseries are an example of the importance of the correlation of J_b^* and $Ri(-h)^{\varphi}$. As noted in Chapter 2, over several days just prior to the beginning of the EPIC timeseries, moderate winds rotated clockwise at close to the inertial period (69 hours), resulting in the strong mixed layer near-inertial motions observed at the beginning of the timeseries (Fig. 2.7). These near-inertial motions generated relatively strong shear at the mixed layer base. However, because winds were light over the first half of the timeseries and consequently the surface-forcing term was small, the entrainment fluxes were relatively weak at $< 2 \times 10^{-8}$ W kg^{-1}—or about 1/5 of the maximum J_b^e observed near the end of the timeseries. This consequence of the product functional form is evident in Figure 3.10, which shows that $\tilde{J}_b^e$ as a function of $Ri(-h)$ alone $[\tilde{J}_b^e(Ri)]$ would have severely over-estimated entrainment fluxes over the first five days of the timeseries. In contrast, the strong near-inertial shear and associated increase in $Ri(-h)^{\varphi}$ that resulted from the large wind stresses around the 25th and 30th of September was positively correlated with the wind stress toward the end of the storms, and as a result generated the largest observed entrainment fluxes (Figs. 3.10, 3.3).

3.6.2 An explanation for variations in functional dependencies

A ubiquitous characteristic of observations relating measured ε (or eddy diffusivity, K) to the finescale ($\sim$10 m) Richardson number is that there appears to be a large shift in the functional relationship between the two at some critical value of $Ri(-h)$ (Ri_c). When $Ri(-h)$ is less than Ri_c, turbulence levels increase much more rapidly with decreasing $Ri(-h)$ than when $Ri(-h)$ is above Ri_c. Although there is significant scatter in their data, this was a primary finding of Peters and Gregg (1988) in their investigation of equatorial and near-equatorial microstructure data from the Tropic Heat program (with $Ri_c \approx 0.4$ in their observations). D'Asaro and Lien (2000b) provide a theoretical framework for this apparent functional shift, suggesting a wave-wave interaction mixing regime at high values of $Ri(-h)$ and a "stratified turbulence" mixing regime at low values of $Ri(-h)$.

Although there is undoubtedly a difference in the mixing dynamics of the two regimes (as there is for thermocline and boundary layer turbulence) here we suggest that shifts in the functional relationship between ε (specifically J_b^e) and $Ri(-h)$ in these data may at least partly be due to the dependence of ε on an additional variable, and that ε is a consequence of the product of this variable and $Ri(-h)$ (i.e. the model functional form). As discussed, the product model functional form of the root N-K model and the modified N-K model presented here [$\tilde{J}_b^e = J_b^* s Ri(-h)^{\varphi}$] prescribes that the effectiveness of each term at generating $\tilde{J}_b^e$ is dependent upon the variability of the other term. If one investigated the statistical relationship between J_b^e and $Ri(-h)$ neglecting the influence of J_b^* on J_b^e, the (log-space) scatterplot would show multiple functional regimes (slopes) that are a consequence of variations in the correlation of J_b^* and $Ri(-h)$. When the two are correlated—which is at times the case during the EPIC timeseries with $r = 0.28$ for the total 19 days—the increase/decrease in J_b^e is much more rapid than one would expect for the variation of each term individually. The parallel is true if one investigates the relationship between ε and J_b^* excluding $Ri(-h)$.

Observations follow this expected consequence of the model form, with scatterplots of J_b^e with Ri^{-1} and u_*^3/h showing shifts in the log-space linear regression slope as anticipated (Figs. 2.12 and 2.10). At weaker values of J_b^* (when $h_b < h$) and it is largely uncorrelated with Ri^{φ}, there is clearly a weaker functional dependence between J_b^e and Ri^{-1} (slope=0.48) than when surface forcing is stronger ($h_b \geq h$) and the two are more closely correlated (slope=0.89) (Fig. 2.12, Tab. 2.2). Similar changes in the functional relationship between J_b^e and u_*^3/h are also apparent (Fig. 2.10, Tab. 2.2). A consequence of including both terms in a product functional form is that these potentially-spurious multiple functional regimes are removed—giving a relatively constant slope in a log-log scatterplot (Fig. 3.4).

3.7 Summary

Here we have used the observations and empirical findings from Chapter 2 as justification for several modifications to the N-K entrainment parameterization that significantly improve the skill of the latter. Specifically these modifications include allowing the stratifying influence of stabilizing surface buoyancy fluxes and penetrative heat fluxes to be cumulative in time if not offset by turbulent mixing, replacing the model term for the bulk mixed layer dynamic stability conditions with the finescale inverse gradient Richardson number at the mixed layer base, and allowing for indirect entrainment generation when the mixed layer is assumed to be stratified, or $h_b < h$. These modifications reduce N-K RMSE over the 19 days by 35% and a mean bias of +40% to less than +2%, with significant improvement of model skill at low levels of entrainment and with the timing of large entrainment events. A comparison of model to observed entrainment buoyancy fluxes indicates that significant error may result from the model not accounting for turbulent mixing due to breaking surface waves. The N-K model form, which consists of the product of a surface forcing term and a term accounting for the dynamic stability conditions, implies that the correlation of these two quantities is important to entrainment flux generation, with the largest entrainment fluxes generated when both are large and the smallest when both are small.

Chapter 4

THE INFLUENCE OF TURBULENT HEAT ENTRAINMENT ON SST WITHIN THE EASTERN PACIFIC WARM POOL

4.1 Introduction

Because the strong air-sea coupling in the eastern tropical Pacific is largely driven by SST and SST gradients (Lindzen and Nigam, 1987; Wallace et al., 1998; Chelton et al., 2001; Raymond et al., 2004; Xie et al., 2005) there has been a significant focus on identifying the dominant processes controlling the region's SST. With this as one of the primary goals, intensive upper-ocean and atmospheric measurements were made within the eastern Pacific warm pool (EPWP) and ITCZ during September 2001 as part of the Eastern Pacific Investigation of Climate (EPIC) process study. Using these observations, Wijesekera et al. (2005) found that all terms were important in the upper 20 m and 25 m heat budget. However, because of large uncertainty in this budget and the relatively short duration of the 19-day timeseries, few conclusions could be drawn concerning the dominant processes controlling SST. Using largely satellite data, Xie et al. (2005) hypothesized that significant spatial and temporal SST variability in the EPWP was connected to thermocline depth, with wind-driven turbulent entrainment increasing and SST resultantly cooling as the thermocline shoals. However, as they recognized, additional observations would be necessary to verify this mechanism. With Kessler (2002, 2006) showing that the mean thermocline topography and its annual variability is largely determined by linear Sverdrup dynamics, or a consequence of the curl of the wind stress, there is an apparent connection between the regional wind stress patterns, thermocline depth and turbulent entrainment of heat that strongly modulates SST.

Here we use the September 2001 EPIC observations along with data from the 10 ° N, 95° W TAO (Tropical Ocean Atmosphere) buoy, QuikSCAT satellite winds, and model results from the semi-empirical entrainment model presented in Chapter 3 to investigate the role of turbulent entrainment on SST variability on timescales of weeks to a year. The primary finding is that the above mechanism strongly influences the seasonal and annual SST variability—or that turbulent heat entrainment is modulated by changes in the thermocline depth, which in turn is largely controlled by wind stress curl patterns.

Specifically, we show that among the largest entrainment heat fluxes, or vertical turbulent heat fluxes at the mixed layer base,—and consequently large drops in SST—occur when consistent upwelling-favorable winds result in an exceptionally shallow mixed layer ($\sim$ 10 m). The increase in the entrainment fluxes appears to be strongly influenced by the decrease in the distance of the strong vertical temperature gradients at the mixed layer base from the surface forcing, and not solely to increased surface forcing. Because the change in mixed layer temperature due to entrainment is inversely proportional to the mixed layer depth, the rapid drops of SST were due to both increased entrainment heat fluxes and a decrease in the mixed layer depth. Thus, the largest entrainment fluxes predominantly occurred when they were most effective at reducing SST. With the depth-averaged mixed layer temperature, T_a, closely following SST on timescales of several days and longer, our approach to showing evidence of the above mechanism and identifying other SST-controlling mechanisms is to investigate the mixed layer temperature budget, and, hence, processes controlling time-changes of T_a. However, because insufficient observations preclude the estimation of all budget terms over a sufficiently long period, our strategy is to first compute the budget over a shorter period when there are sufficient observations to close the budget—specifically over 19 days in September 2001—and then use these results to justify inferences about the seasonal and annual budget that are drawn primarily from TAO buoy and QuikSCAT observations. A key aspect of this analysis is the estimation of the variability of the entrainment heat fluxes over 2001 by using TAO buoy data to evaluate the diagnostic, semi-empirical entrainment model presented in Chapter 3, with the model results constrained by the EPIC timeseries entrainment measurements.

This Chapter begins by including a brief discussion of the oceanographic context of the observations (Section 4.2) followed by a description of the sampling, budget methodology and approach to estimating entrainment flux variability (Section 4.3). Section 4.4 presents results of the 19-day, September 2001 mixed layer temperature budget and then Section 4.5 expands on these findings to draw conclusions about the seasonal and annual mixed layer temperature budget over 2001. The

Chapter concludes with a discussion and summary of the findings in Section 4.6.

4.2 Oceanographic Background and Observational Context

Because the findings presented here link the small scale, high frequency dynamics of turbulent mixing with the region's large-scale, low frequency variability, structure and dynamics, it is appropriate and illuminating to briefly describe the latter. More comprehensive reviews of the region's dominant atmospheric and oceanic dynamics and features are included in Xie et al. (2005) and Kessler (2006). The sampling location, nominally at 10 ° N, 95° W, is within the eastern Pacific warm pool (Fig. 4.1), which is classified as SST $>$ 27.5°C extending eastward from 120° W to the west coast of Central America. At its largest extent in late summer the EPWP spans about 5 ° N to 15° N, encompassing much of the northeast tropical Pacific. The simplicity of its definition, however, belies the region's complex structure of mean currents and thermocline variablity. Largely because of strong winds blowing through gaps in the Central American cordillera and the proximity of the Central American landmass, the mean upper-ocean circulation of the northeast tropical Pacific deviates considerably from the largely zonal currents in the north-central tropical Pacific. West of 110 ° W this circulation is dominated by the westward-flowing North Equatorial Current (NEC) spanning roughly 9 °–15° N and the eastward-flowing North Equatorial Countercurrent (NECC) directly south of the NEC at 5°–9° N. East of about of 110° W, however, the flow becomes less zonal with both the NEC and NECC influenced by strong cyclonic circulation around a persistent upward-doming of the thermocline centered at roughly 9 ° N, 90° W known as the Costa Rica Dome (CRD), and a typically weaker and smaller anticyclonic eddy to the NW of the CRD referred to as the Tehuantepec Bowl (Kessler, 2006). The relative strengths of the NEC, NECC and the persistent eddies (CRD and Tehuantepec Bowl) exhibit a seasonal variability that is strongly linked to the position of the ITCZ (Farrar and Weller, 2006) and the annual variability of the mountain gap winds.

Superimposed upon this mean flow is an active mesoscale eddy field (Giese et al., 1994; Fiedler, 2002). The generation of these predominantly westward-propagating eddies is attributed to a number of physical processes including negative wind stress curl of the mountain gap winds Clarke (1988); McCreary et al. (1989), the interaction of the NECC with the coast of Central America

(Hansen and Maul, 1991), and baroclinic instability of the NEC (Farrar and Weller, 2006). Although the sampling location is located within the NEC, or equivalently the NW quadrant of the CRD (Kessler, 2006), the influence of the eddies causes considerable variablity of the sub-inertial currents, with occasional prolonged (weeks to month) reversals of the mean westward flow. Suggesting that the region's mesoscale eddies may be important to air-sea coupling, Wijesekera et al. (2005) found evidence that anticyclonic eddies with anomalously warm water can become preferential sites for rainfall as they propagate westward. As will be discussed, there is an expectation of reduced entrainment heat fluxes within these eddies because of both the increased rainfall and the anomalously deep thermocline/mixed layer associated with shallow, anticyclonic geostrophic flow.

Kessler (2002) showed that the mean circulation of the northeast tropical Pacific and the associated thermocline structure is largely a consequence of linear Sverdrup dynamics, or the regional patterns of wind stress curl. Formally this dynamical balance is expressed as $\beta V = \nabla \times (\tau/\rho)$, where V is the vertically-integrated meridional velocity. Changes in the thermocline depth associated with this balance are due to water column stretching from meridional geostrophic flow, or equivalently Ekman pumping, and can be expressed as:

$$\partial h_t/\partial t = -w_{Ek} = -\nabla \times \left(\frac{\tau}{f\rho}\right) , \tag{4.1}$$

where w_{Ek} is the Ekman pumping velocity and h_t the thermocline depth anomaly (positive downward). Kessler (2006) further showed that a simple time-dependent solution of these dynamics—essentially long Rossby waves forced by time-varying wind stress curl—accounts for much of the annual evolution of the region's large-scale thermocline structure and upper-ocean circulation. Specifically, the strong annual modulation of the mountain gap winds as well as the meridional oscillation of the ITCZ generates a westward-propagating Rossby wave, which, when superimposed on thermocline variability due to direct wind stress curl forcing results in a southwesterly-propagating annual signal of the thermocline.

The region's wind stress curl forcing, and thus the thermocline depth anomaly, is largely dictated by the mountain gap winds and the ITCZ. Although at times the mountain gap winds can be sufficiently intense to generate large entrainment and latent heat fluxes which result in rapid SST cooling (McCreary et al., 1989), as noted by Xie et al. (2005) the largest SST drops are typically not co-located with the strongest winds next to the coast, but several 100 km offshore. This observation, along with elevated chlorophyll levels co-located with areas of colder SSTs, led to the supposition that the thermocline depth may be important to the magnitude of entrainment fluxes, and, thus, SST—motivating and supporting the analysis presented here. The sampling region is directly influenced by the ITCZ when it is at its most northerly position in August–October and the gap winds primarily when they are strongest in late autumn through spring. As will be discussed, the active atmospheric convection of the ITCZ with its associated heavy rainfall ($\sim$ 0.6–0.9 m/month, 20–30 mm/day), increased cloudcover and short-lived but often intense storms can significantly alter the mixed layer temperature budget from the dominant balance found at non-ITCZ times.

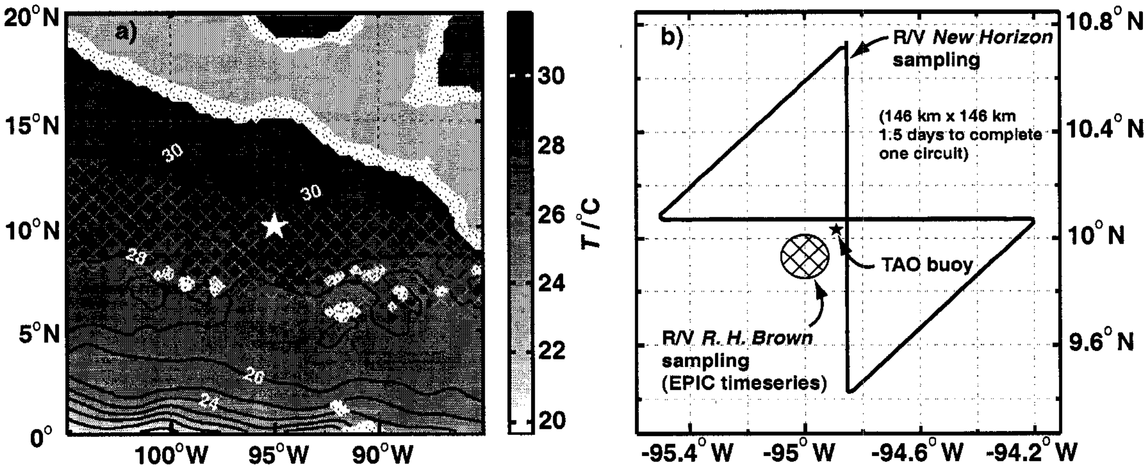

Figure 4.1: a) SST of the eastern tropical North Pacific as measured by the TRMM satellite. The star shows the location of the 10°N, 95°W EPIC timeseries and TAO buoy. SST's at 0.25° resolution are smoothed over 2° and averaged over 4 days (9/12/01–9/15/01). Cross-hatching shows the approx. mean position of the ITCZ during Aug.–Oct. 2001 based on integrated water vapor. Stippling indicates data gaps. b) Sampling track line of the R/V *New Horizon* with the locations of the R/V *R. H. Brown* sampling (EPIC timeseries) and the TAO buoy.

4.3 Methods

4.3.1 Data Sampling

The observations used in this study are centered on a timeseries of upper-ocean microstructure and velocity complimented by extensive atmospheric measurements collected aboard the R/V *R. H. Brown* (RHB) during the EPIC 2001 field study from September 12 to October 1, 2001 (hereafter referred to as the EPIC timeseries). This timeseries was collected while the *Brown* maintained a position within 5 nm (9.25 km) of 9.93° N, 95° W (Fig. 4.1). Bulk surface fluxes were computed using version 2.6 of the COARE algorithm, which at the time of this study was the most recent version of that presented by Fairall et al. (1996). The surface momentum flux (wind stress) was specifically parameterized with the Large and Pond (1981) bulk algorithm. The primary oceanographic instruments used aboard the R/V *Brown* were the free-falling, loosely-tethered Modular Microstructure Profiler (MMP) and a hull-mounted, 150 kHz, narrowband RD Instruments acoustic Doppler current profiler (ADCP). The MMP recorded profiles of microscale pressure, conductivity, temperature, oxygen and velocity shear to nominally 300 m about every 20 minutes, and the ADCP recorded profiles of upper-ocean finescale (4 m) velocity to about 250 m every minute. In addition to being used to determine the time-evolution of the mixed layer temperature and depth, MMP data were also used to calculate the turbulent entrainment fluxes. *Ron Brown* ADCP data were used to calculate the horizontal advective fluxes. Details of ADCP and MMP processing as well as the turbulent entrainment flux calculations are included in Appendix A.

For the duration of the EPIC timeseries the R/V *New Horizon* sampled the upper-ocean spatial variability with a hull-mounted 150 kHz RDI ADCP and dual SeaBird CTDs (conductivity-temperature-depth) mounted on the SeaSoar towed platform, completing 146 × 146 km "butterfly" pattern circuits centered on 10.07° N, 94.85° W about every 1.5 days (Fig. 4.1 b). The CTD data provided by the R/V *New Horizon* has a horizontal resolution of about 1.9 km and was averaged into 8-m depth bins spanning 16–256 m. These data are used along with the *Ron Brown* ADCP data to compute the horizontal heat fluxes. Details of this calculation are included Appendix C.

Data from NOAA's Tropical Atmosphere-Ocean (TAO) buoy nominally located at 10° N, 95°

W, were used to investigate the seasonal and annual mixed layer temperature budget over 2001. As part of EPIC, from late 1999 to 2003 the 10° N, 95° W buoy along with other TAO buoys along 95° W was augmented with instrumentation to provide hourly-averaged surface heat fluxes in addition to hourly or finer resolution measurements of basic atmospheric conditions and upper-ocean temperature, salinity and pressure. Cronin et al. (2006) found that the overall uncertainty of the net surface heat fluxes was near ± 10 W m^{-2}. An empirical model of solar penetrative radiation presented by Ohlmann (2003) was used to compute the penetrative heat fluxes. Since this model was largely based on transmission profiles collected during the EPIC timeseries, rms and maximum error are small with estimates of 0.9 and 1.5 W m^{-2} respectively [1]. The upper-ocean temperature data, which were used here to estimate mixed layer depth, SST and depth-averaged mixed layer temperature, were recorded at fixed depths of 1, 5, 10, 20, 40, 60, 80, 100, 120, 140, 180, 300 and 500 m. Four-meter buoy winds were adjusted to 10 m using a log-profile estimated from EPIC timeseries LIDAR wind profiles prior to computing wind stress, which was done using the Large and Pond (1981) bulk algorithm. Further details of TAO buoy instrumentation, measurements and measurement errors are discussed in Cronin et al. (2006) and McPhaden et al. (2007).

Satellite measured surface winds from the QuikSCAT scatterometer were used to calculate wind stress curl and Ekman pumping velocity. Objectively mapped QuikSCAT wind data averaged over 3 days with a 1° spatial resolution were generously provided by K. Kelley and S. Dickinson of the University of Washington's Applied Physics Laboratory. Surface wind stress was computed with the Large and Pond (1981) bulk algorithm. QuikSCAT wind data were processed similarly to the NSCAT wind processing described in detail in Kelly et al. (1999).

4.3.2 Calculating the mixed layer temperature budget

The choice to investigate a mixed-layer budget that integrates to a time-varying mixed layer depth, $h(t)$, and not a fixed-depth or level budget is motivated by several factors. First, because of the characteristically strong turbulence within the mixed layer, vertical gradients are homogenized on timescales of typically several days or less. Thus, changes in SST closely follow mixed layer tem-

---

[1] This error estimate assumes an average Q_{sw} of 200 W m^{-2}

perature changes on these timescales and longer. Computing budgets over a surface layer shallower than the mixed layer depth would capture rapid SST changes, but would necessitate the measurement of vertical turbulent fluxes within the weakly stratified or unstratified mixed layer—a requirement essentially beyond present observational capabilities (Osborn, 1980; Moum, 1990). Secondly, calculating the budget over a time-variable mixed layer depth shows the importance of variations in h to changes in depth-averaged mixed layer temperature, and thus, SST. Because the change in T_a expected for a given mixed layer vertical flux imbalance is inversely proportional to h, the relatively shallow mixed layer of the EPWP (~10–40 m) results in T_a being particularly sensitive to both changes in h and vertical fluxes. Calculating a mixed layer budget—opposed to a level budget—is largely possible because of the availability of direct measurements of turbulent entrainment heat fluxes. As will be shown, knowing the entrainment heat flux greatly simplifies the budget equations—consequently greatly reducing uncertainty in the results.

After Emery (1976) and Moisan and Niiler (1998) the temperature conservation equation integrated over a time and space variable mixed layer depth, $h(x, y, t)$, is:

$$\begin{aligned}\overbrace{\frac{\partial T_a}{\partial t}}^{1} &= -\overbrace{\mathbf{u}_a \cdot \nabla T_a}^{2} - \overbrace{\frac{1}{h}\nabla \cdot \left(\int_{-h}^{0} \hat{\mathbf{u}}\hat{T} dz\right)}^{3} \\ &-\overbrace{\left(\frac{T_a - T(-h)}{h}\right)\left(\frac{\partial h}{\partial t} + \mathbf{u}(-h) \cdot \nabla h + w(-h)\right)}^{4} + \overbrace{\frac{-[Q - Q_{sw}(-h)]}{\rho c_p h}}^{5}\end{aligned} \tag{4.2}$$

where the ∇ operator is the horizontal divergence only ($\frac{\partial}{\partial x}, \frac{\partial}{\partial y}$), $\mathbf{u}$ is the horizontal velocity vector $[\mathbf{u}(u, v)]$, h is the mixed layer depth (positive), and T_a and $\mathbf{u}_a$ are the average mixed layer temperature and horizontal velocity, or formally:

$$T_a = \frac{1}{h}\int_{-h}^{0} T(z)dz; \quad u_a = \frac{1}{h}\int_{-h}^{0} u(z)dz; \quad v_a = \frac{1}{h}\int_{-h}^{0} v(z)dz$$

Additionally, $\hat{T}$ and $\hat{\mathbf{u}}$ are the deviations of $T(z)$ and $\mathbf{u}(z)$ from T_a and $\mathbf{u}_a$, or, $T = T_a + \hat{T}$ and $\mathbf{u} = \mathbf{u}_a + \hat{\mathbf{u}}$. The first term of Equation 4.2 is the time-rate-of-change of the depth-averaged mixed layer temperature. Term 2 represents the change in T_a due to the depth-mean mixed layer currents advecting horizontal gradients of T_a, with term 3 accounting for advective fluxes due to the correlation of the vertical perturbations, $\hat{T}$ and $\hat{\mathbf{u}}$. Term 4 is the bulk entrainment across the mixed layer base, which removes the effect adiabatic changes in h due to horizontal and vertical advection from the local changes in mixed layer depth. Term 5 accounts for changes in mixed layer heat content due to the difference between the total surface heat flux (Q) and the downward shortwave (solar) radiative heat flux at $z = -h$ $[Q_{sw}(-h)]$. In equation 4.2 the seawater density (ρ) and specific heat (c_p) are assumed to be constant over the depth of the mixed layer (1021 kg m $^{-3}$ and 4006 J $(kg°\mathrm{K})^{-1}$ respectively). For Q and Q_{sw} negative values indicate downward heat flux. With a mean mixed layer depth of only about 25 m over both the 19-day September 2001 timeseries and all of 2001, a large fraction ($\sim$10%) of Q_{sw} penetrated below the mixed layer. Penetrative radiation was computed using an empirically-derived fit using data collected over the September 2001 timeseries with a profiling radiometer (Ohlmann, 2003). The canonical model water type (Jerlov II) (Paulson and Simpson, 1977) gives a mean penetrative heat flux that is about half of the 2001-mean of $\sim$18 W m^{-2} computed with the Ohlmann (2003) model, a difference that would result in roughly a 3 °C warmer mixed layer at the end of a year.

The connection between the bulk entrainment term (term 4 of Eqn. 4.2) and turbulent heat entrainment—or the vertical turbulent heat flux at $z = -h$—is readily evident if we first define a bulk "entrainment velocity", w_e, that is the difference between observed and adiabatic or advective rates of change of h:

$$w_e \equiv \frac{\partial h}{\partial t} + \mathbf{u}(-h) \cdot \nabla h + w(-h) \ . \tag{4.3}$$

Following De Szoeke and Richman (1981),

$$w_e \left[T_a - T(-h)\right] = -\overline{w'T'}|_{-h} \ , \tag{4.4}$$

or the bulk entrainment flux is equal to the negative of the vertical turbulent temperature flux at $z = -h$ (where $|_{-h}$ indicates the evaluation at $z = -h$). With the turbulent entrainment heat flux is defined as

$$J_q^e \equiv \rho c_p \overline{w'T'}|_{-h} \ , \tag{4.5}$$

the following substitution can be made for term 4 of equation 4.2:

$$\left(\frac{T_a - T(-h)}{h}\right)\left(\frac{\partial h}{\partial t} + \mathbf{u}(-h)\cdot\nabla h + w(-h)\right) = \left(\frac{T_a - T(-h)}{h}\right) w_e = -\frac{J_q^e}{\rho c_p h}\ . \tag{4.6}$$

Thus, knowing the turbulent entrainment flux, J_q^e, simplifies the mixed layer temperature budget by removing the need to account for horizontal advection of gradients of h and non-turbulent vertical advection. Since the latter term typically has large uncertainty as found in Wijesekera et al. (2005), this simplification leads to significantly improved confidence in the overall budget results.

Continuous microstructure profiling over the EPIC timeseries enabled the direct estimation of J_q^e, which is approached by calculating a vertical turbulent diffusivity, K_T, using profiles of the turbulent dissipation rate, ε, and stratification, so that:

$$J_q^e \approx -\rho c_p K_T(-h)\frac{\partial T}{\partial z}(-h)\ . \tag{4.7}$$

Specific details of this approach for estimating J_q^e are discussed in Chapter 2 and Appendix B.

4.3.3 Defining the mixed layer

A rather important but subtle aspect of the budget calculations is the definition of the mixed layer depth, h. Dynamically speaking, here the mixed layer refers to the upper layer of the ocean within which large, surface-driven vertical turbulent fluxes rapidly transport scalars (heat, salt, etc.) and momentum. Resultantly, these properties are homogeneous or the vertical gradients are weak. Here "rapidly" refers to timescales of several days or less. Thus, the depth-averaged mixed layer temperature, T_a, follows SST on these timescales and longer. This definition excludes diurnal and shorter period variations of the instantaneous mixed layer depth and, therefore, includes periods of (typically weak) restratification. An advantage of this definition, however, is that it avoids complexities in calculating budget terms (such as advective and entrainment fluxes) that arise from large variability in the depth of the instantaneous mixed layer due to rapid, shallow restratification associated with heavy rain and strong solar insolation.

This dynamically-defined mixed layer is well-represented by "hydrographically" defining the mixed layer depth using vertical density and temperature data. When high vertical resolution density data are available (i.e. during the EPIC timeseries) h is estimated as the maximum depth at which $\Delta\sigma_\theta/\Delta z > -0.07$ kg m−2, or equivalently the 1-m buoyancy frequency squared $N^2 > 6.7 \times 10^{-4}$ s^{-2} ($\sim$15 cph) when decreasing in depth from the seasonal thermocline. This approach has the advantage of excluding short-lived instances when the near-surface is strongly stratified due to heavy rain/strong solar insolation.

When using TAO buoy data, h is defined with daily-averaged temperature since density measurements are recorded at coarser depth intervals. Specifically h is defined as the shallowest depth that is at least 1.5 °C cooler than the 5-m temperature with linear interpolation between thermistor depths ($z = 1, 5, 10, 20, 40, 60, 80, 100, 120, 140$ m). In comparison to other values of ΔT (specifically 0.5, 1, and 2 °C) a 1.5°C temperature difference results in the lowest mean bias with MMP-determined h ($+0.9$ m with 2σ of ±5.2 m). Additionally, it captures a deep mixed layer in March of 2001 that is weakly temperature stratified but has little or no density stratification because of compensation from $\partial S/\partial z > 0$. Over most of 2001, however, the large vertical gradients of temperature (and density) at the mixed layer base result in the estimated value of h being rather insensitive to the chosen value of ΔT and usually coincident with the top of the thermocline (Fig. 4.2). As shown in Appendix C, an analysis based on well-resolved EPIC-timeseries MMP profiles indicates that estimating the temperature profile by linear interpolation between buoy thermistor depths results in an overestimate of the actual ΔT between $T(5\text{ m})$ and $T(h)$ by an average of 1 °C over the EPIC timeseries, with the seeming-large value of 1.5 °C somewhat compensating for the coarse resolution to improve the estimate of the mixed layer depth. Ultimately, the temperature-based definition of h is consistent with the goal to investigate the mechanisms driving week-to-year variations in SST, with T_a tracking SST at timescales of week and longer (Fig. 4.3a).

4.3.4 Estimating J_q^e variability over 2001

The variablity of the turbulent entrainment heat flux over 2001 is estimated by evaluating the semi-empirical entrainment model presented in Chapter 3 with TAO buoy data and an estimate of the finescale ($\sim$8 m) gradient Richardson number $Ri \equiv N^2/Sh^2$ at $z = -h$ based on results from the Pollard and Millard (1970) mixed layer slab model. Largely because of uncertainty in the estimate of

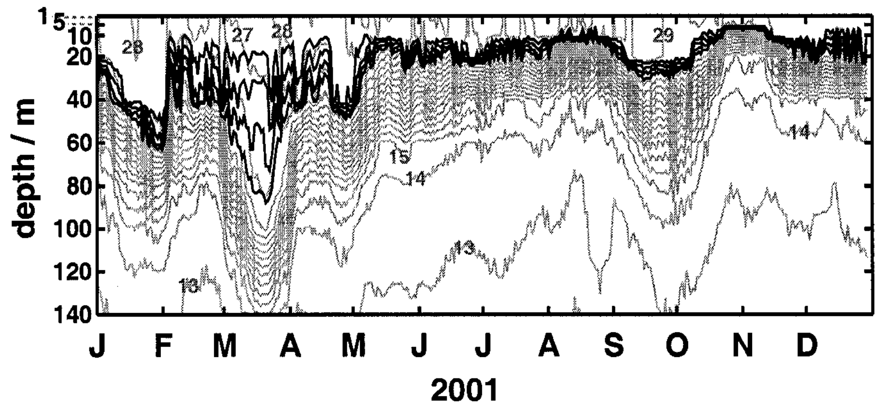

Figure 4.2: Contours of potential temperature from the 10 ° N, 95° W TAO buoy over 2001 (gray), with different calculations of h over-plotted (black) using $T(5\text{ m}) - T(z) > 0.5, 1, 1.5,$ and 2° C. Contours are at 1°C intervals and thermistor depths are indicated as y-axis ticks (1 m, 5 m, 10 m, 20 m...). Considering only the temperature contribution to density, the temperature differences are equivalent to $\rho(z) - \rho(5\text{ m}) > 0.16, 0.32, 0.49,$ and 0.65 kg m^{-3} respectively.

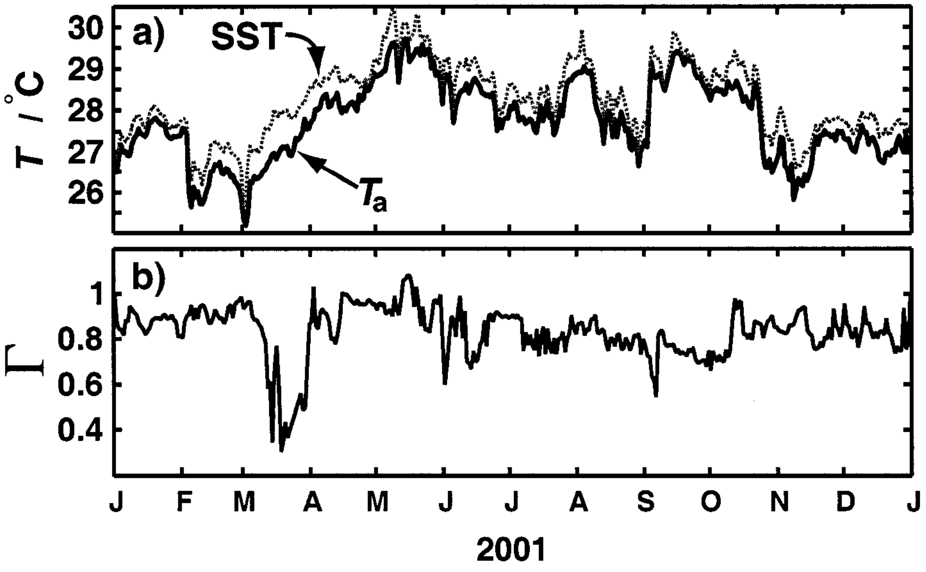

Figure 4.3: a) SST (gray dashed) and T_a (black) from the 10° N, 95° W TAO buoy over 2001 showing that on timescales of about a week+ T_a follows SST. b) Ratio of the contribution of temperature stratification ($\partial T/\partial z$) to the total stratification ($\partial\rho/\partial z$) at h, showing stratification at h is almost always temperature dominated.

$Ri(-h)$, the model is not expected to give reliable estimates of the variablity of J_q^e on timescales of less than several days. Thus, the interpretation of the model results are largely limited to conclusions about the role of entrainment over week timescales and longer.

Estimating Ri

All entrainment model input variables with the exception of the finescale gradient Richardson number at the mixed layer base are either given by or can be calculated directly from TAO buoy measurements. Because of this it is necessary to estimate $Ri(-h)$ variability over 2001 using the Pollard and Millard (1970) mixed layer slab model and empirical relationships between shear at the mixed layer base and mixed layer velocity from the EPIC timeseries.

As shown in Chapter 2, the variability of $Ri(-h)$ over the EPIC timeseries was primarily due to changes in finescale shear, which was in turn largely near-inertial. With these observations as justification, here it is assumed that shear at h spanning 2001 can be estimated from the magnitude of the mixed layer inertial currents, which are estimated with the wind-driven Pollard and Millard (1970) mixed layer slab model. This approach is supported by the significant correlation between observed U_i^2, or inertial current magnitude-squared, and observed $Sh^2(-h)$ over the EPIC timeseries ($r^2 = 0.41$ for 24-hr boxcar smoothed data) in addition to the respectable skill of the slab model at replicating the observed inertial currents ($r^2 = 0.67$ using 2.5 hr-averaged data). One of the primary limitations of this approach is that it does not account for sub-inertial (geostrophic) shear, which, as shown in Chapter 2 can strongly modulate total shear at $z = -h$.

Finescale shear-squared is computed by applying the regression coefficients to the model U_i^2 with $Sh^2(-h) = 0.0074U_i^2 + 3.0 \times 10^{-5}$. The slab model is forced with TAO buoy winds and has a mixed layer depth explicitly set from the TAO buoy observations. The one tunable parameter of the slab model, the Rayleigh damping coefficient, r, is set to a value of $1/5$ days^{-1} based on a comparison of observed and modeled EPIC timeseries mixed layer inertial currents. The buoyancy frequency at h is determined from TAO buoy temperature and salinity observations with 8-m N^2 computed after linearly interpolating the observations onto a 1-m depth grid. This computation of finescale N^2 at h shows excellent agreement with MMP-determined N^2 over the EPIC timeseries.

Lastly, the form of the Richardson number used in the model, $Ri(-h)^m$, where m an empirically-derived constant of -0.87, is regressed to EPIC timeseries observations to obtain the best fit and to reduce potential bias before using the modeled value as input for the entrainment parameterization. The final correlation between estimated and observed $Ri(-h)^m$ is 0.60 for 24-hr smoothed data. However, because of the more dominant role of direct wind stress in driving entrainment over the EPIC timeseries, the entrainment model using the estimated $Ri(-h)^m$ and TAO buoy data as input accounts for more than 50% of the variance of entrainment buoyancy flux, J_b^e, for hourly data ($r = 0.73$). Most of the error is a consequence of underestimated values of Ri^m (or overestimated Ri) over the last several days of the timeseries, when the correlation of Ri^m and the model surface forcing term, J_b^*, which includes the influence of direct wind stress and surface buoyancy fluxes, led to the largest entrainment levels over the timeseries (see Chapter 3). Error is also introduced by the difference in locations of the TAO buoy and the *R. H. Brown*, which are about 16 km apart on average.

Estimating entrainment heat fluxes from entrainment buoyancy fluxes

With stratification at h largely coincident with and due to large vertical temperature gradients, entrainment heat fluxes within the EPWP are typically proportional to entrainment buoyancy fluxes. However, as shown in Chapter 2, EPIC timeseries observations indicate that at times salinity gradients can dominate stratification at h, with entrainment buoyancy fluxes during these periods largely due to entrainment salt fluxes—while entrainment heat fluxes are weak or even negative (upward heat). Entrainment buoyancy fluxes estimated from the empirical entrainment model are converted to entrainment heat fluxes using the relation:

$$J_q^e = J_b^e \left[\frac{\rho c_p \Gamma}{g\alpha} \right] \tag{4.8}$$

where Γ is the ratio of the contribution of temperature stratification to the total stratification, or:

$$\Gamma = \frac{\rho\alpha \frac{\partial T}{\partial z}}{\frac{\partial \rho}{\partial z}}, \quad \text{and} \quad \alpha \equiv -\frac{1}{\rho}\frac{\partial \rho}{\partial T}\,. \tag{4.9}$$

Here Γ is computed with hourly-averaged values of 1-m $\Delta T/\Delta z$ and $\Delta\rho/\Delta z$ at h, which are estimated by linearly interpolating TAO buoy T and S measurements onto a 1-m grid. The hourly value of Γ is then boxcar-averaged over a day. Typically, temperature gradients are responsible for about 80% of the density stratification at h (Fig. 4.3b).

After converting the entrainment buoyancy fluxes to heat fluxes, to reduce the potential for bias the model results are adjusted by a constant to match the EPIC timeseries mean J_q^e of -16 W m^{-2}. The correlation of model output and measured EPIC timeseries entrainment heat fluxes with both averaged over 1.5 days is 0.86 (Fig. 4.4). This skill level is taken to be satisfactory considering the factor-of-two uncertainty in the entrainment observations and the intended use of the model—which is to investigate entrainment variablity on timescales of roughly a week to a year.

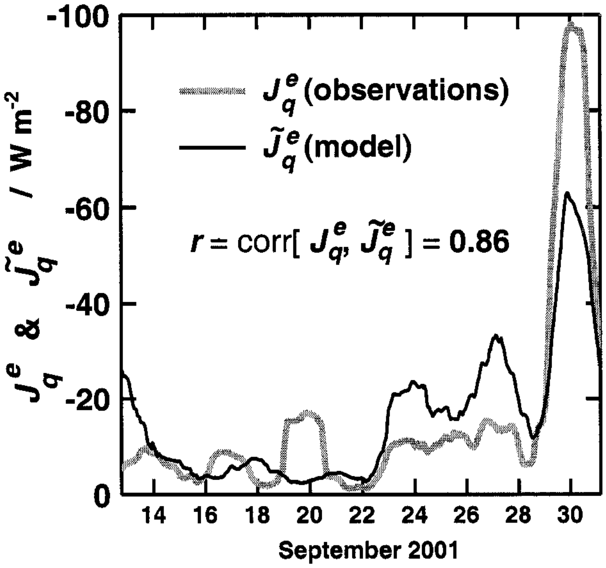

Figure 4.4: Comparison of the observed (J_q^e) and modeled $(\tilde{J}_q^e)$ entrainment heat flux over the EPIC timeseries with quantities boxcar-averaged over 1.5 days.

4.4 Results Part I: The September 2001 Temperature Budget

The direct measurement of entrainment fluxes along with upper-ocean T and ρ profiles, surface and penetrative heat fluxes, and horizontal temperature gradients permitted the closure of the mixed layer temperature budget over the 19-day EPIC timeseries within limitations of uncertainty. This result strongly supports the methodology used, including the specific budget equations, the measurement methods and the various bulk parameterizations. It also indicates that any of the individual budget terms can be inferred from the sum of the remaining terms, or as a residual. Because there are insufficient observations to estimate all primary budget terms over 2001, this result is the basis for the analysis of the seasonal to annual budget variability. Although the primary purpose for presenting the EPIC timeseries budget is to show the above result and prove the budget methodology, despite the brevity of the timeseries the observations also suggest mechanisms by which mesoscale eddies and the ITCZ may strongly influence the mixed layer temperature budget.

The intensive sampling over the 19 days allowed the estimation of all budget terms except for term 3 of Equation 4.2, or the correlation of the vertical perturbations of the velocity and mixed layer temperature. This term, however, was estimated to be significantly smaller than other terms (see Appendix C) and, therefore, is neglected as has been done in previous studies (Emery, 1976; Moisan and Niiler, 1998). With the exception of the depth-mean horizontal temperature gradients, ∇T_a, all variables needed to estimate the remaining budget terms were sampled at a relatively high frequency (>1/hr), resulting in similarly-resolved estimates of these terms. The slow variability of $T_a(x, y)$ relative to the spatial sampling period (1.5 days), however, justified its linear interpolation onto a finer time grid (1 hr) (see Appendix C). This interpolation takes advantage of the high-frequency sampling of $\mathbf{u}_a$ and results in much-improved resolution of horizontal advective flux estimates—which consequently enables a time-dependent budget calculation that demonstrates the variability of budget balances over the 19 days.

Budget closure within estimated uncertainty is indicated by good agreement between a timeseries of measured ΔT_a and that inferred from the time-integration of the sum of terms on the r.h.s. of Equation 4.2 (term 2+term 4+term 5) (Fig. 4.5a). This result, however, obscures the large uncer-

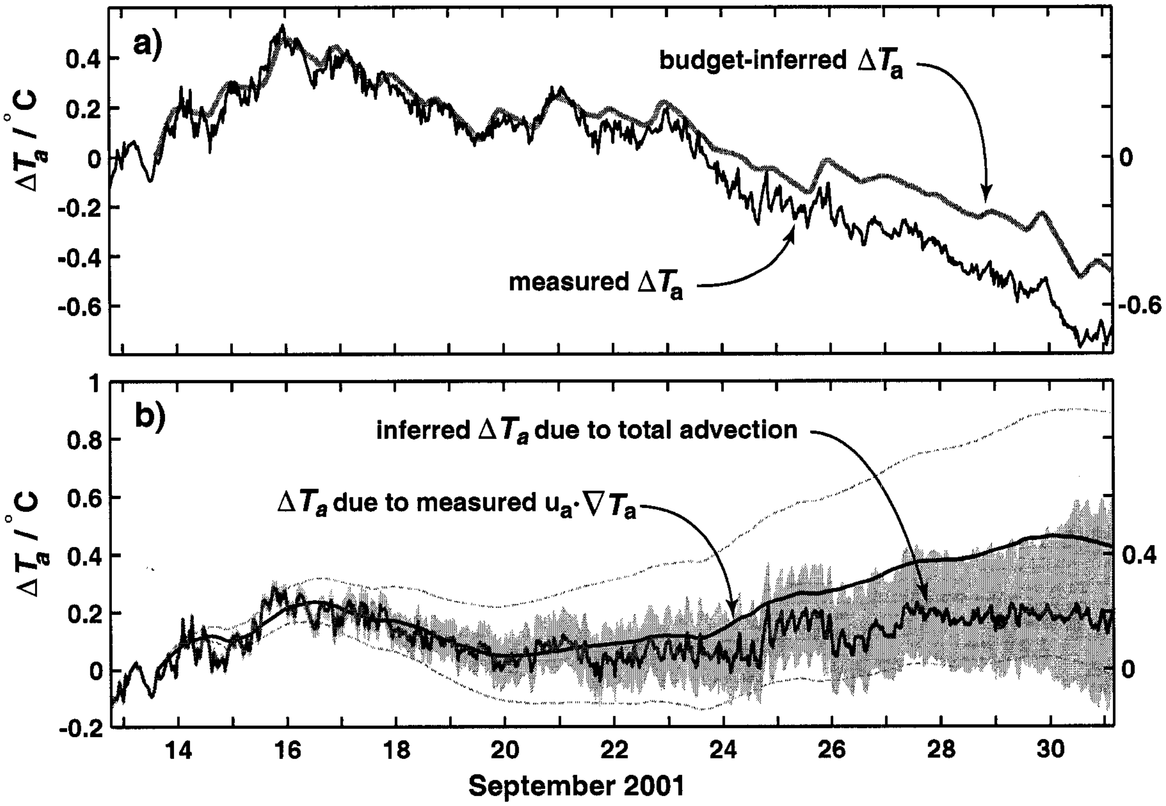

Figure 4.5: a) Budget closure is indicated by relatively good agreement between measured ΔT_a (time-integrated term 1) (black) and ΔT_a inferred from the time-integrated sum of the measured terms on the r.h.s. of Equation 4.2 (term 2+term 4+term 5) (gray). The close match is despite large uncertainty of inferred ΔT_a ($\sim \pm 0.8$°C at the timeseries end) that is principally due to uncertainty in the estimate of the mean advective term (term 2). b) Comparison of ΔT_a due to measured depth-mean horizontal advection (term 2) (black) and that inferred from the difference of the remaining budget terms (gray), indicating that inferred ΔT_a from advection has less uncertainty than the measured quantity over the EPIC timeseries. Approximate uncertainty is shown with gray shading (inferred) and gray dashed lines (measured). Here $\Delta T_a = T_a(t) - T_a(t_0)$, with t_0 the start of the advective term measurements (1453 on 9/13).

tainty in the estimates of the depth-mean horizontal advection (term 2) (Fig. 4.5b) and the roughly factor-of-two uncertainty in the entrainment heat flux estimate, which are the main contributors to the roughly $\pm 0.8°$C total uncertainty in ΔT_a at the end of the 19-days. In addition to supporting the budget methodology, measurement methods and various bulk parameterizations, budget closure also provides after-the-fact support for the interpolation of T(x,y) onto a finer time grid. It is readily apparent that preserving the time-variablity of individual budget terms versus calculating the time-averaged budget over the 19 days adds weight to the results by showing that the budget is continuously closed within expected uncertainty on timescales of several days and longer. Even on shorter timescales there is considerable agreement between the two curves, especially noting that large variablity at timescales of $\sim$4 hrs in the observations are largely due to contamination from spatial variability introduced by the sampling approach (ship movement). The steadily increasing difference in the curves that begins about mid-timeseries suggests a positive bias of the estimates of terms on the r.h.s. of Eqn. 4.2, or even the possibility of a relatively steady contribution from term 3 (advection from perturbations) that is not accounted for.

As discussed in Appendix C, uncertainty in the depth-averaged advective term is largely due to the coarse sampling period of the horizontal gradients of T_a ($\sim$1.5 days), which aliases the time-variability of small scale ($<$40 km) gradients and, consequently, results in sensitivity to the scale used to calculate ∇T_a. A comparison of ΔT_a due to measured depth-mean horizontal advection (term 2, Eqn. 4.2) and the *inferred* influence of total advection (terms 2 and 3) on ΔT_a (by summing the remaining budget terms, or term 1 $-$term 4$-$term 5) indicates that budget-inferred advection likely has less uncertainty than the measured quantity (Fig. 4.5b). This result is a consequence of the relatively low uncertainty in the storage (term 1) and surface flux terms (term 5) (Tab. 4.4) as well as the typically weak entrainment fluxes over the EPIC timeseries which kept uncertainty in this term significantly smaller than that of measured advection. Large variablity at timescales of $\sim$4 hrs in the inferred advective ΔT_a and its uncertainty is due to contamination of the storage term (term 1) from spatial variability introduced from the sampling. It is important to note that the difference between inferred ΔT_a from total advection (includes term 2 and 3) and that due to the measured depth-mean advective term (measured term 2) is due to both error and the arguably small term 3 contribution (the correlation of $\hat{T}$ and û).

With most of the uncertainty in the measured depth-mean advective term and in the entrainment estimate, it follows that the combined effect of total advection and entrainment (terms 2+3+4) can be inferred from the other budget terms (term 1 −term 5) with relatively low uncertainty. This finding is important to the analysis of the 2001 seasonal to annual budget variability since there are no observations to directly estimate the advective and entrainment terms.

A comparison of the cumulative contribution of each term to observed T_a time-changes indicates that the divergence of the net surface heat flux (Q) and the downward solar heat flux at the mixed layer base $[Q_{sw}(-h)]$ had the largest influence on the observed changes in mixed layer temperature (Fig. 4.6e, Table 4.4). Observed ΔT_a closely follows that expected from $Q - Q_{sw}(-h)$ which is a consequence of both the weaker roles of the advective and entrainment fluxes compared to the surface heat flux and to the fact that these terms partly offset one another, with horizontal advection warming and entrainment cooling the mixed layer. Except during the last several days of the timeseries when wind stress was large (Sept. 29–30) (Fig. 4.6a), entrainment heat fluxes had only a minor role in changing T_a. More than half of the total turbulent entrainment of heat over the 19 days occurred during this time ($\sim$10% of the timeseries) and accounted for more than half of the 0.25° drop in T_a over the two days. Entrainment heat fluxes over this period were in excess of -100 W m^{-2}, while the 19-day average J_q^e was only -16 W m^{-2} (Fig. 4.6d,e, Table 4.4), indicating that turbulent entrainment within the EPWP can be extremely episodic.

The influence of an anticyclonic eddy

The advective fluxes over the 19 days were strongly influenced by an anticyclonic eddy that was evident in sea surface height anomaly data (Wijesekera et al., 2005), from an Expendable Current Profile (XCP) survey (Shay et al., 2003), and as shown here, using a combination of satellite SST and *New Horizon* ADCP velocities (Fig. 4.7). The latter shows a mixed layer velocity pattern that is consistent with the expected eddy flow pattern assuming that SST is a relatively good indicator of geopotential within the EPWP. However, consistent with the advective heat flux over the first several days of the timeseries estimated from *New Horizon* ADCP and SeaSoar data (Fig. 4.6d) the

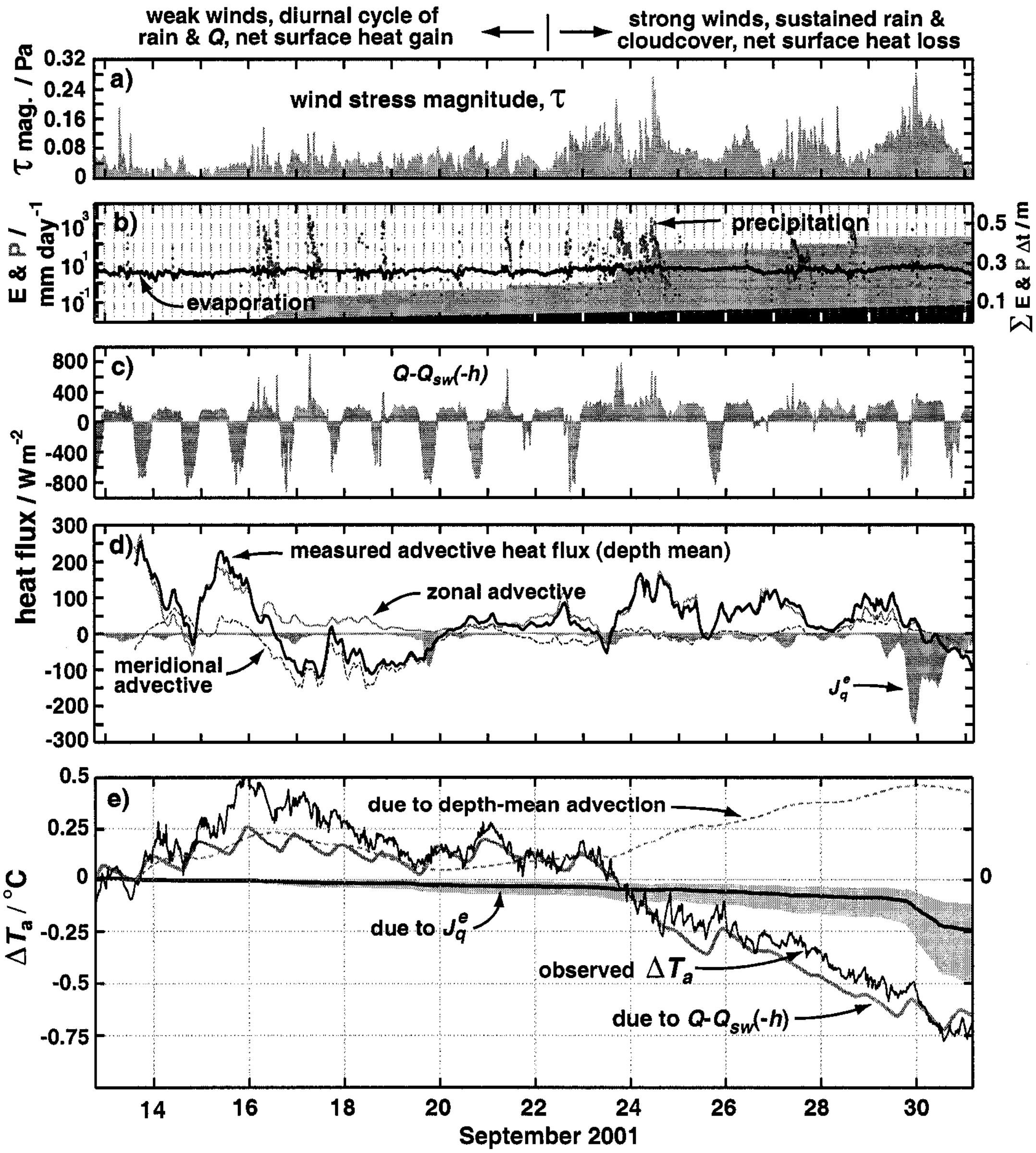

Figure 4.6: a) Wind stress magnitude, τ. b) Rates of evaporation, E, (black) and precipitation, P, (gray points) with cumulative values (shading). E and P are plotted on a $\log_{10}$ scale. c) $Q - Q_{sw}(-h)$. d) Depth-mean advective heat flux (black), the zonal (solid gray) and meridional (dashed-gray) advective components, and the measured entrainment heat flux, J_q^e (gray fill). e) Cumulative impact of mixed layer temperature budget terms on ΔT_a. Plotted are observed mixed layer ΔT_a (thin black) and ΔT_a due to $Q - Q_{sw}(-h)$ (thick gray), entrainment heat fluxes, J_q^e (thick black), and ΔT_a expected from measured depth-mean horizontal advection (term 2) (dashed). Gray shading indicates a factor of two confidence interval for J_q^e (Peters et al., 1988; Moum et al., 1995), and $\Delta T_a = T_a(t) - T_a(t_0)$ where t_0 is the start of the advective term measurements (1453 on 9/13).

mixed layer velocity vectors largely point somewhat down SST-gradient, indicating local advective warming over this period.

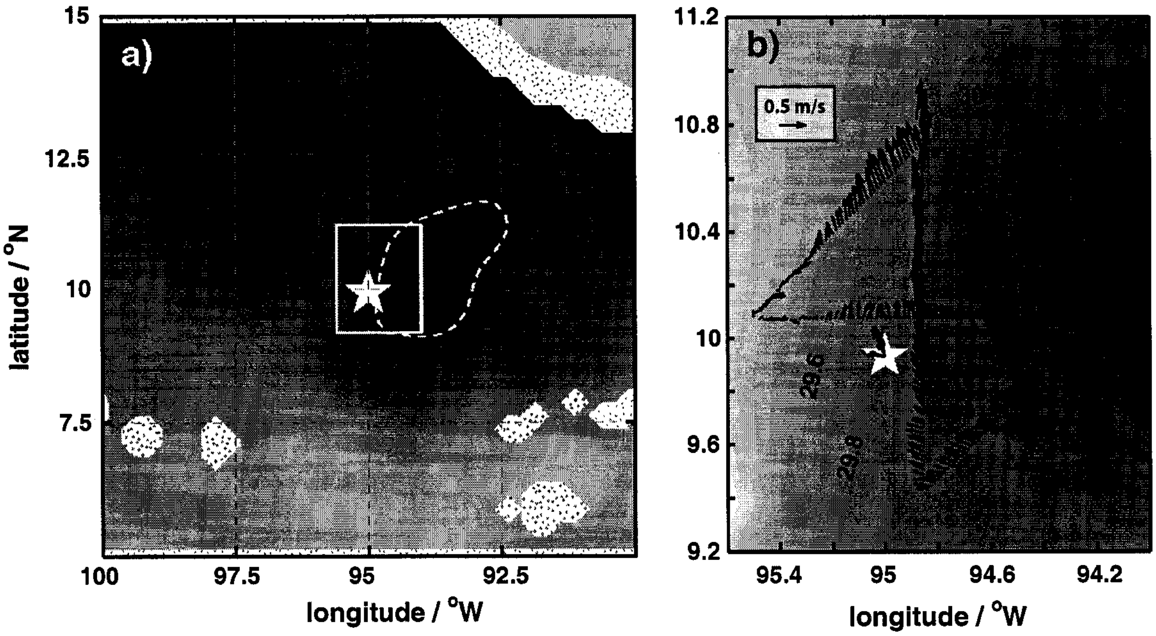

Figure 4.7: a) TRMM satellite SST averaged over 3 days (9/13/01–9/15/01) showing a warm mesoscale eddy just to the east of the EPIC timeseries location. Contour intervals are 0.2 °C, with the 30.0°C contour indicated with a white dashed line. The white box indicates the zoomed-in area shown in (b), which in addition to SST also shows *New Horizon* and *R. H. Brown* mixed layer ADCP velocity vectors for the same period. The mixed layer velocity vectors are largely consistent with the expected flow pattern of the anticyclonic eddy assuming SST is an indicator of sea-surface height anomaly—despite the fact the ADCP velocities also include ageostrophic flow. The star shows the location of the EPIC timeseries and stippling in (a) indicates data gaps.

The EPIC sampling station was situated within the lower half of the eddy as it propagated westward at roughly 0.05 m s^{-1}, with mixed layer sub-inertial flow initially to the W-NW at ~0.3 m s^{-1} rotating counterclockwise over the 19 days to the SE and decreasing to about 0.2 m s^{-1}. The predominantly westward flow advected warmer water from the east into the sampling region, resulting in a net warming of roughly 0.1–0.5 ° C from advection (Fig. 4.5). This estimate, which was derived from *New Horizon* data, is consistent with SST gradients indicated in Figure 4.7 assuming the SST gradients are not strongly modified by other budget terms as they are advected. Although the 19-day average advective flux was moderate ($\sim$30 W m^{-2}), at times—such as over the first several days of the timeseries when both $\mathbf{u}_a$ and ∇T_a were large—fluxes were in excess of 200 W m^{-2} (Fig. 4.6d).

The expectation that the thermocline is bowled, or deeper within the shallow, anticyclonic eddy is consistent with the timeseries of upper-ocean temperature (Fig. 4.2) showing that over a $\sim$40-day period spanning the EPIC timeseries the mixed layer and thermocline were anomalously deep by roughly 10 m. It follows, then, that the expectation of decreased entrainment with an increase in mixed layer depth given constant surface forcing suggests that the presence of the eddy may have led to reduced entrainment fluxes over the EPIC timeseries. Additionally, the observation of increased rainfall over the anomalously warm water advected westward by the eddy (Wijesekera et al., 2005) further suggests that entrainment heat fluxes in particular may have been suppressed. As discussed in Chapter 2, although buoyancy entrainment was large during the first storm (September 23–24), entrainment heat fluxes were relatively weak during this period—a result of the strengthening of $\partial S/\partial z$ at h by the rainfall and the weakening of $\partial T/\partial z$ at h from large surface heat losses. As will be shown in the next section, the expectation of weaker entrainment within the eddy is supported by evidence of significantly smaller entrainment heat fluxes over the EPIC timeseries than over periods before and after the timeseries when h was $\sim$10–15 m shallower, while average wind stress and destabilizing $J_b(0)$ over the EPIC timeseries were larger than over these periods.

The influence of the ITCZ

A distinct difference in atmospheric forcing between the first and second halves of the timeseries highlights the strong influence of the ITCZ on mixed layer temperature. While the first half (9 days) was characterized by light winds, strong solar heating and a diurnal pattern of rainfall, the second half was dominated by prolonged periods of atmospheric deep convection with strong winds, heavy cloudcover and sustained, heavy rainfall (Fig. 4.6a–c). This difference resulted in a net surface heat gain over the first half of the timeseries and a net surface heat loss over the second half. Consequently, the total drop in T_a by -0.70°C over the 19 days occurred entirely during the second half of the timeseries. Petersen et al. (2003) showed that the deep convection observed at 10 ° N, 95° W during the EPIC timeseries was a result of easterly waves modulating convection within the ITCZ—an observation which connects the presence of the ITCZ to the observed changes in T_a, and, thus, SST.

A longer timeseries of time-integrated Q over 2001 and a comparison to other years shows that the net surface heat loss over the second half of the EPIC timeseries was a departure from the typical conditions at 10° N, 95° W of nearly continuous heat input at the surface (Fig. 4.8). Extended periods (weeks+) of net surface heat loss almost exclusively occur when the ITCZ is north of the equator (May through mid-October), and, in particular, when it spans 10° N, 95° W at its most northern extent from about mid-August to mid-October. The net surface heat losses during these times are primarily a result of the interruption of solar heating by cloudcover. In addition to influencing the surface heat fluxes, the ITCZ—specifically the associated heavy rainfall—may have suppressed entrainment heat fluxes by the mechanism previously discussed.

4.5 Results Part II: The Role of Entrainment over 2001

Because of strong solar heating and comparatively small latent, longwave and sensible heat losses within the EPWP, the divergence of the surface and penetrative heat fluxes $[Q - Q_{sw}(-h)]$ would, acting alone, warm the mixed layer by about 23 °C over 2001 (Fig. 4.9). As indicated by Figure 4.8, this strong solar heating is relatively consistent from year-to-year in the EPWP. Since interannual variability of T_a (and SST) is near zero, this large input of heat must be offset by turbulent entrainment and horizontal advection, with these latter terms necessarily cooling the mixed layer by $\sim$23°C over 2001. Here an investigation of the role of entrainment heat flux in the mixed layer temperature budget over 2001 suggests that it plays a significant if not a dominant part in offsetting the net warming from $Q - Q_{sw}(-h)$. The analysis presented here primarily focuses on three mixed layer cooling events that span less than 20% of 2001 but account for roughly half of the $\sim$23°C of net annual cooling expected from both advection and entrainment and, thus, are events that are important to the seasonal and annual budgets. There is strong evidence that elevated entrainment was a primary cause of two of the cooling events, and while the remaining cooling event appears to have been due largely to advection, the findings suggest that entrainment fluxes contributed significantly

Table 4.1: Net mixed layer ΔT_a and time-mean heat fluxes over the EPIC timeseries.

budget terms	ΔT_a (°C)	mean heat flux (W m^{-2})
observed (storage)	-0.70	-48.0
$Q - Q_{sw}(-h)$	-0.65 [-0.81, -0.48]	42.6 [31.1, 54.1]
Q	-0.48 [-0.63, -0.34]	31.3 [21.3, 31.3]
$Q_{sw}(-h)$	-0.17 [-0.15 ,-0.19]	-11.4 [-12.9, -10.9]
entrainment, J_q^e	-0.25 [-0.50, -0.12]	-16 [-32, -8]
$\mathbf{u}_a \cdot \nabla T_a$	0.42 [-0.02, 0.87]	30.7 [-0.5, 62]
inferred storage	-0.47 [-1.3, 0.3]	-32 [-91, 18]
inferred total advection	0.20 [-0.09 0.61]	13 [-6.5, 41.4]

Net mixed layer temperature changes (ΔT_a) and time-mean fluxes are calculated from 1453 on 9/13 to 0408 on 10/01. Fluxes for the storage terms represent the mean time rate of change. Lower and upper bounds based on estimated errors of turbulent fluxes (Peters et al., 1988; Moum et al., 1995), air-sea flux bulk formulae (Fairall et al., 1996), and penetrative solar radiation (Ohlmann, 2003) are shown in brackets. Positive (negative) values of vertical fluxes indicate an upward (downward) flux of heat.

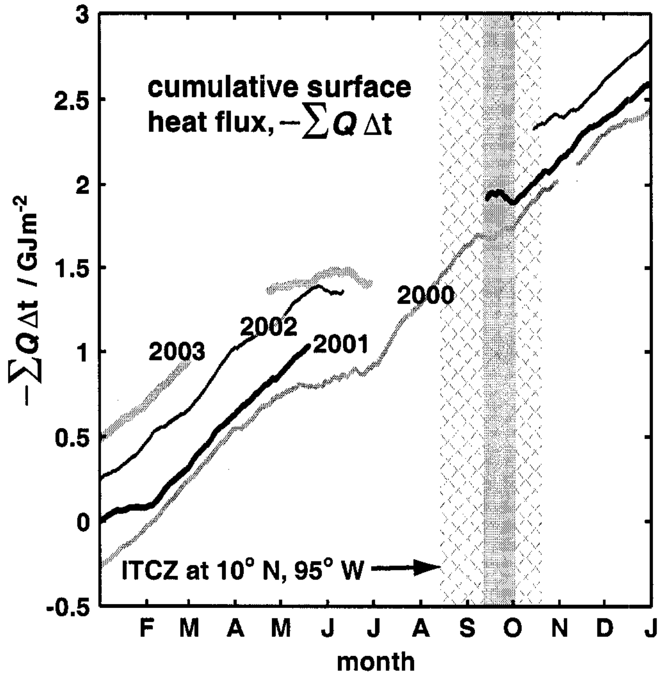

Figure 4.8: Cumulative annual surface heat flux ($-\Sigma Q \Delta t$) from the 10° N, 95° W TAO buoy with data from 1999-2003 showing that the net surface heat loss over the 2001 EPIC timeseries (heavy, black line w/in gray shading) was a deviation from the typical conditions of strong surface heating. Data from 2000 also show surface heat losses on timescales of weeks during the period that the ITCZ spans 10° N, 95° W (cross-hatched fill), suggesting that extended periods of net surface heat loss are a characteristic of the mixed layer temperature budget within the ITCZ. Periods of weaker surface warming and sustained net surface heat losses almost exclusively occur when the ITCZ is north of the equator (May–mid-October). For clarity the plots from each year are started 0.5 GJ m^{-2} apart, with linear interpolation between data gaps using the mean Q over 2000 (-80 W m^{-2}).

to cooling over this period. Results indicate that the decrease in mixed layer depth, h, prior to and during these cooling episodes strongly amplifies entrainment driven by wind-stress and modulated by the dynamic stability conditions at h, $Ri^m(-h)$. Additionally, it appears that the exceptionally-shallow mixed layer depth over two of these periods may have allowed turbulence from breaking surface waves to significantly contribute to turbulent entrainment.

Additionally, since the expected change in T_a due to entrainment is inversely proportional to h (Eqn.. 4.2), the shallower mixed layer also amplifies the effect of the entrainment fluxes on T_a, and, therefore, SST. Thus, a disproportionately large fraction of the mixed layer cooling due to entrainment occurs when the mixed layer is exceptionally shallow. Consistent with the findings of Kessler (2002), QuikSCAT wind stress data indicate that the shallow mixed layer and thermocline during two of the three cooling episodes was likely influenced by sustained periods of upwelling-favorable winds.

4.5.1 Observations and Budget Inferences

Upper-ocean temperature data from the 10 ° N, 95° W TAO buoy shows three large, rapid drops in T_a over 2001 (>1.5°C in less than 3 weeks) with one in early February, one in August and the last in mid-October to mid-November (Fig. 4.10c). These cooling episodes are referred to as CE1, CE2 and CE3 respectively. The rapid, large decrease in T_a at the beginning of the three cooling periods occurred while the mixed layer was shoaling, or h was decreasing (Fig. 4.10 c, d). For CE1 this change in h was abrupt and large (~40 m in less than a week), but for CE2 and CE3 the change was much more gradual with h decreasing by 10–17 m over a period of 2–3 weeks. For CE2 and CE3 the end of the cooling was marked by an equally-rapid increase in T_a by >1°C and coincident mixed layer deepening.

With the EPIC timeseries budget closure as basis, the combined role of entrainment and advection (terms 2+3+4 of Eqn. 4.2) is inferred as a residual, or the difference of observed ΔT and that expected from $Q - Q_{sw}(-h)$ (term 1–term 5) (Fig. 4.11c). Results show a net addition of heat from $Q - Q_{sw}(-h)$ over CE1 and CE3 that alone would have warmed the mixed layer by approximately 1.4°C and 2.7°C respectively (Table 4.2). In order to produce the observed drops in T_a over these

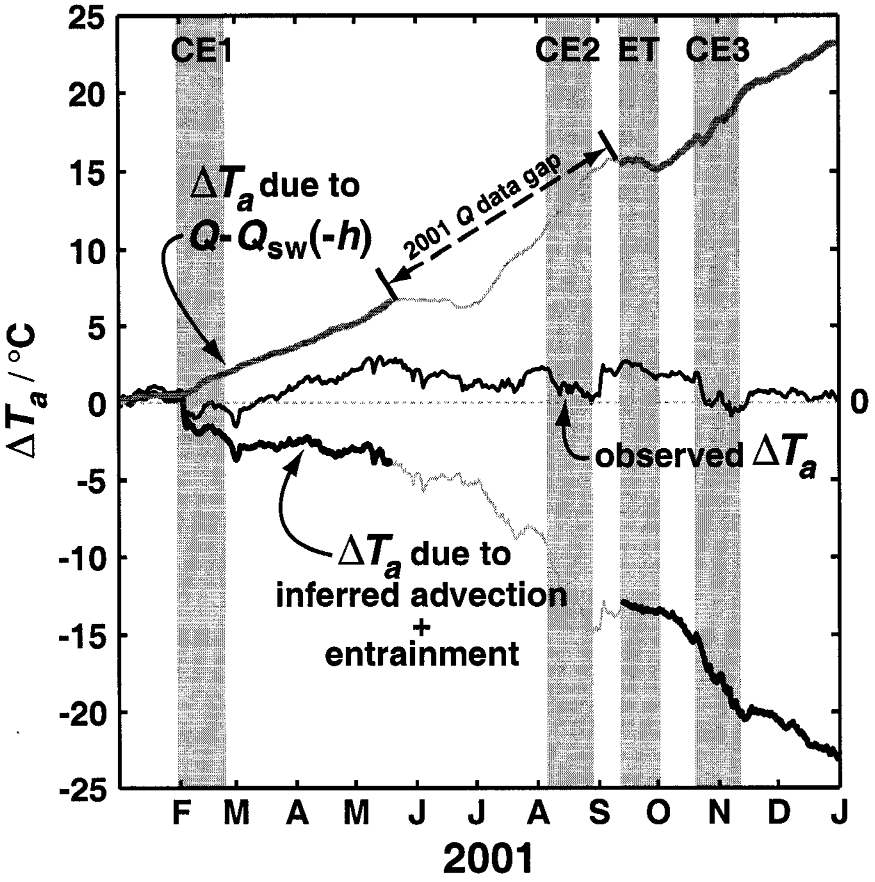

Figure 4.9: Observed changes in T_a over 2001 (thin black) compared to ΔT_a expected from $Q - Q_{sw}(-h)$ (thick gray) and advection + J_q^e inferred as a residual from the T_a budget (thick black). The net ΔT_a over 2001 due to advection + J_q^e is necessarily large to offset the strong, nearly continuous warming from $Q - Q_{sw}(-h)$ of ~ 23°C over a year. As seen in Fig. 4.8, this large solar heating is relatively consistent from year to year within the EPWP. Changes over data gaps (thin gray) are estimated with the mean timeseries of Q over the gap period using data from 2000, 2002 and 2003. Three cooling episodes (CE1, CE2, and CE3) selected for detailed analysis and quantitative comparison with the EPIC timeseries are indicated with gray shading.

Table 4.2: Comparison of atmospheric forcing, mixed layer properties, entrainment model terms and temperature budget terms at 10°N, 95°W over five periods of 2001.

	Period				
	ET	CE1	CE2	CE3	all of 2001
time interval	**9/12–10/2**	1/31–2/24	8/6–8/29	10/20–11/12	1/1–12/31
	Atmospheric Forcing & Mixed Layer Properties				
τ [Pa]	**0.042**	0.074 (1.7)	0.034 (0.8)	0.037 (0.9)	0.042 (1.0)
$J_b(0)$ [10^{-8} W kg^{-1}]	**−2.9**	−5.4 (4.8)	—	−4.1 (1.4)	−4.6 (1.6)
ΔT [°C]	**1.4**	1.1(0.8)	1.5(1.1)	1.8 (1.3)	1.3(0.9)
h [m]	**25**	37	11	8	25
$\frac{\partial T}{\partial z}$ at h [°C m^{-1}]	**0.27**	0.10 (0.4)	0.66 (2.4)	1.0 (3.8)	0.32 (1.2)
8-m N^2 at h [10^{-3} s^{-2}]	**1.1**	0.38 (0.3)	2.4 (2.1)	3.2 (2.8)	1.1 (1.0)
8-m Sh^2 at h [10^{-3} s^{-2}]	**0.26**	0.16 (0.6)	0.71 (2.8)	1.8 (7.1)	0.39 (1.5)
inertial KE [J m^{-2}]	**345**	145 (0.4)	430 (1.2)	698 (2.0)	291 (0.8)
w_E [10^{-6} m s^{-1}]	**−6.4**	−6.2	3.9	8.9	0.8
$10H_s/h$	**0.27**	0.41	0.54	0.87	0.36
	Entrainment Model Terms				
$Ri^{-0.87}$	**0.13**	0.27 (2.1)	0.16 (1.3)	0.25 (1.9)	0.17 (1.3)
J_b^* [10^{-7} W kg^{-1}]	**2.5**	3.4 (1.3)	3.9 (1.5)†	6.8 (2.7)	2.7 (1.1)
u_*^3/h [10^{-8} W kg^{-1}]	**0.9**	1.7 (1.9)	1.7 (1.9)	3.0 (3.3)	1.2 (1.4)
	ΔT_a & Mean Heat Fluxes				
ΔT_a [°C]					
observed	**−0.75**	−1.01	−1.69	−1.83	0.32
due to $Q - Q_{sw}(-h)$	**−0.65**	1.4	—	2.7	23† [18, 27]
due to $Q_{sw}(-h)$	**−0.17**	−0.17	—	−3.6	−9.6† [-9.0, -10.2]
due to inferred advection + J_q^e	**−0.06**	−2.4	—	−4.6	−23† [-18, -27]
due to modeled J_q^e ($\tilde{J}_q^e$)	**−0.25**	−1.2	−1.6†	−7.1	−19.4† [-9.7, -39]
heat flux [W m^{-2}]					
storage	**−48**	−82	−41	−31	9
$Q - Q_{sw}(-h)$	**43**	−85	—	−41	−60† [-48, -72]
$Q_{sw}(-h)$	**−11**	−10	—	−54	−18† [-17.5 -19.5]
inferred advection + J_q^e	**−3**	−166	—	−72	−49† [-37, -61]
modeled J_q^e ($\tilde{J}_q^e$)	**−16**	−67	−37	−107	−36† [-18, -72]

Values are based on data from the 10° N, 95° W TAO buoy, with inertial KE, Sh^2, and $Ri^{-0.87}$ estimated by forcing the Pollard and Millard (1970) slab model with buoy-measured wind stress. Also, values are time-averages except for ΔT_a, which is the net change of T_a over the period. Numbers in parentheses for CE1, CE2, CE3 and all of 2001 are the factor difference with the EPIC timeseries values in boldface. Positive (negative) values of vertical fluxes indicate an upward (downward) flux, and † indicates that values are estimated by using a mean timeseries of Q with data from 2000, 2002 and 2003 replacing the 115-day data gap over 2001, or for model results a mean surface buoyancy flux value of -6.0×10^{-8} W kg^{-1}. Values within brackets are estimates of upper and lower uncertainty bounds.

periods, entrainment and advection must have acted to cool the mixed layer by a total of -2.4 °C and -4.6°C respectively (or average fluxes of $\sim$-166 and -72 W m^{-2}). Although a data gap in Q precludes the inference of the combined advective and entrainment terms over CE2, $\Delta T_a/\Delta t$ (term 1) over this period implies that all other budget terms must act to cool the mixed layer by -1.7 ° over 22 days, or at an average rate of -41 W m^{-2}. The observation that daily-averaged SST is almost always greater than T_a over this period (Fig. 4.3) suggests that there was likely a net input of heat from Q. Thus, the contribution from advection and entrainment over CE2 is at the very least 1.7 °C of cooling, or if we assume that Q over CE2 is similar to that observed over CE3, then entrainment and advection together could have had the effect of cooling T_a by more than 4°C over CE2. The total expected cooling by entrainment and advection over all three periods, then, could have accounted for roughly 50% of the necessary 23 °C of cooling over 2001, with the three periods only spanning 18% of the year.

Advective warming

If we assume that entrainment heat fluxes are always negative, which is equivalent to assuming that $\frac{\partial T}{\partial z}(-h)$ is always positive, then all values of the budget-inferred combined advective+entrainment heat flux that are positive are a consequence of positive (warming) advective fluxes over-riding negative entrainment fluxes. It is important to note that these values only represent a lower estimate of the warming from advection since weaker entrainment cooling may also be present. Interpreting the observations in this way leads to the conclusion that advection caused the smaller but significant mixed layer warming events that were embedded within the larger CE1 and CE3 cooling events (Fig. 4.11). Although advection may also have been important to minor warming events over CE2, the lack of surface heat fluxes does not permit the distinction between surface and advective warming. Results also show that the rapid mixed layer warming following CE3 (Fig. 4.11) was due to horizontal advection and that advective warming was also the cause for the 2°C rise in T_a following CE2 (in early September) since warming was much too rapid to result from surface heating alone. As apparent from Figures 4.10d and 4.11, most advective warming events were accompanied by a *decrease* in mixed layer salinity which indicates the advection of a mixed layer density front past the TAO buoy location (Fig. 4.10d).

The influence of mixed layer depth on T_a-changes

The strong influence of the variability of the mixed layer depth on T_a changes is apparent from a comparison of the magnitude of the budget-inferred heat flux to the expected changes in T_a from this flux over periods CE1 and CE3. Over the two cooling episodes both the inferred flux (the combined advective and entrainment terms) and resultant ΔT_a show rapid decreases coincident with the onset of the cooling. However, because the expected change in T_a for a given flux is inversely proportional to h [i.e., for ΔT_a expected from entrainment, $\partial T_a/\partial t = -J_q^e/(\rho c_p h)$], the significantly shallower mixed layer over CE3 results in a change in T_a that is six times that over CE1 even though the budget-inferred fluxes over CE3 are less than half of those over CE1 (Tab. 4.2).

An additional consequence of a shallower mixed layer is to increase the downward penetrative heat flux at the mixed layer base. Using the observed shortwave fluxes (Q_{sw}) and the Ohlmann (2003) model for penetrative radiation, the decrease in h from 25 to 8 m before and during CE3 has the effect of increasing the penetrative flux, $Q_{sw}(-h)$, from -15 to -54 W m^{-2}, or a change of -39 W m^{-2} that acts to cool the mixed layer (or, more precisely, to decrease the net heat flux from Q_{sw} into the mixed layer) (Table 4.2). However, the increased sensitivity of T_a to imbalances of the vertical flux terms as a result of the decrease in h nearly offsets this effect, with the increase in magnitude of $Q_{sw}(-h)$ acting to reduce the heating from $Q - Q_{sw}(-h)$ by –2.4°C over CE3 and the decrease in h acting to magnify the influence of $Q - Q_{sw}(-h)$ on ΔT_a by +2.3°C.

4.5.2 Entrainment model results

Entrainment heat flux estimates from the empirical entrainment model presented in Chapter 3 indicate that among the largest entrainment fluxes over 2001 occurred during the three cooling events and that these large entrainment fluxes were a consequence of the shallower mixed layer over these periods (Fig. 4.11). Model-estimates of entrainment flux magnitude, which are supported by a close agreement with budget-inferred fluxes (advection + entrainment), suggest that entrainment was a primary cause of CE2 and CE3 and contributed to roughly half of the necessary 2.4 °C of cooling

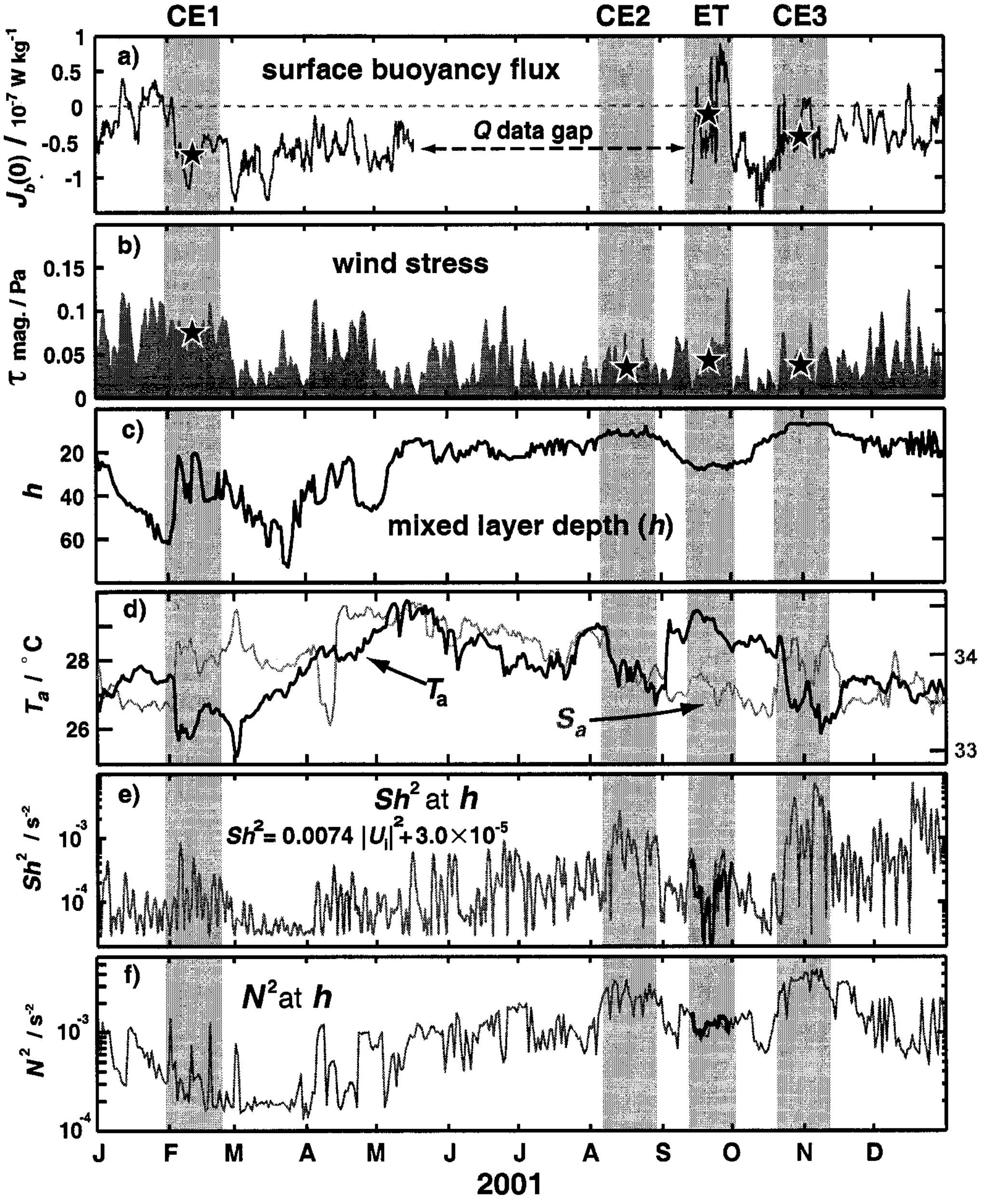

Figure 4.10: Timeseries of select variables at 10 ° N 95° W over 2001. a) 2-day boxcar-averaged $J_b(0)$, b) surface wind-stress, τ c) mixed layer depth, h; d) T_a (black) and depth-averaged mixed layer salinity, S_a (gray); e) Shear-squared at h estimated from the Pollard and Millard (1970) slab model (gray) with measured 8-m $Sh^2(-h)$ over the EPIC timeseries (black), and f) 8-meter N^2 at h estimated from TAO buoy data (gray) and from EPIC timeseries MMP data (black). The stars in plots a) and b) show mean values over the three cooling episodes (CE1, CE2, and CE3) and the EPIC timeseries (ET). Values h, T_a and S_a are daily-averages, with all other variables boxcar-averaged over 2 days (with either hourly or 10-min original resolution).

over CE1. In addition to supporting the modeled entrainment fluxes, the comparison of the budget-inferred advective+entrainment terms to modeled entrainment also suggests that model results may at times significantly underestimate the actual entrainment fluxes. One potential reason for this may be the absence of the influence of breaking surface waves in the entrainment model, which a coarse estimate suggests could increase the entrainment fluxes at times by 50%.

A comparison of the mixed layer depth to the modeled entrainment fluxes over 2001 (Fig. 4.11) shows that significantly-enhanced periods of entrainment are coincident with periods of exceptionally shallow mixed layer depth (CE2 and CE3) or when the mixed layer rapidly shoaled from deeper than average values (CE1). Somewhat counter to expectations, surface forcing in the form of wind stress and destabilizing surface buoyancy flux was not invariably stronger during the periods of elevated entrainment when compared to times of weaker entrainment fluxes such as the EPIC timeseries (Fig. 4.10a, b, Tab. 4.2). This is a consequence of the inverse h-dependence of the model terms for wind stress mixing, u_*^3/h, and the influence of the dynamic stability conditions at h on entrainment, or $Ri^m(-h)$ ($m = -0.87$). Although the inverse h-dependence of the former is immediately apparent, that for $Ri^m(-h)$ is not and will therefore be discussed further below.

The influence of direct wind stress

At the beginning of CE2 and CE3 the model wind stress term, u_*^3/h, rapidly increased by a factor of 2–5 in <3 days—coincident with the large initial drops in T_a (Figs. 4.12a and 4.13). The timing of the increase in the wind stress entrainment measure is primarily due to a rapid elevation in τ (where $\tau = \rho u_*^2$) from relatively weak stresses of <0.025 Pa (wind speed of ~4 m s^{-1}) to moderate stresses of 0.05–0.075 Pa (~6–7 m s^{-1}) (Fig. 4.10b, d). However, the exceptionally shallow h at the onset of the stronger stresses (13 m and 11 m respectively) greatly amplifies the impact of the τ increase on u_*^3/h. Thus, although wind stress itself was weaker during CE2 and CE3 than over the EPIC timeseries by 20% and 10% respectively, because of the significantly shallower mixed layer during these periods, u_*^3/h was 1.9 (CE2) and 3.3 (CE3) times the EPIC timeseries levels (Tab. 4.2). The influence of the shallower mixed layer depth over CE2 and CE3 is readily apparent in a comparison of u_*^3/h to $u_*^3/\overline{h}$, where $\overline{h}$ is the annual mean h (Fig. 4.12a). Dark shaded areas in Figure 4.12a

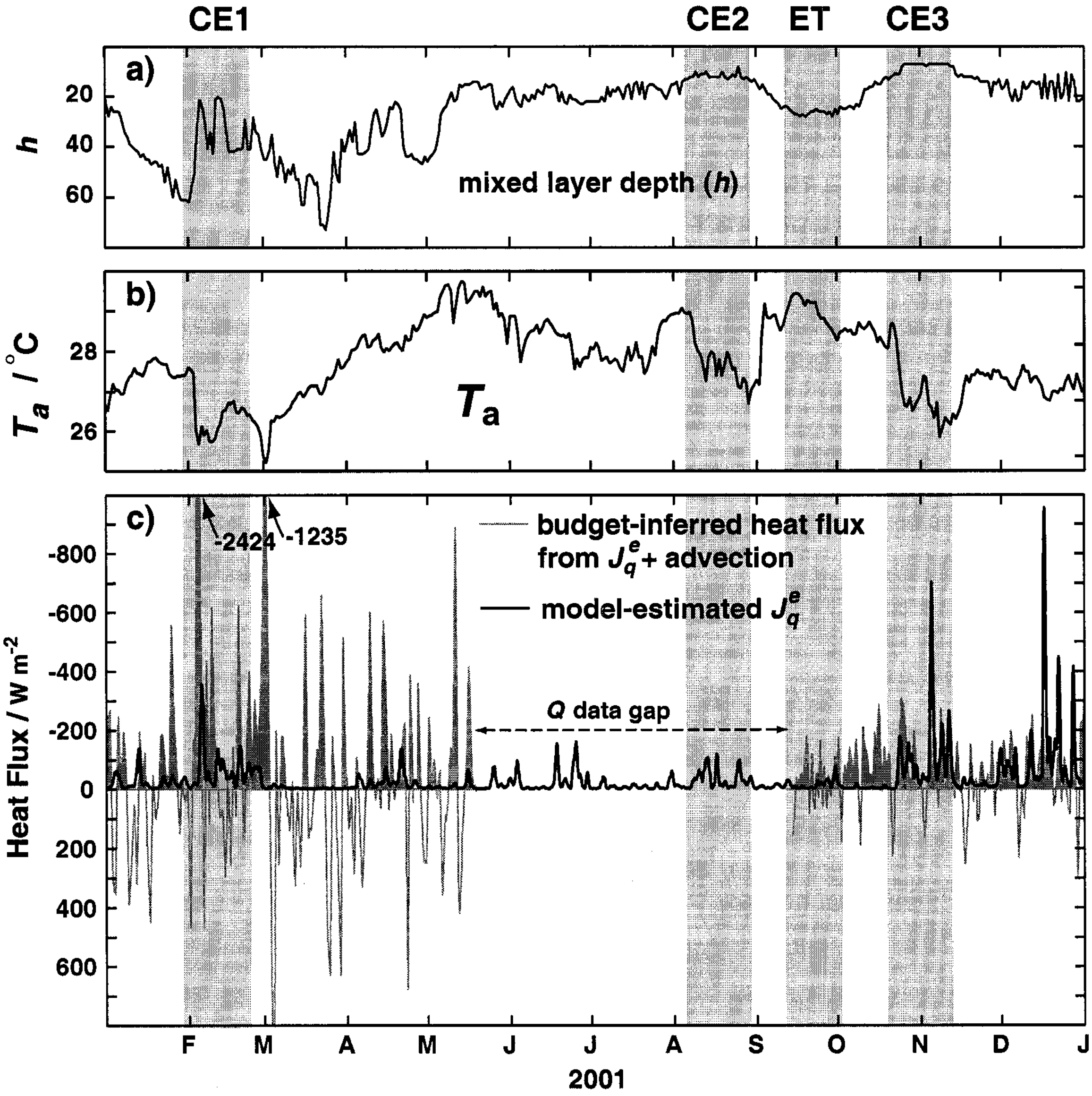

Figure 4.11: Entrainment heat flux variability over 2001 estimated with the empirical entrainment model presented in Chapter 3 suggests J_q^e is amplified when the mixed layer depth, h, shoals, contributing to mixed layer cooling episodes (CE1, CE2 and CE3). a) T_a. b) h. c) Model entrainment heat flux, $\tilde{J}_q^e$ (black) and the budget-inferred heat flux from the combined entrainment and advective terms of Equation 4.2 (terms 2+3+4 inferred from term 2 −term 5). Flux values have been boxcar-averaged over a day.

indicate an increase in the wind stress term that is a consequence of the shoaling of h to values less than the annual mean. Although the average mixed layer depth over the first cooling episode, CE1, was $\sim$10 m deeper than over the EPIC timeseries, as a result of the steady, relatively large wind stress over this period u_*^3/h was nearly twice the average over the EPIC timeseries.

The influence of Ri

Also somewhat contrary to expectations for weaker wind stress over CE2 and CE3 than the EPIC timeseries, average values of the entrainment model term accounting for the dynamic stability conditions at h, or specifically Ri^m where $m = -0.87$, was elevated 1.3 and 1.9 times above the EPIC timeseries respectively (Fig. 4.12b). This was principally due to elevated finescale inertial shear as estimated from the Pollard and Millard (1970) slab model (as described in Section 4.3) (Fig. 4.10e, Table 4.2) which is a consequence of the shallower mixed layer and, thus, greater mixed layer current speeds and depth-integrated kinetic energy for a given wind stress. With mixed layer velocity magnitude as described by the Pollard and Millard (1970) model having a h^{-1} functional dependence, the empirical form used here to estimate shear-squared at h where $Sh^2 \propto |U_i|^2$ suggests that shear-squared would have a h^{-2} functional dependence. Although insufficient data do not permit a test of this specific functional relationship, with $|U|$ shown to be inversely proportional to h we would expect some inverse h-dependence for shear-squared.

Over much of 2001 the 8-m buoyancy frequency at h varied similarly to shear at timescales of roughly a week+, but varied over a range that was about a decade less than that of shear (Fig. 4.10e, f). With the magnitude of dynamically-stable shear limited by the existing stratification, the significant correlation of the largely-independent estimates of N^2 and Sh^2 at h ($r^2 = 0.3$ over 2001) lends additional credence to the estimates of Sh^2 and, thus, Ri. The increase in stratification at h over CE2 and CE3 is associated with positive vertical displacements of isopycnals (and isotherms) within the main thermocline. In general, TAO buoy data indicate that stratification at h is greater when thermocline isotherms are displaced upwards from a mean state (e.g. CE2 and CE3) and weaker when isotherms are displaced downwards from a mean state (the EPIC timeseries and much of March) (Fig. 4.2). With the mixed layer depth coincident with the top of the thermocline over most of 2001, N^2 is roughly inversely-proportional to h. Observations presented later in this Chapter and the findings of Kessler (2002) suggest that the changes of $N^2(-h)$ may be largely due to local Ekman pumping (or specifically the rate of straining, $\partial w/\partial z$ Sun and Kunze (1999)), although the propagation of Rossby waves and the advection of mesoscale eddies are also likely important factors in changing $N^2(-h)$.

Despite the stronger winds over CE1, the greater mixed layer depth and less variable winds over this period resulted in weaker inertial motions, and thus weaker estimated finescale Sh^2 than during the EPIC timeseries and other two cooling events. Shear-squared over CE1, however, was elevated above prior and subsequent levels in January and March. In contrast to CE2 and CE3, N^2 at h was near its lowest 2001 level over CE1 at roughly 2×10^{-4} s^{-2} and shows a significant decrease in stratification from prior levels. Thus, the increase in Sh^2 and decrease in N^2 over this period also resulted in a significant increase in the average Ri^m over CE1 to more than 2 times the EPIC timeseries levels and 2–6 times previous levels (Fig. 4.12b).

The influence of surface buoyancy fluxes

The expectation that destabilizing surface buoyancy fluxes, $J_b(0) > 0$, would have a much weaker influence on entrainment generation than direct wind stress is supported by both the empirically-derived entrainment model constants (see Chapter 3) and by observations showing that $u_*^3/(\kappa h)$ is roughly 2–7 times more effective than $J_b(0) > 0$ at producing SBL turbulence (Oakey and Elliott, 1982; Lombardo and Gregg, 1989). Additionally, the observation that the two-day averaged surface buoyancy flux is dominantly negative, or stabilizing (with one of the exceptions the EPIC timeseries) (Fig. 4.10a), also suggests that destabilizing surface buoyancy fluxes likely had a relatively small role in entrainment generation over 2001.

The role of stabilizing surface buoyancy fluxes, $J_b(0) < 0$, in suppressing entrainment by preventing SBL turbulence from reaching the mixed layer base appears to be significant, however. As discussed in Chapter 3, the entrainment model employs a term that allows indirect entrainment when the mixed layer is weakly stratified by stabilizing surface buoyancy fluxes and surface-forced turbulence is unable to penetrate to h. Indirect entrainment is roughly half of direct entrainment val-

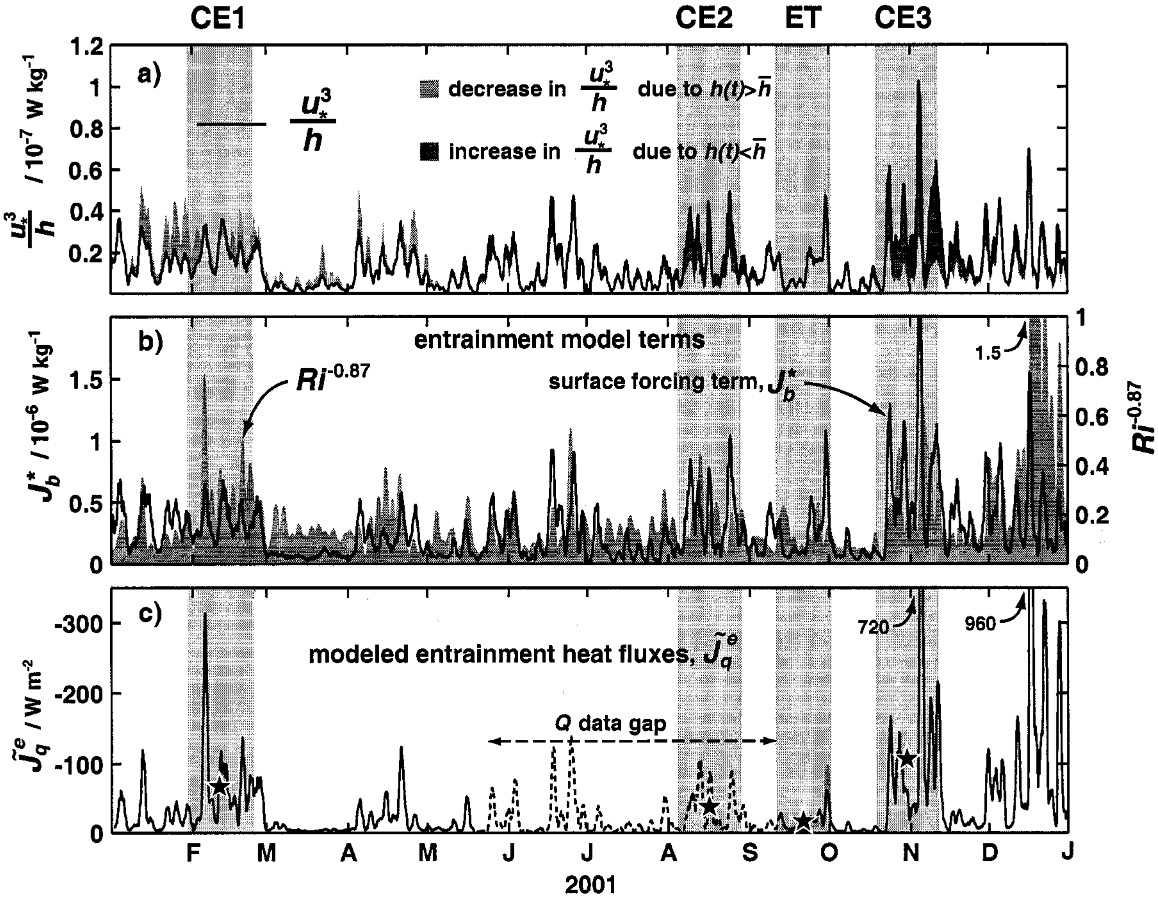

Figure 4.12: Entrainment model results for 2001. a) plot of the wind stress term $[u_*^3/(\kappa h)]$ included in the general surface forcing term, J_b^*, showing that the variability of the modeled entrainment heat fluxes $(\tilde{J}_q^e)$ is largely due to direct wind stress. The influence of the mixed layer depth, h, on this term is shown with gray shading. Light gray shading indicates values of $u_*^3/(\kappa h)$ that are decreased because $h(t)$ is greater than the 2001 mean of 25.5 m $(\bar{h})$, and dark gray shading indicates an increase in $u_*^3/(\kappa h)$ because $h(t) < \bar{h}$. b) The model surface forcing term, J_b^*, and finescale gradient Richardson number dependence, $Ri^{-0.87}$. c) Modeled entrainment heat fluxes, $\tilde{J}_q^e$. A dashed line is used to indicate that $J_b(0)$ is estimated using a mean value over this period derived from data from 2000, 2003 and 2003 (-6×10^{-8} W kg^{-1}) because of a data gap in Q. Stars show mean $\tilde{J}_q^e$ values over the four periods (see Table 4.2.

ues with all else equal. Model results indicate that entrainment was driven indirectly—or the SBL depth was less than h—over roughly 50% of the time when $J_b(0)$ data were available over 2001 (see Fig. 4.10a), suggesting that the region's strong stabilizing surface buoyancy fluxes significantly reduced entrainment fluxes.

Mixed layer cooling from entrainment

Period-averaged values of modeled entrainment heat flux over the three cooling episodes indicate that entrainment may have been predominantly responsible for the cooling observed over CE2 and CE3 and may have significantly added to cooling over CE3 that was principally caused by advection. Over CE2 and CE3 period-averaged modeled entrainment heat fluxes are estimated at roughly -37 and -107 W m^{-2}, respectively, which would account for 95% and 150% of the cooling necessary from both the advective and entrainment terms to result in the observed drops in T_a over these periods. Over CE1 the period-averaged entrainment is estimated at -67 W m $^{-2}$, which would result in about half of the budget-inferred expected drop of -2.4 °C from advection and entrainment.

A relatively close comparison of the modeled entrainment fluxes to negative values of the budget-inferred combined advection + entrainment flux lends significant support to the model results (Figs. 4.11 and 4.13). Specifically, despite the influence of advection on the budget-inferred flux, over CE2 and CE3 modeled entrainment ($\tilde{J}_q^e$) shows a significant correlation at near-zero lag with negative values of the latter, with a number of peaks in the budget-inferred flux coincident with peaks in the modeled heat flux. The increase in modeled entrainment at the beginning of CE3 is in particularly good agreement with the inferred flux needed to result in the initial large drop in T_a over this period. For both CE2 and CE3 there is also a strong correspondence between times of weak modeled entrainment and *positive* values of inferred budget fluxes. Assuming that entrainment is largely uncorrelated with advection and $Q - Q_{sw}(-h)$—a presumption supported by the EPIC timeseries budget—the above findings strongly suggest that entrainment was responsible for much of the variability of the negative values of the budget-inferred advective+entrainment flux over CE2 and CE3, and, thus, had a significant role in the large drop in T_a over these periods.

The observation that budget-inferred fluxes often reverse, becoming positive, when modeled entrainment is weak, then, suggests that for CE2 (when Q data were not available) the cooling from entrainment is possibly being offset by advection and/or surface heating, and for CE3, in addition to the relatively steady warming from $Q - Q_{sw}(-h)$, advection is also at times acting to warm the mixed layer (Tab. 4.2, Fig 4.9) and may at times be offsetting entrainment cooling. This is a possible explanation why the model-estimated entrainment over CE3 is 150% (or in excess) of the combined advective+entrainment flux needed to result in the net drop in T_a by $-1.8°$.

As shown in Figure 4.13h & i, at times there is a larger correlation between the budget-inferred heat fluxes and the entrainment model wind stress term, $u_*^3/(\kappa h)$, than between inferred fluxes and modeled entrainment. This suggests that error in the timing and magnitude of the model term Ri^m may be introducing significant errors in the modeled entrainment flux estimates. If this is the case, then one might expect that the correlation between the actual entrainment fluxes and the negative values of the budget-inferred combined advective+entrainment fluxes may be even larger than that between the latter and $u_*^3/(\kappa h)$—further suggesting that entrainment resulted in the mixed layer cooling over CE2 and CE3.

Mixed layer cooling from horizontal advection

Advective cooling In contrast to the CE2 and CE3 observations, the 1.8 °C plunge in T_a at the beginning of CE1 *preceeded* significant increases in both wind stress and modeled entrainment heat flux by about a day—despite the rapid decrease in h that was coincident with the T_a drop (Fig. 4.13 a, d, g). Consequently, the very large peak in the combined advective and entrainment flux ($\sim$-2400 W m^2) that is associated with the rapid cooling occurs about 1.5 days before a much smaller peak in modeled entrainment of -300 W m^{-2}. This observation and the weak correlation between modeled entrainment and the budget-inferred advective+entrainment fluxes over CE1 indicates that the initial drop in T_a and subsequent cooling over CE1 was largely due to horizontal advection. Supporting this conclusion, horizontal gradients of TRMM satellite SST at 10 °N, 95°W that were computed over a 2° span in latitude and longitude show a very large shift in the meridional gradient that is coincident with the onset of the initial cooling.

Despite the apparent dominant role of advection over CE1, as previously discussed it appears that the decrease in h at the beginning of CE1 was largely responsible for the elevated entrainment fluxes over CE1. The cooling influence of these fluxes, however, was likely masked by very large advective fluxes.

If we believe the values of the modeled entrainment fluxes despite their large uncertainty, then the budget-inferred advective+entrainment flux implies that advective cooling was also important to the large initial drop in T_a at the beginning of CE3 and may have been the primary reason for the initial drop in T_a over CE2 (Fig. 4.13). The apparent correlation between advective and entrainment fluxes (as at the beginning of CE3) can heuristically be explained by considering a finite spatial scale of the cooling due to entrainment. With no reason to expect that entrainment cooling is largest at the TAO buoy location, then one would expect that if mixed layer currents are significant there will be coincident advective changes in T_a. This conclusion is further supported by the fact that both entrainment and mixed layer velocity (and thus advective fluxes) are a function of the wind stress.

4.5.3 Potential underestimates of modeled entrainment

A close comparison of the model-predicted entrainment fluxes and the budget-inferred advective+entrainment flux (Fig. 4.11) indicates that despite the significant correlation of model results with negative values of the latter, the entrainment estimates are almost always smaller (less negative) than the budget-inferred negative fluxes. The few exceptions to this are during CE3 and over much of December 2001. The difference in magnitude between predicted entrainment fluxes and budget-inferred advective+entrainment flux is most apparent over the first five months of 2001, and in particular during April and May. During these times very large peaks in the budget-inferred flux (< -400 W m^{-2}) are coincident with much smaller increases in modeled entrainment. Although there are reasons to expect a correlation between advection and entrainment as was previously discussed, we would not expect that the advective flux would almost always be greater than entrainment and that it would almost always have the same sign. For these reasons it is suspected that the entrainment model may at times significantly underestimate the actual entrainment heat fluxes.

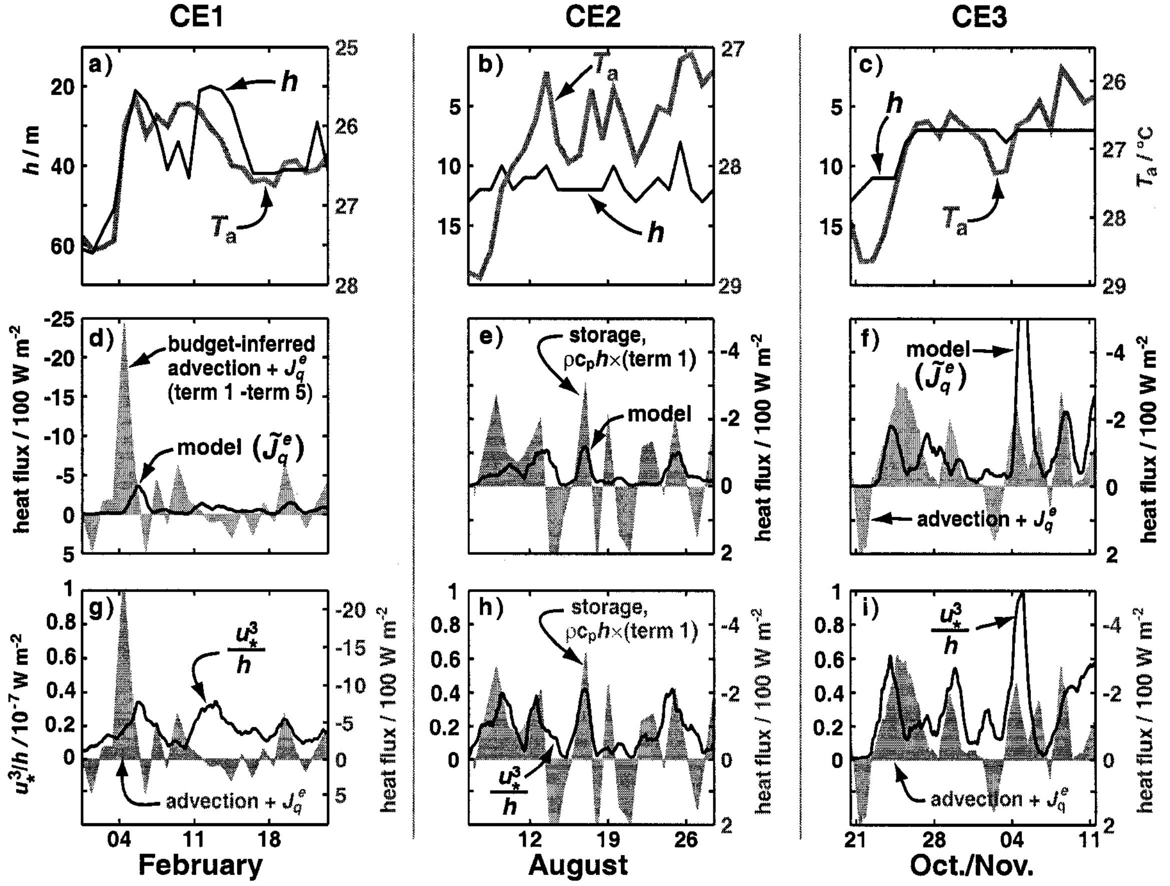

Figure 4.13: a–c) mixed layer depth, h, (black) and T_a (gray with reversed y-axis) over the three cooling events (CE1, CE2, CE3). d–f) comparison of modeled entrainment heat flux, $\tilde{J}_q^e$, (black line) with the budget-inferred combined advective and entrainment heat flux terms (over CE1 & CE3) and the storage flux, $\rho c_p h \Delta T_a/\Delta t$, over CE2 since Q data are not available (gray fill). g–i) comparison of u_*^3/h (black line) with the combined advective and entrainment heat flux terms over CE1 & CE3 or $\rho c_p h \Delta T_a/\Delta t$ over CE2 (gray fill). Significant correlation between budget-inferred heat fluxes and both modeled entrainment and u_*^3/h for CE2 and CE3 suggests entrainment played a dominant role in these cooling events. Note that the axis limits for the heat flux in panels d & g differ from those in e, f, h & i.

The influence of breaking surface waves

One possible explanation for the suspected underestimate of the modeled entrainment heat fluxes is the influence of breaking surface waves on SBL turbulence and entrainment. The empirically-based estimate of the penetration of turbulence from breaking surface waves discussed in Chapter 3 indicates that this mechanism may have significantly contributed to entrainment over both CE2 and CE3. Because of the extremely shallow mixed layer during these cooling episodes, there were extended durations when the estimated depth of turbulence from surface wave-breaking, $10H_s$, (where H_s is the significant wave height) was greater than h, or $10H_s/h > 1$ (Fig. 4.14). It is worth mentioning that although the influence of breaking surface waves is treated here as a binary process (either contributes or does not contribute to entrainment), even if the turbulence from breaking surface waves may not reach h, it will likely contribute to work done to erase mixed layer stratification, and, thus, may enhance the effectiveness of destabilizing surface forcing (wind stress and $J_b(0) > 0$) at generating entrainment. Because of large uncertainty in both the maximum penetration depth of turbulence from wave-breaking and the expected depth-dependence (z^{-2} to z^{-4}), quantitative estimates of entrainment due to this mechanism are only a best-guess and have large uncertainty. However, a rough calculation using the z^{-2} depth dependence and typical values of H_s over CE3 of 1.2 m (or $10H_s/h \approx 1.5$) suggests that at times surface wave-breaking could have elevated entrainment fluxes by $> 50\%$.

4.5.4 *Implications for the annual T_a budget*

The cumulative influence of entrainment as predicted from the entrainment model indicates that it may have been primarily responsible for the net annual $\sim$ 23°C of cooling necessary to offset the strong warming from the surface, or from $Q - Q_{sw}(-h)$ (Fig. 4.15). Although results are subject to considerable uncertainty, they indicate that in addition to the cooling over the three identified cooling events, there was exceptional cooling from entrainment following CE3 until the end of 2001. Much of this, however, appears to have been offset by advective and surface warming to result in a relatively constant mixed layer temperature over late November and December. Both advection and entrainment have their largest influence on mixed layer temperature from about July

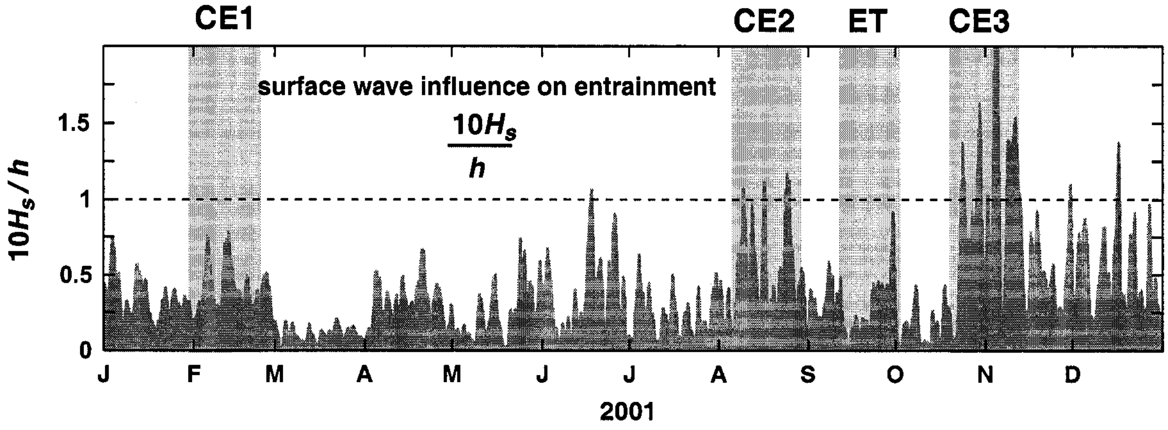

Figure 4.14: a) Plot of $10H_s/h$ where H_s is the significant wave height of surface waves and $10H_s$ indicates the maximum penetration depth of turbulence from breaking surface waves. Values of $10H_s/h > 1$ indicate periods when turbulence from breaking surface waves may penetrate to h and directly contribute to entrainment, suggesting that this mechanism may have significantly contributed to entrainment heat fluxes over CE2 and CE3. Values of $10H_s/h$ have been boxcar-averaged over a day.

to March—when there is typically strong heating from $Q - Q_{sw}(-h)$ but T_a remains relatively constant or even decreases. Over a 3–4 month period beginning in early March, T_a roughly follows changes expected from $Q - Q_{sw}(-h)$, suggesting that entrainment and advection largely offset one another over this period or are both small. The latter case is suggested by the model-predicted estimate of the influence of entrainment on ΔT_a showing that entrainment is likely weak over this period.

In order to provide additional support for these results we investigated the role advection at the same location but over the span of a year from October 2002 until October 2003. This specific time interval was chosen because the measurement of mixed layer velocities from a TAO buoy single-point acoustic current meter (ACM) allowed rough estimates of depth-mean advective fluxes (term 2, Eqn. 4.2). Specifically, the depth-mean advective fluxes are estimated using the ACM mixed layer velocities and T_a gradients estimated from TRMM satellite SST data (see Appendix C). These results, shown in Figure 4.16, support the 2001 findings by indicating that horizontal advection

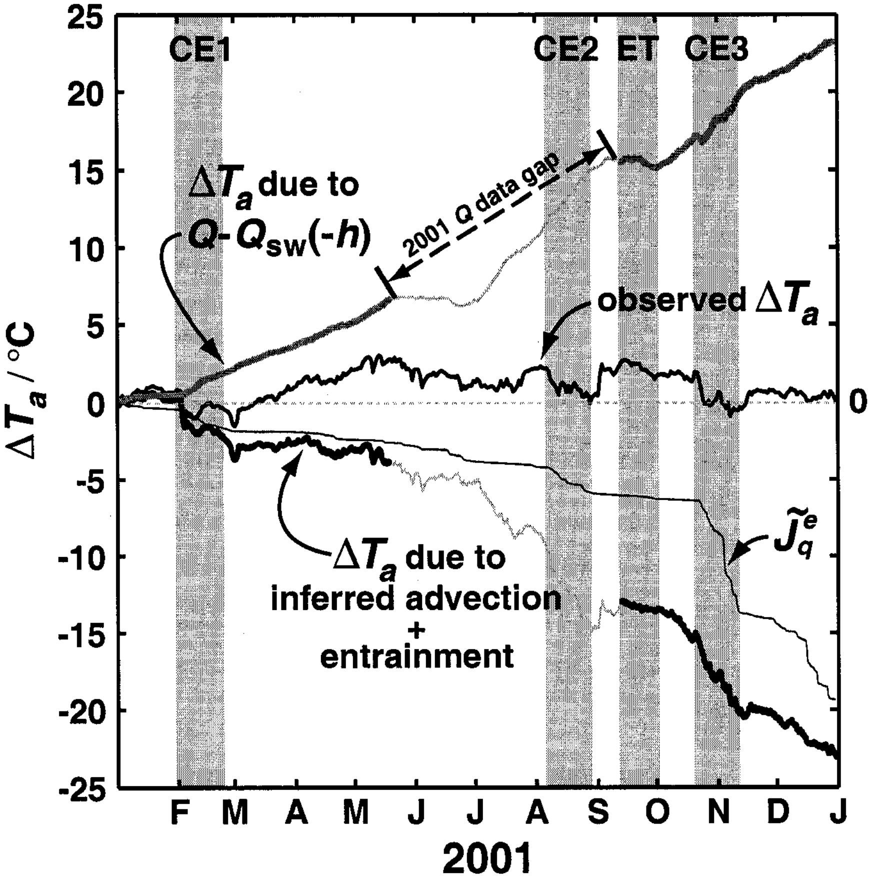

Figure 4.15: Same as Fig. 4.9 but now showing the cumulative contribution of modeled entrainment heat flux, $\tilde{J}_q^e$ (thin black). The similar variability the budget-inferred influence of advection + entrainment to the model results bolsters model credibility, and although uncertainty is large the entrainment model suggests that entrainment is principally responsible for offsetting the net warming from $Q - Q_{sw}(-h)$ over 2001.

may play only a small role in net annual T_a and SST changes—specifically estimated at smaller than $\pm5°$C (see Appendix C for uncertainty estimation). A comparison of ΔT_a associated with the 2001 modeled entrainment fluxes and budget-inferred ΔT_a due to entrainment over the 2002/2003 time span shows a general agreement. A difference in timing of the largest entrainment-induced cooling may stem from differences in the evolution of the mixed layer depth over the two time-frames, with the shallowest h in 2001 during August and October–November while in 2002/2003 the shallowest values of h occur over much of September. Here it is important to point out that large data gaps in wind stress and surface buoyancy fluxes precluded running the entrainment model over the 2002/2003 period and also required estimating Q over the gaps with data from 2000-2002.

4.5.5 The influence of wind stress curl

In agreement with the findings of Kessler (2002), QuikSCAT wind stress data indicate that the mixed layer/thermocline depth—which here has been shown to be important to entrainment—is largely influenced by the regional patterns of wind stress curl. A timeseries of wind stress curl over 2001 computed from QuikSCAT data shows a clear annual cycle of the mixed layer depth that consistent with the expected influence of the wind stress curl field, with the deepest mixed layer/downwelling-favorable winds predominant over the first four months of 2001 and upwelling-favorable winds/a shallow mixed layer from May until about mid-November (Fig. 4.17). Since the calculation of the Ekman pumping velocity, w_{Ek}, does not include the time-dependent Sverdrup solution (propagating Rossby waves), or for that matter the influence of mesoscale eddies on the mixed layer/thermocline depth, these dynamics likely account for much of the variability of h not described by changes in w_{Ek} (e.g. over the EPIC timeseries and CE1). With this in mind, it is worth noting that the two periods of the shallowest mixed layer depth (CE2 and CE3) were coincident with strong, steady, upwelling-favorable winds. In particular, the rapid increase in wind stress curl to the highest levels of 2001 (1.5×10^{-5} m s^{-1}/ $\sim$1.3 m day^{-1}) is coincident with the shoaling of the mixed layer depth prior to and during CE3, suggesting that Ekman pumping may be largely responsible for the observed changes in h over this period, and, thus, the resultant amplification of entrainment fluxes.

Maps of Ekman pumping velocity indicate that because of its central location within the EPWP,

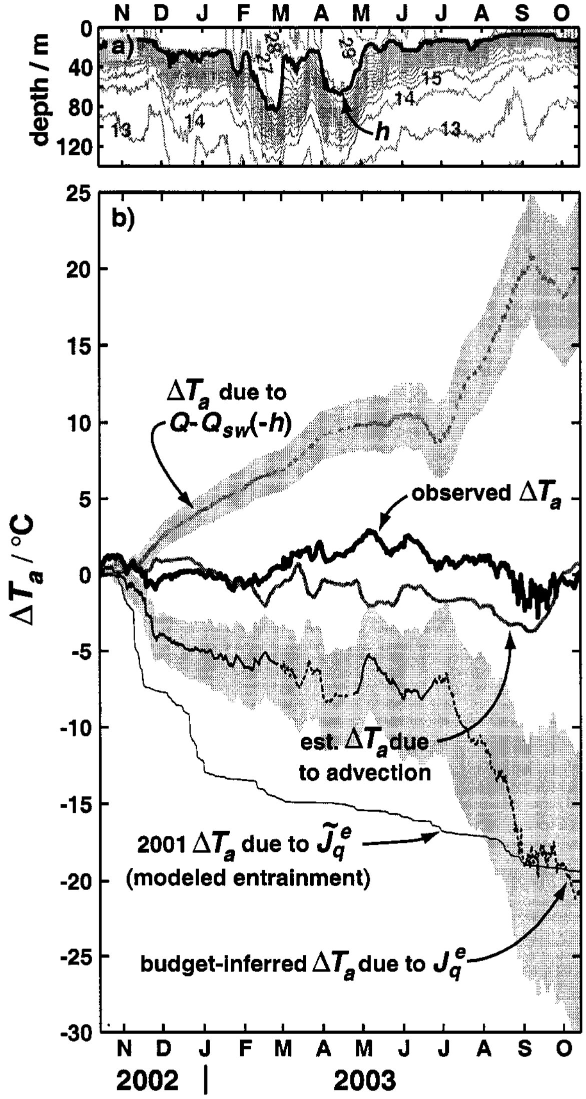

Figure 4.16: a) Upper-ocean temperature contours (1°C intervals) and h spanning Oct. 2002–Oct. 2003. b) A small estimated contribution from horizontal advection to net ΔT_a over a year (thick gray) suggests that predominantly entrainment heat fluxes offset the large net annual input of heat from $Q - Q_{sw}(-h)$. Although large gaps in Q and τ precluded running the entrainment model over this period, the net annual ΔT_a due to budget-inferred entrainment ($\sim$ 20°C) (black) is comparable to 2001 model-estimated entrainment ($\sim$ 19°C) (thin black). Advective fluxes are estimated from single-point ACM velocity data from the 10 °N, 95°W TAO buoy (available 10/2002–10/2003) and SST data from the TRMM satellite (see Appendix B). Gaps in Q, which are replaced with an average timeseries using data from 2000–2002, are shown as dashed lines in the $Q - Q_{sw}(-h)$ and entrainment terms. Gray shading about ΔT_a due to $Q - Q_{sw}(-h)$ indicates ± 10 W m^2 error bias (Fairall et al., 1996), while that about ΔT_a due to budget-inferred entrainment includes this uncertainty plus uncertainty in the advective heat flux estimate, or a total of ± 15 W m^{-2}.

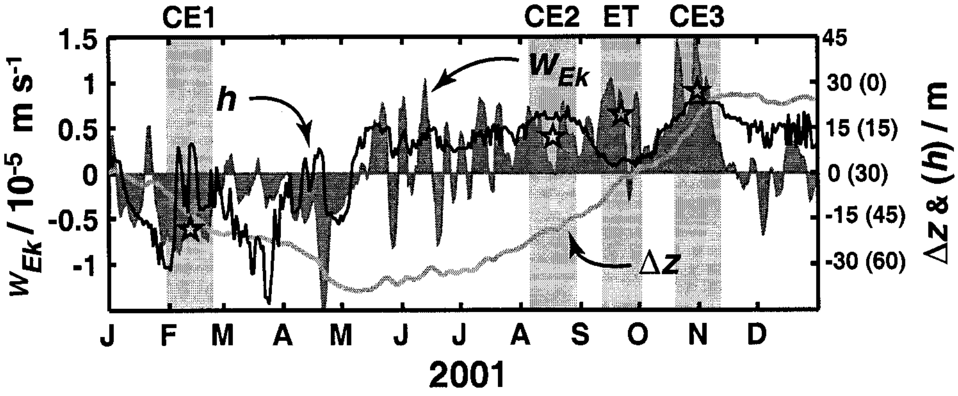

Figure 4.17: Timeseries of Ekman pumping velocity, w_{Ek}, at $z \approx -h$ (shading, left axis), corresponding Δz from time-integration of w_{Ek} (gray line, right axis), and the mixed layer depth (black line, right axis) showing that the mixed layer depth appears to be strongly influenced by local Ekman pumping. Values of w_{Ek} are the average over a 2° lat./lon. box centered on 10°N, 95°W as shown in Fig. 4.18. Stars show time-average values of w_{Ek} over the cooling episodes (CE1, CE2, CE3) and the EPIC timeseries (ET) (see Table 4.2).

local upwelling/downwelling at 10°N, 95°W is influenced by several different regional wind patterns (Fig. 4.18). As suggested by a zonal band of positive wind stress curl centered at about 9 °N, upwelling over CE2 appears to be largely driven by the presence of the ITCZ. Over the EPIC timeseries this pattern is somewhat evident but broken—potentially by the strong influence of deep convection. Over CE3, on the other hand, upwelling appears to be a result of the Tehuantepec Jet wind field. Downwelling favorable-winds at 10° N, 95° W, which are strongest from January through April and span CE1, appear to be most influenced by strong Papagayo Jet winds, with the upwelling influence of the Tehuantepec wind jet weaker during this period.

Entrainment estimates from a 1-D upwelling balance

With a knowledge of the Ekman velocity and time-changes in mixed layer depth we can make some simplifying assumptions about the entrainment term in the temperature budget equation (term 4, Eqn. 4.2) to give estimates of heat entrainment that are independent of the entrainment model results. Assuming that the vertical velocity at $z = -h$ is dominated by the Ekman pumping velocity,

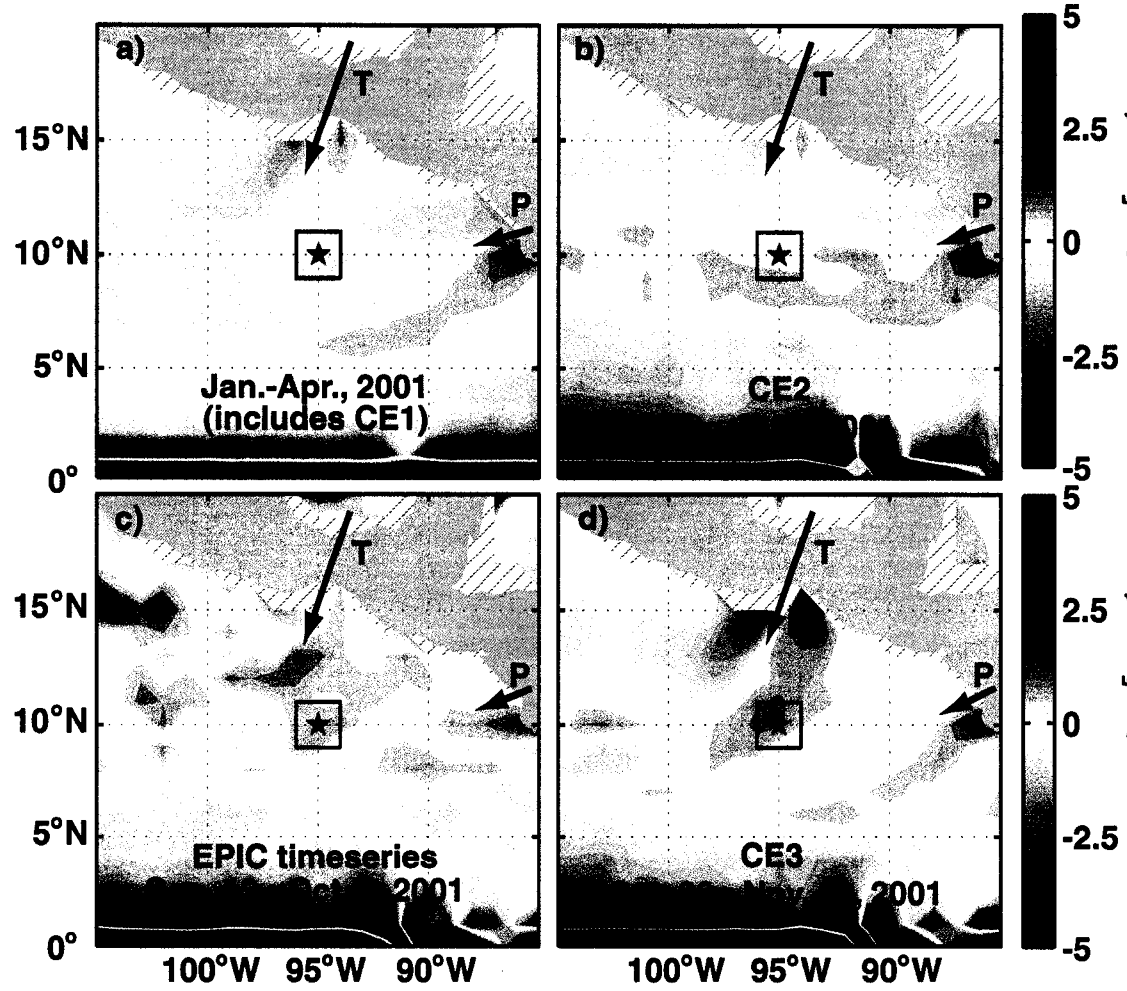

Figure 4.18: Ekman pumping velocity, w_{Ek}, averaged over four periods in 2001: a) 1 Jan.–31 Apr.(includes CE1), b) Aug. 6–29 (CE2), c) Sep. 12–Oct. 2 (EPIC timeseries) and d) Oct. 20–Nov. 12 (CE3). The box shows the averaging area for the w_{Ek} timeseries shown in Fig. 4.17, ★ marks the EPIC timeseries location, and arrows show locations of the Tehuantepec (T) and Papagayo (P) mountain gap wind jets. Ekman pumping velocity was computed by first-differencing 4-day-averaged QuikSCAT Large and Pond (1981) wind stress over 1° in latitude and longitude.

or $w(-h) \approx w_{Ek}$, and that the influence of advection of horizontal gradients of $h(x, y)$ is small compared to both w_{Ek} and $\partial h/\partial t$, then the entrainment term of equation 4.2 becomes:

$$\frac{\Delta T}{h}\left[\frac{\partial h}{\partial t} - w_{Ek}\right] = \frac{J_q^e}{\rho c_p h}\,, \tag{4.10}$$

where $\Delta T = [T_a - T(-h)]$.

One way of interpreting the above relation is that the non-turbulent, vertical advective heat flux due to Ekman pumping through the surface described by h must match the turbulent entrainment heat flux. Although there are insufficient data to confirm that horizontal advection of $h(x, y)$ was insignificant at the timescales of interest, the above equation is used to obtain coarse estimates of period-mean J_q^e over CE2 and CE3 that are independent of the entrainment model results (Fig. 4.19). Because of the likely influence of horizontal advection on time-changes of mixed layer depth during CE1 and the EPIC timeseries, these periods are excluded from this analysis.

Although apparently straightforward, equation 4.10 is very sensitive to the method for determining the bulk vertical temperature difference $\Delta T = T_a - T(-h)$, or physically the difference between T_a and the temperature of the entrained water. If interpreted literally, a well-mixed mixed layer with $T_a = T(-h)$ would give a ΔT of zero and an erroneous entrainment heat flux of zero. The approach used here to address this ambiguity is to compute period-averaged estimates of J_q^e using multiple mixing lengthscales, or using various distances below h to compute "$T(-h)$". Observations presented in Chapter 2 indicate that SBL turbulence has in most cases decayed to background levels within 5 meters below h, so this length is used as an upper-bound (Fig. 2.4). Also, to match the 4-day average of QuikSCAT winds and to reduce the influence of inertial-pumping (heaving of h at a near-inertial period) the mixed layer depth was boxcar-averaged over 4 days prior to computing $\Delta h/\Delta t$. Although uncertainty is large in both model and budget-estimated values of $\overline{J_q^e}$ for CE2 and CE3, results are comparable, thus providing additional support for the conclusion that Ekman upwelling significantly contributed to the entrainment fluxes over these two periods (Fig. 4.19). The rough agreement of the two independent entrainment flux estimates specifically suggests that relatively strong upwelling may have offset mixed layer deepening due to entrainment, thus helping to maintain elevated entrainment fluxes and the increased sensitivity of T_a to these fluxes.

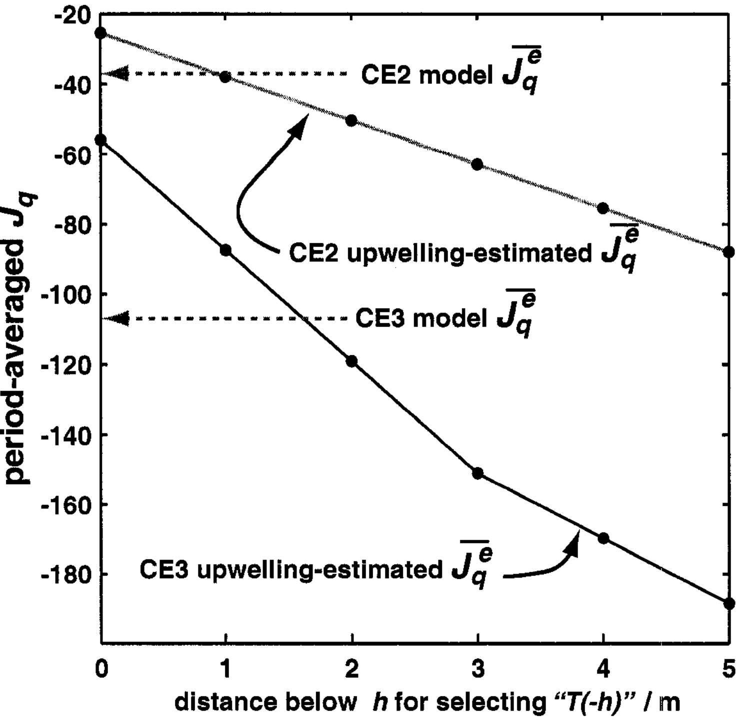

Figure 4.19: Comparison of period-averaged entrainment heat fluxes over CE2 and CE3 calculated using the semi-empirical entrainment model (dashed lines) and estimates obtained by simplifying the entrainment term of the budget equation (Eqn. 4.2) to a balance between vertical Ekman pumping (w_{Ek}) and time-changes in mixed layer depth ($\partial h/\partial t$) (solid lines with data points). Because of ambiguity in selecting "$T(-h)$", or the temperature of the entrained water, multiple depths (d) below h are shown, i.e. $T(-[h+d])$.

4.6 Summary and Discussion

4.6.1 Summary

Intensive atmospheric and upper-ocean measurements recorded during the EPIC 2001 field program over 19 days in September 2001 allowed the measurement or estimation of all primary mixed layer temperature budget terms at relatively short intervals (<hour). Findings from these data were:

- A close comparison between the measured depth-averaged mixed layer temperature, T_a, over the timeseries with that inferred from the budget showed that within expected uncertainty the budget was continuously closed on timescales of roughly a day and longer. Despite the large uncertainty of the advective and entrainment term estimates, these results provide strong support for the budget methodology (i.e. the specific equations), the measurement techniques, and the various surface flux parameterizations.

- A comparison of the influence of the individual terms on time-changes of T_a showed that mixed layer temperature was most strongly controlled by the divergence of the surface and penetrative radiation [term 5, $Q - Q_{sw}(-h)$], which was primarily responsible for the -0.70°C net drop in T_a over the 19-days. Advection and entrainment had somewhat smaller net influences on T_a with the former likely warming T_a by 0.1 to 0.5°C and the latter cooling the mixed layer by roughly -0.25°C.

- The relatively weak entrainment fluxes over the EPIC timeseries may have been partly a consequence of the presence of a warm, anticyclonic mesoscale eddy, that had an anomalously deep mixed layer and potentially greater rainfall (Wijesekera et al., 2005) than the surrounding ocean.

- The influence of the ITCZ and its modulation by easterly waves on the mixed layer temperature budget was manifested as two distinct atmospheric forcing regimes over the EPIC timeseries: weak atmospheric convection and strong solar heating over the first half of the timeseries resulting in a net surface heat gain and deep atmospheric convection during the second half of the timeseries resulting in a net surface heat loss that was primarily due to increased cloudcover and secondarily to increased latent and sensible heat losses. Analysis of surface heat fluxes from multiple years suggests that the presence of the ITCZ may interrupt the dominant state of net mixed layer warming from Q.

TAO buoy upper ocean and atmospheric observations, results from a semi-empirical entrainment model, and QuikSCAT satellite wind data allowed an investigation of the role of entrainment in controlling T_a and SST over 2001. Results indicate that the largest entrainment fluxes over 2001 occurred when the mixed layer depth was shallowest ($<$ 20 m), which resulted in or significantly contributed to the largest drops in T_a and SST observed over the year. The shallow mixed layer enhanced entrainment fluxes because of the inverse h-dependence of mechanisms governing entrainment, i.e. wind stress $[u_*^3/h]$, dynamic stability at h (Ri^m), and a formulation for the contribution from breaking surface waves. The decrease in h also amplified the impact of these fluxes on mixed layer temperature changes since ΔT_a due to J_q^e is inversely proportional to h. Thus, most of the entrainment flux occurred when it was most effective at reducing mixed layer temperature.

TAO buoy surface fluxes and an empirical penetrative radiation model (Ohlmann, 2003) showed that the net influence of the divergence of the surface and penetrative heat fluxes [$Q - Q_{sw}(-h)$] would be to warm the mixed layer by as much as 23°C over a year within the EPWP. Model results suggest that entrainment could contribute to most of the annual cooling necessary to offset this warming, meeting the requirement of a near-zero interannual variability of T_a and SST. Because entrainment predominantly occurs when it is most effective at reducing T_a (when h is shallow), the estimated average entrainment heat flux over 2001 (~ -36 W m^{-2}) is only about 60% of the flux from $Q - Q_{sw}(-h)$ (-60 W m^{-2}) while their influences on net T_a changes over 2001 are more similar in magnitude (about -19°C and $+23$°C respectively).

In agreement with the findings of Kessler (2002) showing that the mixed layer and thermocline depth in the EPWP is largely governed by linear Sverdrup dynamics, there is strong evidence suggesting that the curl of the wind stress field and associated Ekman pumping significantly contributed to the exceptionally shallow mixed layers during two of the cooling events. With the elevated entrainment over these periods shown to be largely due to the decrease in h, this implies that Ekman pumping led to the elevated entrainment fluxes and the periods of mixed layer cooling.

4.6.2 Discussion

A potential negative feedback mechanism for controlling SST

The fact that SST has only a small interannual variability ($<$ 1°C) while the net surface heat flux within the EPWP would alone warm SST by >20°C in a year suggests strong negative feedback mechanisms between anomalously warm SST and processes that work to reduce these anomalies such as turbulent entrainment and advective cooling. In particular, these results suggest a mechanism by which anomalously warm SST may drive winds with positive wind stress curl which would induce SST-cooling by simply shoaling the mixed layer depth and increasing entrainment fluxes. This potential mechanism would be rather efficient at reducing warm SST anomalies because in addition to elevating entrainment fluxes, the reduction of h increases the sensitivity of T_a to the entrainment fluxes. It is important to note, however, that the divergence necessary to lift the mixed layer/thermocline transports much of the heat stored in the mixed layer out of the region—so this mechanism would effectively hand off much of the excess heat to another location by advection. The existence of such a feedback mechanism within the EPWP is suggested by observations from other ocean regions and model results showing a connection between anomalously warm SST and increased activity/intensity of tropical cyclones [e.g. Emanuel (1999); Chan et al. (2001)]. With hurricanes/tropical cyclones long known to shoal the mixed layer by Ekman divergence [e.g. Leipper (1967)] and found to cool the mixed layer largely via turbulent entrainment (D'Asaro, 2003), there is some similarity to the mechanism suggested above. However, since pressure gradient-driven gap winds are important to the regional wind stress curl patterns within the EPWP, a potential negative feedback mechanism is likely to involve these dynamics in addition to local processes (e.g. tropical cyclogenesis).

Future work

The findings presented here showing a connection between the larger patterns of wind stress and local entrainment generation highlight the importance of understanding the details of the region's atmosphere-ocean coupling if we are to accurately model this system. These results imply that in order to model entrainment fluxes to within any degree of accuracy the depth of the thermocline/mixed layer must be modeled properly. Following from the findings of Kessler (2002), correctly determining the latter requires a proper representation of Rossby dynamics, and thus proper resolution of the wind stress. Since winds within the eastern tropical Pacific are strongly forced by SST and SST gradients (Lindzen and Nigam, 1987; Wallace et al., 1998; Chelton et al., 2001), and thus are likely influenced by entrainment and the mixed layer depth, it is clear that the details of the ocean-atmosphere dynamic and thermodynamic coupling would be difficult to extract without extensive observations to constrain modeling studies.

Although the EPIC research program has significantly contributed to our understanding of the region's dominant dynamics, there still remains a large gap in this understanding that is directly attributable to a large gap in both the time and space coverage of observations. In this study the large uncertainty in the advective and entrainment term estimates severely limits the conclusions that can definitively be made concerning the region's mixed layer temperature budget. Efforts to improve estimates of the budget advective terms would likely be more tractable and fruitful than efforts to improve the uncertainty and coverage of entrainment estimates. Additionally, better resolution of advective changes in T_a may lead to improved entrainment estimates since budget-inferred entrainment may have lower uncertainty than direct measurements or modeled estimates, and, thus, may serve as a way of quantifying uncertainty and identifying error in the latter. One potential approach to improving advective term estimates is to simply enhance the present TAO buoy array with localized mixed layer thermistor arrays that would be capable of resolving the dominant T_a gradients and fluctuations of these gradients. Data from these arrays could be used in conjunction with TAO buoy mixed layer velocity data to provide accurate advective term estimates. In addition to being used to better quantify the seasonal to annual variability in mixed layer temperature budget terms, these observations could also be used to verify/calibrate estimates of T_a gradients based on satellite

SST. The enhancement of TAO buoy observations to include velocity profiles, which would allow the calculation of $Ri(-h)$ instead of an estimate from the Pollard and Millard (1970) model, would likely improve the estimation of entrainment fluxes obtained from the semi-empirical entrainment model. However, because the model is specifically tuned for the conditions encountered at 10 °N, 95°W, and extention of the model to other locations would likely need to be accompanied by direct measurements of entrainment fluxes.

The present analysis also showed that the uncertainty of the budget term estimates could be significantly reduced by increasing the present vertical resolution of the TAO buoy upper ocean measurements of temperature, conductivity and pressure. Because of the rapid changes in salinity and temperature with depth below the mixed layer within the EPWP, the vertical spacing of the thermistors/conductivity sensors was nearly prohibitive for a mixed layer budget study. A vertical spacing of least every 5 meters within the upper 40 m and 10 m thereafter to 80 m would reduce the present uncertainty in h by at least 50% and significantly improve estimates of vertical gradients of temperature and salinity at h necessary for budget calculations.

Chapter 5

CONCLUSIONS

The finding that the smallest scales of motion (turbulent mixing) within the EPWP strongly influence SST and are coupled to among the largest scales of motion (Ekman pumping and Rossby waves) indicates that accurately modeling both scales of motion is essential to predicting the evolution of the atmosphere-ocean system within the northeastern tropical Pacific. With the seasonal to annual evolution of the region potentially important to the timing and intensity of El Niño/ La Niña events [e.g. Zebiak and Cane (1987); Battisti and Hirst (1989); Latif et al. (1994)] we are left with the conclusion that entrainment fluxes within the EPWP may influence climate and weather well outside the region. Because of strong air-sea coupling within the tropics and the sensitivity of entrainment to the details of atmospheric forcing, however, accurately modeling entrainment within the EPWP is a daunting task which could be compared to a dog chasing its tail. Even if turbulent mixing is perfectly resolved, its accuracy will be limited by the ability to resolve the atmospheric forcing. If there is any hope for modeling this complex system, it likely will involve significantly improved sampling of both the atmosphere and ocean for the purpose both constraining model results and to add to our understanding of the region's dynamics. Specifically, more studies comparing results from entrainment parameterizations/upper-ocean models to observations are needed to identify and address model shortcomings. It follows that we must also improve our ability to measure the upper-ocean—reducing uncertainty in observations including but not limited to the vertical turbulent fluxes. The results presented here suggest several potential areas of research, including the role of internal waves, breaking surface waves, and mesoscale eddies in controlling entrainment and SST.

As is often the case in science, this research has generated many more questions than it has answered. It seems appropriate to conclude with a list of some of these questions.

1. What is the role of mesoscale eddies in controlling entrainment fluxes? Specifically, are entrainment fluxes significantly different in anticyclonic vs. cyclonic eddies? Are there positive-feedback mechanisms involving entrainment fluxes that help to maintain cold SST in cyclonic eddies and warm SST in anticyclonic eddies?

2. What are the specific dynamics/thermodynamics involved in the coupled air-sea negative feedback that results in only small interannual variability of SST while surface heating alone would warm the mixed layer and SST by more than 20 °C?

3. What is the role of near-inertial internal waves in the regional mixed layer energy budget and in entrainment generation? What factors determine the percent and rate at which energy is lost from the mixed layer due to the radiation of internal waves? Do observations within the EPWP agree with the findings from mid-latitude studies [e.g. Levine and Zervakis (1995); D'Asaro et al. (1995); D'Asaro (1995)]?

4. How can the influence of internal waves on mixing/entrainment be incorporated into OGCMs or upper-ocean models?

5. Do the relative roles of entrainment and advection vary significantly from year to year within the EPWP? Does one compensate for the other to help maintain small interannual variability of SST? Are there substantial differences in the mixed layer temperature budget between La Niña and El Niño conditions?

6. What is the explicit role of biology (phytoplankton concentration) to SST variability within the EPWP. With higher concentrations of phytoplankton in upwelling regions/regions of large entrainment cooling [e.g. the Costa Rica Dome, (Xie et al., 2005)], does it play an important role in controlling SST in these regions by altering the absorption profile of solar penetrative radiation?

BIBLIOGRAPHY

Alford, M. H. and M. C. Gregg, 2001: Near-inertial mixing: Modulation of shear, strain and microstructure at low latitude. *J. Geophys. Res.*, **106**, 16,947–16,968.

Anderson, S. P., R. A. Weller, and R. Lukas, 1996: Surface buoyancy forcing and mixed layer of the western Pacific warm pool: Observations and 1-d model results. *J. Clim.*, **9**, 3056–3085.

Anis, A. and J. N. Moum, 1995: Surface wave-turbulence interactions: scaling $\varepsilon(z)$ near the sea surface. *J. Phys. Oceanogr.*, **25**, 2025–2045.

Ball, F. K., 1960: Control of inversion height by surface heating. *Q. J. R. Meteorol. Soc.*, **86**, 483–494.

Battisti, D. S. and A. C. Hirst, 1989: Interannual variability in the tropical atmosphere-ocean system: Influence of the basic state and ocean geometry. *J. Atmos. Sci.*, **46**, 1687–1712.

Boccippio, D. J., W. A. Petersen, R. Cifelli, and S. A. Rutledge, 2002: Diurnal cycle of convection in the east pacific itcz during epic-2001. In *Preprint Volume, 25th Conference on Hurricanes and Tropical Meteorology, American Meteorological Society*, San Diego.

Brainerd, K. and M. Gregg, 1993a: Diurnal restratification and turbulence in the oceanic surface mixed layer. part i: Observations. *J. Geophys. Res.*, **98**, 22,645–22,656.

Brainerd, K. and M. Gregg, 1993b: Diurnal restratification and turbulence in the oceanic surface mixed layer. part ii: Modeling. *J. Geophys. Res.*, **98**, 22,657–22,664.

Brainerd, K. E. and M. C. Gregg, 1995: Surface mixed and mixing layer depths. *Deep-Sea Res.*, **42**, 1521–15443.

Brost, R. A. and J. C. Wyngaard, 1978: A model study of the stably stratified planetary boundary layer. *J. Atmos. Sci.*, **35**, 1427–1440.

Cairns, J. L. and G. O. Williams, 1976: Internal wave observations from a midwater float, 2. *J. Geophys. Res.*, **81**, 1943–1950.

Chan, C. L., Y. Duan, and L. K. Shay, 2001: Tropical cyclone intensity change from a simple ocean-atmosphere coupled model. *J. Atmos. Sci.*, **58**, 154–172.

Chelton, D. B., S. K. Esbensen, M. G. Schlax, N. Thum, M. H. Freilich, F. J. Wentz, C. L. Gentemann, M. J. McPhaden, and P. S. Schopf, 2001: Observations of coupling between surface wind stress and sea surface temperature in the eastern tropical Pacific. *J. Climate*, **14**, 1479–1498.

Clarke, A. J., 1988: Inertial wind path and sea surface temperature patterns near the gulf of tehuantepec and gulf of papagayo. *J. Geophys. Res.*, **93**, 15,491–15,501.

Crawford, G. B. and W. G. Large, 1996: A numerical investigation of resonant inertial response of the ocean to wind forcing. *J. Phys. Oceanogr.*, **26**, 873–891.

Cronin, M. F., C. W. Fairall, and M. J. McPhaden, 2006: An assessment of buoy-derived and numerical weather prediction surface heat fluxes in the tropical Pacific. *J. Geophys. Res.*, **111**, C06038.

Cronin, M. F. and M. J. McPhaden, 1997: The upper ocean heat balance in the western equatorial Pacific warm pool during September–December 1992. *J. Geophys. Res.*, **102**, 8533–8552.

D'Asaro, E., C. E. Eriksen, M. D. Levine, P. Niiler, C. A. Paulson, and P. V. Meurs, 1995: Upper-ocean inertial currents forced by a strong storm, Part I, Data and comparisons with linear theory. *J. Phys. Oceanogr.*, **25**, 2909–2936.

D'Asaro, E. A., 1995: Upper-ocean inertial currents forced by a strong storm. Part II, modeling. *J. Phys. Oceanogr.*, **25**, 2937–2952.

D'Asaro, E. A., 2003: The ocean boundary layer below Hurricane Dennis. *J. Phys. Oceanogr.*, **33**, 561–579.

D'Asaro, E. A., 2004: Air-sea heat flux measurements from nearly neutrally buoyant floats. *J. Atmos. Ocean. Tech.*, **21**, 1086–1094.

D'Asaro, E. A. and R.-C. Lien, 2000b: The wave-turbulence transition for stratified flows. *J. Phys. Oceanogr.*, **30**, 1669–1678.

Davey, M., M. Huddleson, K. Sperber, P. Braconnot, F. Bryan, D. Chen, R. Colman, C. Cooper, U. Cubasch, P. Delecluse, D. DeWitt, L. Fairhead, G. Flato, C. Gordon, T. Hogan, M. Ji, M. Kimoto, T. Knutson, M. Latif, H. L. Treut, T. Li, S. Manabe, C. Mechoso, G. Meehl, S. Power, E. Roeckner, L. Terray, A. Vintzileos, R. Voss, B. Wang, W. Washington, I. Yoshikawa, J. Yu, S. Yukimoto, and S. Zebiak, 2004: STOIC: a study of coupled model climatology and variability in tropical ocean regions. *Clim. Dyn.*, **18**, 403–420.

De Szoeke, R. A. and J. G. Richman, 1981: The role of wind-generated mixing in coastal upwelling. *J. Phys. Oceanogr.*, **11**, 1534–1547.

Donelan, M., M. Skafel, H. Graber, P. Liu, D. Schwab, and S. Venkatesh, 1992: On the growth rate of wind-generated waves. *Atmos.–Ocean*, **30**, 457–478.

Drennan, W. M., M. Donelan, E. Terray, and K. Katsaros, 1996: Oceanic turbulence dissipation measurements in SWADE. *J. Phys. Oceanogr.*, **26**, 808–815.

Efron, B. and G. Gong, 1983: A leisurely look at the bootstrap, the jackknife, and cross-validation. *Am. Statist.*, **37**, 36–48.

Egbert, G. D., A. F. Bennett, and M. G. G. Foreman, 1994: TOPEX/POSEIDON tides estimated using a global inverse model. *J. Geophys. Res.*, **99**, 24821–24852.

Ellison, T. and J. Turner, 1959: Turbulent entrainment in stratified flows. *J. Fluid Mech.*, **6**, 423–448.

Emanuel, K. A., 1999: Thermodynamic control of hurricane intensity. *Nature*, **401**, 665–669.

Emery, W., 1976: The role of vertical motion in the heat budget of the upper northeastern Pacific Ocean. *J. Phys. Oceanogr.*, **6**, 299–305.

Fairall, C. W., J. B. E. E. F. Bradley, D. P. Rogers, and G. S. Young, 1996: Bulk parameterization of air-sea fluxes for Tropical Ocean-Global Atmosphere Coupled-Ocean Atmosphere Response Experiment. *J. Geophys. Res.*, **101**, 3747–3764.

Farrar, T. J. and R. A. Weller, 2006: Intraseasonal variability near 10 °n in the eastern tropical Pacific Ocean. *J. Geophys. Res.*, **111**, C05015.

Fiedler, P. C., 2002: The annual cycle and biological effects of the costa rica dome. *Deep-Sea Res.*, **49**, 321–338.

Freitag, P., M. McPhaden, C. Meinig, and P. Plimpton, 2002: Mooring motion bias of point-Doppler current meter measurements. Technical Report NOAA Tech. Memo, Pacific Marine Environmental Laboratory, NOAA.

Garrett, C. J. R. and W. H. Munk, 1975: Space-time scales of internal waves: A progress report. *J. Geophys. Res.*, **80**, 291–297.

Giese, B. J., J. A. Carton, and L. J. Holl, 1994: Sea level variability in the eastern tropical pacific as observed by topex and Tropical Ocean-Global Atmosphere Tropical Atmosphere-Ocean Experiment. *J. Geophys. Res.*, **99**, 24,739–24,784.

Gill, A. E., 1982: *Atmosphere-Ocean Dynamics*. Academic Press.

Gill, A. E., 1984: On the behavior of internal waves in the wake of a storm. *J. Phys. Oceanogr.*, **14**, 1129–1151.

Gonella, J., 1972: A rotary-component method for analysing meteorological and oceanographic vector time series. *Deep-Sea Res.*, **19**, 833–846.

Gregg, M., 1987: Diapycnal mixing in the thermocline. *J. Geophys. Res.*, **92**(C5), 5249–5286.

Gregg, M. C., H. Peters, J. C. Wesson, N. S. Oakey, and T. J. Shay, 1985: Intensive measurements of turbulence and shear in the equatorial undercurrent. *Nature*, **318**, 140–144.

Gregg, M. C., H. E. Seim, and D. B. Percival, 1993: Statistics of shear and turbulent dissipation profiles in random internal wave fields. *J. Phys. Oceanogr.*, **23**, 1777–1799.

Hansen, D. V. and G. A. Maul, 1991: Anticyclonic current rings in the eastern tropical Pacific ocean. *J. Geophys. Res.*, **96**, 6965–6979.

Hosegood, P., M. Gregg, and M. Alford, 2007: Restratification of the surface mixed layer with submesoscale lateral density gradients: Diagnosing the importance of the horizontal dimension. *J. Phys. Oceanogr.*, **submitted**.

Hutchinson, T. P. and C. D. Lai, 1991: *The Engineering Statistician's Guide to Continuous Bivariate Distributions*. Rumsby Scientific Publishing, Adelaide, South Australia, first edition.

Imberger, J. and C. Ivey, 1991: On the nature of turbulence in a stratified fluid. part II: Application to lakes. *J. Phys. Oceanogr.*, **21**, 659–681.

Ivey, G. N. and J. Imberger, 1991: On the nauture of turbulence in a stratified fluid: Part I:The energetics of mixing. *J. Phys. Oceanogr.*, **21**, 650–658.

Kantha, L. H. and C. A. Clayson, 1994: An improved mixed layer model for geophysical applications. *J. Geophys. Res.*, **99(C12)**, 25235–25266, doi:10.1029/94JC02257.

Kelly, K. A., S. Dickinson, and Z.-J. Yu, 1999: NSCAT tropical wind stress maps: Implications for improving ocean modeling. *J. Geophys. Res.*, **104**, 11,291–11,310.

Kessler, W. S., 2002: Mean three-dimensional circulation in the northeast tropical pacific. *J. Phys. Oceanogr.*, **32**, 2457–2471.

Kessler, W. S., 2006: The circulation of the eastern tropical pacific: A review. *Progress in Oceanography*, **69**, 181–217.

Large, W. G. and G. B. Crawford, 1995: Observations and simulations of upper-ocean response to wind events during the ocean storms experiement. *J. Phys. Oceanogr.*, **25**, 2831–2852.

Large, W. G. and G. Danabasoglu, 2006: Attribution and impacts of upper-ocean biases in CCSM3. *J. Climate*, **19**, 2325–2346.

Large, W. G., J. C. McWilliams, and S. C. Doney, 1994: Oceanic vertical mixing: a review and a model with a nonlocal boundary layer parameterization. *Reviews of Geophys*, **32**, 363–403.

Large, W. G., J. C. McWilliams, and P. P. Niiler, 1986: Upper ocean thermal response to strong autumnal forcing of the northeast pacific. *J. Phys. Oceanogr.*, **16**, 1524–1550.

Large, W. G. and S. Pond, 1981: Open ocean momentum flux measurements in moderate to strong winds. *J. Phys. Oceanogr.*, **11**, 324–336.

Latif, M., T. P. Barnett, M. A. Cane, M. Flügel, N. E. Graham, H. von Storch, J.-S. Xu, and S. E. Zebiak, 1994: A review of ENSO prediction studies. *Climate Dyn.*, **9**, 167–179.

Leaman, K. D. and T. B. Sanford, 1976: Observations on the vertical polarization and energy flux of near-inertial waves. *J. Geophys. Res.*, **6**, 894–908.

Leipper, D. F., 1967: Observed ocean conditions and Hurricane Hilda. *J. Atmos. Sci.*, **24**, 182–196.

Levine, M. D. and V. Zervakis, 1995: Near-inertial energy propagation from the mixed layer:theoretical considerations. *J. Phys. Oceanogr.*, **25**(11), 2890–2908.

Lien, R., M. J. McPhaden, and M. C. Gregg, 1996: High frequency internal waves at 0°, 140° w and their possible relationship to deep-cycle turbulence. *J. Phys. Oceanogr.*, **26**, 581–600.

Limpert, E., W. A. Stahel, and M. Abbt, 2001: Log-normal distributions across the sciences: keys and clues. *BioScience*, **51**, 341–352.

Lindzen, R. S. and S. Nigam, 1987: On the role of sea-surface temperature-gradients in forcing low-level winds and convergence in the tropics. *J. Atmos. Sci.*, **44**, 2418–2436.

Lofquist, K., 1960: Flow and stress near an interface between stratified liquids. *Phys. Fluids*, **3**, 158–175.

Lombardo, C. and M. Gregg, 1989: Similarity scaling of viscous and thermal dissipation in a convecting surface boundary layer. *J. Geophys. Res.*, **94**, 6273–6284.

Ma, C. C., C. R. Mechoso, A. Arakawa, and J. D. Farrara, 1994: Sensitivity of tropical climate in a coupled ocean-atmosphere general circulation model. *J. Climate*, **7**, 1883–1896.

MacKinnon, J. A. and M. C. Gregg, 2003b: Mixing on the late-summmer New England shelf - solibores, shear and stratification. *Journal of Physical Oceanography*, **33**(7), 1476–1492.

McCreary, J. P., H. S. Lee, and D. B. Enfield, 1989: The response of the coastal ocean to strong off shore winds: With application to circulations in the Gulfs of Tehuantepec and Papagayo. *J. Mar. Res.*, **47**, 81–109.

McPhaden, M. J., M. F. Cronin, and D. C. McClurg, 2007: Meridional structure of the surface mixed layer temperature balance on seasonal time scales in the eastern tropical Pacific. *J. Climate*, **accepted**.

Mechoso, C. R., A. W. Robertson, N. Barth, M. K. Davey, P. Delecluse, P. R. Gent, S. Ineson, B. Kirtman, M. Latif, H. L. Treut, T. Nagai, J. D. Neelin, S. G. H. Philander, J. Polcher, P. S. Schopf, T. Stockdale, M. J. Suarez, L. Terray, O. Thual, and J. J. Tribbia, 1995: The seasonal cycle over the tropical Pacific in coupled ocean-atmosphere general circulation models. *Mon. Wea. Rev.*, **123**, 2825–2838.

Mellor, G. L. and T. Yamada, 1982: Development of a turbulence closure model for geophysical fluid problems. *Rev. Geophys. Space Phys.*, **20**, 851–875.

Moisan, J. R. and P. P. Niiler, 1998: The seasonal heat budget of the North Pacific: net heat flux and heat storage rates (1950–1990). *J. Phys. Oceanogr.*, **28**, 401–421.

Monin, A. S. and A. M. Yaglom, 1975: *Statistical Fluid Mechanics: Mechanics of Turbulence*, volume 2. MIT Press, Cambridge, MA, second edition.

Moon, I. J., T. Hara, I. Ginia, S. E. Belcher, and H. L. Tolman, 2004: Effect of surface waves on air-sea momentum exchange. part i: Effect of mature and growing seas. *J. Atmos. Sci.*, **61**, 2321–2333.

Moum, J. N., 1990: The quest for k_ρ — preliminary results from direct measurements of turbulent fluxes in the ocean. *J. Phys. Oceanogr.*, **20**, 1980–1984.

Moum, J. N. and D. R. Caldwell, 1985: Local influences on shear-flow turbulence in the equatorial ocean. *Science*, **230**, 315–316.

Moum, J. N., M. C. Gregg, R. C. Lien, and M. E. Carr, 1995: Comparison of turbulent kinetic energy dissipation rate estimates from two ocean microstructure profilers. *J. Atmos. Ocean. Tech.*, **12**, 346–366.

Niiler, P. P. and E. B. Kraus, 1977: One-dimensional models of the upper ocean. In E. B. Kraus, editor, *Modelling and Prediction of the Upper Layers of the Ocean* , 143–172, Permagon Press, New York.

Oakey, N. S., 1982: Determination of the rate of dissipation of turbulent energy from simultaneous temperature and velocity shear microstructure measurements. *J. Phys. Oceanogr.*, **12**, 256–271.

Oakey, N. S. and J. A. Elliott, 1982: Dissipation within the surface mixed layer. *J. Phys. Oceanogr.*, **12**, 171–185.

Ohlmann, J. C., 2003: Ocean radiant heating in climate models. *J. Clim.*, **16**, 1337–1351.

Osborn, T. R., 1980: Estimates of the local rate of vertical diffusion from dissipation measurements. *J. Phys. Oceanogr.*, **10**, 83–89.

Paulson, C. A. and J. J. Simpson, 1977: Irradiance measurements in the upper ocean. *J. Phys. Oceanogr.*, **7**, 953–956.

Peters, H. and M. C. Gregg, 1988: Some dynamical and statistical properties of equatorial turbulence. In J. Nihoul and B. Jamart, editors, *Small-Scale Turbulence and Mixing in the Ocean, Proceedings of the 19th International Liège Colloquium on Ocean Hydrodynamics* , 185–200, Amsterdam, Elsevier.

Peters, H., M. C. Gregg, and T. B. Sanford, 1994: The diurnal cycle of the upper equatorial ocean: Turbulence, fine-scale shear, and mean shear. *J. Geophys. Res.*, **99**, 7707–7721.

Peters, H., M. C. Gregg, and J. M. Toole, 1988: On the parameterization of equatorial turbulence. *J. Geophys. Res.*, **93**, 1199–1218.

Petersen, W. A., R. Cifelli, D. J. Boccippio, S. A. Rutledge, and C. Fairall, 2003: Convection and easterly wave structures observed in the eastern pacific warm pool during epic-2001. *J. Atmos. Sci.*, **60**, 1754–1772.

Plueddemann, A. J. and J. T. Farrar, 2006: Observations and models of the energy flux from the wind to mixed-layer inertial currents. *Deep Sea Res. II*, **53**, 5–30.

Pollard, R. T. and R. C. Millard, 1970: Comparison between observed and simulated wind-generated inertial oscillations. *Deep-Sea Res.*, **17**, 153–175.

Pollard, R. T., P. B. Rhines, and R. Thompson, 1973: The deepening of the wind-mixed layer. *Geophys. Fluid Dyn.*, **3**, 381–404.

Price, J. F., 1979: Observations of a rain-formed mixed layer. *J. Phys. Oceanogr.*, **9**, 643–649.

Price, J. F., R. A. Weller, and R. Pinkel, 1986: Diurnal cycling: Observations and models of the upper ocean response to diurnal heating, cooling, and wind mixing. *J. Geophys. Res.*, **91**, 8411–8427.

Pyatt, H. E., B. A. Albrecht, C. Fairall, J. E. Hare, N. Bond, P. Minnis, and J. K. Ayers, 2003: Evolution of marine atmospheric boundary layer structure across the Cold-Tongue-ITCZ Complex. *J. Clim.*, **18**, 737–753.

Raymond, D. J., S. K. Esbensen, M. C. Gregg, and C. S. Bretherton, 2004: Epic2001 and the coupled ocean-atmosphere system of the tropical east Pacific. *Bull. Am. Meteor. Soc.*, **(submitted)**, 1341–1354.

RDI, 1988: *RD-VM Model Acoustic Doppler Current Profiler with IBM compatible DAS operation and maintenance manual*. RD Instruments, 9855 Businesspark Ave., San Diego, CA, change 1.

Schopf, P. S. and M. J. Suarez, 1988: Vacillations in a coupled ocean-atmosphere model. *J. Atmos. Sci.*, **45**, 549–566.

Serra, Y. L. and R. A. Houze, 2002: Observations of variability on synoptic timescales in the East Pacific ITCZ. *J. Atmos. Sci.*, **59**, 1723–1743.

Shay, L., T. Cook, S. D. Jacob, C. Zhang, and M. McGauley, 2003: Airborne expendable current, temperature and salinity profiling in epic. In *EPIC2001 Workshop Poster Abstracts and Agendas, September 16–18, 2003, Boulder, Colorado*.

Shay, T. and M. Gregg, 1986: Convectively driven turbulent mixing in the upper ocean. *J. Phys. Oceanogr.*, **16**, 1777–1798.

Skyllingstad, E. D., W. D. Smyth, J. N. Moum, and H. Wijesekera, 1999: Upper-ocean turbulence during a westerly wind burst: A comparison of large-eddy simulation results and microstructure measurements. *J. Phys. Oceanogr.*, **29**, 5–28.

Snedecor, G. W. and W. G. Cochran, 1967: *Statistical Methods*. Iowa State University Press, Ames, Iowa, 6th edition.

Sun, H. and E. Kunze, 1999: Internal wave–wave interactions. Part i: The role of internal wave vertical divergence. *J. Phys. Oceanogr.*, **29**, 2886–2904.

Taylor, G. I., 1935: Statistical theory of turbulence. *Proc. of the Royal Soc. of London, Series A*, **151**, 421.

Tennekes, H. and J. L. Lumley, 1972: *A First Course in Turbulence*. MIT Press.

Terray, E. A., M. A. Donelan, Y. C. Agrawal, W. M. Drennan, K. K. Kahma, A. J. W. III, P. A. Hwang, and S. A. Kitaigorodskii, 1996: Estimates of kinetic energy dissipation under breaking waves. *J. Phys. Oceanogr.*, **26**, 792–810.

Terray, E. A., W. M. Drennan, and M. A. Donelan, 1999: The vertical structure of shear and dissipation in the ocean surface layer. In M. L. Banner, editor, *The Wind-Driven Air-Sea Interface, Electromagnetic and Acoustic Sensing, Wave Dyanmics and Turbulent Fluxes*, 239–245, ADFA Document Production Centre, Canberra, New South Wales.

Thorpe, S. A., 1971: Experiments on the instability of stratified shear flows: miscible fluids. *J. Fluid Mech.*, **46**, 299–320.

Thorpe, S. A., 1977: Turbulence and mixing in a Scottish Loch. *Phil. Trans. Roy. Soc. London*, **286**, 125–181.

Turner, J. S., 1969: Buoyant plumes and thermals. *Ann. Rev. Fluid Mech.*, **6**, 37–56.

Wallace, J. M., E. M. Rasmusson, T. P. Mitchell, V. E. Kousky, E. S. Sarachik, and H. von Storch, 1998: On the structure and evolution of ENSO-related climate variability in the tropical pacific: Lessons from TOGA. *J. Geophys. Res.*, **103**, 14241–14259.

Wang, B., T. M. Li, and P. Chang, 1995: An intermediate model of the tropical Pacific Ocean. *J. Phys. Oceanogr.*, **25**, 1599–1616.

Wang, D., J. C. McWilliams, and W. G. Large, 1998: Large-eddy simulation of the diurnal cycle of deep equatorial turbulence. *J. Phys. Oceanogr.*, **28**, 129–148.

Weinstock, J., 1981: Energy dissipation rates of turbulence in the stable free atmosphere. *J. Atmos. Sci.*, **38**, 880–883.

Wesson, J. C. and M. C. Gregg, 1994: Mixing at Camarinal Sill in the Strait of Gibraltar. *J. Geophys. Res.*, **99**, 9847–9878.

Wijesekera, H. W. and M. C. Gregg, 1996: Surface layer response to weak winds, westerly bursts, and rain squalls in the western Pacific Warm Pool. *J. Geophys. Res.*, **101**, 977–997.

Wijesekera, H. W., D. Rudnick, C. A. Paulson, S. A. Pierce, S. Pegau, J. B. Mickett, and M. C. Gregg, 2005: Upper ocean heat and freshwater budgets in the eastern Pacific warm pool. *J. Geophys. Res.*, **110**, C08004.

Winters, K. B., P. N. Lombard, J. J. Riley, and E. A. D'Asaro, 1995: Available potential energy and mixing in density-stratified fluids. *J. Fluid Mech.*, **289**, 115–128.

Xie, S. P., H. Xu, W. S. Kessler, and M. Nonaka, 2005: Air-sea interaction over the eastern Pacific warm pool: Gap winds, thermocline dome, and atmospheric convection. *J. Clim.*, **18**, 5–20.

Zebiak, S. E. and M. A. Cane, 1987: A model El Niño southern Oscillation. *Mon. Wea. Rev.*, **115**, 2262–2278.

Appendix A

INSTRUMENTATION

A.1 MMP

A total of 1180 profiles (drops 12306–13485) of microscale shear, pressure, temperature, conductivity, and oxygen were collected with the modular microstructure profilers 1–3 (MMP1,MMP2,MMP3). The microstructure shear fluctuations were used to calculate the dissipation rate of turbulent kinetic energy, ε, which were recorded in half-overlapping, ~0.6-m depth bins (Oakey, 1982; Wesson and Gregg, 1994). Peters et al. (1988); Moum et al. (1995) estimate that absolute errors of ε are about a factor of 2. Due to possible contamination by surface waves and the ship's wake, all ε data at depths $<$8 m have been discarded and data at depths $<$12 m are considered suspect. A comparison of profiles released roughly 15 m astern of the ship's transom with those released within ~1–3 m from the transom indicates that the ship's wake elevates the dissipation measurements by up to 2 decades in the top ~ 11 m of the water column.

Profiles typically extended from near-surface to the instrument's maximum operating depth of 300 m. Profiles were collected from the stern while the ship was on a relatively constant heading (within 45° of the wind direction) and instruments were swapped as necessary to recharge their batteries. When the *Brown* neared the edge of the station circle the instrument was typically recovered for a downwind, 12-kt ship transit at to the opposite side of the circle. Wind shifts, etc. dictated repositioning of the ship at other times. The nature of this sampling resulted in a maximum drop-rate of around 4 drops per hour over a period of about 3–4 hours, followed by a ship-repositioning which reduced the drop rate to around 0.7 drops per hour. Drop rates were also reduced by CTD casts and other science operations.

A.2 ADCP

Upper-ocean fine-scale velocity data were collected with a hull-mounted, narrowband 150-kHz RD Instruments Acoustic Doppler Current Profiler (ADCP)(Model VM-150-18HP, 153.6 kHz). Velocity data recorded into 4-m depth bins at a nominal ping-rate of 1-Hz were averaged into 1-minute ensembles. Further time-averaging over 150-minutes was necessary to reduce noise in vertical shear calculations to acceptable levels. Reliable data typically extended from the shallowest bin at 13 m to about 250 m.

A.2.1 Noise Levels

Velocity rms errors of the 1-min ensembles are too large to unambiguously separate true ocean variance from noise. Since ADCP velocity random error is Gaussian with a mean of zero, however, we can reduce velocity rms error by time-averaging. This theoretically reduces rms error by $\sqrt{N}$ where N is the number of ensembles averaged together. The trade-off, of course, is that too much averaging will remove true ocean variance.

Assuming the ADCP noise is white, we can calculate the rms error of the 1-min absolute velocities e_{vel} by integrating the noise floor S_N from zero to the Nyquist frequency or Nyquist wavenumber. For the frequency spectral estimate this is formally:

$$e_{\text{vel}} = \sigma_{\text{noise}} = \left(\int_0^{f_{\text{Nyquist}}} S_N \, \partial\omega \right)^{\frac{1}{2}} \tag{A.1}$$

When the rms error of the 1-min absolute velocities is computed from the noise levels from the frequency and wavenumber spectral estimates, we find they are different. The frequency spectral estimates yielded a rms error of 0.046 m s^{-1}, whereas the wavenumber spectral estimate yielded a rms error of 0.071 m s^{-1}. An rms error of ± 0.071 m s^{-1} is equivalent to a frequency noise floor of 0.6 m^2 s^{-2} Hz^{-1} (about twice as large as that observed). Noise levels in both frequency and wavenumber spectra are reduced by time-averaging. Assuming that the rms velocity error is equal for both frequency and wavenumber spectra (not a good assumption for these data), we can estimate the effect of time-averaging on the wavenumber spectral noise level of velocity S_{N,k_z} according to the following equation:

$$S_{N,k_z} = S_N / t_{\text{avg}} / k_{z,Ny} \ , \tag{A.2}$$

where t_{avg} is the averaging period and $k_{z,Ny}$ is the Nyquist wavenumber (0.125 cpm) (Alford and Gregg, 2001). Because of the difference in spectral estimates of e_{vel} using frequency and wavenumber spectra, however, we determine S_{N,k_z} directly with wavenumber spectral estimates of absolute velocities.

Without time-averaging the 1-min absolute velocities, 8-m shear-squared (S_8^2) random errors are too large ($\sim 6.5 \times 10^{-5}$ s^{-2}) to identify all but the largest true shears. Shear random errors can be determined several ways. The velocity random errors from the vertical spectral estimate can be used to generate normally distributed samples with means of zero and $\sigma = e_{\text{vel}}$. Differencing these velocities to produce shears can yield an estimate of shear errors. Shear random errors can also be found by integrating model shear noise from zero to the Nyquist wavenumber. We can model shear spectral noise as:

$$Sh_N = S_{N,k_z} \times (2\pi k_z)^2 \tag{A.3}$$

where $(2\pi k_z)^2$ is the ideal differentiator obtained by taking the vertical derivative of the Fourier Transform. Multiplying the white velocity spectral noise floor by the ideal differentiator results in blue noise in shear, with most noise variance at the highest wavenumbers.

An investigation of the influence of different averaging intervals on the shear noise levels led us to choose 150 min (2.5 hours) as the averaging period (Figure A.1). This amount of smoothing reduced S_8^2 rms error to acceptable levels. By subtracting the modeled noise floor from the spectral estimate, we found that we can believe spectral estimates of shear to 1/16 (0.062) cpm to be dominated by true ocean variance. Also using this technique, we found that most of the variance removed by time-averaging was likely measurement noise and not true ocean variance (with frequencies between 1-min and the averaging period). Integrating the shear spectral noise from zero to 1/16 cpm, we arrive at an 8-meter S_8^2 rms random error of $\sim 8 \times 10^{-6}$ s^{-2}.

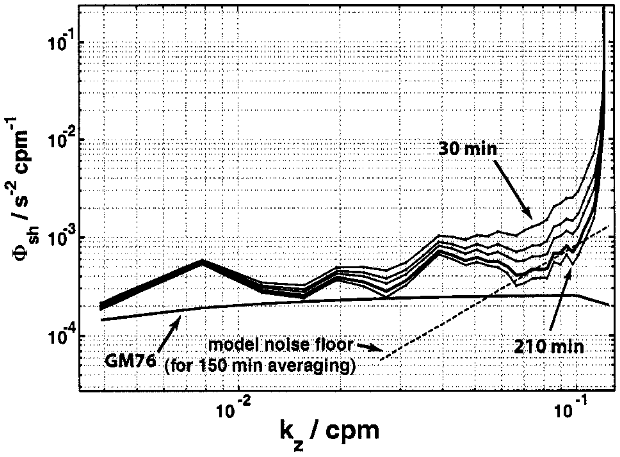

Figure A.1: Vertical spectral estimates of 8-m shear with various degrees of time-smoothing velocity. The GM76 (Garrett and Munk, 1975; Cairns and Williams, 1976) model shear spectrum is included as is the model shear noise floor for 150-min smoothed velocities. Spectra were computed at depths from 29 to 213 m and from yearday 261.6 to 265.1.

Appendix B

ESTIMATING ENTRAINMENT FLUXES FROM TURBULENCE MEASUREMENTS

B.1 The dissipation method

Turbulent fluxes are computed via the dissipation method (Osborn, 1980), which is based on a simplified balance of the turbulent kinetic energy (TKE) equation. With TKE $= q^2 \equiv \overline{u_i u_i}/2$, the TKE conservation equation (neglecting the small viscous transport term) is expressed as:

$$\frac{\partial q^2}{\partial t} + U_j \frac{\partial q^2}{\partial x_j} + \frac{\partial \overline{u'_j q^2}}{\partial x_j} + \frac{1}{\rho} \frac{\partial \overline{u'_i p'_i}}{\partial x_i} \tag{B.1}$$

$$= -\overline{u'_i u'_j} \frac{\partial U_i}{\partial x_j} - \frac{g}{\rho_0} \overline{w' \rho'} - \varepsilon$$

Where U is the non-turbulent, background flow and overbars denote some appropriate time or space averaging. The dissipation method assumes Equation B.1 reduces to a balance between shear production, buoyant suppression and dissipation:

$$\overline{u'_i u'_j} \frac{\partial U_i}{\partial x_j} = -\frac{g}{\rho_0} \overline{w' \rho'} - \varepsilon \tag{B.2}$$

or

$$-P = J_b - \varepsilon \tag{B.3}$$

This balance requires the terms on the l.h.s. of Equation B.1—the local time-derivative, the transport by the mean flow, the transport by the turbulence and the divergence of the pressure-velocity correlations—sum to a value with a magnitude much smaller than any of magnitudes of the terms on the r.h.s. of Equation B.1. Using scaling arguments, Monin and Yaglom (1975) showed that for parallel shear flow without a destabilizing buoyancy flux (outside convective regions) the pressure-velocity correlation and the turbulent diffusion terms can be neglected. At the EPIC station a strong, relatively steady background horizontal shear field in the upper thermocline suggests that these scalings apply. However, the estimates of turbulent fluxes will necessarily be restricted to non-convecting regions where positive or nonlocal buoyancy fluxes are negligible.

LES model results provide additional support for the dissipation method assumptions, showing that the balance shown in Equation B.3 dominates in stratified regions and regions not actively convecting. For example, using a LES model designed to investigate the diurnal cycle of turbulence in the Pacific equatorial undercurrent (Wang et al., 1998) show that 6-hour averages of the TKE budget over the upper 80 m are largely a balance between shear production, dissipation and buoyant suppression. Thus, although the instantaneous TKE conservation equation may not uphold the assumed balance, some amount of time-averaging will improve the applicability of the assumptions.

B.1.1 Evaluating time changes of TKE

Since ε is directly related to the level of TKE (see Equation B.5 below), it follows that q^2 at h_e is also dominated by surface forcing and local instability criteria (from Section 2.4 results). Observations suggest that the surface forcing varies on time-scales shorter or typical of those of variations of Ri_8 at h_e, thus, a rough upper-bound estimate of $\partial q^2/\partial t$ can be determined from the Monin-Obukhov turbulent velocity scales for wind forcing $\left(u_* = \sqrt{|\tau|/\rho}\right)$ and a destabilizing surface buoyancy flux $\left[w^* = (-J_b(0)h)^{1/3}\right]$. Here $h = 25$ m is used to compute w^*. Figure B.1 shows values of $\partial q^2/\partial t$, where $q^2 \approx (u^{*2} + w^{*2})/2$, with various amounts of time-averaging. It is apparent that time-averaging reduces the magnitude of $\partial q^2/\partial t$, and, thus, improves the liklihood of the balance represented by Equation B.3. In general, time-averaging will reduce the magnitude of all terms that are principally distributed about zero.

The magnitude of TKE (q^2) and $\partial q^2/\partial t$ can also be estimated from the measurements of ε and the overturn (Thorpe) scales L_{ot} (Thorpe, 1977), which are found by comparing sorted and

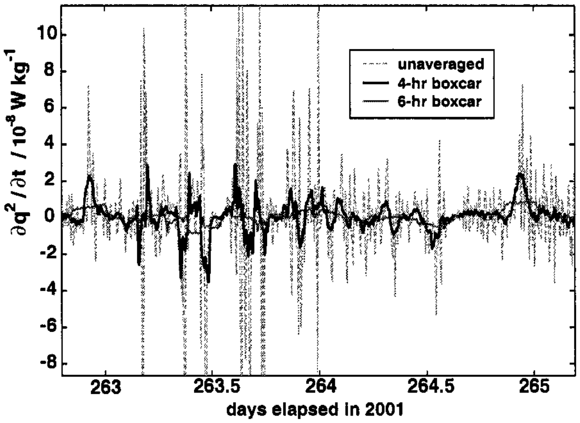

Figure B.1: Local time-derivative of TKE ($\partial q^2/\partial t$) computed from the Monin-Obukhov velocity scales u_* and w_* plotted vs. time over a subset of the EPWP time-series. Various amounts of time-averaging are shown.

unsorted profiles of σ_θ. A simple scaling argument based on the idea that the decay-rate of the largest overturns (which contain the most TKE) dictates the rate of energy transfer to smaller scales (and thus ε) (Tennekes and Lumley, 1972) gives:

$$C\frac{u^3}{L_{\mathrm{ot}}} = \varepsilon \tag{B.4}$$

$$q^2 = \frac{1}{2}(\varepsilon L_{\mathrm{ot}}/C)^{2/3} \tag{B.5}$$

The constant C has been found empirically in a number of studies [e.g. Brainerd and Gregg (1993b); Brost and Wyngaard (1978); Weinstock (1981)], with values ranging from 0.02 to 0.19. Here the value determined by Brainerd and Gregg (1993b) ($C = 0.04$), which involved fitting observed dissipation decay in the remnant mixed layer to a simple model, is used since the other values were determined from atmospheric boundary layer vice oceanic SBL observations. Additionally, since this is nearly the smallest reported value for C, it results in an upper bound estimate of q and $\partial q^2/\partial t$. Here the $\log_{10}$-space mean of ε over each overturn was multiplied by the root-mean-square (rms) overturn length $\left(L_{\mathrm{rms}} \equiv \sqrt{\overline{L_{\mathrm{ot}}^2}}\right)$. Figure B.2 shows the rms values of $\partial q^2/\partial t$ vs. depth with various amounts of time-averaging. Gaps in the profiles indicate an insufficient number of overturns greater than our resolution length of 0.05 m to allow averaging. As with the results shown in Figure B.1, time-averaging is shown to significantly reduce $\partial q^2/\partial t$. Boxcar-filtering (running average) over 4 hrs appears the best compromise between reducing $\partial q^2/\partial t$ and retaining time-resolution. This amount of time-averaging will also remove much of the spatial variability introducing by the sampling method. Figure B.2 indicates that the time-derivative term decreases with depth, reflecting the fact that $\partial q^2/\partial t$ within the SBL is dominated by direct surface forcing.

Since q^2 in both cases was determined from simple scaling arguments, these are only rough estimates of $\partial q^2/\partial t$. The actual values of $\partial q^2/\partial t$, in other words, are to be taken lightly. The most significant result of this analysis is that time-averaging significantly reduces the rms value of $\partial q^2/\partial t$. Thus, it is expected that the terms of a *time-averaged* TKE equation will more closely meet the assumption of Equation B.3 and improve the reliability of turbulent fluxes estimated via the dissipation method. Specifically, this means computing J_b and K_ρ using time-averaged values of ε, with a boxcar-averaging window of 4 hours chosen here.

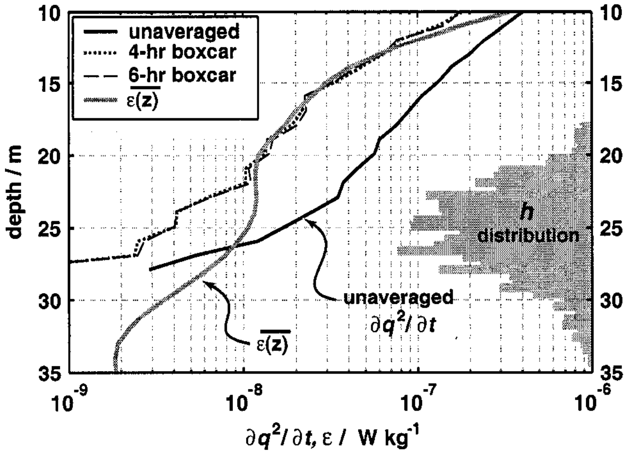

Figure B.2: Root-mean-square values of $\partial q^2/\partial t$ vs. depth with various amounts of time-averaging. The distribution of the mixed layer depth, h is shown with gray shading.

B.1.2 Evaluating the advective terms

With the presence of strong upper-ocean currents and significant vertical displacements of isopycnals at the EPWP station, one might expect that the advection of TKE gradients contributes significantly to local time-changes of TKE ($\partial q^2/\partial t$). Within the upper pycnocline turbulent patches tend move with vertically-displaced isopycnals ($U_3 \partial q^2/\partial x_3$ term). However, computing turbulent fluxes in a semi-Lagrangian sense, or along isopycnal surfaces (or along the top of the seasonal pycnocline as is the case) reduces the influence of this kinematic time-variability. The results of Section 2.4 suggest that most of the variability of J_b^ε—and thus ε and TKE—at h is due to surface forcing and local instability criteria. Thus, horizontal advection of TKE gradients likely has a minor role in driving time-changes of TKE.

B.1.3 Evaluating R_f

The validity of using the canonical flux Richardson number ($R_f = 0.15$) to compute J_b and $K_\rho$was tested using a functional form for a general flux Richardson number presented in Ivey and Imberger (1991). The general R_f is defined as the ratio between the turbulent buoyancy flux and the remaining TKE equation terms excepting dissipation. It is a function of the turbulent Froude number $Fr_T = (\frac{L_O}{L_{\text{rms}}})^{2/3}$ (where $L_O = (\varepsilon/N^3)^{1/2}$ is the Ozmidov scale and L_{rms} is the rms overturn scale) and the turbulent Reynolds number $\text{Re}_T = (\varepsilon^{1/3} L_{\text{rms}}^{4/3})/\nu$ (where ν is the kinematic viscosity of seawater). Results show that within stratified regions of the SBL and upper thermocline, R_f was surprisingly close to the canonical value (Fig. B.3). Additionally, the inclusion of all the mechanical energy terms in the generalized form of R_f suggests that the requirement of a balance between production, dissipation and buoyant suppression may not be entirely necessary to obtain reasonable estimates of turbulent buoyancy flux.

B.2 Accounting for positive J_b

The calculations of J_b and K_ρ using the dissipation method have carefully excluded regions where ε may be influenced by nonlocal or positive J_b associated with active buoyant convection. Including these regions could result in overestimates of the (negative) turbulent buoyancy fluxes and oversteps

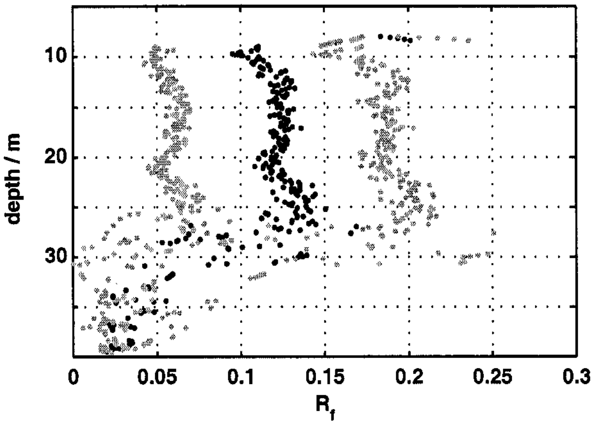

Figure B.3: General flux Richardson number R_f vs. depth estimated from data and functional form in Ivey and Imberger (1991). • shows the time-series mean profile, with gray points showing $\pm\sigma$.

assumptions of the Osborn (1980) method. Specifically, depths of weak stratification identified by $\sigma_\theta(z) - \sigma_\theta(2\text{ m}) < 0.01\text{ kg m}^{-3}$ (or the surface to the instantaneous mixed layer depth, h_i), have been excluded. Additionally, we calculated the maximum penetration depth of near-surface static instabilities (overturning scales), and excluded measurements less than this depth. As is shown in Figure 2.8d, the latter constraint is for the most part met by the stratification condition. One limitation of this technique, however, is that density in the upper several meters of the SBL is not measured. Notwithstanding, because water is entrained (and density decreases) as the convective plumes sink, overturning scales are likely to be a conservative estimate of the penetration depth of the positive J_b. In all, the constraints of the dissipation method preclude the use of about 50% of the mixed layer ε measurements, or about 50% of the mixed-layer above h and below 8 m in the estimates of K_ρ.

Appendix C

DETAILS OF THE MIXED LAYER HEAT BUDGET CALCULATIONS

C.1 Estimating the mixed layer depth

As discussed in Section 4.3, the mixed layer depth over 2001 is estimated from TAO buoy upper-ocean temperature data with h defined as the shallowest depth that is at least 1.5 °C cooler than the 5-m temperature with linear interpolation between thermistor depths ($-z = 1, 5, 10, 20, 40, 60, 80, 100, 120, 140$ m). An investigation of the effect of the relatively course thermistor resolution on the estimates of h is presented here by comparing 1179 highly-resolved MMP temperature profiles (gridded to 1-m) recorded over the EPIC timeseries with test profiles created by linearly-interpolating temperature between thermistor depths (Fig. C.1). Results show that the test profile consistently under-resolved the rapid temperature changes at the mixed layer base/top of the thermocline, and as a consequence nearly always resulted in an unrealistically-shallow mixed layer (Figure C.1a). This bias, however, can be partly compensated for by choosing a value for ΔT significantly larger than a value that would identify h using a highly-resolved T profile. Figure C.1a shows this consequence of coarse vertical resolution and linear interpolation—and that a seemingly-large ΔT of 1.5°C can somewhat compensate for this effect.

A histogram of the actual ΔT between 5 meters depth and the TAO-buoy estimated mixed layer depth (h determined using the linearly-interpolated profile and a ΔT of 1.5°C) shows a large spread in actual ΔT (-0.3 to 1.7°C) and a mean over the EPIC timeseries that is about 1°C less than 1.5°C, or 0.44°C (Fig. C.1b). The TAO buoy temperature-based estimate of h (using a ΔT of 1.5°C) shows good agreement with the density-based estimate of h used for the EPIC timeseries ($\Delta\rho/\Delta z < -0.07$ kg m^{-4}), with a mean bias of +0.9 m and 2σ of ± 5.2 m (Fig. C.1c). Trials with finer thermistor spacing (5 m spacing to 40 m and then 10 m spacing to 80 m) show a significant reduction in the error between buoy-estimated and actual ΔT (a mean buoy underestimate of 0.07 ± 0.34°C)

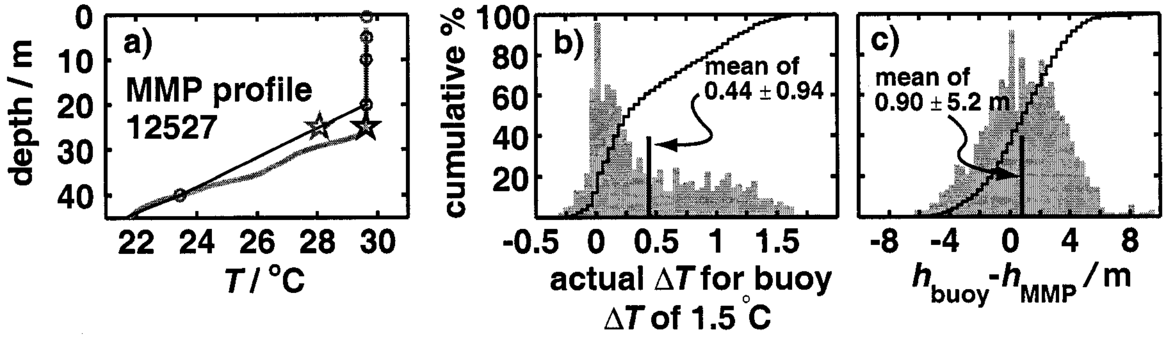

Figure C.1: The effects of discrete TAO buoy thermistor depths on the estimation of h: a) Comparison of a typical MMP profile (drop 12527) in gray to a profile linearly interpolated between TAO thermistor depths (thin black line with thermistor depths gray circles). A seemingly-large $\Delta T = T(z) - T(5\text{ m})$ of 1.5°C typically compensates for the coarse thermistor resolution, improving the estimate of h over smaller values of ΔT. The gray star shows h calculated using $\Delta T = 1.5$°C and the interpolated profile, with the black star showing this depth along the MMP temperature profile. b) Histogram (gray) and cumulative histogram (black) of the actual ΔT between $T(5\text{ m})$ and $T(h)$, with h determined using the linearly-interpolated profile and $\Delta T = 1.5$°C. The mean of the actual ΔT is 0.44 ± 0.94 (2σ). c) As in b) but the difference in TAO buoy (interpolated profile) and MMP-calculated h, with a mean difference of 0.90 ± 5.2 m.

as well as an improved determination of h ($+0.2 \pm 4$ m).

C.2 Advective Flux Estimation and Error Analysis

Here we describe the methods used to calculate the depth-mean advective temperature flux within the mixed layer (term 2 of Equation 4.2), provide an analysis of the potential sources and sizes of error, and estimate the influence of term 3 of Equation 4.2 (advective flux from correlated perturbations).

C.2.1 Calculation of $\mathbf{u_a} \cdot \nabla T_a$

The depth-mean meridional and zonal temperature gradients (∇T_a in term 2 of Equation 4.2) are computed using SeaSoar temperature data from the 146 × 146 km "butterfly" circuits centered on 10° N, 95° W (Figure 4.1). The vertical grid size of SeaSoar data (8-m) precluded an accurate determination of the mixed layer depth, and, thus, its spatial variability. For this reason T_a was taken to be the value of the shallowest bin that is centered at 16 m and an average of T from 12–20 m. As will be discussed, this approximation is a potential source of error in the estimates of ∇T_a.

With SeaSoar circuits completed about every 1.5 days, ∇T_a was measured at relatively coarse time intervals. However, because the dominant gradients in T_a were relatively steady between successive circuits [(Wijesekera et al., 2005) Fig. 13], we were able to take advantage of the finer time-resolution of the ADCP velocities by linearly interpolating the temperature transects onto a finer (hourly) time grid. Gradients were calculated by both smoothing then first-differencing over 40 km and by a linear fit over the same distance with excellent agreement between the two methods. The differencing scale was chosen since it is roughly the distance a parcel within the mixed layer is advected over the sampling interval of the T_a gradients (1.5 days). Additionally, this scale is smaller than the dominant scale of T_a gradients, which are on the order of $>$ 60 km, and, thus, does not alias the dominant gradients. As will be discussed the advective fluxes and the cumulative effect of these fluxes on T_a over the EPIC timeseries was rather sensitive to this scale.

The depth-mean velocity over the mixed layer, $\mathbf{u_a}$, is computed using 150 min-averaged ADCP velocity profiles from the EPIC timeseries, nominally centered at 9.93° N, 95° W (Figure 4.1). With the shallowest of the 4-m depth bins centered at 13 m depth [1], nearly half of the ~25 m deep mixed layer is not sampled. For this reason velocities are linearly extrapolated to the surface. Additionally, to better isolate mixed layer velocities from those below, the 4-m bins are linearly interpolated onto a 1-m grid prior to depth-averaging over the mixed layer.

C.2.2 Error Analysis

There are several potential sources of error in term 2 of Equation 4.2 that could result in significant errors in ΔT_a expected from advection over several days and longer. We are primarily concerned with bias error, and not random error, since time-integration should greatly reduce the influence of the latter while amplifying the effect of the former. Bias error in the estimation of $\mathbf{u_a}$ is likely to arise from the coarse vertical sampling of the ADCP. This error is estimated by examining differences between values of $\mathbf{u}_a$ calculated using linear extrapolation to the surface and those estimated from the average of the 4-m ADCP bins at 13, 17 and 21 m. Bootstrap (Efron and Gong, 1983) 95% confidence intervals about the time-mean difference of the two estimates suggests a 19-day bias less than ± 0.01 m s^{-1}. This adds to the long-term instrument bias error of about ± 0.01 m s^{-1} (RDI, 1988) and a similar bias introduced in the determination of absolute velocities for an estimated 19-day total bias error of about ± 0.03 m s^{-1}.

Bias error may also arise in the determination of the horizontal gradients of T_a. One of the more obvious potential sources of error is the mismatch in the locations of the T_a gradient calculations (zonal along 10.07° N and meridional along 94.85° W) and the mixed layer velocities (~ 9.93° N, 95° W) by an average of 16 km (Fig. 4.1). To minimize this error, zonal and meridional gradients were estimated at the closest points to the EPIC timeseries location (i.e. 10.07° N, 95° W and 9.93° N, 94.85° W) and not at the circuit intersection (10.07° N, 94.85° W). Because the dominant variability of T_a is on scales $>$ 60 km, however, it is expected that bias error introduced by this difference is small compared to other errors.

Sampling error introduced by the approximation of T_a with the average of T from 12–20 m is

---

[1] The triangular weight function applied to the acoustic return spans 9–17 m. Half-overlapping weight functions result in 4-m bins.

estimated using the 1-m gridded MMP profiles. The full mixed layer depth estimate of T_a is rarely more than ± 0.1 degrees different than the 12-20 m average with a long-term (19-day) bias in the latter estimate smaller than -0.004 °C (bootstrap at 95%). Assuming the maximum difference in bias over the differencing distance (40 km), and doubling this value to account for two gradient directions, the maximum bias error introduced by sampling is estimated at ± 0.01 °C, or an equivalent gradient of $\pm 2.5 \times 10^{-7}$ °C m^{-1} . This bias combined with the bias in $\mathbf{u_a}$ leads to a variability of expected ΔT_a over the 19 days of $\pm 0.14°$ C.

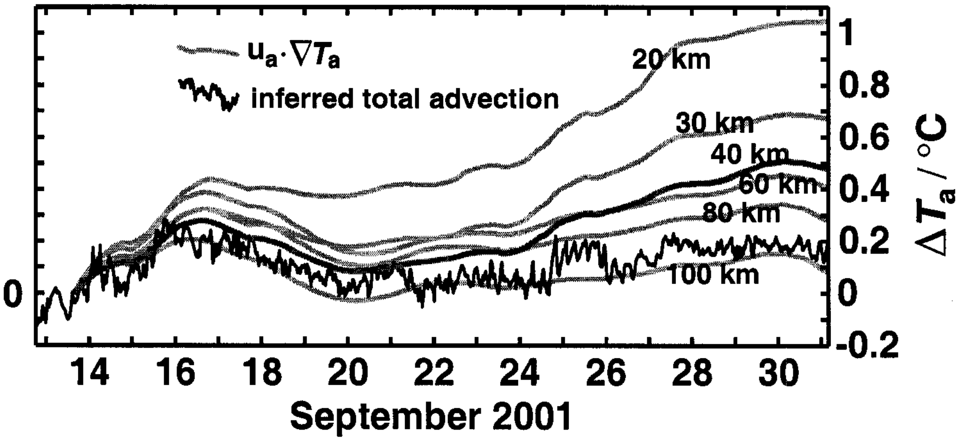

Figure C.2: Comparison of ΔT_a expected from $\mathbf{u_a} \cdot \nabla T_a$ using various differencing scales for the computation of ∇T_a (gray lines). The scale used in the EPIC timeseries budget (40 km) is dark gray and the budget inferred total advection (term 1 −term 4−term 5) is shown in black.

The largest source of error in estimating ∇T_a appears to be that introduced by the choice of scale used to estimate the gradient. If the selected scale of 40 km were reduced by half, for example, the expected ΔT_a due to advection at the end of the EPIC timeseries would increase from 0.41 °C to 1.0 °C, or a 144% increase. Doubling the differencing scale to 80 km would reduce the expected ΔT_a to 0.22 °C or by 46% (Fig. C.2). This sensitivity is likely a result of both the limited temporal resolution of ∇T_a and the aliasing of smaller-scale spatial variability with first-differencing/a linear fit. This uncertainty combined with the potential measurement bias error leads to an estimate of total uncertainty of ± 0.44°C over the 19 days.

C.2.3 Estimating the role of the perturbation advective flux

Inadequate vertical resolution (8 m) of the spatial T data did not allow for the direct estimation of Equation 4.2 term 3, which accounts for changes in T_a due to the horizontal divergence of the flux from the correlated vertical perturbations of mixed layer temperature and velocity (or deviations from the depth mean values). Typically this term is considered to be relatively small and is ignored (Emery, 1976; Moisan and Niiler, 1998). With the mixed layer in the EPWP often very slab-like, or well-mixed with relatively uniform velocities over its depth, it is expected that the influence of term 3 on changes in T_a over week+ timescales is also small for this particular case.

With the intent of forming a rough estimate of the upper-bound influence of term 3 on net changes in T_a over the EPIC timeseries, $\hat{\mathbf{u}}$, $\hat{T}$, and the vertical integration of their correlation over the mixed layer were calculated using MMP and ADCP data from the EPIC timeseries. The depth-integrated correlations show relatively large fluctuations (up to ± 0.01 m s^{-1} $^\circ$ C^{-1}) , dominant at the diurnal period, with an expected average value over the 19 days of $\pm 8 \times 10^{-4}$ m s^{-1} $^\circ$ C^{-1} (bootstrap method at 95%). The maximum expected gradient is taken to be twice the confidence limits of the average correlations (for two gradient directions) divided by the first-differencing scale. The appropriate value of the differencing scale is likely to be related to the dominant scales of $\mathbf{u}$ and T variability within the mixed layer, which are on the order of $>$ 60 km. At these scales term 3 has a minor influence on the net change in T_a over the 19 days, with an upper-bound estimate of $\pm 0.05^\circ$ C, or about 15 times smaller than the influence of term 5 $[Q - Q_s(-h)]$. If the estimated flux differences occur on scales $\leq$ 20 km, however, then term 3 may become important to the mixed layer temperature budget on timescales of several days or longer.

C.2.4 Calculating Advective Fluxes from 10/2002 to 10/2003

With no mixed layer current velocity data available for 2001, we investigated the role of the advective flux term in the annual mixed layer temperature budget using a combination of TAO buoy velocities at 10° N, 95° W spanning 10/2002 to 10/2003 and TRMM satellite SST from the same period. TAO buoy velocities were recorded with the Sontek Argonaut single-point ACM at a depth of 10 m with averaging over 20 minute intervals. Freitag et al. (2002) estimate that the long-term bias error is less than 0.02 m s^{-1}. Horizontal gradients of T_a are estimated using 3 day-averaged, 0.25° spatial resolution, daily TRMM SST. Gradients ($\Delta T_a/\Delta x$ and $\Delta T_a/\Delta y$) are estimated from a linear fit to the SST data over a distance of 220 km (8 data points), which results in the best agreement with the gradients measured by the *New Horizon* during the EPIC timeseries (Fig. C.3). As with the estimation of gradients using the *New Horizon* data, the results are sensitive to the chosen scale of the linear fit (Fig. C.4). Accounting for this uncertainty, bias error in the current velocities and considering error introduced by estimating T_a with SST, we roughly estimate an uncertainty of $\pm 5°C$ over a year.

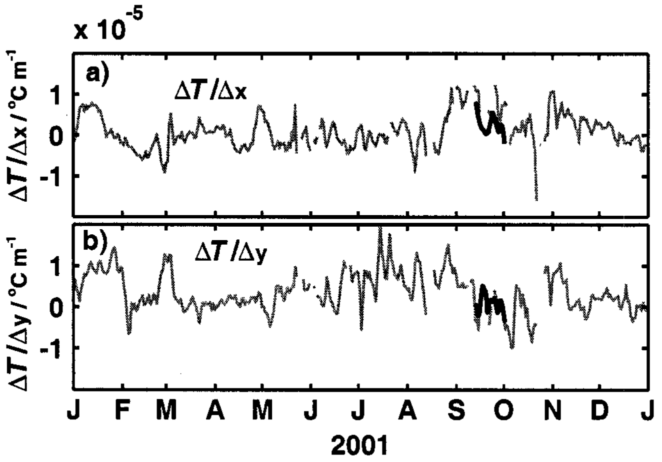

Figure C.3: Comparison of zonal (panel a) and meridional (panel b) temperature gradients estimated from TRMM satellite SST (gray) with those computed from the EPIC timeseries spatial survey (black). TRMM satellite SST gradients are estimated with a linear fit over 220 km (8 data points). EPIC timeseries gradients are computed over 80 km, which had the closest agreement with the satellite estimates of ∇T_a. The disparity of scales is potentially due to the different sampling methods and possible aliasing of larger scales by the comparatively slow sampling of the R/V *New Horizon*.

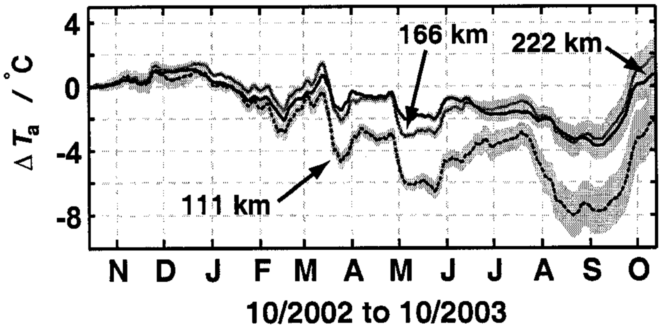

Figure C.4: Comparison of expected advective ΔT_a using various linear fit scales for the computation of ∇T_a from TMI SST data. Gray shading indicates an estimate of potential bias error introduced by the ACM current measurements (± 0.02 m s^{-1}).

Appendix D

NOTATION

Table D.1: Notation

E_p	depth-integrated mixed layer available potential energy
b	buoyancy
b'	turbulent fluctuations of buoyancy
CGCM	coupled global climate model
c_p	specific heat of seawater
E	evaporation rate
Fr_T	turbulent Froude number
g	gravitational acceleration
h	mixed layer depth (top of the seasonal thermocline)
h_e	entrainment depth
h_i	instantaneous mixed layer depth
h_b	SBL depth or mixing layer depth
H_s	significant wave height
$J_b,\ \overline{w'b'}$	vertical turbulent buoyancy flux
J_b^{sw}	buoyancy flux equivalent of shortwave radiative heat flux
$J_b(0)$	total surface buoyancy flux
$J_b(0)^-$	stabilizing (negative) surface buoyancy flux
$J_b(0)^+$	destabilizing (positive) surface buoyancy flux
$J_q,\ \rho c_p \overline{w'\theta'}$	vertical turbulent heat flux
$J_s,\ \overline{w'S'}$	vertical turbulent salt flux
$J_b^e,\ \overline{w'b'}\|_{-h}$	entrainment buoyancy flux
$J_{b,r}^e,\ \overline{w'b'}\|_{-h}$	residual entrainment buoyancy flux
$\tilde{J}_b^e$	modeled entrainment buoyancy flux
$J_q^e,\ \rho c_p \overline{w'\theta'}\|_{-h}$	entrainment heat flux
$\tilde{J}_q^e$	modeled entrainment heat flux
$J_s^e,\ \overline{w'S'}\|_{-h}$	entrainment salt flux
J_b^*	surface forcing term of entrainment model
K_ρ	vertical turbulent diffusivity of density
K_S	vertical turbulent diffusivity of salt
K_T	vertical turbulent diffusivity of temperature
L	Monin-Obukhov lengthscale
L_O	Ozmidov lengthscale
L_{rms}	root-mean-square displacements within an overturn
L_{ot}	overturn scale
N	buoyancy frequency
OGCM	ocean general circulation model
P	precipitation rate

Q	total surface heat flux
Q^{sw}	shortwave heat flux
Q^{lw}	longwave (IR) surface heat flux
Q^{s}	sensible surface heat flux
Q^{r}	rain surface heat flux
Q^{l}	latent surface heat flux
q^2	turbulent kinetic energy
r	Pearson correlation coefficient
r_{no}	Pearson correlation coefficient in $\log_{10}$-space
r_{log}	correlation of lognormally-distributed variables
Ri	finescale (8-m) gradient Richardson number
Ri_b	mixed layer bulk Richardson number
Re_T	turbulent Reynolds number
R_ρ	density ratio
S	salinity
S'	turbulent fluctuations of salinity
SBL	surface boundary layer
Sh	vertical shear
Shx, Shy	zonal and meridional vertical shear
T	*in situ* water temperature
T'	turbulent fluctuations of *in situ* water temperature
T_a	depth-averaged mixed layer temperature
$\hat{T}$	deviations of mixed layer $T(z)$ from T_a
u	zonal water velocity
u_a	zonal depth-averaged mixed layer velocity
$\hat{u}$	deviations of mixed layer $u(z)$ from u_a
U_i	mixed layer inertial velocity magnitude
$\vec{\mathbf{U}}_i$	mixed layer inertial velocity vector
$\vec{\mathbf{U}}$	mixed layer velocity vector
u', v', w'	turbulent velocity fluctuations
v	meridional water velocity
v_a	meridional depth-averaged mixed layer velocity
$\vec{\mathbf{v}}$	slab model mixed layer velocity magnitude
$\hat{v}$	deviations of mixed layer $v(z)$ from v_a
w	vertical water velocity
w_e	entrainment velocity
w_{Ek}	Ekman pumping velocity
U_{10}	wind speed at $z = 10$ m
u_*	turbulent friction velocity
w_*	turbulent convective velocity scale
ε	viscous dissipation rate of turbulent kinetic energy
ν	molecular viscosity

θ	potential temperature
θ'	turbulent fluctuations of potential temperature
ρ	density
ρ'	turbulent fluctuations of density
ρ_θ	potential density
σ_θ	ρ_θ-1000
τ	surface wind stress
κ	Von Karman's constant (0.40)

VITA

John Mickett was born in New Haven, Connecticut. He received a Bachelor of Science degree from the U.S. Coast Guard Academy in 1994 with a focus on Marine Science and, upon graduation, reported for his first assignment as the navigator aboard the U.S. Coast Guard Cutter *Planetree* stationed in Ketchikan, Alaska. In 1996 John was reassigned to Coast Guard Marine Safety Office Hampton Roads in Norfolk, Virginia, and served as the Chief of the Port Safety and Security Branch and as a Command Duty Officer. John left the active duty Coast Guard in 1999 and joined the Coast Guard Reserves to pursue a Master's degree in Physical Oceanography at the University of Washington, which he completed in December of 2003. In August 2007 he earned a Doctor of Philosophy from the University of Washington in Physical Oceanography.